CLEAR-AIR ANALYTICAL AND EMPIRICAL K-FACTOR DETERMINATION AND CHARACTERIZATION FOR TERRESTRIAL MICROWAVE LOS LINK APPLICATIONS

ABRAHAM MUTUNGA NYETE

UNIVERSITY OF KWAZULU-NATAL

OCTOBER 2013

CLEAR-AIR ANALYTICAL AND EMPIRICAL K-FACTOR DETERMINATION AND CHARACTERIZATION FOR TERRESTRIAL MICROWAVE LOS LINK APPLICATIONS

by

Abraham Mutunga Nyete

Dissertation submitted in fulfillment of the requirement for the degree

MASTER OF SCIENCE IN ENGINEERING: ELECTRONIC ENGINEERING

in the

School of Engineering

UNIVERSITY OF KWAZULU-NATAL

October 2013

Supervisor: Prof. Thomas Joachim Odhiambo Afullo

As the candidate's supervisor, I have approved this dissertation for submission.

Signed…….. Date……

Name: Prof. Thomas J.O. Afullo

Declaration 1 - Plagiarism

I, **Abraham Mutunga Nyete**, declare that

1. The research reported in this thesis, except where otherwise indicated, is my original research.

2. This thesis has not been submitted for any degree or examination at any other university.

3. This thesis does not contain other persons' data, pictures, graphs or other information, unless specifically acknowledged as being sourced from other persons.

4. This thesis does not contain other persons' writing, unless specifically acknowledged as being sourced from other researchers. Where other written sources have been quoted, then:

a. Their words have been re-written but the general information attributed to them has been referenced

b. Where their exact words have been used, then their writing has been placed in italics and inside quotation marks, and referenced.

5. This thesis does not contain text, graphics or tables copied and pasted from the Internet, unless specifically acknowledged, and the source being detailed in the thesis and in the References sections.

Signed ..... Date: 25/10/2013

Abraham Nyete

Declaration 2 – Publications

The following list of papers has been published and part of the work in them has been used in this dissertation:

Published journal papers:

1. **Abraham M. Nyete** and T. J. O. Afullo, "Seasonal distribution modeling and mapping of the effective earth radius factor for microwave link design in South Africa," *Progress In Electromagnetics Research B Journal*, vol. 51, pp. 1-32, 2013, ISSN: 1937-6472.

In this paper, three-year seasonal curve fitting and kernel models of the k-factor are developed for the seasons of February, May, August and November for Seven locations in South Africa using k-factor statistics processed from radiosonde data obtained from the South African Weather Service for a three year period (2007-2009). These seasonal models are optimized using the integral of square error. From these models, median k-factor values are obtained. Two spatial interpolation techniques: inverse distance weighting (IDW) and kriging are then used to interpolate the seasonal discrete median k-factor data to cover the rest of South Africa where data measurements were unavailable. The root mean square error (RMSE) is used to compare the performance of the interpolation techniques. Four semivariogram models are used for the kriging interpolation, and the model that produces the least interpolation error is used for contour mapping of the median k-factor for South Africa, together with the IDW method.

Published conference papers:

1. **Abraham M. Nyete** and T.J.O Afullo, "Non-parametric and parametric modelling and characterization of the effective earth radius factor for South Africa," *Progress In Electromagnetics Research Symposium Proceedings*, Taipei, Taiwan, March 25-28, 2013, pp. 653-659, ISBN: 978-1-934142-24-0.

In this paper, both parametric (curve fitting) and non-parametric (kernel density estimation) three-year annual models of the k-factor for seven locations in South Africa are formulated from radiosonde data obtained from the South African Weather Service for a three year period (2007-2009). The models are optimized using the integral of square error (ISE) criterion. From these models and the measured probability density scatter plot, median and effective values of the k-factor are obtained. A comparison of the obtained k-factor values is also done. The error performance comparison of the two methods used for the modeling and characterization is also carried out. The different kernels used for the modeling are also compared in terms of the ISE.

2. **Abraham M. Nyete** and T. J. O. Afullo, "Interpolation and mapping of the median k-factor for terrestrial link applications in South Africa," *IEEE AFRICON2013 Conference Proceedings*, 9-12 September 2013, Mauritius, pp. 208-211, ISBN: 978-1-4673-5941-2.

In this paper, both inverse distance weighting and kriging interpolation methods are used to extend three-year annual discrete median k-factor statistics for seven locations in South Africa to cover the rest of the country. The k-factor statistics are processed from radiosonde measurements obtained from the South African Weather Service for a three year period (2007-2009). Both the root mean

square error and the mean absolute error criteria are used to compare the performance of the interpolation techniques. Results of the interpolated median k-factor values are then represented in the form of contour maps.

3. **Abraham M. Nyete** and T. J. O. Afullo, "On the application of radial basis functions for the interpolation of the seasonal effective earth radius factor for South Africa," *Southern Africa Telecommunication Networks and Applications Conference*, 1-4 September 2013, Spier, Stellenbosch, Western Cape, South Africa, pp. 365-368, ISBN: 978-0-620-57883-7.

In this paper, radial basis functions are explored for the interpolation of three-year seasonal median k-factor data for seven locations in South Africa. The k-factor data is processed from radiosonde data obtained from the South African Weather Service for a three year period (2007-2009). Two radial basis functions; the thin plate splines and the multiquadrics, are used for the interpolation. The root mean square error and the mean absolute error are used to compare the interpolation error performance of the two radial basis functions used. The method that produces the least errors is taken as the best method, and its interpolation results are then presented in form of contour maps of the median k-factor for South Africa for the months of February, May, August and November.

Signed…..... Date: 25/10/2013

Abraham Nyete

Acknowledgements

First and foremost, I wish to thank Jehovah, the Lord God Almighty for granting me perfect health and other resources, to be able to complete this work without missing even a day. Secondly, I wish to extend my heart felt gratitude to my supervisor, Prof. Thomas Joachim Odhiambo Afullo for his unending support and positive criticism throughout the period of the study. His guidance and suggestions throughout the study period cannot go unmentioned.

Thirdly, I wish to extend my warm salutation to my dear wife, Lilian Kenyuri Nyamwamu, for painstakingly taking care of our two sons, Allan Nyete and Alvin Mutungwa, during the entire study period.Additionally,i wish to thank my dear mum Agnes Kavele Nyete and my late dad Joel Nyete for taking care of me for all the days of my life. I would also not forget to thank my brothers and sisters for their support and prayers during this journey. Without their encouragement and permission to leave and pursue this dream, this dissertation would not be a reality today!

Lastly, I wish to thank my senior colleagues, Peter Akuon, Mike Asiyo, Akintunde Alonge and Adetan Wumi for their support and guidance throughout the study period. I also wish to thank my office colleagues, Rasigan Govender and Fulatsa Zwane for creating an enabling environment for the successful completion of this work, and all the times we shared. I also thank the University of Nairobi and University of KwaZulu-Natal management for granting me this opportunity to pursue graduate studies. So many other people contributed in one way or another towards the successful completion of this work, but all their names can't be listed here; but i wish to thank them also.

To all of you, may God shower his blessings upon you, show you mercy and grant you his favour always.

Abstract

The transmission media, that is, the atmosphere, through which terrestrial and satellite signals traverse, is irregular. Thus, one requires proper knowledge on how variations in atmospheric refractive conditions will affect the optimal performance of terrestrial and satellite links. Under clear-air conditions, atmospheric changes will mainly involve variations in atmospheric pressure, relative humidity and temperature, which are the key to defining the way signals are refracted as they travel from the transmitter to the receiver. Accurate knowledge of these variations can be acquired through proper modeling, characterization and mapping of these three atmospheric quantities, in terms of the refractive index, refractivity gradient or the effective earth radius factor (k-factor).

In this dissertation, both parametric and non-parametric modeling and characterizing, interpolation and mapping of the k-factor for South Africa is done. Median ($k_{50\%}$) and effective ($k_{99.9\%}$) k-factor values are the ones that determine antenna heights in line of sight (LOS) terrestrial microwave links. Thus, the accurate determination of the two k-factor values is critical for the proper design of LOS links by ensuring that adequate path clearance is achieved, hence steering clear of all obstacles along the radio path. Thus, this study is critical for the proper design of LOS links in South Africa. One parametric method (curve fitting) and one non-parametric method (kernel density estimation) are used to develop three-year annual and seasonal models of the k-factor for seven locations in South Africa. The integral of square error (ISE) is used to optimize the model formulations obtained in both cases. The models are developed using k-factor statistics processed from radiosonde measurements obtained from the South African Weather Service (SAWS) for a three year period (2007-2009).

Since the data obtained at the seven locations is scattered, three different interpolation techniques are then explored to extend the three-year annual and seasonal discrete measured k-factor values for the seven locations studied to cover the rest of the country, and the results of the interpolation are then presented in the form of contour maps. The techniques used for the interpolation are kriging, inverse distance weighting (IDW) and radial basis functions (RBFs). The mean absolute error (MAE) and the root mean square error (RMSE) are the metrics used to compare the performance of the different interpolation techniques used. The method that produces the least error is deemed to be the best, and its interpolation results are the ones used for developing the contour maps of the k-factor.

Table of Contents

List of Figures

List of Tables

Chapter 1

Introduction

1.1 Motivation

There has been a tremendous demand for the transmission of high volumes of data, voice and video traffic over wireless media recently, especially with the widely used Global System for Mobile Communications (GSM), Universal Mobile Telecommunications System (UMTS), popularly known as 3G, and Long Term Evolution (LTE) mobile networks for land mobile wireless communications. These rapid and dynamic demands have led to even greater need for the design of reliable and high availability terrestrial Very High Frequency (VHF), Ultra High Frequency (UHF), microwave and millimeter-wave radio link networks necessary for the transmission of this traffic over the wireless channel (atmosphere). Even with the use of the fiber networks becoming more and more common, to take care of the high volumes of backbone traffic, there is still need for the use of terrestrial links for the access (last mile) and distribution layers of transmission networks and even for backbone (backhaul) transmission using high capacity radios where the deployment of fiber is not possible due to terrain constraints. Radio links are often preferred due to their lower deployment cost, ease of installation, ability to transmit data over rugged and irregular terrain, reliability, ability to reduce or even avoid right-of-way bottlenecks, ease of growth (expansion), negligible operational costs and better adaptation to handle natural calamities like earthquakes [1].

However, the transmission media, that is, the atmosphere, through which terrestrial as well satellite signals traverse, is irregular and not ideal [2]. Thus, one requires proper knowledge on how variations in atmospheric refractive conditions from time to time, place to place and with height will affect the optimal performance of terrestrial and satellite links. As such, poorly designed radio links will experience periodic outages, which in turn leads to decrease in system throughput, increase in system latency and in worst case scenario, total system failure, and thus loss of revenue. The changes in atmospheric conditions will mainly involve variations in atmospheric pressure, relative humidity and temperature [3], which are the key to defining the way signals are affected as they travel from the transmitter to the receiver, mainly under the so called clear-air conditions. Prior and accurate knowledge of these variations can be acquired through proper modeling, characterization and mapping of these three atmospheric quantities, in terms of the refractive index, refractivity gradient or the effective earth radius factor (k-factor). However in precipitation conditions, rain still remains the predominant threat to the proper and reliable performance of terrestrial wireless links operating in the 10 GHz and above range. Under clear-air conditions, however, the variations in the refractive properties of the atmosphere will result in signal distortion mainly due to multipath fading as a result of surface reflection, diffraction fading, multipath cross-polarization discrimination (XPD) reduction, and beam spreading. Atmospheric gas attenuation is also a major challenge under clear-air propagation conditions [4]. Multipath propagation occurs when a signal travelling from the transmitting antenna to the receiving antenna follows more than one path resulting in different copies of the transmitted signal arriving at the receiver at different time delays, amplitude and phase from the main signal. Such effects occur when the signal is reflected by the ground or building walls or in the presence of severe atmospheric temperature inversion layers, which in turn lead to extreme refractive gradients [5, 6].

Another major cause of clear-air signal attenuation is diffraction (k-factor) fading. Diffraction fading occurs when the signals are obstructed as they traverse the atmosphere between the transmitter and the receiver. The source of obstruction could be multiple objects or a single knife-edge obstacle. If there is a clear line-of-sight between the transmitter and the receiver, and the wrong value of the effective earth radius factor (k-factor) is used for the link design, the signal could bend either towards or away from the earth severely resulting in diffraction fading. Thus the correct local k-factor should be used during link design if its available or different path profiles drawn for various values of the k-factor, and the one that provide the desired path clearance used in the design. The k-factor is critical for accurate antenna height determination using the procedures outlined in [4]. The use of proper antenna heights ensures that the required path clearance is achieved in an economical way. Hence, accurate determination of the point refractivity statistics necessary for the computation of the k-factor is a critical success factor in attaining adequate path clearance to avoid any problems associated with diffraction fading. In [7], emphasis is placed on the need for local determination of the refractivity and refractivity gradients necessary for the determination of the k- factor. In [8], Olsen notes that radioclimatological databases are sparse and the ones that are available are not up-to-date, and the situation is even worse in the African continent, with most of the databases thirty years or even older. This situation is compounded by the lack of proper institutional framework necessary to carry out meaningful research as well as lack of enough resources in terms of technical knowledge and funds. Also, radiosonde launches, a great source of data necessary for the accurate determination of the refractivity characteristics of the troposphere, are expensive and most of the meteorological stations are scattered. Therefore, even in cases where the radiosonde data measurements are available, they are scattered, and there remains a challenge to extend the measurements to cover all the regions within a particular area, for example, around a whole country or across a continent.

Therefore, even after the successful determination of radioclimatic variables necessary for accurate modeling and characterization of the atmospheric effects on radio link performance under precipitation and clear-air conditions, there is need to extend the results of such study to enable total coverage of the radioclimatic variable under study across a particular region. This would entail the use of different techniques for modeling, interpolation and mapping of the radioclimatic variables. Modeling techniques would range from parametric to non-parametric approaches. Parametric methods are characterized by different coefficients like the mean, median, variance, percentiles and standard deviation, among others. These coefficients are always key in providing a summary of the distribution of any variable. Some parametric methods include the Log-normal, Weibull and the Gaussian (normal) distributions. Non-parametric methods require modeling directly from the data. They include histograms and the kernel density estimation.

Interpolation techniques are used to predict the value of the variable in areas where data is not available. Some interpolation techniques include; inverse distance weighted (IDW), kriging, radial basis functions (RBFs), minimum curvature method, modified shepard's method, nearest neighbor, natural neighbor, polynomial regression, triangulation with linear interpolation, moving average, as well as the data metrics technique [9, 10]. Of these techniques, three spatial interpolation techniques are the most widely used. They are the IDW, kriging and RBFs [11]. Spatial interpolation techniques are based on the proposition that things that are closer to one another are more similar than those further apart [12]. Spatial interpolation differs from modeling in that it take into account the

geographic position of the measured data points. Some of the methods, for example, kriging, have the advantage of incorporating information regarding the degree and extent of dependence between the data points at different locations- referred to as spatial autocorrelation or covariance [13, 14].

The current study is focused on the determination of the k-factor for South Africa. The study is specifically aimed at understanding the distribution of the effective earth radius factor for South Africa through parametric and non-parametric modeling and characterizing, interpolation and mapping. The k-factor statistics can be determined mainly from radiosounding data measurements or using meteorological sensors placed at regular or irregular intervals on a tower or even using the refractometer mounted on an aircraft, which is a more expensive method [15, 16]. Meteorological radiosounding data can be obtained from weather service stations for a particular period. From the radiosounding data, atmospheric parameters of pressure, humidity and temperature are normally extracted for the determination of the refractivity gradient. The refractivity gradient statistics are then used to compute the k-factor from the procedures outlined in [7]. From the k-factor statistics obtained, mainly for the first 200 m above ground level, it is possible to model and characterize the distribution of k-factor with a view to determining the median ($k_{50\%}$) and effective values ($k_{99.9\%}$) of the same. The k-factor statistics for the first 200 m above ground level are critical since this is where much of terrestrial communication takes place; most communication masts are less than 200 m in height [17]. Accurate determination of local median and effective values of the k-factor is necessary since the refractive properties of the atmosphere change with geographical location. As such, the four thirds (4/3) value of the median and 0.67 value of the effective k-factor, given for average temperate climate may only be used for gross planning. Where local data is available, the same should be determined and used for optimum link budgeting. This will minimize wastage of resources by avoiding unnecessarily long or short antennas that may result in expensive reverse engineering or optimization procedures [4, 18].

There is continued research in the area of atmospheric refraction. Most of the work is concentrated on the analysis of refractivity statistics, refractivity gradients and less often on the k-factor. These studies are mainly focused on the daily, weekly, monthly and annual variations of these refraction statistics, (see for example [16, 19-22]). Little work has been done on a regional basis with regard to mapping these statistics especially in Africa. Also, not much effort has been applied to develop a universal model that can be used to predict the effective earth radius behavior across different regions as is the case with precipitation modeling and measurements studies. The work in this study is aimed at filling in the gaps that do exist in so far as efforts to develop a universal model and maps for the k-factor are concerned. And, it is believed that this approach can be adopted in different regions in a more aggressive campaign aimed at updating the current clear-air databases as well as developing new models and maps of the k-factor distribution. In the Southern African region, Palmer and Baker were able to develop a novel empirical cumulative distribution model of the k-factor for South Africa which was found to be more suitable for summer inland rainfall areas. They also used results obtained using the model to develop a contour map of the k-factor exceeded 0.001 of the time for South Africa [23, 24]. Odedina and Afullo have also reported on the k-factor for Maun, Botswana and Durban, South Africa [18, 20].

1.2 Research Questions

The basis of this study is to model, characterize and map the effective earth radius factor for South Africa using radiosonde data. The study seeks to evaluate the seasonal, annual and geographical variability of k-factor with the ever changing atmospheric composition through non-parametric and parametric data modeling and as well as interpolation and mapping. Some of the keys issues to be looked at include but not limited to:

1. What are the different methods used in the determination of refractivity gradients?
2. How does the k-factor vary from place to place, season to season, and annually?
3. What are the different ways of modeling and characterizing the k-factor?
4. What are the options available for the interpolation and mapping of the k-factor?
5. What is the significance of the k-factor in wireless communication systems?

1.3 Objectives of the Study

The following are the objectives of this study:

1. To determine the seasonal and annual median and effective values of the k-factor.
2. To model and characterize the seasonal and annual values of the k-factor.
3. To interpolate the seasonal and annual values of the k-factor.
4. To map the seasonal and annual values of the k-factor.

1.4 Research Methodology

The followings steps will be applied to accomplish the objectives of this study:

1. Literature Review: This is to establish a theoretical background of the subject matter and related literature and highlight on the progress made so far on the research area by different researchers.
2. Data gathering: Radiosonde data measurements will be obtained from the South African Weather Service (SAWS).
3. Data processing and analysis: This will involve extraction of raw air temperature, air pressure and relative humidity measurements from the radiosonde data. Correlation equations and expressions necessary for the determination of the k-factor will then be formulated.
4. Modeling and characterization: Both parametric and non-parametric models of the k-factor will be determined from the raw k-factor statistics.
5. Comparison and validation of results obtained with those obtained by other researchers.
6. Mapping and Interpolation: Discrete seasonal and annual values of the k-factor will be extended to cover the whole of South Africa by utilizing an error-based interpolation approach for optimized k-factor contours.

1.5 Significance of the Study

Proper knowledge on the characteristics of the atmosphere under clear-air and precipitation conditions is necessary for the design of cost-effective, reliable and high availability radio links. This

will ensure optimal performance of the links hence increased revenues for telecommunication providers as well as a satisfied clientele. The k-factor is the key to ensuring that links do not suffer from diffraction (k-factor) fading related problems. As such, the k-factor is the single radioclimatic variable used for the accurate determination of appropriate antenna heights in terrestrial link design applications. Appropriate antenna heights will ensure optimal utilization of initial set up capital and avoid unnecessary reverse engineering and optimization processes. Thus the determination of the local effective and median k-factor for South Africa will add value to the proper design of terrestrial communication links.

The work by Odedina and Afullo only covered one location in South Africa (Durban) and another one in Botswana (Maun). Thus, the current study is intended to extend and confirm the results obtained in their study for Durban. Given the paucity of their data, no effort was made to map the k-factor for South Africa and this will also be addressed in the current research. In addition, the work by Palmer and Baker was mainly carried out using ground data and they were only able to develop maps of the k-factor exceed 0.001 of the time. In this study we have extended their work by developing maps of the k-factor not exceeded more than 50% of the time and values exceeded 99.9% of the time. The data used here is also extended to 200m above ground level which gives a better value of the k-factor averaged over this height range since that is where much of terrestrial communication takes place. Actual models for the distribution of the k-factor over this range for most of the locations they obtained k-factor values for will also be developed, both parametrically and non-parametrically. Thus, overall, the gaps that left behind by Odedina and Afullo, and Palmer and Baker will be addressed in the current study as well as bringing new ideas into this area of research.

1.6 Scope of the Dissertation

This study is concerned with the distribution of the k-factor in South Africa and does not seek to cover regions outside South Africa. It does not delve into diffraction fading measurements and modeling, which is a consequence of poor k-factor choices, but is strictly restricted to the accurate determination of the k-factor which is sufficient in addressing any diffraction fading issues in terrestrial links. The study is also not concerned with other link impairments ranging from rain, gas to multipath effects and their related radioclimatic variables.

1.7 Organization of the Dissertation

The rest of the dissertation is organized as follows:

Chapter two deals with the basics of radio link engineering. The necessary steps required for the proper design of radio links is discussed in detail. The chapter also addresses the issue of the power budget, which determines the robustness of any radio link. Frequency planning is also discussed with a specific look at the way efficient radio frequency channel assignments can be achieved.

Chapter three delves into signal propagation through the troposphere, with a major focus on clear-air propagation. The different mechanisms through which the signal propagates are treated here. Also, different clear-air wireless propagation models are presented. Previous work one on the k-factor in the Southern Africa region is also presented here. Finally, the chapter addresses the refraction of

electromagnetic waves as they traverse the troposphere. The radio refractivity and the k-factor as well as their importance are discussed.

In chapter four, modeling and characterization of the k-factor is done. Both annual and seasonal curve fitting and kernel models of the k-factor for seven locations in South Africa are determined. From these models both the seasonal and annual median and effective values of the k-factor are then determined. Comparisons of the seasonal and annual median and effective values of the k-factor obtained from measurements, curve fitting and kernel models are finally drawn.

Chapter five deals with the interpolation and mapping of the measured discrete values of the k-factor. Three spatial interpolation techniques namely, the inverse distance weighting, kriging and radial basis functions are used. The root mean square error and the mean absolute error are used to compare the performance of the three spatial interpolation techniques. The best performing method in terms of the error criterion is then used to map the annual and seasonal k-factor values for South Africa.

In chapter six, conclusions of the study are presented. Recommendations for future work are also presented here.

Chapter 2

Terrestrial Microwave Line of Sight Radio Link Engineering

2.1 Introduction

The proper design and installation of terrestrial microwave radio links cannot be over-emphasized owing to its impact on the link availability and reliability. However, the task requires good planning and understanding of the terrain in which the link will be installed as well as frequency allocation constraints that could be a potential bottleneck due to inference problems. Terrestrial microwave links may comprise of either a single hop or several hops depending on path length. The hops typically span over a distance of between 10 km to 100 km [3]. Terrestrial links can be used for carrying both analogue and digital traffic. Different rules that are rooted in mathematical equations and formulae as well as various models that can either be empirical or analytical, and many other complex procedures and analyses are critical for the proper design of terrestrial links. However, all these cannot be a substitute for practical experience as well as sound engineering judgements that are necessary to avoid common errors that might result in system downtime. A solid transmission plan is the beginning of a sound link design. This plan outlines the deliverables for the design as well as specific performance criteria that has to be met. A full understanding of what the end product would look like and customer needs could be the most difficult task in the initial stages of the link planning. Thus the design process is usually iterative in nature for the optimal design objectives to be met. It is important that the radio link engineer understands the levels of the quality desired and any risks that have to do with failure of the transmission resulting from the adoption of a particular design methodology or topology [25].Often, the design goals have to be converted to a route diagram before any planning process that is detailed can start. Detailed link planning would entail the transformation of the route plan into the actual link design and the identification of both proper active and passive repeater stations as may be deemed necessary. This is needed for the radio planner to be able to carry out a thorough radio survey so as to accurately plan the tower stations and routes.

There has been a tremendous evolution of radio equipment since the first one by Marconi and therefore the choice of the right radio equipment is key to ensuring cost-effectiveness of the design as well as its high performance. Therefore, the designer needs to thoroughly understand the characteristics as well as the configurations of the various radio equipment required to build the link/network. Anomalous propagation conditions normally affect the performance of the link and therefore proper knowledge of attenuation sources and propagation mechanisms will ensure that the link designed is able to withstand harsh climatic conditions like very heavy rainfall or extreme refractivity gradients. The radio link engineer is also required to identify suitable frequency bands that the link will use for operation in consultation with the regulatory authorities. Thus the engineer will have to apply for the allocation of available radio frequency channels. The radio link engineer also has to possess a good knowhow on how to do an efficient and accurate frequency plan. The performance of most radio links will be affected by the following factors: frequency of operation, transmit power, atmospheric conditions, terrain profile, hop length, antenna type, as well as coupling and waveguide losses.

The rest of this chapter is devoted to the basics of the microwave link planning and budgeting, and frequency planning and management.

2.2 Radio Link Planning

The planning of new radio links as well as the expansion and re-design of existing links is a very common occurrence today since these links are the key to traffic transmission in the access or backbone layers of the transmission network for Global System for Mobile communications (GSM), Universal Mobile Telecommunications System (UMTS) and Long Term Evolution (LTE) networks, which are the key modes of land mobile communications currently. Most of the transmissions between Base Stations (BTSs), Base Station Controllers (BSCs) and Mobile Switching Centres (MSCs) are still interconnected using radio equipment, even as fibre optic communication slowly replaces radio in cases where there are huge volumes of traffic to be carried. However, in very hilly and extremely difficult terrain, only radio and satellite links can be used to carry traffic and therefore radio links remain relevant all along. Transmission teams in mobile companies as well as those companies that offer transmission bandwidth for lease, always get involved with upgrades and rolling out of new links/networks on a very regular basis. Such a process would involve several steps to ensure that the whole exercise is procedural and produces optimal results with all the design goals met. The main steps involved in the planning of a new link would comprise of the following [3, 25, 26]:

1. Planning brief
2. Initial planning and selection of sites
3. Path profiling
4. Site survey

It is important to point out that link planning is not just as straight forward as these steps may imply, but it actually takes an iterative procedure among the steps until the best design is achieved. Figure 2.1 is a flow chart of some of the possible link planning procedures with possible iterations shown by arrows.

2.2.1 Planning Brief

This is the first step in effectively rolling out a successful radio link. In this stage, the services required and related bandwidth is defined as well the end-to-end connections plus the desired performance goal. The services to be transmitted could include voice, data, video and broadcast television traffic. It is at this stage that a proper understanding of the number of links or circuits required and associated bandwidth is defined. This ensures that the engineer can then freely choose from the design options at his proposal. The design engineer will have to fully understand the problem statement of what he is supposed to implement at this stage. The engineer will need to understand how traffic aggregation will be made to the existing links and where to make inserts or drops. This Engineer will have to make a brief report on how he intends to implement the link and the processes and key items that critically will determine the success or failure of the whole process.

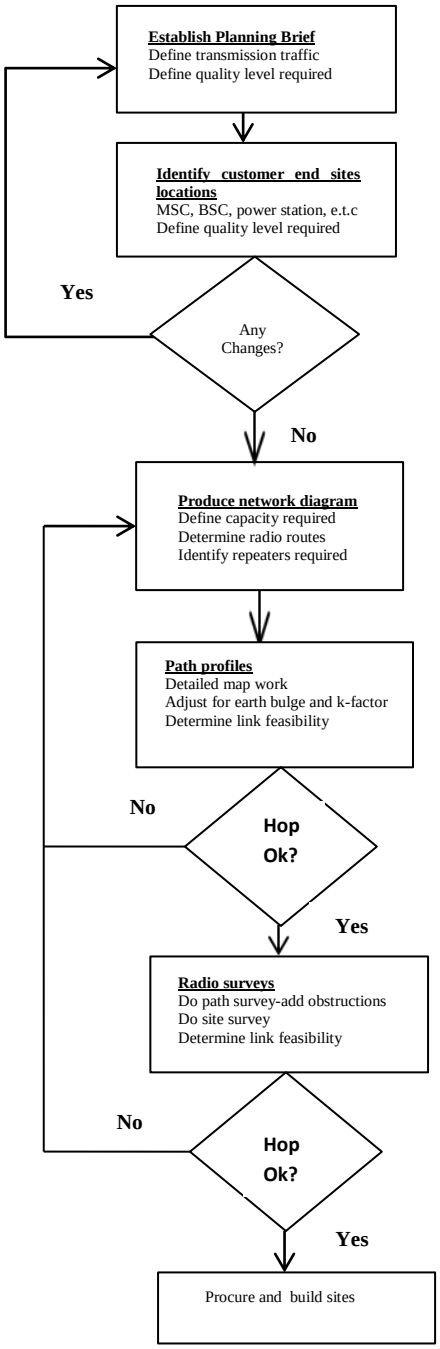

Figure 2.1: Link planning flow chart [25]

2.2.2 Initial Planning and Selection of Sites

The main aim of this particular step is to develop an initial topology showing how the radio link/network will look like and the way different network elements will be interconnected. A circuit diagram with the connections and link capacities is developed. Practically, development of the network is iterative in nature owing to the physical placement of different features on the actual sites

where the links are to be installed and other coverage issues that may arise during the network roll out. Allocations for different connection capacities like E1, E3 or STM links are considered here so as to get an idea of the bandwidth requirements and type of radio equipment that may be required for the task. The next step would involve the assignment of the actual site locations (coordinates).

The location of radio link towers is a critical issue due to the path clearance criteria and has to be carefully dealt with in line of sight radio links. As a first but very necessary step, ensuring the physical (optical) line of sight between the transmitting antenna and the receiving antenna is of paramount importance. In the modern world of link planning, there are different software planning tools that utilize Global Positioning System (GPS) readings to specifically locate the site coordinates. These software-based tools have made link planning easier but they require proper understanding of their use to avoid unnecessary errors. For the best results, though expensive, GPS systems operating in differential mode or surveyed coordinates with beacons and a theodolite are used [25]. In addition, the traffic to be carried by the link must be quantifiable in terms of the number of data, voice and video channels or just the aggregate capacity in terms of the bit rate for digital links. The growth and expansion projections and any possible upgrades should also be catered for here. In general, growth considerations may affect some of the following [3]:

(i) Air conditioning and space requirements
(ii) Bandwidth allocations
(iii) Installation redundancy
(iv) Equipment compatibility considerations

The length of the route will impact on the number of hops that a single terrestrial link can have. A short link will comprise of a single hops while a long one will comprise of many hops. In long links there may be necessity to install repeater sites between the transmitting and receiving end of the link for the sole purpose of boosting the transmitted signal which normally gets attenuated for every kilometre travelled. However, it is upon the designer to ensure that the number of repeater stations is minimum while at the same time not compromising the availability and reliability of the radio network. This ensures that there is cost-effectiveness in the link design while at the same time not compromising on quality.

The initial choice of site locations will almost entirely depend on the path clearance and the availability of other resources like land and electricity and the different points at which the link will be interconnected with other existing network infrastructure. The path clearance is normally visualised once the path profile is drawn. But, before making the final decision on where to plant the sites, the following factors must be put into considerations [3, 27]:

(i) Land/space availability
(ii) Site accessibility
(iii) Regulatory guidelines and rules
(iv) Site topography
(v) Area climatic conditions
(vi) Possibility of anomalous propagation conditions
(vii) The maximum hop length
(viii) Angle offsets and tilts from hop to hop

(ix) The necessity to include repeater sites
(x) Existing structures within the chosen site area

In summary, the initial planning and choice of site locations involves the following [27]:

(i) Regulatory guidelines and restrictions
(ii) Identification of the terminal ends of the link
(iii) Identification of the required capacity as well as the service to be carried
(iv) Statement of quality goals to be met
(v) Frequency planning
(vi) Radio equipment selection
(vii) Development of the network topology

After a successful tentative choice of site locations, the actual design will iteratively involve the following [27]:

(i) Configuration and design of the hops
(ii) Performance prediction for each hop
(iii) Marking of critical hops
(iv) Revision of the chosen site locations and routes
(v) Revision of the design and configuration of hops

2.2.3 Path Profiling

A path profile graphically represents the path between the transmitting antenna and the receiving antenna [25, 28]. From the path profile, the height of the radio towers are derived, and the necessary adjustments carried out to ensure that adequate path clearance is achieved, mainly for the first Fresnel zone. The same should also be done to avoid any reflective surfaces from coming into contact with the signal. Path profiling is mainly done using three common methods [3, 28]:

1. 4/3 Earth method
2. Curvature method
3. Fully linear method

1. 4/3 Earth method: In this method, the $R = 4/3$ earth paper is needed. Also, the real obstacle heights along the path can be used. The greatest limitation of this method is that the value of k-factor is fixed at 4/3. Figure 2.2 shows an example of a path profile using this method.

2. Curvature method: This method utilizes a linear graph paper. Here, the actual obstacle heights are also used. A reference straight line and then a curved line are drawn from the transmitter to the receiver and vice versa. The curvature of the curved line is kR, where k is the chosen k-factor and R is the actual radius of the earth.

3. Fully linear method: In this method, a straight line from the transmitter to the receiver is drawn on a common linear graph paper producing a tangential clearance above all obstacles.

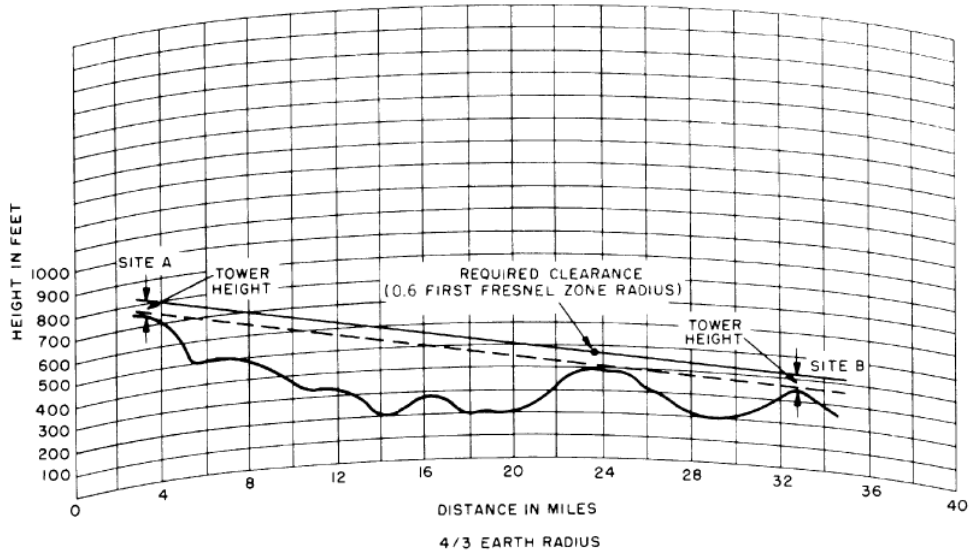

Figure 2.2: An example of a path profile using $R = 4/3$ earth graph paper [3].

Another straight line is also drawn from the receiving antenna to the transmitting antenna. The refraction of radio waves is usually compensated by adjusting the height of each obstacle by an equivalent earth bulge given by [25, 28]:

$$h = \frac{d_1 d_2}{12.75k} \tag{2.1}$$

where h is the vertical distance change from the horizontal reference line and d_1 is the distance from the transmitting antenna to the obstacle, d_2 is the distance from the obstacle to the receiving antenna. This method is preferred since it allows for the testing of different values of the k-factor on the same chart and eliminates the need for any spherical earth curvature paper or plotting of curved lines; that is, only straight lines are plotted. This makes path profiling more efficient and a lot easier. From the initial path profile plot, one is then able to make the necessary adjustments for the k-factor and earth bulge variations to ensure that an optical line of sight exists between the transmitter and the receiver. The following steps outline the procedure for path profile plotting [3, 18]:

Step 1: On the topographical map, draw a straight line between the transmitter and the receiver.

Step 2: Mark any points of obstruction along the path as well as any reflection points. Draw the horizontal location at each of these points on the graph paper.

Step 3: Mark the path mid-point, which is normally treated as an obstacle since it represents the point of maximum earth bulge.

Step 4: Compute the k-factor. If local measurements are not available, plot the path profiles for the following k-factor values; 1.33, 1.0 and 0.5. After the field survey, the appropriate value can be chosen.

Step 5: Compute the earth bulge for each obstacle using equation (2.1).

Step 6: Calculate the clearance of the first Fresnel zone for all the obstacles as well as the mid-point.

Today, due to technological advancements in transmission planning, the use of software planning tools is the method adopted by many radio equipment companies. The path profile drawn using these software tools are based on the fully linear method. Figure 2.3 shows one such profile generated using computer software for a 6.73 km LOS link between Howard College and Westville Campuses of the University of KwaZulu-Natal, Durban, South Africa.

2.2.4 Site Survey

This entails a physical assessment of the locations where the radio links are to be installed and mainly serves as a verification exercise of what is contained in the path profile, among other tasks. The following is summary of some of the information that needs to be gathered during the site visit [3, 25, 27]:

(i) A sketch of the actual site locations as well as photographs of the same.
(ii) A short description of the site locations, for example, soil types, vegetation, accessibility, drainage and terrain physical features.
(iii) A short path description. The path should be surveyed and any special features marked. Any features that the topographical map may have missed out on should be included.
(iv) A report on commercial power availability with regard to distance, phase frequency and voltage as well as feeder sizes.
(v) Accessibility to resources such a diesel fuel or natural gas.
(vi) A documentation of any zoning restrictions and regulations.
(vii) A report of any seismic activities.
(viii) A record of weather/climatic conditions.
(ix) A report on the accessibility of the sites and sketches of possible routes.
(x) A report on Electromagnetic Interference (EMI) tests.

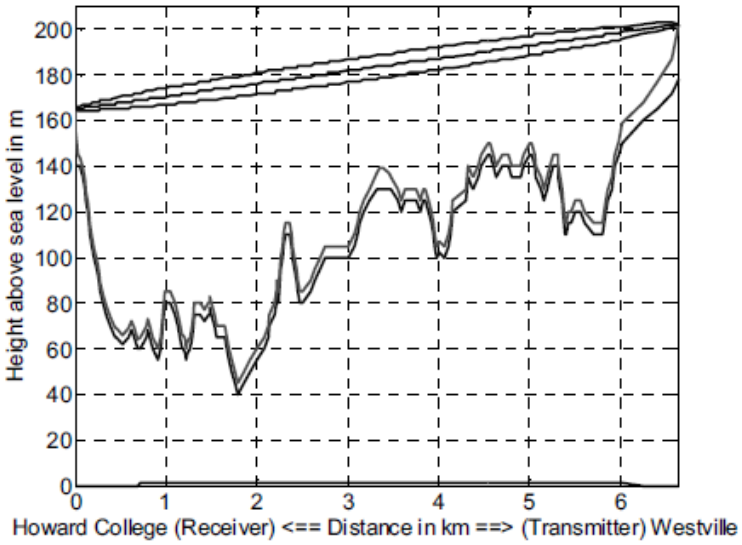

Figure 2.3: Computer-generated path profile [29].

2.3 The Link Budget

The link budget refers to the mathematical composition of the transmit power, receive and transmit gains and all losses associated with environmental factors, cable connections, antenna misalignments and other miscellaneous losses [2, 3, 25, 27] for the communication link. The link budget is also sometimes referred to as the power budget [25] or path analysis [3, 30]. For link planning purposes, a link budget is normally prepared that puts into account the transmitter and receiver gains, coupling losses, cable losses, waveguide losses, transmit power as well as a safe fade margin. The received signal level and the receiver sensitivity are important in determining the probability of any system outage occurring. The difference between the nominal received power and the receiver sensitivity is usually referred to as the fade margin. In the most basic form, the link margin is usually computed using the following expression [2]:

$$Link\ margin\ (dB) = EIRP + L_p + G_{rx} - TH_{rx} \tag{2.2}$$

where $EIRP$ is the effective isotropically radiated power, L_p is the path loss, G_{rx} is the gain of the receiver and TH_{rx} is the receiver threshold.

The link margin is dependent on several factors, among them: the modulation scheme, transmit antenna power, antenna gains, coupling and waveguide losses, radome loss as well as the path loss [2]. The modulation scheme used will affect the fade margin by impacting on the bit error rate or signal-to-noise ratio (SNR). The antenna gains, other transmission losses and the transmit power will have a direct impact on the fade margin as well as the received signal level. The path loss mainly comprises of the free space loss as well as other losses due to weather or environmental conditions. We note here that, some literature works use the terms path loss and free space loss (free space path loss) interchangeably to mean the same thing but the two are used in this context with reference to different losses. The link margin is usually an indication of how robust a link is. A very small link margin would mean that the link is not very robust unless of course the losses and gains are thoroughly understood and characterized. For a safe link margin, the designer will also have to include some fading allowance for other losses which are not always present like multipath, diffraction and rain fading, so as to ensure that the availability of the link remains as high as possible. A typical example of a link budget for a terrestrial millimetre wave link is shown in Figure 3.4 below.

It is always the norm to take into account all the parameters in the link budget to ensure that the designer can replicate the calculations if desired. To this effect, the antenna polarizations and frequency of operation can also be included in the link budget. Link budget formats and what it should contain is a hot issue but the basic items relating to transmit and receive power, antenna gains and path loss are always part of the link budget. As such, Figure 2.4 is just one example and is not exhaustive in any way.

2.3.1 Path Loss

The path loss is the component of most significance as far as the link budget is concerned, and to a large extent in so far as RF and microwave propagation is concerned. The path loss is comprised of free-space loss, absorption loss mainly due to gases and water vapour, and any other losses that are

function of the frequency used and weather/environmental conditions. This equation includes the gains of the antennas. The gains of the antennas describe the directivity as well as the efficiency of the antenna, while all the other terms in the equation account for the spherical wave-front spreading [2, 30].

Some of the additional losses that cannot be quantified are usually accounted for by ensuring that the link margin is sufficient, so as to ensure accurate prediction of the received signal level and the resultant SNR. In most of the cases, the radio equipment manufacturers will specify the magnitude of the losses. Otherwise, an experienced link designer can still estimate the allowance accurately. Some of these losses are related to band-limiting and/or modulation losses [2].

Frequency	38.6 GHz
Wavelength	0.0078 m
Polarization	Vertical
Link Distance	2 km
Tx Power	10.0 dBm
Tx Loss	-1.5 dB
Tx Antenna Gain	32.0 dB
Radome Loss	-2.0 dB
EIRP	**38.5 dBm**
Path Loss	-130.2 dB
Tx Pointing Error	-1.0 dB
Atmospheric Loss	-0.2 dB
Total Path Losses	**-131.4 dB**
Radome Loss	-2.0 dB
Rx Antenna Gain	32.0 dB
Polarization Loss	-0.2 dB
Rx Loss	-2.0 dB
RX Pointing Error	-1.0 dB
Total Rx Gain	**26.8 dB**
RSL	**-66.1 dBm**
Interference Margin	-1.0 dB
Rx Noise Figure	7.0 dB
Noise Bandwidth	25.0 MHz
Total Noise Power	**-93.0 dBm**
Signal-to-Noise Ratio	8.9 dB
Threshold	-88.0 dBm
Link Margin	**21.9 dBm**

Figure 2.4: Sample detailed link budget: partially adopted from [2].

Filters used in the transmission equipment control spectral spreading but in turn create additional insertion losses, since some modulation schemes are less efficient due to transmit carrier components. Sometimes, the gain of the antenna is reduced and its noise level increases if there is a radome covering it. The problem is even escalated further is the radome is wet or dirty. Therefore, it is of paramount importance that the waveguides are firmly fixed and the proper choice of coaxial cables for the particular frequency of operation be made. In most point-to-point radio links, directional antennas are normally used so as to increase the amount of energy directed at the receiver. This could in effect lead to increase in transmit range or a reduction in transmit power close to the link. Poor alignment of directional antennas leads to pointing losses. Also depending on the orientation of the transmitter and the receiver polarization vectors and the axial ratio, varying degrees of polarization losses will occur. Transfer of power is usually affected by polarization vector mismatches. At high frequencies, rain, water vapour as well as oxygen absorption losses are very significant attenuation components. In the most basic form, the path loss can be computed from the following expression [2, 3, 30]:

$$PL\ (dB) = FSL + FM + L_{misc} \tag{2.3}$$

where PL is the path loss, FM is the budgeted fade margin and L_{misc} represents all the other miscellaneous losses discussed in this sub-section and others that may not have been mentioned.

2.3.2 Receiver Sensitivity

The receiver sensitivity is also known as the receiver threshold and it refers to the minimum signal power that the demodulator and decoder at the receiver require so as to work at specific bit error rate (BER) without any errors [25, 31]. In most cases these thresholds will be defined in terms of the minimum power in decibels that the receive antenna requires to function without errors or the bit error rate at which the receiver operates without any errors. Two thresholds are defined in terms of the BER, one at 10^{-3} and another at 10^{-6}. The BER of 10^{-3} is based on the cut-off BER for audio applications while that at 10^{-6} is based on the minimum BER required for acceptable data throughput. In Asynchronous Transfer Mode (ATM) applications, for example, which constitutes part of 3G cellular networks (UMTS), a BER of 10^{-9} is needed, which then raises concerns about how suitable radio links are for this kind of application [25]. It is observed that under zero fading conditions, radio links operate at a BER of 10^{-3}, similar to fibre systems, and therefore the debate is only about where the cut-off threshold should be defined, especially given that networks today are integrated using different technologies. In many radio applications, a BER of 10^{-6} is normally used due to concerns about data transmission. The receiver threshold is normally determined by the SNR at the receiver input, receiver's front-end noise figure and the thermal noise (p_n) given by [25]:

$$p_n = kTB \tag{2.4}$$

where k is the Boltzman constant ($1.38 \times 10^{-23}\ J/K$), T is the kelvin temperature and B is the bandwidth. Usually, the radio equipment manufacturer will specify the receiver threshold with regard to different frequencies of operation.

2.3.3 Link Budget Power Parameters

The definition of different terminologies with regard to the different power parameters that can be measured or described at different points of transmission along the radio path is critical for understanding the power budget and what can be measured at what point along the link. Some of the power parameters are defined below.

a) Effective isotropic radiated power (EIRP)

This refers to the algebraic sum of the transmit power output, transmit antenna gain and the transmission losses pertaining to the different connection elements at the transmit antenna. It is given by [30, 31]:

$$EIRP\ (dBW) = P_{tx} + G_{tx} + L_{tx} \tag{2.5}$$

where P_{tx} is the transmit power, G_{tx} is the transmit antenna gain and L_{tx} is the total sum of the losses at the transmit antenna.

b) Isotropic receive level (IRL)

This refers to the power that impacts on the receiver. This would specifically be the power measured at the isotropic receiver base. It is the algebraic sum of the $EIRP$, free-space loss and other absorption losses. It is given by [3, 30]:

$$IRL\ (dBW) = EIRP + FSL + L_a \tag{2.6}$$

where L_a is the absorption loss and FSL is the free space loss.

c) Receive signal level (RSL)

This refers to the power that enters the initial active stage of the receiver including receiver losses. It is the algebraic sum of the IRL, the receiver gain and the receiver line losses. It is also referred to as the nominal receive power [27, 32]. It is given by [2, 27, 32]:

$$RSL\ (dBW) = IRL + G_{rx} + L_{rx} \tag{2.7}$$

where G_{rx} is the receiver gain, L_{rx} receiver losses. Therefore, the RSL can be directly computed from individual gains and losses and transmit power from [31]:

$$RSL\ (dBW) = P_{tx} + G_{tx} + L_{tx} + FSL + L_a\ \ + G_{rx} + L_{rx} \tag{2.8}$$

Depending on the information available, the sum of the FSL and the L_a can be replaced by the path loss. The RSL, can also be computed from [33]:

$$RSL\ (dBW) = P_{tx} + G_{tx} + G_{rx} + FSL + L_g + L_R + L_w + L_{tx} + L_{rx} \tag{2.9}$$

where L_g is the gaseous absorption loss, L_R is loss induced by rain, L_w is the loss arising from antenna wetness or dirtiness. All in all, the RSL is calculated depending on the information available and the environmental conditions. For, example, rain would be a big determinant in areas that

receive a lot of rainfall throughout the year while multipath could be big determinant across coastal areas faced with very extreme refractive gradients.

2.3.4 Link Margin

The link margin is also referred to as the fade margin or safe operating margin (SOM). It is the difference between the received signal level and the receiver threshold [30-32]. It is given by [30-32]:

$$Link\ margin\ (dB) = RSL - RX_{sensitivity} \tag{2.10}$$

It represents the difference between what power level is measured at the receiver and what level is required for the receiver to be able to perform demodulation and decoding of the signal without errors, as pointed out earlier. By computing the link margin, one will be able to do a comparison of the different designs and determine how much "safety cushion" the link will theoretically have [31]. The higher the link margin, the better, but there are is no particular answer to the least allowance set for it, except in terms of the availability requirements and the cost considerations. However most designers agree that at least 20 dB or more will provide reasonable robustness. Some systems will work at lower values but of course their safety margin will highly compromised. This leaves the link exposed to frequent outages resulting mainly from interference, antenna misalignments, adverse atmospheric conditions, water droplets on the coaxial cable, dirt or even ice on the radome [2, 30, 31]. In the real world, the link margin is not the only factor that determines how feasible a link is, but actually the SNR is also a key indicator of the link reliability.

As the received signal level drops, the SNR also drops and the performance worsens in terms of the errors recorded, that is, the BER becomes degraded. This would essentially lead to variations in the RSL and subsequent fading. This fading phenomenon usually varies with frequency, duration as well as severity. It is almost impossible to fully eliminate fading in link design, but it is possible to moderate the effects through mitigation techniques. One of the key and available tools for such task would be a safe fade margin; in terms of the surplus decibels in the link design. If the link was designed with free space loss considered as the only source of fading, then availability requirements would only be met for about 50% of the time [30]. Time availability refers to the time percentage that the link will be able to meet BER requirements. To improve on the time availability, it is necessary to increase the link margin. But, the question is by how much. Several techniques do exist for the computation of the required safe margin. Of the many, the most common and convenient way of getting out of this is by making the assumption that the fading phenomenon follows a Raleigh distribution. Raleigh fading is considered as the most severe form of fading [30]. Based on this assumption, different link margins are applicable depending on the time availability goals as shown in Table 2.1. A sample computation of the link margin is shown in Figure 2.5 for a 2.4 GHz 20 mile link with amplifiers. In this figure, RX is an abbreviation for the receiver.

All in all, the link margin is needed for the sole purpose of coping with short term degradation of the signal levels resulting mainly from rain attenuation, multipath fading and diffraction fading. The link margin can also be expressed in terms of the threshold degradation and the equipment threshold. Threshold degradation is mainly as a result of the degrading effects of ground reflections as well as

Table 2.1: Link margins for different time availability requirements based on Raleigh fading [30]

Time availability (%)	Link margin required (dB)
90	8
99	18
99.9	28
99.99	38
99.999	48

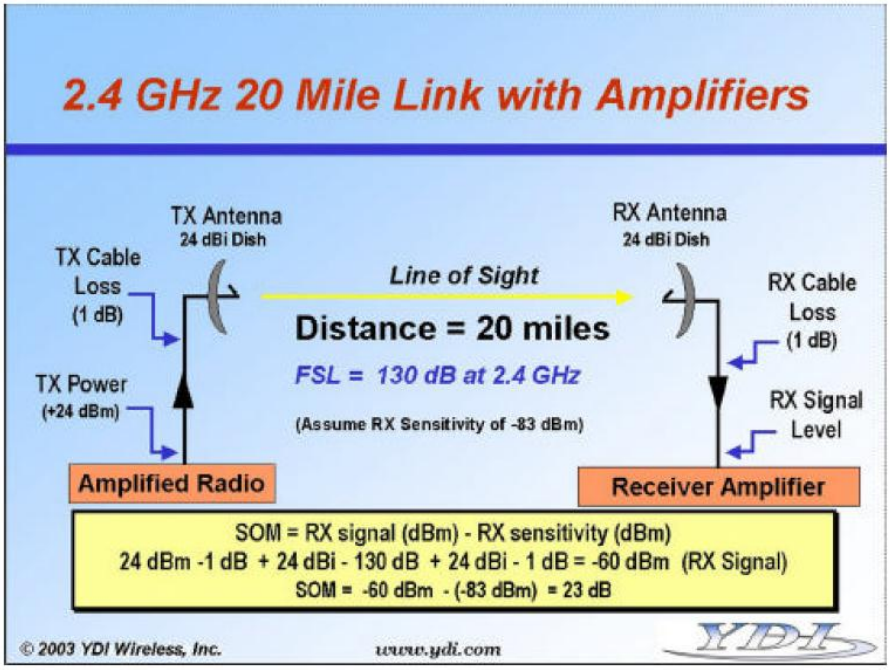

Figure 2.5: Sample link margin calculation [31].

interference. A summarized visualization of all the elements involved in the computation of the link margin is shown in Tables 2.2 and 2.3; where:

$$Hop\ threshold = Equiment\ threshold + Threshold\ degradation \tag{2.11a}$$

$$Link\ margin\ (dB) = Nominal\ recieved\ power - Hop\ threshold \tag{2.11b}$$

2.4 Frequency Planning

The continued increase in the number of services that have to be allocated a frequency band in the radio spectrum have necessitated the efficient planning and management of the radio spectrum. This in turn ensures optimum utilization of the limited available spectral resources and also eliminates the chances of interference taking place, which then results in high standards of service delivery to clients. The efficient utilization of the spectrum also forms the basis for hitless expansion of the network in the future as need arises.

Table 2.2: Detailed nominal receive power elements [27].

Power level (dBm)	Gains (dB)	Losses (dB)
Tx Power at radio equipment output flange		
		Tx Branching Filter Tx Feeder Other Tx Losses
Power at antenna input		
	Tx Antenna Gain	
		Propagation Losses: Free Space Obstruction Atmospheric absorption Other
	Rx Antenna gain	
Power at antenna input		
		Rx Feeder Rx Branching Filter Other Rx Losses
Nominal Rx Power at radio equipment input flange		

Table 2.3: Detailed fade margin elements [27].

Power	Threshold	Margin
Nominal Rx Power		
	Equipment Threshold	
	Threshold Degradation Reflections Interference	
	Rx Antenna gain	
	Hop Threshold	
		Fade margin

This then means that the issue of frequency planning should be approached from a long term perspective. The maximum utilization of the available frequency bands rests on the shoulders of the network operators and not on the frequency regulation authorities. Efficient and error-free frequency planning practices call for proper knowledge on the subject matter. The main aim of frequency

planning in a radio network is to allocate frequencies for specific transmission and reception radio frequency (RF) channels as well as specify the polarization method to be used. The management of the radio spectrum is usually overseen by regional bodies, mostly on a country basis, but the international body responsible for the coordination of spectrum management activities is the ITU-R through its Radio Regulations sector [25, 27].

The bandwidth requirement of a link is determined by the number of radio channels and the capacity of each channel. The number of channels is determined by the operational characteristics of the link to be designed with special regard to the number of active and reserve channels as well as diversity application. The most basic link would comprise of only one radio channel and it is usually termed as a 1+0 configuration. However most practical links will comprise of a number of active service channels, say K channels, as well as several other reserve channels, say L channels, and such a link would be said to have a K+L configuration. The RF channel plan for the frequency band chosen for the design determines the RF frequencies to be allocated and the ITU-R provides several guidelines on how the channel assignments should be done through its F Series Recommendations. Efficient use of the radio spectrum would most often call for the implementation of frequency reuse schemes that ensure coordinated equipment installation over a particular radius [34].

2.4.1 Frequency Management

The RF spectrum is a fixed shared resource that is not possible to extend or recreate in any way and has to be utilized for many applications, and therefore requires vigilant service assignment procedures and coordination activities. As mentioned earlier, the ITU-R is the body that deals with the international coordination of the allocation of the radio spectrum to different services through its Radio Regulations sector. However, each country has its own frequency regulatory authority whose mandate is to decide on different channel allocation schemes and what services are carried in which frequency band within the country's boundaries. Even though frequency plans in two different countries may be similar, that does not mean they are compatible, and this will call for coordination and cooperation at the switching interconnection centres between them.

Radio spectrum management falls under three distinct categories: command and control, needed for earth-space and aeronautical systems; market forces, where economic aspects are applied to ensure efficient and economical use of the spectrum and licence exempt where link registration is only allowed under specific controls such as power limitations without any assurances for interference-free operation [25]. In some countries, the frequency resources are normally purchased or leased for a period of time by the network operators from the frequency regulatory authority. Some of the frequency management and coordination bodies are discussed below.

(a) ITU-R frequency management

The ITU-R has two groups that normally handle frequency coordination and regulation activities. One of these bodies is the World Radiocommunication Conference (WRC), earlier known as the World Administrative Radio Conference (WARC), whose mandate is to assign particular frequency resources for particular current and future radio-based services. This body carries out any necessary review and revision of the existing frequency regulations and is solely responsible for governing the

use of the radio spectrum. It is through this body that different organizations push for the allocation of radio spectrum resources for any new services they want to introduce in to the market [25, 35].

The second body is tasked with the spectrum coordination activities and is known as the Radio Regulations Board (RRB), earlier known as the International Frequency Registration Board (IFRB). This body outlines the rules that govern the international frequency assignments within the limits put in place by the WRC. It also resolves any issues that are referred to it by the Bureau which could not be solved by the application of existing rules of procedure and provides any necessary guidance to other Radiocommunication Conferences and Assemblies. This board also handles appeals lodged against the Radiocommunication Bureau concerning certain frequency allocations by radio equipment manufacturers or member countries. It also gives approval of any procedural rules that are applied by the Radiocommunication Bureau in dealing with the Radio Regulation provisions and registration of frequency allocations made by member countries [36].

(b) Federal Communications Commission (FCC) frequency management

The FCC is tasked with interstate as well as international regulation of any radio communications through radio, cable, wire, satellite and television in the United States of America. The commission is organized in seven bureaus whose activities are licence application processing, dealing with any grievances from customers and frequency regulation rules formulation. The FCC's microwave body is known as the Wireless Telecommunications Bureau (WTB). The WTB has two divisions: the broadband division services which is in charge of fixed wave services and the mobility division in charge of broadband and cellular services. FCC licences are either carrier owned and usually regional or owned by the FCC and the assigned to private network operators. The FCC also requires that some antenna types be registered with it due to air safety concerns [25].

2.4.2 Terrestrial Link Frequency Bands

Today, most terrestrial links operate in the Gigahertz frequency range, largely between 3 GHz and 90 GHz [25, 27]. Depending on the chosen operating frequency, the link characteristics will be affected in terms of hop length, maximum data throughput and the dominant sources of attenuation. In the subsections that follow below, a broad classification of the different available frequency bands is presented [25, 27, 37].

2.4.2.1 Below 3 GHz

The 400 MHz band is used for microwave links that are analogue. The 1.4 GHz band is used for the design of digital links that are of low capacity. The 2.4 GHz band is reserved for unlicensed frequency links. The preferable hop length is 60 km or more. Various antenna types are used including parabolic and simple horn fed antennas.

2.4.2.2 3-11 GHz

This frequency range is mainly used for links that are of medium to high capacity and are digital. The common bands here are 4 GHz, 6 GHz, 8 GHz and 11 GHz. The 5.8 GHz band is used for unlicensed links. The optimum hop length is 50 km and the dominant sources of attenuation are rain and multipath. This frequency band requires full line of sight.

2.4.2.3 13-38 GHz

There is abundance of spectrum in this frequency range and it's mainly applied for short hop links. However, rain attenuation is usually severe in this frequency range. For 13 GHz and 15 GHz, a hop length of 30 km is deemed good enough while a 5 km hop length or less is ideally suitable for the 38 GHz band. Other bands available in this frequency range are: 18 GHz, 23 GHz, 26 GHz (ETSI), 32 GHz (new band) and 38 GHz. Here, 24GHz is also reserved for unlicensed radio links.

2.4.2.4 60-90 GHz

The main bands available in this frequency range are 70 GHz (71GHz to 76 GHz), 80GHz (81GHz to 86 GHz) and 90 GHz (92 GHz and 95 GHz). This frequency range would be economical for links with very short hops (typically 1-2 km). 60 GHz is reserved for unlicensed links in this frequency range. This band continues to gain popularity as more and more radio equipment is integrated into existing networks to support the ever expanding land mobile networks base stations, base station controllers as well as switching equipment.

2.4.3 Radio-Frequency Channel Arrangements

The particular frequency band chosen for the link is usually subdivided into several radio channels depending on the channel spacing, polarization and the transmit-receive separation adopted for the design. For most of the available bands, the ITU-R provides guidelines on how the radio channels can be derived through its F series Recommendations. These guidelines specify different channel separations, RF separation between the outermost channels and the guardband as well as the RF separation between the centre frequencies of adjacent RF channels that are on the same polarization and transmitting in the same direction. The thing with RF channel allocations is that the go channels and return channels have to be at different frequencies and separated by a reasonable band so as to allow for both uplink and downlink communication without intersystem frequency interference. Usually, this is achieved by subdividing the chosen frequency band into two equal sub-bands around a centre frequency, f_o, and then each sub-band is again subdivided into numerous radio channels depending on the modulation scheme, channel spacing and target data throughput [27,37].

RF channel assignment schemes can broadly be classified as alternated, interleaved frequency reuse and co-channel frequency reuse [3, 37]. These three RF channel assignment schemes are depicted in Figure 2.6, Figure 2.7 and Figure 2.8 respectively. From these figures several parameters stand out and they defined below:-

(a) XS- This is the separation distance between the centre frequencies of two adjacent RF channels that are transmitting in the same sub-band (same direction transmission direction) and using the same polarization scheme. This parameter is twice the channel separation in Figure 2.6 and the same as the channel separation in Figures 2.7 and 2.8., as per the ITU-R Recommendation F.1191.
(b) YS- This is the RF separation between a go and return channel that are closest to one another.

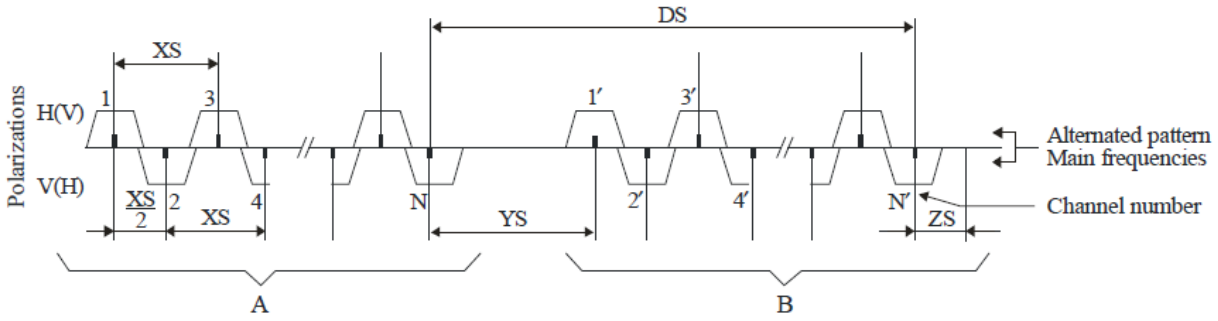

Figure 2.6: Alternated RF channel arrangement [37].

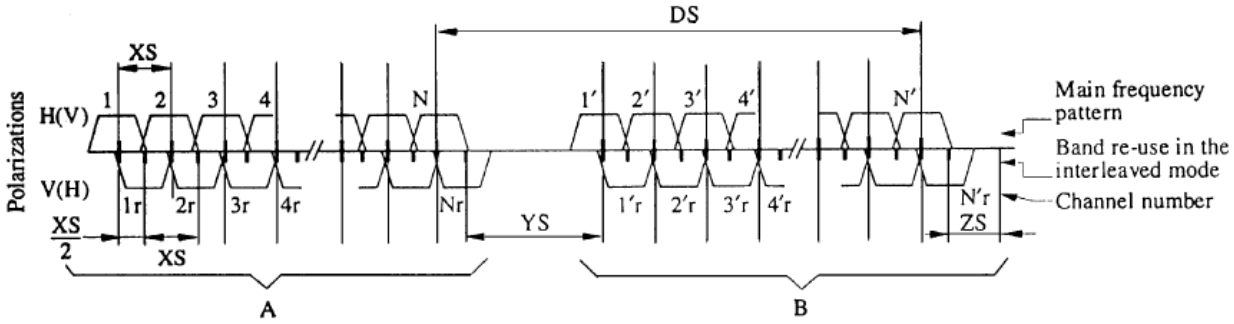

Figure 2.7: Interleaved RF channel arrangement [37].

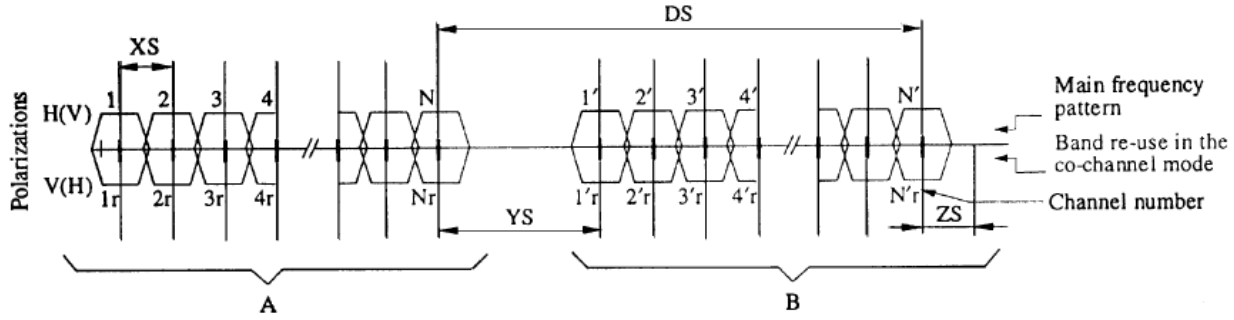

Figure 2.8: Co-channel RF channel arrangement [37].

(c) ZS- This is the RF separation between the guardband and the outermost channel. Z_1S refers to the lower band spacing while Z_2S refers to the upper separation in cases where the two are not the same.

(d) DS- This is the RF separation between two corresponding go and return RF channels, constant for each set of corresponding channels.

The choice of the RF assignment plan is dependent on the values of the net filter discrimination (NFD) and cross-polar discrimination (XPD) given by [3, 37]:

$$XPD_{H(V)} = \frac{Received\ power\ on\ polarizatio\ H(V) transmitted\ on\ \ polarization\ H(V)}{Received\ power\ on\ opposite\ \ polarizatio\ V(H) transmitted\ on\ \ polarization\ H(V)} \quad (2.12)$$

$$NFD = \frac{Received\ power\ on\ adjacent\ RF\ channel}{Received\ power\ on\ the\ main\ reciever\ after\ RF,IF\ and\ BB\ filters} \quad (2.13)$$

These two parameters contribute to the carrier-to-interference ratio (C/I) and determine the type of channel scheme best suitable to particular applications.

Alternated RF channel scheme is used if (neglecting contribution from the co-polar adjacent channel interference) [3]:

$$XPD_{min} + (NFD - 3) \geq (C/I)_{min} \text{ dB} \quad (2.14)$$

Co-channel RF channel scheme is used if [3]:

$$10\log\frac{1}{\frac{1}{10^{\frac{XPD+XIF}{10}}}+\frac{1}{10^{\frac{NFD_a-3}{10}}}} \geq (C/I)_{min} \text{ dB} \quad (2.15)$$

Interleaved RF channel scheme is used if [3]:

$$10\log\frac{1}{\frac{1}{10^{\frac{XPD+(NFD_b-3)}{10}}}+\frac{1}{10^{\frac{NFD_a-3}{10}}}} \geq (C/I)_{min} \text{ dB} \quad (2.16)$$

where NFD_a is the value of NFD evaluated at XS frequency separation, NFD_b is the value of NFD evaluated at half XS frequency separation and XIF is the XPD improvement factor of any cross-polar interference countermeasure, if implemented at the interfered receiver.

Depending on the target data rate, ITU-R Recommendation F.746-10 provides the following classification of fixed wireless system (FWS) links [37]:

(i) Low-capacity FWS links: These links are suitable for applications whose target throughput is 10 Mbit/s or less.
(ii) Medium-capacity FWS links: These links are suitable for applications whose target throughput is between 10 Mbit/s and 100 Mbit/s.
(iii) High-capacity FWS links: These links are suitable for applications whose target throughput is more than 100 Mbit/s.

As an example of how to derive the RF channel arrangement, we consider FWS whose band of operation is 10.7-11.7 GHz. The RF channel derivation proceeds as follows [38]:-

Let:

f_o be the centre frequency (MHz)

f_n be the centre frequency of one RF channel in the lower sub-band (MHz)

f_n' be the centre frequency of one RF channel in the upper sub-band (MHz)

Case 1: If the duplex spacing is chosen as 530 MHz and the carrier spacing used is 28 MHz, 14 MHz and 7 MHz, the channel arrangements is as follows:

(a) for 28 MHz

$$f_n = f_o - 505 + 28n \quad (2.17a)$$
$$f_n' = f_o + 25 + 28n \quad (2.17b)$$

where, n=1, 2... 16;

(b) for 14 MHz

$$f_n = f_o - 498 + 14n \quad (2.18a)$$
$$f_n' = f_o + 32 + 14n \quad (2.18b)$$

where, n=1, 2... 32;

(c) for 7 MHz

$$f_n = f_o - 494.5 + 7n \quad (2.19a)$$
$$f_n' = f_o + 35.5 + 7n \quad (2.19b)$$

where, n=1, 2... 65;

These RF channel arrangements discussed are illustrated in Figures 2.9, 2.10 and 2.11 respectively. More elaborate summary of RF channel arrangements are tabulated in Annexes 1 and 2. The reader is referred to the relevant F series ITU-Recommendations as given in the annexes for more details.

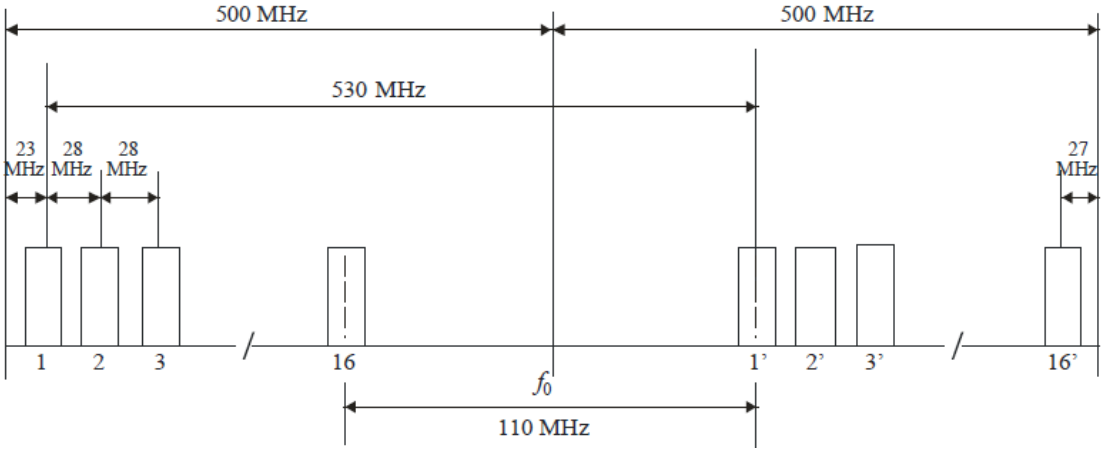

Figure 2.9: RF channel arrangement for FWS, carrier spacing 28 MHz [38].

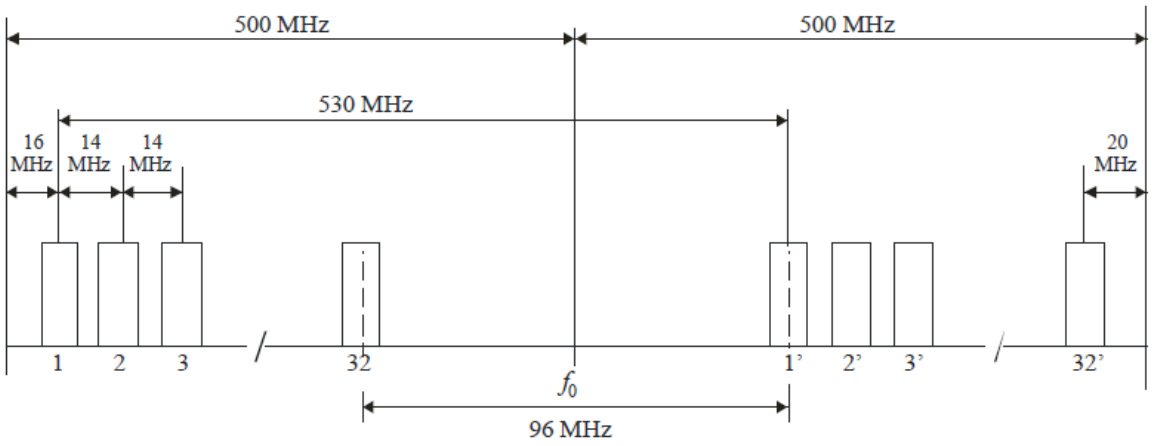

Figure 2.10: RF channel arrangement for FWS, carrier spacing 14 MHz [38].

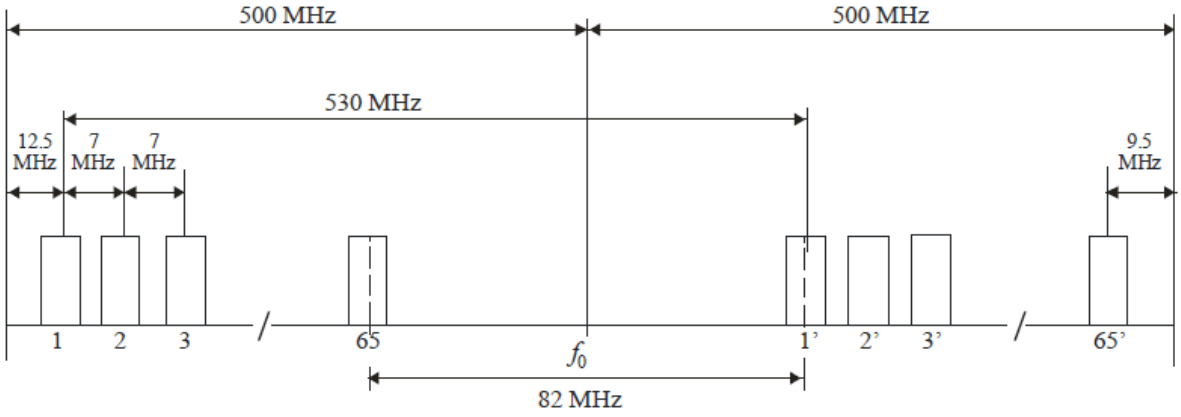

Figure 2.11: RF channel arrangement for FWS, carrier spacing 7 MHz [38].

2.5 Chapter Summary

The key to a proper link design is a robust link plan. This plan will involve the definition of the link parameters, site selection, site visit and survey, path analysis and path profiling. The link budget is a mathematical representation of all the different power parameters between the receiving and the transmitting antenna. One of the major link budget parameters is the link margin, which determines how much safety cushion a link has against outages due to all manner of fading mechanisms. The larger the link margin the more cushioned the link is and vice versa. A path profile is a graphical representation of the radio path between the transmitting antenna and the receiving antenna. Different path profiles are drawn for various values of the k-factor for cases where the local k-factor is not known and then the one that provides the required path clearance chosen for the design. Another key component of microwave link planning is the frequency plan. The frequency plan normally defines how many and how the radio channels are assigned. The common frequency channel arrangements are the interleaved, co-channel and the alternated.

Chapter 3

Clear-Air Propagation

3.1 Terrestrial Wireless Communication

3.1.1 Introduction

Wireless communications is based on the historical theoretical work of Maxwell on wireless communication using radio frequency energy and later the experimental verification of the electromagnetic wave propagation by Hertz. Wireless communications revolve around the transfer of information between the transmitter and the receiver through the use of electromagnetic radio waves over the air (atmosphere) [39]. The motivation that one is able to establish communication links without the need to use cables and the ability to communicate while on the move has evoked the desire to study and research on wireless communication. This technology evolved tremendously since Marconi first demonstrated the ability of the radio to provide communication constantly to ships that were sailing along the English Channel in 1897 and thereby deploying the first practical commercial radio in the early 20^{th} Century [39, 40]. Since then, in the decades that followed, mobile wireless communication grew in big volumes ignited by the radio frequency and digital circuit fabrication and miniaturization techniques that are able to produce portable radio equipment which are cheaper and even more reliable.

On the other hand, the use of digital techniques for the switching operations has enabled the deployment of large scale wireless networks. The use of this technology is however limited by the very inherent nature of the atmosphere. The atmosphere is very susceptible to different kinds of impairments which include multipath, diffraction and noise, among others. The presence of such impairments in turn leads to fading, time delays and sometimes complete distortion of the signal. Wireless communication systems include land mobile communication systems, direct broadband satellite (DBS) television service, wireless local area networks (WLANs), global positioning satellite service (GPS), paging systems, broadcast radio and television as well as radio frequency identification systems [39], among others.

This chapter deals with clear-air wireless propagation. Different propagation mechanisms are presented first, followed by a review of the different clear-air propagation models applicable to terrestrial microwave links. Finally, the refraction of radio waves as they travel through the troposphere is dealt with, in terms of the atmospheric radio refractivity and the effective earth radius factor.

3.1.2 Propagation Mechanisms

Although the diversity of propagation mechanisms can be wide, they can generally be attributed to three basic propagation mechanisms that impact on the propagation of signals in wireless communication systems. These three main mechanisms include diffraction, reflection, scattering [41, 42].

3.1.2.1 Diffraction

Diffraction occurs when the signal propagating through the atmosphere between the transmitting and the receiving antenna is obstructed by either a single obstacle or multiple obstacles whose dimensions are larger when compared to the wavelength of the signal, thus causing the formation of secondary waves behind the obstacle. It is also referred to as shadowing because the field that is obstructed can still reach the receiving antenna even when the obstacle is impenetrable [42]. This in effect turns a line of sight link into a non-line of sight link. A diffraction phenomenon is best described using a wave front. A wave front is a surface that is defined by a locus of points that have similar phase and path length from the source. The wave front and the ray that represents the radio wave are perpendicular to each other. The wave front problem is normally solved using the Huygens' Principle [41] which states that "Each point on a wave front acts as a source of secondary wavelets. The combination of these secondary wavelets produces the new wave front in the direction of propagation". A simple geometry of the diffraction problem is shown in Figure 3.1. In the wave front, if we take an infinitesimal surface A, the strength of the E-field generated at the receiver R by A will be dependent on the distance between them and the angle θ as shown in Figure 3.2. The phase of the E-field will also be dependent on the distance between A and R. In order to be able to compute the field in R, we consider every infinitesimal element on the wave front and then sum up all the E-fields generated by each element (Figure 3.3).

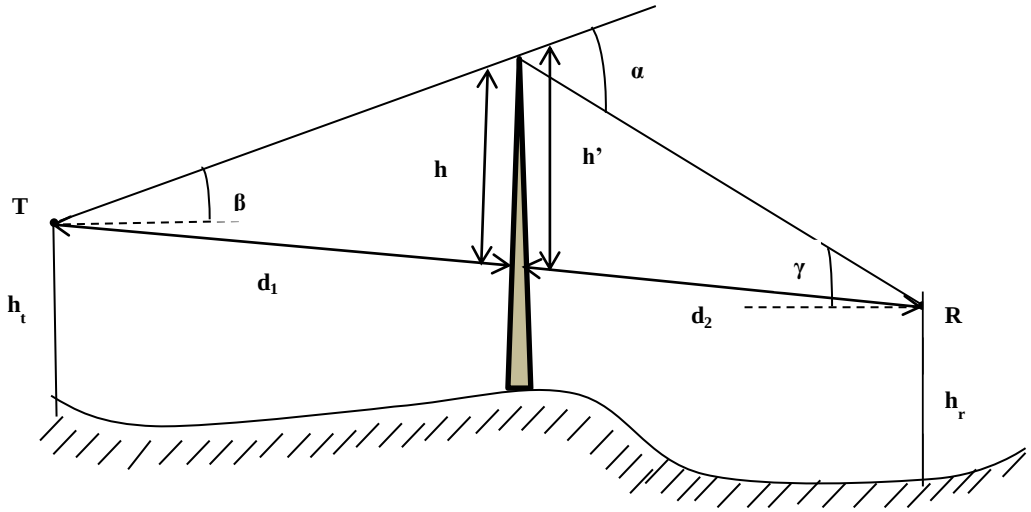

Figure 3.1: Geometry of knife-edge diffraction when the transmitter and receiver are not of the same height [43].

The vector sum of the E-fields is obtained as shown in Figure 3.4, where d_r represents an infinitesimal increment in distance. The E-field increases as far as $d_r = \lambda/2$, where the phase is π and then decreases as far as $d_r = \lambda$ where the phase is 2π.

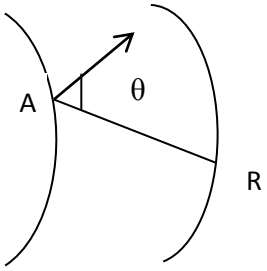

Figure 3.2: E-field generated by A in *R* [41].

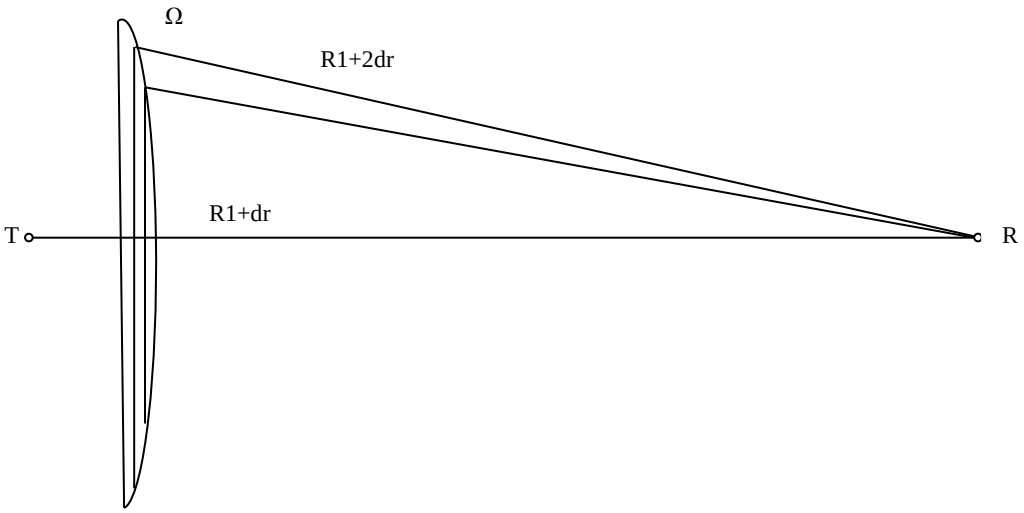

Figure 3.3: E-field generated by each infinitesimal element in *R* [41].

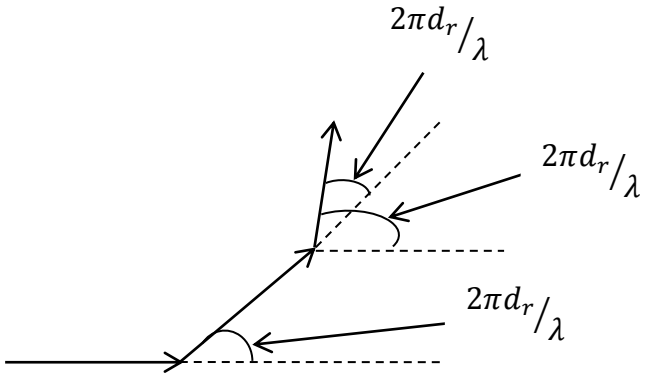

Figure 3.4: Vector sum of the E-field [41].

Diffraction loss concept as a function of path difference around an obstacle is best explained using Fresnel zones. Fresnel zones represent successive regions where secondary waves have a path length

from the transmitting and receiving terminals which are $n\lambda/2$ greater than the total path length of a LOS propagation path. Fresnel zones are characterized by an elliptic shape with the transmitter and receiver at their foci. Concentric circles (Figure 3.5), represent the boundaries of successive Fresnel zones. The successive Fresnel zones provide both constructive and destructive interference to the received signal level. The radius of the nth Fresnel zone is given by [3, 44]:

$$F_n = \sqrt{\frac{n\lambda d_1 d_2}{d_1 + d_2}} \tag{3.1}$$

where n is an integer, λ is the wavelength of the electromagnetic wave, d_1 is the distance (km) from the transmitter antenna to the point where the Fresnel ellipsoid is calculated and d_2 is the distance (km) from the point where the Fresnel ellipsoid is calculated to the receiver antenna. This expression is only valid for $d_1, d_2 \gg R_n$, where R_n is the radius of the n^{th} Fresnel zone.

3.1.2.2 Reflection

Signals travelling from the transmitting antenna to the receiving antenna undergo reflections when it impinges on a smooth surface whose dimensions are very large compared to its wavelength. This reflection causes fluctuations in in the received signal amplitude and phase and the net effect could either be destructive or constructive [41, 42]. Figure 3.6 shows the reflection of a signal that hits a wall. But, ideally, a radio wave that impinges on a smooth surface whose dimensions are large compared to its wavelength will undergo partial reflection, partial absorption and partial transmission thus resulting in undesirable phase and amplitude shifts [45]. While the reflected wave is a result of multiple reflections against a surface, for example, a wall, the net effect is usually represented as a single ray for simplicity.

When the radio wave hits a reflecting surface which is a perfect dielectric, part of the energy will be transmitted into it and part will be reflected back without any energy absorption occurring.

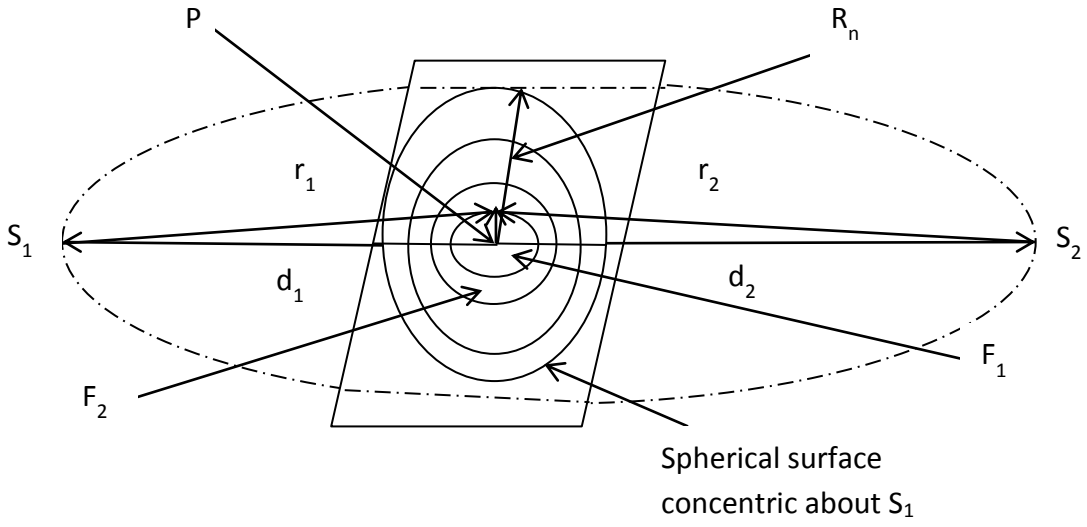

Figure 3.5**:** Successive Fresnel zones defined by the boundaries of concentric circles [3].

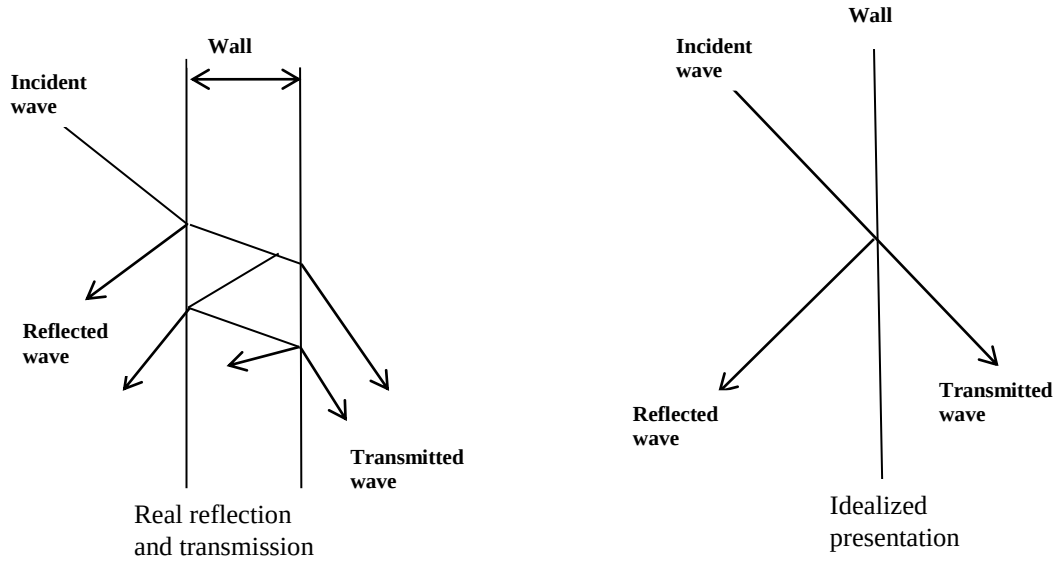

Figure 3.6: Real and idealized signal reflection on a wall [45].

However, if the reflecting surface is perfect conductor, then all the energy that is incident on it will be reflected back without any losses. The reflection of radio waves on a surface is described using the reflection coefficient.

The reflection coefficient in turn describes the relationship between the intensity of transmitted wave and the reflected waves. It is dependent on the wave's frequency, the angle of incidence, material properties of the reflecting surface, and the polarization [46, 47].

The vector sum of the reflected and transmitted waves differs from the incident wave because the multiple reflections that the wave undergoes lead to losses [45]. The dependence of the reflection coefficient on the material properties is elaborated further as shown in Table 3.1, which shows different material properties at various frequencies of operation. The relationship between the incident, reflected and transmitted wave electric field intensities for both parallel and perpendicular polarizations is shown in Figure 3.7.

Table 3.1: Different material properties at various frequencies of operation [41]

Material	Relative	Conductivity,	Frequency (MHz)
Poor ground	4	0.001	
Good ground	25	0.02	100
Typical ground	15	0.005	100
Fresh water	81	$1*10^{-3}$	100
Sea water	81	5	100
Limestone	7.51	$28*10^{-3}$	4000
Brick	4.44	$1*10^{-3}$	1000
Glass, corning 707	4	$5*10^{-3}$	1000
Glass, corning 707	4	$27*10^{-6}$	100
Glass, corning 707	4	$18*10^{-8}$	1

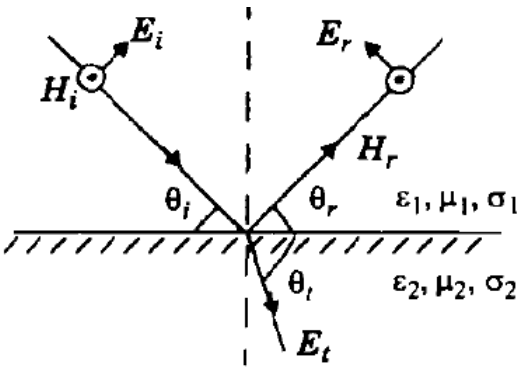

(a) E-field in the plane of incidence

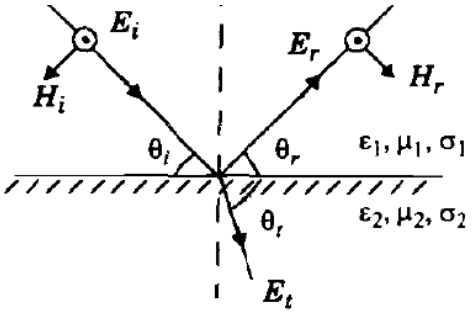

(b) E-field normal to the plane of incidence

Figure 3.7: Geometry of parallel and perpendicular polarization reflection [43]

The reflection coefficient, r_i, dependence on the type of polarization and angle of incidence and angle of transmission is summarized by the following equations [41, 46]:

$$r_{\parallel} = \frac{E_r}{E_i} = \frac{\eta_{2}\sin\theta_t - \eta_1 \sin\theta_i}{\eta_{2}\sin\theta_t + \eta_1 \sin\theta_i}, \text{ for parallel polarization} \tag{3.2}$$

$$r_{\perp} = \frac{E_r}{E_i} = \frac{\eta_{2}\sin\theta_i - \eta_1 \sin\theta_t}{\eta_{2}\sin\theta_i + \eta_1 \sin\theta_t}, \text{ for perpendicular polarization} \tag{3.3}$$

where η_i is the intrinsic impedance of the i-th material, θ_t is the angle of the transmitted wave, θ_i is the angle of the incident wave, E_r is the reflected wave and E_i is the incident wave.The boundary conditions that govern Equations (3.2) and (3.3) obey Snell's law at the surface of incidence [41]. This therefore means that the angle of incidence and that of the reflection are equal and the electromagnetic field vector of the transmitted and reflected waves is proportional to the incident one.

3.1.2.3 Scattering

Scattering propagation phenomenon takes place when the signal bumps on either a large rough surface or any other type of surface whose dimensions are in the order of its wavelength or less, thus causing the signal energy to be scattered or reflected in all directions [42]. Channel irregularities can also cause scattering to occur. Scattering may either be caused by a single object, rough surface or

several objects. These different types of scattering phenomena are shown in Figure 3.8. Scattering in many wireless communication systems is usually caused by trees, lamp posts, street signs and foliage [41, 47]. Depending on the surface roughness factor there are three types of scattering that can occur. As the value of the roughness factor increases, more energy is spread in directions that are different from the normal specular reflection (Figure 3.9).

3.1.3 Free Space Propagation Model

Free space propagation assumes that the region between the transmitting antenna and the receiving antenna is free from any atmospheric effects that may cause signal distortion mainly through reflections, multipath propagation, absorption and diffraction. Under these assumptions, within the transmitting and receiving region, the atmosphere behaves as a non-absorbing and ideal uniform medium. And furthermore, the earth is normally assumed to be having a reflection coefficient that is negligible, or being infinitely far away from the signal [42]. Normally, under the free space propagation assumptions, the signal will only be attenuated according to an inverse law. Thus, the received power will be attenuated by some factor, whose magnitude varies inversely with the square of the distance of separation between the transmitting and receiving antenna, usually referred to as the path loss, free space loss or free space loss factor.

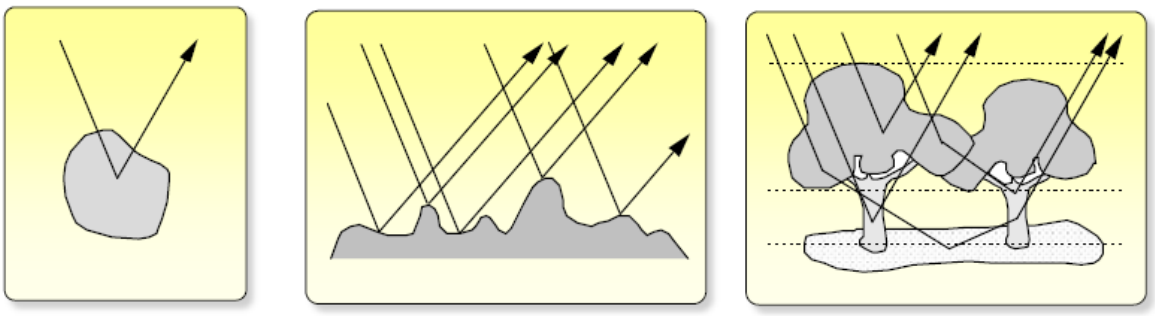

(a) Point scatter (b) Rough surface scattering (c) Volume scattering

Fig 3.8: Scattering from relatively small objects, statistically rough surfaces and volumes containing many objects [47].

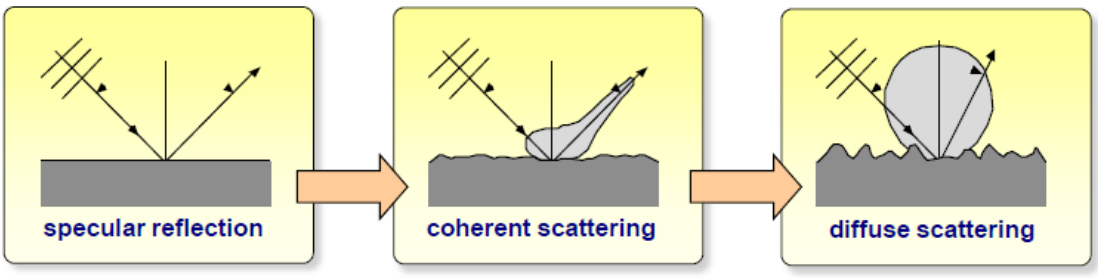

(a) Specular reflection (b) coherent scattering (c) diffuse scattering

Figure 3.9: Possible scattering mechanisms depending on the roughness factor [47].

But, for all practical purposes, this model is inadequate in describing the behavior of the signals propagating near the ground and in the troposphere and thus is not sufficient in predicting how a system is likely to perform [3, 55, 56].

Free space path loss (FSPL) is used to predict the received signal level when there is a clear line of sight path between the transmitting and receiving antennas with no obstacles to cause diffraction or reflections. On the other hand, the Friis transmission equation models the coupling between two isotropic antennas under the assumption of far-field and free-space conditions. The Friis transmission equation is of great importance in antenna and field strength measuring device design and calibration [48, 49].

If we assume that the transmitting antenna is isotropic and that its transmit power is P_{tx},then, the power radiates uniformly in all directions away from this idealized point source. The power density, p, of the plane wave incident on the receiving antenna at a distance d, from the transmitting one is given by the expression [3, 48, 50]:

$$p = \frac{P_{tx}}{4\pi d^2} \tag{3.4}$$

where d is the separation distance between the transmitting and receiving antenna.

If the transmitting antenna gain is G_{tx}, then the power density now becomes [3,48, 50]:

$$p = G_{tx}\frac{P_{tx}}{4\pi d^2} \tag{3.5}$$

Again, if the receiving antenna effective area or aperture is, A_{rx}, then the received power, P_{rx} will be given by [3,48, 50]:

$$P_{rx} = A_{rx}G_{tx}\frac{P_{tx}}{4\pi d^2} \tag{3.6}$$

The effective area or aperture for any isotropic antenna is given by the following expression; in terms of the signal wavelength and the gain of the antenna [3, 48, 50]:

$$A_e = G\frac{\lambda^2}{4\pi} \tag{3.7}$$

where λ is the wavelength of the radio signal.

Substituting for A_{rx} in terms of Equation (3.7) in (3.6), we obtain the following [3,48, 50]:

$$P_{rx} = G_{rx}G_{tx}\frac{P_{tx}\lambda^2}{(4\pi d)^2} \tag{3.8}$$

Equation (3.8) is known as the Friis transmission equation. This equation is mainly applicable to the far field, which means that both the transmitting and receiving antennas have to be at least Rayleigh distance, d_R, in separation distance. This separation distance is also commonly referred to as the Fraunhofer distance and is given by [48]:

$$d_R = \frac{2{L_a}^2}{\lambda} \tag{3.9}$$

where L_a is the biggest dimension of the antenna. Far field requires that the separation distance be much greater than the wavelength of the signal and the Rayleigh distance. On the other hand, free-space path loss does not account for such factors as the gain of the antennas or any losses associated with hardware imperfections. Thus from Equation (3.8), the path loss is given by [3, 48, 50]:

$$\text{Free Space Path Loss} = \frac{(4\pi d)^2}{\lambda^2} \tag{3.10}$$

The wavelength is related to the speed and frequency of the wave by [48]:

$$\lambda = {}^{c}/_{f} \tag{3.11}$$

where f is the frequency of the radio signal.Therefore, substituting for λ in (2.42), we obtain [3,48, 50]:

$$\text{Free Space Path Loss} = \left(\frac{4\pi df}{c}\right)^2 \tag{3.12}$$

Simply put, the free-space path loss is the ratio of the received to the transmitted signal level, ignoring the antenna gains and others sources of signal distortion and is given by [3,48- 50]:

$$\text{Free Space Path Loss} = \frac{P_{tx}}{P_{rx}} \tag{3.13}$$

It is always more convenient to express the Free Space Path Loss in terms of decibels as follows [3, 48- 50]:

$$\text{Free Space Path Loss (dB)} = 10\log_{10}\left\{\left(\frac{4\pi df}{c}\right)^2\right\} \tag{3.14}$$

$$\text{Free Space Path Loss (dB)} = 20\log_{10}\left\{\frac{4\pi df}{c}\right\} \tag{3.15}$$

If we substitute for c=$3.0 \times 10^8 m/s$ in (3.15), we obtain [3, 48- 50]:

$$\text{Free Space Path Loss (dB)} = 20\log_{10} d + 20\log_{10} f + 92.45 \tag{3.16}$$

where the distance of separation between the antennas, d is in km and the transmitting frequency f is in GHz.

Or [3, 48-50],

$$\text{Free Space Path Loss (dB)} = 20\log_{10} d + 20\log_{10} f + 32.44 \tag{3.17}$$

If d is in km and f is in MHz.

3.1.4 Diffraction Propagation Models

3.1.4.1 Single Knife-Edge Diffraction Model

Diffraction in any link is likely to occur if the choice of the minimum (effective) k-factor is not properly done. In the absence of local data, this value is often taken to be 0.67 although this value was only obtained for a 30 km radio path length in France [25]. Thus this value continues to be used, regardless of the path length, the world over, posing a challenge by increasing the chances of diffraction fading occurring along a radio path. Diffraction takes place if the signal impinges on a sharp obstacle, commonly referred to as the knife edge. Sometimes however, the signal in intercepted by several sharp obstructions leading to what is known as multiple knife-edge diffraction. Thus adequate path clearance is essential during link budgeting so as to reduce or even fully eliminate any chance of diffraction ever occurring along a radio path. Diffraction fading is a slow fading event, which therefore means that if at all it happens, link outage will be experienced for several minutes if not hours [25]. When the signal is intercepted by an obstacle, secondary signals (waves) are produced in the shadowing region in line with Huygen's principle. This scenario is depicted in Figure 3.10.

Now, we consider a transmitting antenna at point T and a receiving antenna at a point R, and a plane normal to the ray representing the electromagnetic wave from T to R as shown in Figure 3.11. If concentric circles representing successive Fresnel zones are constructed on the plane, then any wave that travels through any point on the concentric circles will definitely go through a longer distance than the direct path from T to R. The resulting excess path length can be obtained from [43]:

$$\Delta \cong \frac{h^2}{2}\left(\frac{d_1+d_2}{d_1 d_2}\right) \tag{3.18}$$

where $h \ll d_1, d_2$.

The corresponding phase difference is given by [51]:

$$\phi = \frac{2\pi\Delta}{\lambda} = \frac{2\pi}{\lambda}\left(\frac{h^2}{2}\right)\left(\frac{d_1+d_2}{d_1 d_2}\right) \tag{3.19}$$

The phase difference in (3.19) is usually expressed in terms of a non-dimensional parameter ν as follows [43, 51]:

$$\phi = \frac{\pi}{2}\nu^2 \tag{3.20}$$

The parameter ν is given by [49, 52]:

$$\nu = h\sqrt{\frac{2(d_1+d_2)}{\lambda d_1 d_2}} \tag{3.21}$$

The parameter ν is known as the Fresnel-Kirchhoff diffraction parameter.Using a simplified version of the knife-edge diffraction geometry (Figure 3.12), we can also obtain the following approximations for the excess phase difference and the parameter ν from [43, 51, 52]:

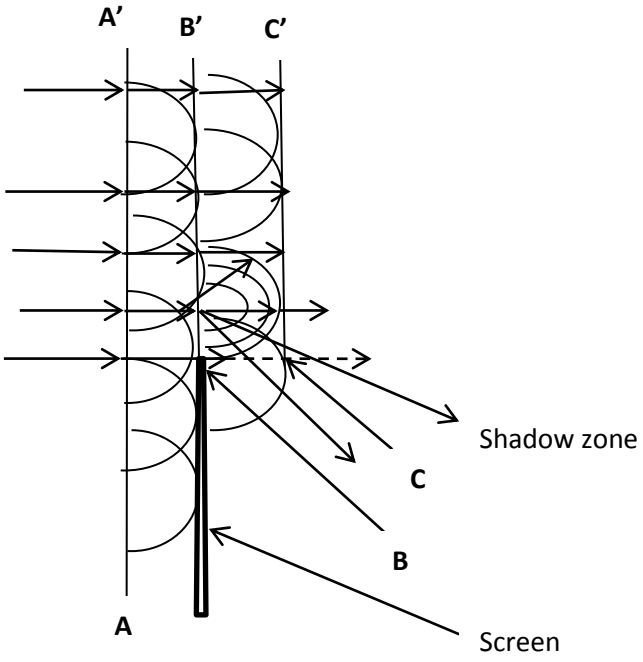

Figure 3.10: Diffraction at the edge of an obstacle (Huygen's principle) [48].

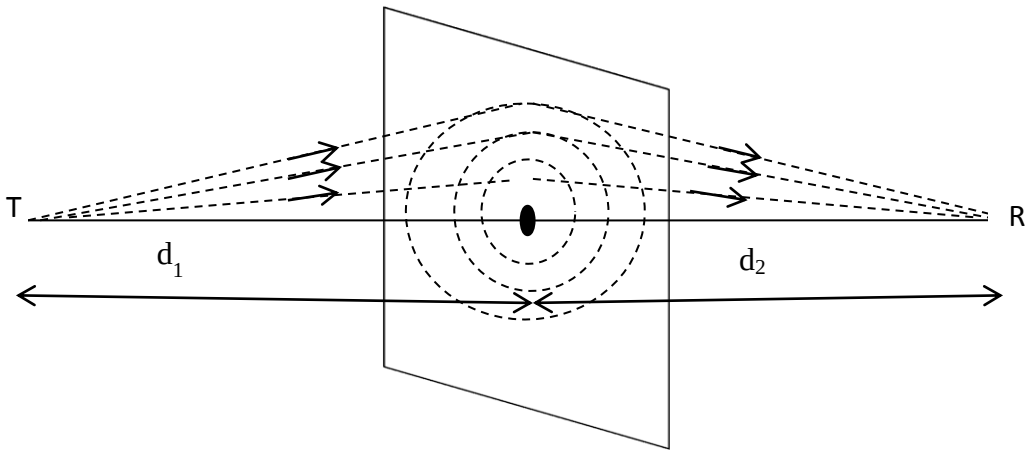

Figure 3.11: Family of circles representing Fresnel zones at point along a radio path [43].

$$\phi = \frac{\pi\alpha^2}{\lambda}\left(\frac{d_1 d_2}{d_1+d_2}\right) \tag{3.22}$$

$$\nu = \alpha\sqrt{\frac{2d_1 d_2}{\lambda(d_1+d_2)}} \tag{3.23}$$

Signal attenuation estimation resulting from radio wave diffraction over obstacles is critical in predicting the signals at the receiver. In practice, this prediction is based on theoretical approximations that are normally modified using the relevant empirical corrections.

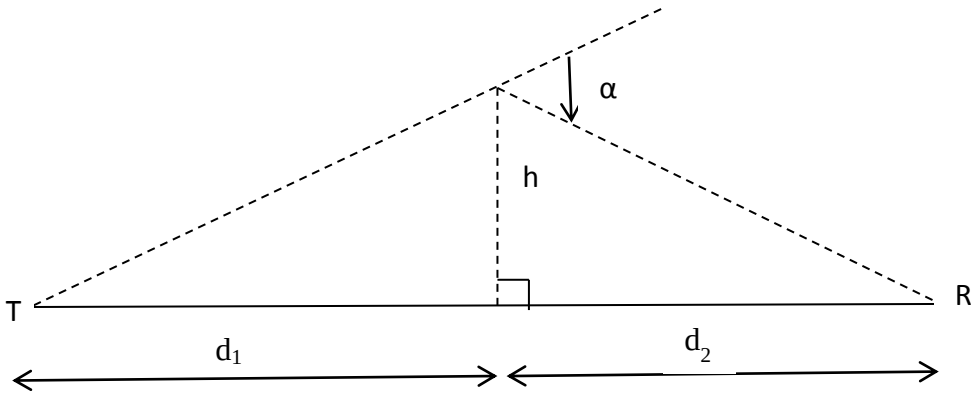

Figure 3.12: Simplified geometry of the knife-edge diffraction [51]

Although the estimation of losses due to diffraction fading over terrain that is complex due to ruggedness is a difficult mathematical problem, different equations have been derived for such computations.

The single knife-edge diffraction model is the simplest case of the diffraction phenomena. The "knife-edge" analogy is normally adopted when an object such as mountain or a hill intercepts the signal causing shadowing (diffraction.) Depending how the knife-edge intercepts the Fresnel zones, there are three possible combinations of the values that α and λ can assume.

These three scenarios are depicted in Figure 3.13.The diffraction losses caused by a single knife edge can easily be solved by applying the classical Fresnel solution for the field generated behind the obstacle [43, 48, 51]. This methodological approach is depicted in Figure 3.14. In Figure 3.14, we consider the receiving the receiving antenna at point R, which lies in the diffraction zone. The strength of the signal at R is a sum of the field vectors of every secondary source in the plane above the obstacle. This strength, E_d, of the diffracted knife-edge wave is given by [43, 49]:

$$\frac{E_d}{E_o} = F(v) = \frac{1+j}{2}\int_v^\infty exp\left(\frac{-j\pi t^2}{2}\right)dt \tag{3.24}$$

where E_o is field strength in free space, E_d is the electric field strength of a knife-edge diffraction wave, $F(v)$ is a complex Fresnel integral. From (3.24) we can write [51]:

$$\int_v^\infty exp\left(\frac{-j\pi t^2}{2}\right)dt = \int_v^\infty \cos\left(\frac{\pi t^2}{2}\right)dt - j\int_v^\infty \sin\frac{\pi t^2}{2}\,dt \tag{3.25}$$

We also have that [51]:

$$\int_v^\infty \cos\left(\frac{\pi t^2}{2}\right)dt = \frac{1}{2} - \int_0^v cos\left(\frac{\pi t^2}{2}\right)dt \tag{3.26}$$

The right hand side of (3.26) can also be expressed as [51]:

$$\frac{1}{2} - \int_0^v cos\left(\frac{\pi t^2}{2}\right)dt = \frac{1}{2} - C(v) \tag{3.27}$$

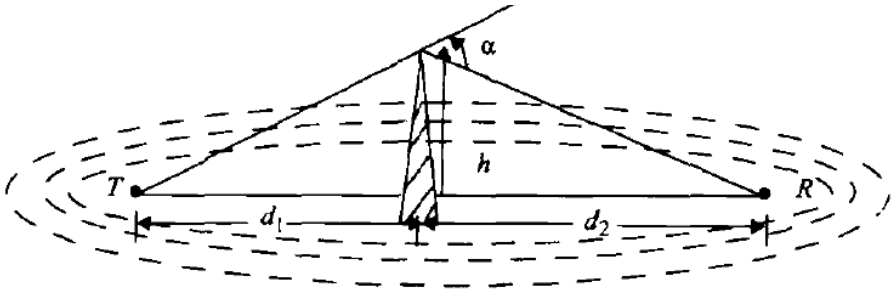

(a) ν and α are positive, h is positive

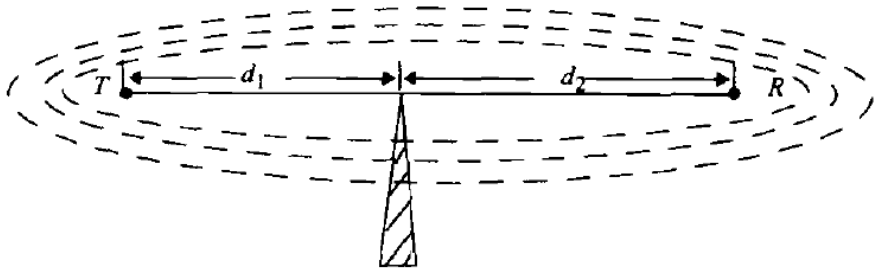

(b) ν and α are equal to zero, h is equal to zero

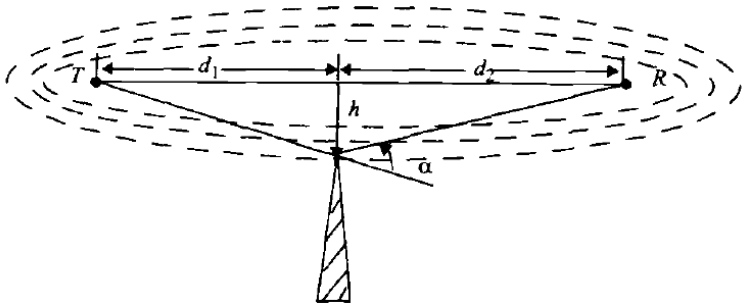

(c) ν and α are negative, h is negative

Figure 3.13: Fresnel zones illustrations for different scenarios of knife-edge diffraction [43].

Similarly,

$$\int_0^{\nu} sin\left(\frac{\pi t^2}{2}\right)dt = \frac{1}{2} - S(\nu) \tag{3.28}$$

From (3.27) and (3.28), the Fresnel integral is then simplified to [51]:

$$\frac{E_d}{E_o} = \frac{1+j}{2}\left\{\left(\frac{1}{2} - C(\nu)\right) - j\left(\frac{1}{2} - S(\nu)\right)\right\} \tag{3.29}$$

Also [51, 52]:

$$C(\nu) - S(\nu) = \int_0^{\nu} exp\left(-j\frac{\pi t^2}{2}\right)dt \tag{3.30}$$

where $C(\nu)$ is the Fresnel cosine integral and $S(\nu)$ is the Fresnel sine integral.

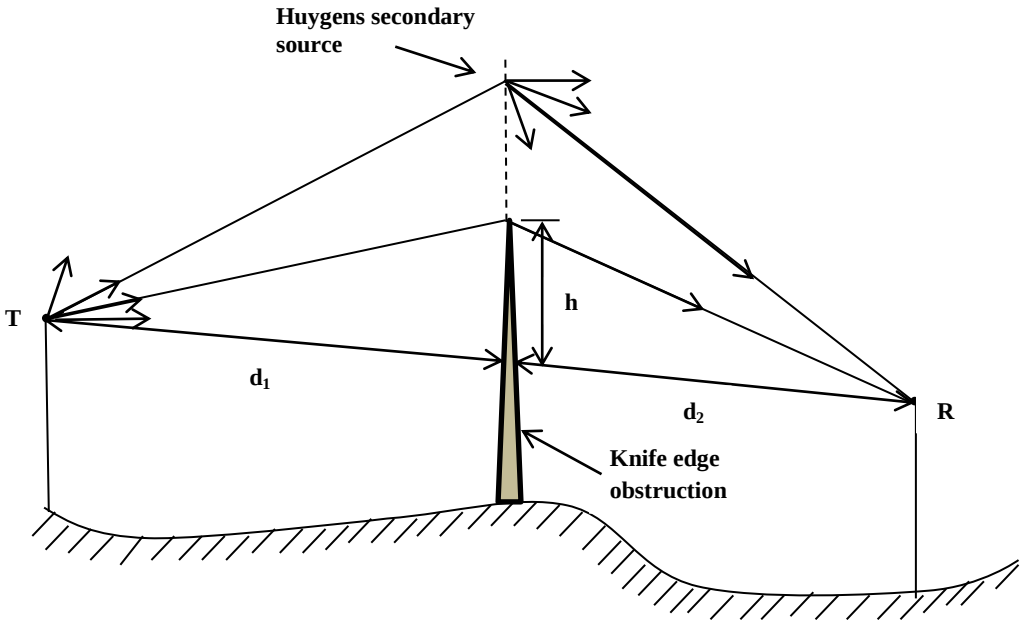

Figure 3.14: Knife-edge diffraction geometry with receiver located in the shadow region [43].

If Equation (3.30) is plotted in the complex plane with C as the abscissa and S as the ordinate, the resulting curve is what is usually referred to as Cornu's spiral; where the values of ν that are positive appear in the first quadrant and those that are negative appear in the third quadrant. Cornu's spiral is shown in Figure 3.15.

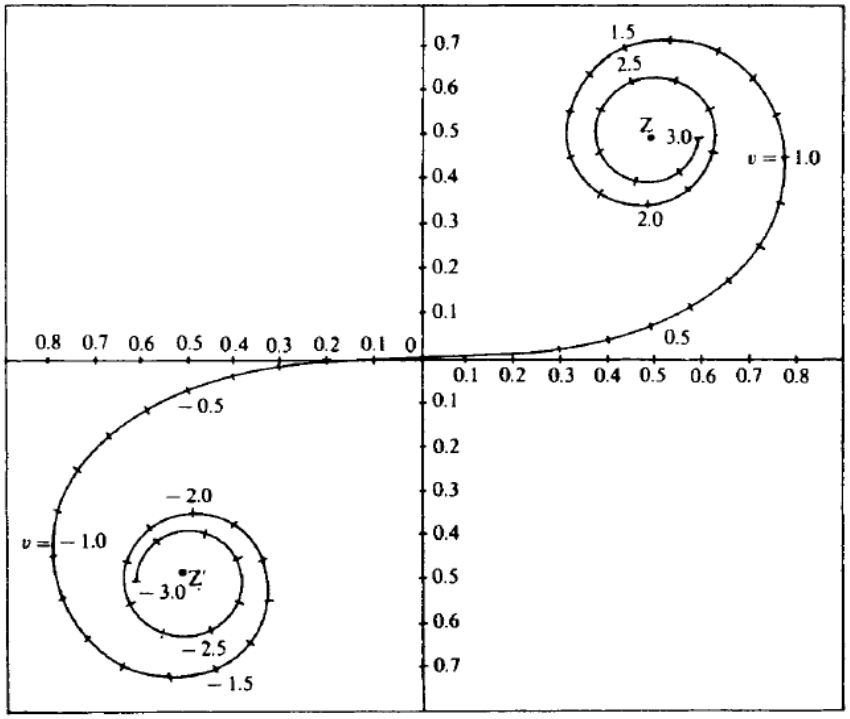

Figure 3.15: Fresnel integral in terms of the diffraction parameter ν (Cornu's spiral) [49].

Cornu's spiral is characterized by the following properties [49]:

(i) Any vector that originates from the origin to any other point on the curve is representative of both the magnitude and phase of Equation (3.30).

(ii) v is equal to the arc length along the curve measured from the origin. And, as $v \to \infty$, the curve winds at an infinite number of times around the pints $\left(\frac{1}{2}, \frac{1}{2}\right)$ and $\left(-\frac{1}{2}, -\frac{1}{2}\right)$.

The Fresnel integral is a function of the Fresnel-Kirchhoff diffraction parameter v and it is commonly evaluated using graphs and tables for given values of v. The diffraction loss or gain resulting from the presence of a knife-edge is given by [41, 43, 51]:

$$G_d(dB) = 20log|F(v)| \tag{3.31}$$

where G_d is the diffraction loss or gain. Numerical or graphical solutions of Equation (3.31) are normally used in computing the gain or loss resulting from knife-edge diffraction in decibels. Some of these solutions by Lee are [41, 43, 51]:

$$G_d(dB) = 0 \qquad v \leq -1 \tag{3.32a}$$

$$G_d(dB) = 20\log(0.5 - 0.62v) \qquad -1 \leq v \leq 0 \tag{3.32b}$$

$$G_d(dB) = 20\log(0.5exp(-0.95v)) \qquad 0 \leq v \leq 1 \tag{3.32c}$$

$$G_d(dB) = 20\log\left(0.4 - \sqrt{0.1184 - (0.38 - 0.1v)^2}\right) \qquad 1 \leq v \leq 2.4 \tag{3.32d}$$

$$G_d(dB) = 20\,log\left(\frac{0.225}{v}\right) \qquad v \geq 2.4 \tag{3.32e}$$

Figure 3.16 shows the variation of the knife-edge diffraction loss in decibels relative to that in free space as a function of the Fresnel parameter v, as given by Equation (3.29). From this figure, we see that above the line of sight path, the loss normally revolves around the free space value, and as Fresnel parameter v becomes more negative the oscillation amplitude decreases.

Also, the loss smoothly increases in the shadow zone that lies below the line of sight path. Again, we see that there is a $6\,dB$ loss when the obstacle experiences a grazing incidence over it which means that the field strength is $0.5E_o$. This loss could as well be avoided if $v \approx -0.8$, which corresponds to approximately 56% first Fresnel zone clearance[49, 51]. Theoretically, then, in the design of line of sight radio links, engineers can try to avoid diffraction losses by making sure that the majority of the first Fresnel zone is clear of any obstacles . In most designs, 100% clearance of the first Fresnel zone using the median k-factor and 60% clearance of the same using the minimum k-factor is used [3, 4].

3.1.4.2 ITU-R Single Rounded Obstacle Diffraction Model

The geometrical representation of a rounded obstacle is shown in Figure 3.17. Here, the distances d_1 and d_2 and height h above the baseline, are all measured to the vertex where the projected rays intersect above the obstacle. The diffraction loss is computed from [52]:

$$A = G_d(v) + T(m, n) \tag{3.33}$$

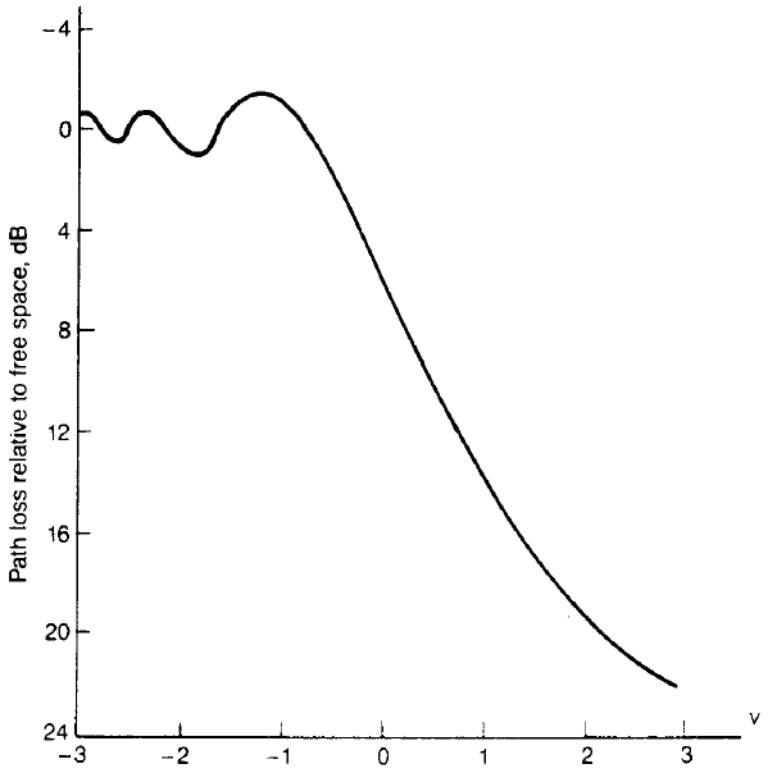

Figure 3.16: Relative knife-edge diffraction loss as a function of the Fresnel parameter v [51].

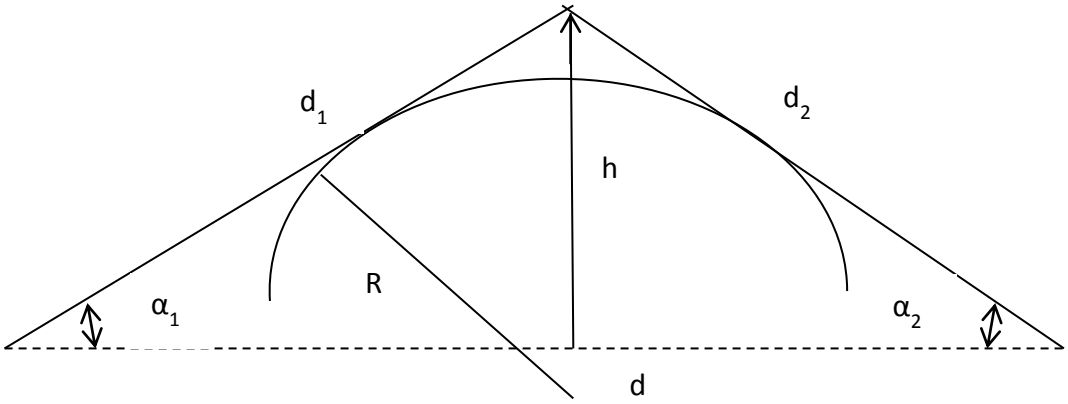

Figure 3.17: Rounded obstacle diffraction geometry construction [52].

where $G_d(v)$ is the diffraction loss due to an equivalent knife-edge with the vertex being its peak and $T(m,n)$ is the extra attenuation caused by the obstacle curvature given by [52]:

$$T(m,n) = 7.2^{1/2} - (2 - 12.5n)m + 3.6m^{\frac{3}{2}} - 0.8m^2 dB \quad \text{for } mn \leq 4 \tag{3.34}$$

$$T(m,n) = -6 - 20\log(mn) + 7.2m^{1/2} - (2 - 17n)m + 3.6m^{3/2} - 0.8m^2 dB \text{ for } mn > 4 \tag{3.35}$$

and,

$$m = R\left[\frac{\left(\frac{d_1+d_2}{d_1 d_2}\right)}{\left[\frac{\pi R}{\lambda}\right]^{1/3}}\right] \tag{3.36}$$

$$n = h\left[\frac{\left[\frac{\pi R}{\lambda}\right]^{2/3}}{R}\right] \tag{3.37}$$

where R is the radius of curvature and $T(m,n)$ tends to zero as R tends to zero and thus in this case, equation (3.33) is effectively reduced to single knife-edge diffraction for a zero cylinder radius.

3.1.5 Multiple Knife-Edge Diffraction Models

The process of determing the diffraction loss due a single knife edge is itself a difficult mathematical problem and therefore if there happens to be more than one obstacle along the radio path, then this would present an even more complicated and formidable mathematical problem. The signal strength in the shadow region of single knife-edge increases with the height of the obstacle and therefore the wave that illumintes a second or third knife edge is bound to be non-uniform, thus maikng it difficult to make a prediction of the additional losses caused by an extra or multiple other knife edges. In order to make an accurate prediction of the net diffraction loss, an n-dimensional integral of the Fresnel equation would ideally be necessary. Although different methods have been put forward as solutions to this problem through publications, these proposed methods are complex and limiting in terms of the computer resources required to execute them. Therefore, it is common to apply approximate methods in solving the multiple knife-edge diffraction problem. The most popular of these approximate methods are the Bullington method, the Deygout method, Epstein-Peterson method and the Japanese method [43, 49].

3.1.5.1 Bullington Method

In this method, all the knife edge obstacles are replaced by a single “equivalent” knife edge obstacle. Thus, this approach oversimplifies the diffraction loss estimation and often produces received signal strengths estimates that are quite optimistic [43]. Thus this method ignores knife edge obstacles that will in real terms affect the received signal strength, and this is a great limitation. The location of the single “equivalent” knife edge obstacle is at the point where the extended lines joining the transmitting antenna and the receiving antenna to their dominant obstacles meet. The diffraction loss is then calculated using the usual procudure applied for the single knife-edge diffraction problem. The greatest advantage of this method lies in its simplicity and ease of implementation but it overlooks important obstacles below the radio path and this can lead to larger errors than those predicated [49,51]. Figure 3.18 illustrates the construction of this method for two knife edge obstacles.

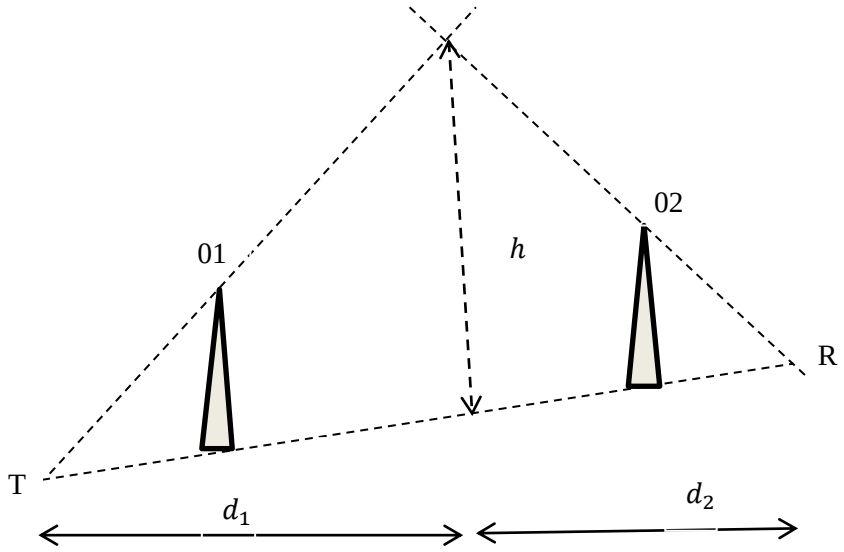

Figure 3.18: Bullington "equivalent" knife edge for two obstacles [51].

3.1.5.2 Epstein-Peterson Method

This method overcomes the key disadvantage of the Bullington by considering all the obstacles along the radio path individually. This is achieved by subdividing the radio path into overlapping "hops" depending on the position of the obstacles with each hop contaning only one obstacle [48]. The net diffraction loss is then obtained by adding the losses in each hop . Figure 3.19 illustrates the sectioning of the radio link in this method. A line is drawn for the transmitting antenna at T to the top of the obstacle 02 and the diffraction loss caused by obstacle 01 is calculated by applying the normal single knife edge diffraction method. Similarly, the diffraction loss caused by obstacle 02 is obtained by joining the tops of obstacles 01 and 03 and then using the height above the joining line as the effective height of obstacle 02. Finally, the diffraction loss due to obstcale 03 is calculated with respect to the line joining the receiving antenna to the top of obstacle 02. The total diffraction loss is the calculated by summing the losses due to individual obstacles.

3.1.5.3 Deygout Method

This method is similar to the Epstein-Peterson method but produces results that are different in many circumstances. The procedure is to first identify the obstacle along the radio path that would produce the largest diffraction loss, otherwise referred to as the dominant obstacle. The loss caused by the dominant obstacle is then determined. The top of this obstacle becomes a virtual transceiver that divides the radio link path into two. For each of these two path sections, a dominant obstacle is also determined and the process of computing the diffraction loss due to each is repeated.

Figure 3.20 is a simple Deygout construction for a three-obstacle radio link path. For this particular example, all the obstacles obstruct the radio path, but the same technique could also be applied if one or more are subpath obstacles encroaching into lower-numbered Fresnel zones [51]. The net diffraction loss is the sum of the losses due to each section identified [49].

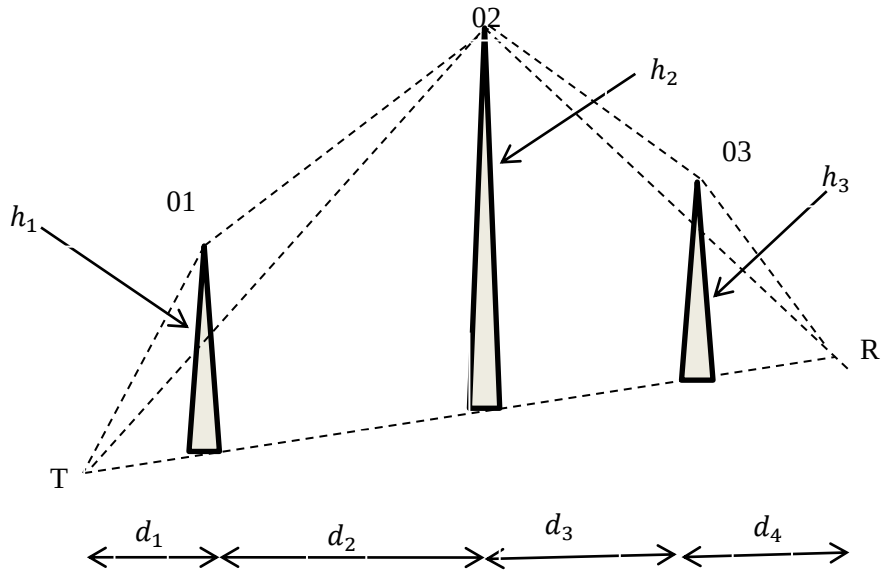

Figure 3.19: The Epstein-Peterson Construction [51].

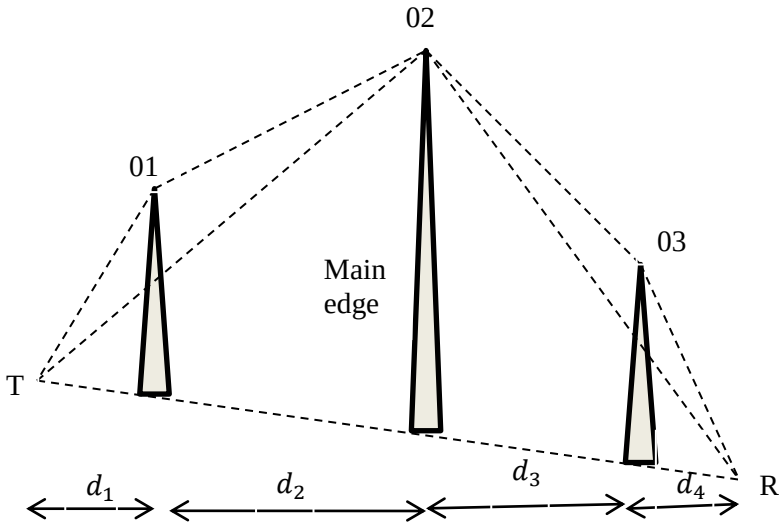

Figure 3.20: Construction of the Deygout diffraction method [51].

A simple algorithm for the evaluation of multiple knife edge diffraction loss is as follows [48]:

i. Determine the diffraction loss between the transmitter and receiver if only the ith obstacle is present (for all i).
ii. Define the dominant obstacle-its index is defined as i_{ms}.
iii. Calculate the diffraction loss between the transmitter and the top of the dominant obstacle caused by the jth obstacle (with j running now from 1 to i_{ms}). The obstacle that produces the largest diffraction loss is called the subsidiary "dominant obstacle". In a similar manner,

calculate the diffraction loss between the dominant obstacle and the receiver, caused by the jth obstacle ($j > i_{ms} + 1$).

iv. Optionally, the procedure can be repeated to create "subsidiary obstacles" etc.

v. Sum up all the diffraction losses resulting from each obstacle.

The Deygout method performs well if actually a dominant obstacle that produces the largest diffraction loss does exist between the transmitter and the receiver. And for this reason, the method is also known as the main edge method [51].

3.1.5.4 Japanese Method

This method is also similar to the Epstein-Peterson method. The main difference between the two lies in the way the diffraction loss due to each obstacle is calculated. Here, the top of the preceding obstacle is not the effective source but the horizon ray projection through that point on to the plane of one of the terminals is [51]. Figure 3.21 illustrates this construction. In this figure, the total diffraction loss can be obtained by summing up L_{01}, L_{02} and L_{03}, where [51]:

$$L_{01} = f(d_1, d_2, h_1) \tag{3.38a}$$

$$L_{02} = f([d_1 + d_2], d_3, h_2) \tag{3.38b}$$

$$L_{03} = f([d_1 + d_2 + d_3], d_4, h_3) \tag{3.38c}$$

Although this method is much better than the Bullington one, it too tends to give optimistic estimates of the received signal strength [51].

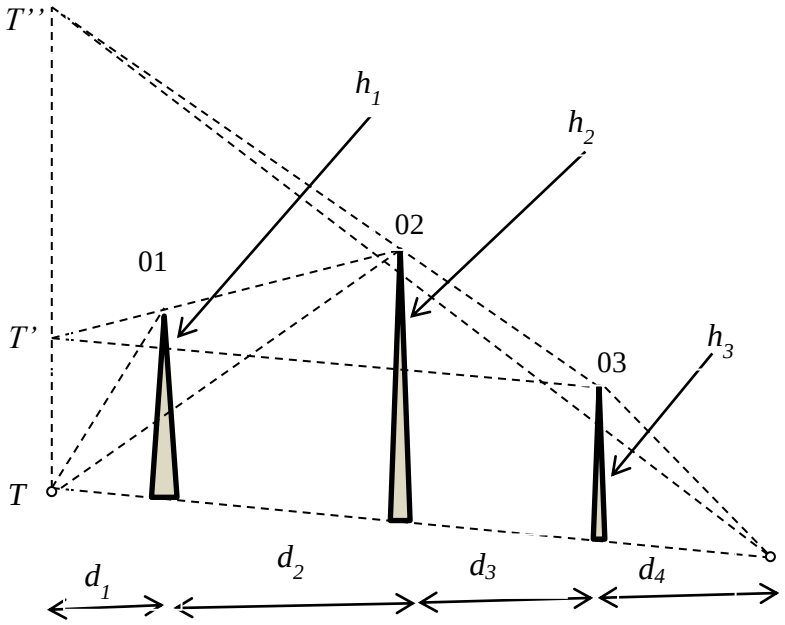

Figure 3.21: Construction of the Japanese diffraction method [51].

3.1.6 ITU-R Diffraction Method for General Terrestrial Path

This method is recommended for cases where for the prediction of the diffraction loss for any path profile category, whether trans-horizon or LOS, and for either smooth or rough terrain, an automatic process is required. This ITU-R model borrows from the Bullington one described in sub-section 3.1.5.2 and makes use of spherical earth diffraction assumptions. This method should be applied in cases where there is no *a priori* information with regard to the propagation path nature or any possible obstacles along the path. The method uses a computer program for path profiles selection from a database of terrain height on a fully automatic basis, without any inspection of individual characteristics of the path. The results obtained using this method are reliable for all types of path, trans-horizon or LOS, smooth or rough, or over large water bodies or the sea. The method is comprised of two sub-models [52]:

a) the Bullington ITU-R diffraction model
b) the complete method

3.1.6.1 Bullington ITU-R Diffraction Model

The procedure for the determination of the diffraction loss for this sub-model is as follows [52]:

Step 1: Obtain the path profile point that is intermediate with the highest slope of the line drawn from the transmitting antenna to the point itself. The slope is given by [52]:

$$s_{tim} = max\left[\frac{h_i + 500C_e d_i(d-d_i) - h_{ts}}{d_i}\right] \; m/km \tag{3.39}$$

where i is the profile index that takes values between 2 and $n-1$, with n being the number of profile points, h_i is the height of the i^{th} profile point in meters above sea level, d_i is the distance of the i^{th} profile point in kilometers above the sea level, C_e is the effective earth curvature in km^{-1}, d is the path length and h_{ts} is the transmitting antenna height in meters.

Step 2: Compute the slope of the line from the transmitting antenna to the receiving antenna with the assumption that the path is LOS, given by [52]:

$$S_{tr} = \frac{h_{rs} - h_{ts}}{d} \; m/km \tag{3.40}$$

where h_{rs} is the height of the receiving antenna in meters,

Step 3: If the path is LOS, obtain the path profile point that is intermediate with the highest diffraction parameter v [52]:

$$v_{max} = max\left\{\left[h_i + 500C_e d_i(d-d_i) - \frac{h_{ts}(d-d_i) + h_{rs}d_i}{d}\right]\sqrt{\frac{0.002d}{\lambda d_i(d-d_i)}}\right\} \tag{3.41}$$

Step 4: Compute the LOS Bullington knife diffraction loss from [59]:

$$L_{uc} = 6.9 + 20\log\left(\sqrt{(v-0.1)^2+1} + v - 0.1\right)\ dB \text{ for } v > -0.78, \text{ 0 otherwise} \quad (3.42)$$

3.1.6.2 Complete Method

Step 1: The method applied for the Bullington ITU-R diffraction model is used for antenna heights and the actual terrain profile. The resulting Bullington diffraction loss for the actual path is set to [52]:

$$L_{ba} = L_{uc} + [1 - exp((-L_{uc})/6)](10 + 0.002d) \quad (3.43)$$

Step 2: Compute the effective transmitting and receiving antenna height relative to a smooth surface fitted to the profile. The profile mean height is obtained from [52]:

$$h_a = \left(\frac{1}{2d}\right)\sum_{i=1}^{n}(d_i - d_{i-1})(h_i - h_{i-1}) \text{ masl} \quad (3.44)$$

The least-squares regression fit slope is given by [59]:

$$m = \left(\frac{1}{d^3}\right)\sum_{i=1}^{n}[3(d_i - d_{i-1})(d_i - d_{i-1} - d)(h_i - h_{i-1} - 2h_a) + (d_i - d_{i-1})^3(h_i - h_{i-1})] \ m/km \quad (3.45)$$

Step 3: Compute the provisional initial values for smooth surface heights at the transmitting and receiving ends of the path given by [52]:

$$h_{stip} = h_a - 0.5md \text{ masl} \quad (3.46)$$

$$h_{srip} = h_a - 0.5md \text{ masl} \quad (3.47)$$

Step 4: Find the highest obstacle height above the straight line path from transmitting antenna to receiving antenna h_{obs}, and the elevation angles of the horizon α_{obt}, α_{obr}, all based on the flat-earth geometry, according to [52]:

$$h_{obs} = max\{h_{obi}\} \quad (3.48a)$$

where:

$$h_{obi} = h_i - [h_{ts}(d - d_i) + h_{rs}d_i]/d \quad (3.48b)$$

$$\alpha_{obt} = max\{h_{obi}/d_i\} \text{ mrad} \quad (3.48c)$$

$$\alpha_{obr} = max\{h_{obi}/(d - d_i)\} \text{ mrad} \quad (3.48d)$$

Step 5: Compute provisional values for the smooth surface heights at the transmitting and receiving path ends. If h_{obs} is equal to or less than zero, then [52]:

$$h_{stp} = h_{stip} \text{ masl} \quad (3.49a)$$

$$h_{srp} = h_{srip} \text{ masl} \quad (3.49b)$$

Else:

$$h_{stp} = h_{stip} - h_{obs}g_t \text{ masl} \tag{3.49c}$$

$$h_{srp} = h_{srip} - h_{obs}g_r \text{ masl} \tag{3.49d}$$

where:

$$g_t = \alpha_{obt}/(\alpha_{obt}+\alpha_{obr}) \tag{3.49e}$$

$$g_r = \alpha_{obr}/(\alpha_{obt}+\alpha_{obr}) \tag{3.49f}$$

Step 6: Compute the final smooth surface heights at the transmitting and receiving ends of the path. If h is less than h_{stp}, then [52]:

$$h_{st} = h \text{ masl} \tag{3.50a}$$

$$h_{st} = h_{stp} \text{ masl} \tag{3.50b}$$

If h_n is less than h_{srp}, then [52]:

$$h_{sr} = h_n \text{ masl} \tag{3.50c}$$

Else:

$$h_{sr} = h_{srp} \text{ masl} \tag{3.50d}$$

Step 7: The method described for the ITU-R Bullington construction is used for a profile that is smooth by setting all the profile heights h_i to zero, and using modified antenna heights [52]:

$$h'_{ts} = h_{rs} - h_{st} \text{ masl} \tag{3.51a}$$

$$h'_{rs} = h_{rs} - h_{sr} \text{ masl} \tag{3.51b}$$

Step 8: The resulting ITU-R Bullington diffraction loss due to a smooth path L_{bs} is now set to L_{ba} as given in Equation (3.43).

Step 9: The method for diffraction over spherical-earth is the applied for the path length with [52]:

$$h_1 = h'_{ts} \tag{3.52a}$$

$$h_2 = h'_{rs} \tag{3.52a}$$

The diffraction loss over spherical-earth L_{sph} is given by [52]:

$$A = \left[1 - \frac{h}{h_{req}}\right] A_h \tag{3.53}$$

where:

h is the smallest clearance height between the ray between the antennas and the curved-earth path a_e and is given by [52]:

$$h = \frac{\left(h_1 - \frac{d_1^2}{2a_e}\right)d_2 + \left(h_2 - \frac{d_2^2}{2a_e}\right)d_1}{d} \tag{3.54a}$$

$$d_1 = \frac{d}{2}(1 + b) \tag{3.54b}$$

$$d_2 = d - d_1 \tag{3.54c}$$

$$b = 2\sqrt{\frac{m+1}{3n}}\cos\left\{\frac{\pi}{3} + \frac{1}{3}arccos\left[\frac{3c}{2}\sqrt{\frac{3m}{(m+1)^3}}\right]\right\} \tag{3.54d}$$

$$c = \frac{(h_1 - h_2)}{(h_1 + h_2)} \tag{3.54e}$$

$$m = \frac{d^2}{4(h_1 + h_2)a_e} \tag{3.54 f}$$

h_{req} is the required clearance for zero diffraction loss above a spherical-earth, given by [52]:

$$h_{req} = 0.552\sqrt{\frac{\lambda d_1 d_2}{d}} \tag{3.54g}$$

A_h is the diffraction loss that is computed using a modified effective earth radius a_{em} in place of the effective earth radius a_e, where a_{em} is given by:

$$a_{em} = 0.5\left(\frac{d}{\sqrt{h_1} + \sqrt{h_2}}\right)^2 \tag{3.55}$$

Step 10: Compute the general path diffraction loss from [52]:

$$L = L_{ba} + max\{L_{sph} - L_{bs}, 0\}\ dB \tag{3.56}$$

However, ITU-R recommendation P.530-14 [4] gives a simplified formula for computing the diffraction loss produced by an average topography for cases where the losses are greater than $15\ dB$. This simplified formula is [4]:

$$A_d = \frac{20h}{F_1} + 10\ \ dB \tag{3.57}$$

where F_1 is the radius of the first Fresnel zone.

Figure 3.22 shows a curve relates the diffraction losses that are greater than $15\ dB$ to the normalized factor $\frac{h}{F_1}$ with extrapolation up to $6\ dB$ for the sake of wider applicability by radio link designers. Here B is the theoretical knife-edge curve, D is the theoretical smooth spherical Earth loss curve at

6.5 GHz, $k = 4/3$, A_d is the empirical diffraction loss given by Equation (3.57), and h is the amount by which the radio path clears the Earth's surface.

3.1.7 Multipath Propagation Models

Multipath happens when the signal from the transmitting antenna takes different paths to the receiving antenna hence arriving with different phases and time delays. This causes random fluctuations of the signal at the receiving antenna. Depending on how the signals superimpose at the receiving antenna, either constructive or destructive interference can occur. Destructive interference in multipath propagation is responsible for multipath fading. Sometimes, deep fading may occur at a particular point in space, time or frequency, leading to severe signal degradation, thus making it difficult to perform accurate detection and decoding at the receiving antenna [53].

There are three common methods used to predict multipath fading in terrestrial line of sight links namely: the Morita and Barnett-Vigants methods used in Japan and North America respectively, and the ITU method used the world over. The ITU method is still used in Japan and North America owing to its regular updates carried out by the Study Group 3 of the ITU Radiocommunications sector. The ITU recommendation P.530 is a source of guidelines for determining fading in terrestrial links and is based on fading measurements of 251 links in different geoclimatic regions [54].

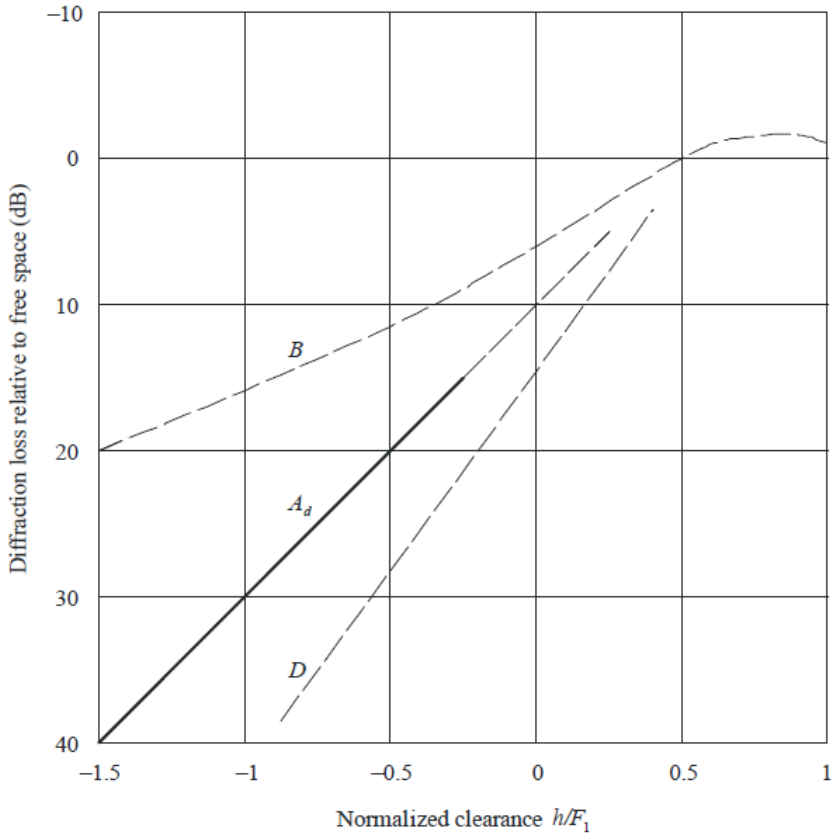

Figure 3.22: Diffraction loss for obstructed line-of sight microwave radio links [4].

Multipath fading depends on the following factors [4, 55]:

a) Atmospheric refractivity gradient

b) Radio wave frequency

c) Percentage of time the fade depth is exceeded

d) Antenna heights

e) Area terrain roughness

f) Inclination of the path

Surface multipath and atmospheric multipath are the two common forms of multipath fading. A particularly severe form of frequency selective fading occurs when beam spreading of the direct signal combines with a surface reflected signal. A method of predicting single-frequency (narrow-band) fading distribution at large fade depths in the average worst month is given in ITU-R recommendation P.530-14 [4]. This method does not make use of the path profile and can be used for the initial planning, licensing or design of LOS terrestrial links. A second method that employs large fade depths and an interpolation procedure for small fade depths is given in the same recommendation. A method for predicting signal enhancement is also given in the same recommendation and the method uses the fade depth predicted in the first method as the only input parameter. Finally ITU-R gives a method for converting the average worst month to average annual distributions. The first two methods are discussed below [4].

3.1.7.1 Method for Small Percentages of Time

Step 1: Determine the geoclimatic factor, K, for the where the path is located for the average worst month using fading data for the location of interest if these are available. If measured data for the geoclimatic factor is missing, and the terrestrial link design is detailed, estimation of the geoclimatic factor, K for the average worst month is obtained from the following the expression [4]:

$$K = 10^{-(4.4+0.0027dN_1)}(10 + S_a)^{-0.46} \tag{3.58}$$

where dN_1 is the point refractivity gradient in the lower 65m of the atmosphere not exceeded for 1% of an average year and S_a is the terrain roughness factor of the area.

For planning purposes, quick estimates of the geoclimatic factor that are fairly accurate are computed using [4]:

$$K = 10^{-(4.6+0.0027dN_1)} \tag{3.59}$$

Step 2: Determine the path inclination magnitude,$|\varepsilon_p|$ from [4]:

$$|\varepsilon_p| = |h_r - h_e|/d \tag{3.60}$$

where d is the distance between the transmitting antenna and receiving antenna, h_r is the receiving antenna height(m) above sea level and $h_e$is the transmitting antenna height(m) above sea level.

Step 3: If a detailed design of the link is required, compute the time percentage ρ_w that fade depth A (dB) is exceeded in the average worst month from [4]:

$$\rho_w = Kd^{3.4}\left(1 + |\varepsilon_p|\right)^{-1.03} f^{0.8} \times 10^{-0.00076h_L - A/10} \quad \% \tag{3.61}$$

where f is the frequency (GHz), h_L is the altitude of the smaller of the transmitting antenna and the receiving antenna and K is the geoclimatic factor obtained using equation (3.58).

In case of quick planning, compute the percentage of time ρ_w that the fade depth A (dB) is exceeded in the average worst month from [4]:

$$\rho_w = Kd^{3.1}\left(1 + |\varepsilon_p|\right)^{-1.29} f^{0.8} \times 10^{-0.00089h_L - A/10} \quad \% \tag{3.62}$$

where the geoclimatic factor, K is obtained from equation (3.59).

3.1.7.2 Method for All Percentages of Time

This method combines the deep fading distribution given in Subsection 3.1.7.1 and an empirical interpolation procedure for shallow fading down to 0 dB for the prediction of the time percentage that a particular fade is exceeded.

Step 1: Using the method described in Subsection 3.1.7.1 above, compute the multipath occurrence factor, p_o from [4]:

$$p_o = Kd^{3.4}\left(1 + |\varepsilon_p|\right)^{-1.03} f^{0.8} \times 10^{-0.00076h_L} \quad \% \tag{3.63}$$

The geoclimatic factor, K is obtained from (3.58).If a detailed design of the link is desired,the multipath correction factor is obtained from [4]:

$$p_o = Kd^{3.1}\left(1 + |\varepsilon_p|\right)^{-1.29} f^{0.8} \times 10^{-0.00089h_L} \quad \% \tag{3.64}$$

The geoclimatic factor, $K$is obtained from (3.59).

Step 2: Using the empirical interpolation procedure, determine the value of the fade depth, A_t at which the transition occurs between shallow-fading and deep-fading distribution from [4]:

$$A_t = 25 + 1.2 \log p_o \tag{3.65}$$

The following procedures below are dependent on whether A is greater or less than A_t.

Step 3a: If the A is equal to or greater than A_t is the required fade depth: determine the time percentage, ρ_t, that A is exceeded in the average worst month [4]:

$$p_w = p_o \times 10^{-A/10} \quad \% \tag{3.66}$$

Step 3b: If A is less than A_t is the required fade depth: determine time percentage, ρ_t that A_t is exceeded in the average worst month [4]:

$$p_t = p_o \times 10^{-A_t/10} \quad \% \tag{3.67}$$

Determine q'_a from the transition fade A_t and transition percentage time p_t [4]:

$$q'_a = -20\log\{-\ln[(100 - p_t)/100]\}/A_t \tag{3.68}$$

Determine q_t from q'_a and the transition fade, A_t [4]:

$$q_t = (q'_a - 2)/[(1 + 0.3 \times 10^{\frac{-A_t}{20}})10^{-0.016A_t}] - 4.3(10^{\frac{-A_t}{20}} + A_t/800) \tag{3.69}$$

Determine q_a from the required fade, A:

$$q_a = 2 + \left[1 + 0.3 \times 10^{\frac{-A}{20}}\right][10^{-0.016A}][q_t + 4.3\left(10^{\frac{-A}{20}} + \mathrm{A}/800\right)] \tag{3.70}$$

Determine time percentage, p_w, that the fade depth A (dB) is exceeded in the average worst month:

$$p_w = 100\left[1 - \exp\left(-10^{\frac{-q_a A}{20}}\right)\right] \quad \% \tag{3.71}$$

With the multipath correction factor, p_0 as a parameter, Figure 2.26 shows a graphical representation of a family of curves for this method.

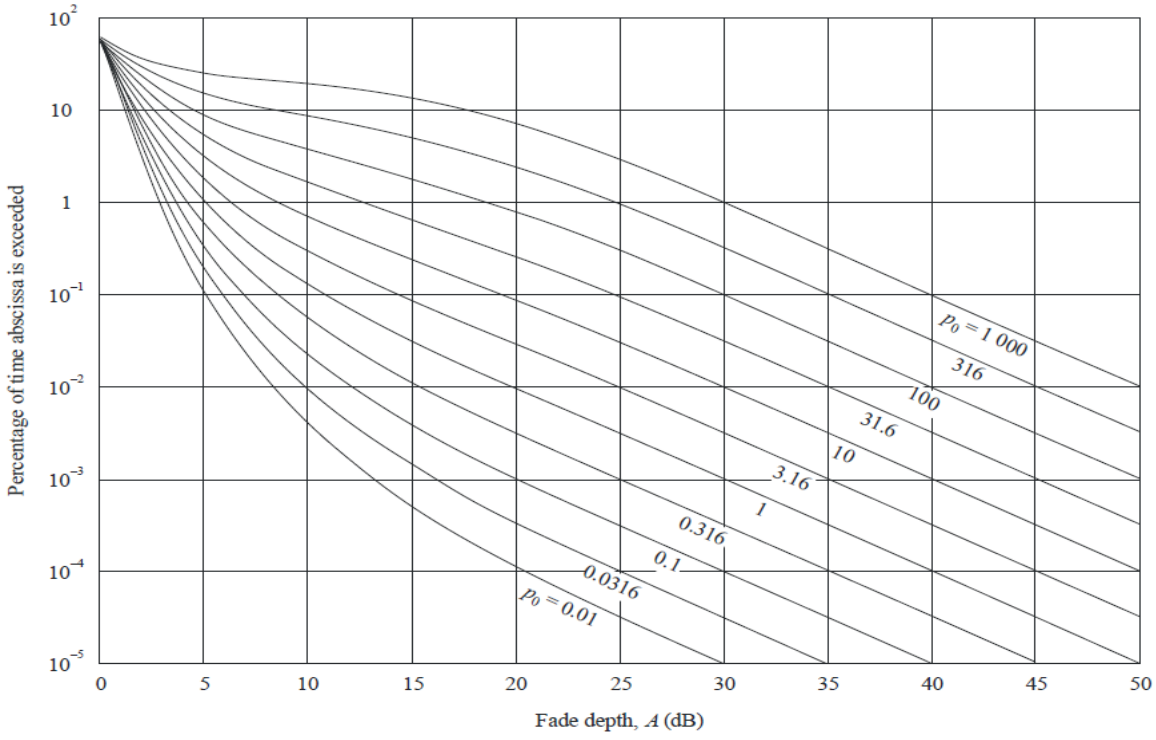

Figure 3.23: Time percentage that a certain fade depth is exceeded in the average worst month [4].

3.2 Atmospheric Radio Refractivity and k-factor

3.2.1 Atmospheric Radio Refractivity

When radio waves travel through the atmosphere, they tend to curve either away from or towards the earth's surface. This is so because the refractive index, n, of the atmosphere is not constant but varies due to its microstructural properties. Thus, the atmospheric refractive index varies from time to time, place to place and with height due to the inhomogeneous composition of the atmosphere. Thus, the atmospheric refractive index forms the basis upon which one is able to characterize the way in which the atmosphere affects waves travelling through it. The value of the refractive index degreases as the height above ground level increases. This is primarily so because the parameters which determine its value at a particular height also tend to decrease with height. The decreasing trend in n is primarily governed by the exponential decrease in the atmospheric pressure. In saturated air, however, the temperature falls in a linear manner with increasing height above the ground level at approximately $10^0 C/Km$. The variation in water vapour with pressure are however more complex in nature [56].

The radio refractive index, n, is defined as the ratio of the velocity of propagation of an electromagnetic wave in a vacuum (free-space) to the velocity in a different (specific) medium. It is determined using the following expression [3, 21,]:

$$n = \frac{c}{v} = \sqrt{\mu\varepsilon} \tag{3.72}$$

Alternatively, n is also given by:

$$n = 1 + N \times 10^{-6} \tag{3.73}$$

where c is the speed of a radio wave in a vacuum (free space), v is the speed of a radio wave in air, μ is the relative permeability, ε is the relative permittivity, N is the radio refractivity and n is the refractive index. In most cases μ=1 so that, $n = \sqrt{\varepsilon}$. The radio refractive index is very close to unity (n=1.000312) and may not be a good way of characterizing the refractive properties of the atmosphere. It is therefore customary to use the radio refractivity, N, that defines the amount by which the refractive index is greater than one, expressed in parts per million, [15, 57,58]:

$$N = (n - 1)10^6 \tag{3.74}$$

The vertical profile of the radio refractivity is normally derived in terms of the existing atmospheric conditions of relative humidity, atmospheric pressure, and the absolute temperature using the relation [57-59]:

$$N = \frac{77.6}{T}\left(P + 4810\frac{e}{T}\right) = \frac{77.6}{T}P + 3.3 \times 10^5 \frac{e}{T^2} \tag{3.75}$$

where P is the atmospheric pressure (hPa), e is the water vapour pressure (hPa), T is the absolute temperature (K).Thus, it can be seen from (2.4) that the radio refractivity consists of two parts [58, 59]:

$$N_{dry} = \frac{77.6}{T}P \tag{3.76}$$

which is known as the dry part, and is a direct consequence of the atmospheric pressure, P variation with height, and [58, 59]:

$$N_{wet} = 3.3 \times 10^5 \frac{e}{T^2} \tag{3.77}$$

which is known as the wet part, and is a direct consequence of the water vapour pressure, e variation with height.

Equation (3.75) is valid for all radio frequencies, up to 100GHz, with errors of less than 0.5% [3, 7] reported. The relationship between the water vapour pressure and the relative humidity is defined by the following equation [3, 60]:

$$e = \frac{He_s}{100} \tag{3.78}$$

where e_s is the saturation vapour pressure, given by the following expression [61, 62]:

$$e_s = aexp(\frac{bt}{t+c}) \tag{3.79}$$

H is the relative humidity (%), t is the Celsius temperature (℃) and a, b and c are constant coefficients. The values of the coefficients a, b, c have been determined for both water and ice conditions [3, 61]:

For water:

a =6.1121, b =17.502, c =240.97. These water values are valid between -20^oC and 50^{o}C with accuracy levels of $\pm$0.2%.

For Ice:

a =6.1115, b =22.452, c =272.55. These ice values are valid between -50^oC and 0^{o}C with accuracy levels of $\pm$0.2%.

The water vapour pressure, e can be obtained from the water vapour density, ρ using the equation [3, 7]:

$$e = \frac{\rho T}{216.7} \tag{3.80}$$

where ρ is expressed in g/m^3 and T is defined in (2.4).

If we assume that the radio refractive index of air varies linearly with height, h, for the first few tenths of a kilometre above the earth's surface and does not vary in the horizontal direction, then we can obtain the refractivity gradient,$\frac{dN}{dh}$ which is measured in N-Units/Km given by [62, 63]:

$$\frac{dN}{dh} = 77.6\left(\frac{1}{T}\frac{dP}{dh} + \frac{4810de}{T^2\,dh}\right) \tag{3.81}$$

It therefore follows that, it is actually the lapse rate on N which causes curvature of rays as they traverse the atmosphere. A 'point form' version of the refractivity gradient, which could be used with ground observations to estimate the value of the refractivity gradient, is given by [64]:

$$\frac{dN}{dh} = 77.6\left|\frac{1}{T}\frac{dP}{dh} - \left(\frac{p}{T^2} + 9620\frac{e}{T^3}\right)\frac{dT}{dh} + \frac{4810}{T^2}\frac{de}{dh}\right| \tag{3.82}$$

Common values of the refractivity gradient exist for two well-known standard conditions [17]:

a) Temperate continental atmosphere ; where $\frac{dN}{dh} = -40\ N - Units/km$

b) Well-mixed atmosphere; where $\frac{dN}{dh} = -21\ N - Units/km$

The average density of the atmosphere varies exponentially with height and therefore, the mean values of the atmospheric refractivity as a function of height are approximated using the following exponential law [65]:

$$N(h) = N_s \exp(-\frac{h}{H}) \tag{3.83}$$

where $N(h)$ is the refractivity at a height h above the Earth's surface, N_s is the surface refractivity, h is the height above the Earth's surface(km) and H is the scale height.

With the surface refractivity extrapolated to sea-level to remove surface height variations that is, topography of the location, then the value of the refractivity at height, h is given by [15, 66]:

$$N(h) = N_o \exp(-\frac{h}{h_o}) \tag{3.84}$$

where N_o is the sea-level refractivity and h_o is the scale height referenced to the sea-level.

The values of N_o and h_o can be determined statistically for different climatic zones (localities). For global reference though, where local data is unavailable, the following values are used [7, 15]:

N_o=315 and h_o=7.35Km,

So that,

$$N(h) = 315\exp(-0.136h) \tag{3.85}$$

The above numerical values of N_o and h_o only apply for terrestrial paths. The value of N_o can however be obtained from the nearest weather bureau for more accurate predictions for different localities or determined from radiosonde data measurements or even ground observations. The local value of the scale height can also be used if available for the particular climatic zone.

Although the vertical gradient variation of the refractivity has mostly been taken to be linear, this is not always the case, and could actually substantially differ from this assumed distribution, which is a monotonic decay, assuming ideal conditions. This has led to the definition of "standard atmospheres" for different regions in the world. These standard atmospheres are expressed by empirical models that are used to correlate the relationship between the surface refractivity, N_s and the refractivity

gradient within the first kilometer above ground level, $\frac{dN_1}{dh}$ .These empirical models can be used to extrapolate refractivity values at heights where data is not available or at nearby areas where measurements have not been taken. For India, Majumdar [67], developed different empirical models for various climatic zones in the country. The models were as follows:

a) For islands and south coast:

$$\frac{dN_1}{dh} = -7.12e^{-0.0054N_s} \tag{3.86a}$$

b) For inland stations:

$$\frac{dN_1}{dh} = -3.49e^{-0.0074N_s} \tag{3.86b}$$

c) For eastern coast:

$$\frac{dN_1}{dh} = -11.53e^{-0.0039N_s} \tag{3.86c}$$

Similar models have been developed for other regions of the world, most notably Germany, United Kingdom , United States of America ,Argentina, Japan, Africa, Qatar and Bahrain. These models are given by [50, 68]:

For Germany:

$$\frac{dN_1}{dh} = -9.30e^{-0.004565N_s} \tag{3.87a}$$

For United Kingdom:

$$\frac{dN_1}{dh} = -3.95e^{-0.0072N_s} \tag{3.87b}$$

For United States of America:

$$\frac{dN_1}{dh} = -7.32e^{-0.005577N_s} \tag{3.87c}$$

Equations (2.18), (2.19) and (2.20) are valid for $250 \leq N_s \leq 400$ and are only applicable to average mean negative gradients close to the ground.

For Argentina:

$$\frac{dN_1}{dh} = -2.60e^{-0.00937N_s} \tag{3.87d}$$

For Japan:

$$\frac{dN_1}{dh} = -3.42e^{-0.00758N_s} \tag{3.87e}$$

For Africa:

$$\frac{dN_1}{dh} = -2.3e^{-0.00863N_s} \quad (3.87f)$$

For Qatar:

$$\frac{dN_1}{dh} = -1.136e^{-0.0122N_s} \quad (3.87g)$$

For Bahrain:

$$\frac{dN_1}{dh} = -0.3e^{-0.016N_s} \text{ , in summer} \quad (3.87h)$$

$$\frac{dN_1}{dh} = -0.33e^{-0.0157N_s} \text{ , in winter} \quad (3.87i)$$

The varying conditions in the troposphere normally cause electromagnetic waves different degrees of bending resulting in four categories of refraction. These are sub-refraction, standard refraction and super-refraction and ducting (trapping) [21, 50, 69]. Standard refraction is only possible in a standard atmosphere where the variations in the refractive gradient are constant and range slightly below or above $-39N/km$. This is however seldom due to anomalies that are usually associated with particular meteorological conditions, like temperature inversions, passage of cold air over warm surfaces (and vice versa) and very high evaporation rates among other reasons. These "abnormal" refractive conditions are discussed below.

3.2.1.1 Substandard Refraction

This category of refraction is also commonly referred to as simply sub-refraction. This kind of refraction occurs when bending of radio waves is upward as compared to the downward bending in standard atmosphere [21]. Thus it is also referred to as inverse beam bending or "earth bulging". Sub-refraction causes the dielectric constant of air to increase with height. This kind of refraction exists where low fog forms as a result of some nocturnal cooling of the ground , where the contribution due to water droplets is less than that of water vapor in as far as the increase in dielectric constant of the air is concerned. This means that the dielectric constant at or near the ground is higher than that at higher elevations, resulting in upward elevation of waves. Thus, this kind of refraction is uncommon in coastal areas. Sub-refraction is defined by the following refractivity gradient range: $^{dN}/_{dh} > -39\ N/Km$ [37].

3.2.1.2 Superstandard Refraction

Superstandard refraction is most commonly simply referred to as super-refraction [3]. This kind of refraction occurs when the bending of electromagnetic waves occurs at a much greater rate than that of normal refraction. This mainly occurs due to abnormal meteorological conditions such as temperature inversions, which occur when temperature increases with increasing height or there is a marked decrease in the total water vapor content in the air. This kind of refraction leads to reduction in the dielectric constant gradient with height. This sort of refraction may be caused by the passage of warm air over a body of water. The evaporation of the water leads to an increase in moisture content of air and a subsequent decrease in temperature near the ground [50, 70]. Super-refraction is defined by the following range of refractivity gradients: $-157 < {}^{dN}/_{dh} < -39\ N/Km$ [21].

3.2.1.3 Ducting (Trapping)

Under the influence of climatic and synoptic weather processes such as surface heating and radio cooling or subsidence advection, there is a tendency for the troposphere to stratify [40]. This type of stratification can take the form of refractivity layering. These layers are defined by the following range of the refractivity gradient: $^{dN}/_{dh} < -157\ N\ Units/Km.$

The layers with strong ducting gradients are commonly on the order of tens of meters in vertical extent (but often much less), and are commonly bounded by layers of localized turbulence. These layers may be horizontally extensive, from tens to hundreds of kilometres in extend, and although the thinnest of these layers may only be kilometres in extent .Tropospheric layering may degrade system performance by [70]:

a) The introduction of additional propagation paths (which produces multipath fading).

b) Diffraction of the service propagation path introducing losses due to the proximity of the radio wave trajectory to media boundaries (such as the earth's surface or base or top of tropospheric layers).

c) Complete isolation of one telecommunications terminal from another (by diverting the radio wave and attenuating the received signal level).

d) Causing interference to other distant services.

These ducting layers have the net effect of guiding (ducting) or trapping radio wave energy in their vicinity. On microwave LOS paths, this ducting may introduce atmospheric multipath or be so efficient as to divert energy away from the intended receiver depressing the received field level far below the median service field level (fading). A ducting layer will cause a radio wave that is incident upon it to be trapped, scattered, or reflected depending on the layer's refractivity gradient, the thickness of the layer in terms of wavelength, the angle of ray incidence measured relative to the layer's boundary tangent, and small scale turbulence fluctuations along the layer boundary.

Among the many features which characterize atmospheric layers, some key parameters have been defined that are of particular importance in radio wave propagation. The most significant one would be the refractivity gradient or the radio refractive index. The bending of a radio wave's trajectory through the atmosphere results mainly from the inhomogeneous nature of the atmosphere which causes the refractive index to vary with the elevation above the surface. Also, in describing the effects of refractivity upon radio propagation, a more refined approach would be to use the modified refractivity, $M(h)$, and the modified refractivity gradient, $\frac{dM}{dh}$, given by [7, 71]:

$$M(h) = N(h) + \left(\frac{h}{a}\right) 10^6 \tag{3.88}$$

Equation (3.88) can be simplified to [7, 71]:

$$M(h) = N(h) + 157h \tag{3.89}$$

And, the modified refractivity gradient given by:

$$\frac{dM}{dh} = \frac{dN}{dh} + 157 \tag{3.90}$$

A geographical transformation from a spherically stratified atmosphere above a spherical earth to a planar stratification above a flatten earth is the one that brings about modified refractivity gradients. Negative values of the modified refractivity gradient are an indication of the presence of ducting phenomenon. There are three categories of ducts. These are ground-based (surface), elevated-surface and elevated ducts. Surface-based ducts extend from the top of the trapping layer to the surface while elevated ducts do not extend to the surface. Surface based ducts are spatially variable and temporal in nature. Elevated ducts are as a result of vertical mixing and circulation on a diurnal scale. Elevated-surface ducts are happen when the surface duct extends to several metres above the surface. The radiometric characteristics of a ducting layer are shown in Figure 3.24, where D is the tropospheric radio duct thickness and δ is the ducting layer thickness. The different types of these ducts are shown in Figure 3.25. The different forms of refraction that are possible depending on the value of the refractive index are shown in Figure 3.26. There are different methods that are used in the determination of atmospheric radio refractivity. They include [15, 16, 58]:

a) Indirect methods: Refractivity determined from pressure, temperature and water vapor pressure profile measurements. Different schemes are employed under this method:
   (i) Meterological sensors placed at regular or irregular intervals on a tower mainly only for the first 100m of the atmosphere.
   (ii) Lidar (light detection and ranging) systems that measure the radiation pulses fired from a laser and the radiation that is backscattered by particles and atmospheric gases is then measured. The raman lidar technique measures the water vapor and the temperature profiles in this manner and is therefore suitable for sensing atmospheric radio refractivity. Although this method reports at high level of accuracy, it is seldom used due to the cost of the equipment.
   (iii) Tethered balloon system used for the first 1Km of the troposphere.

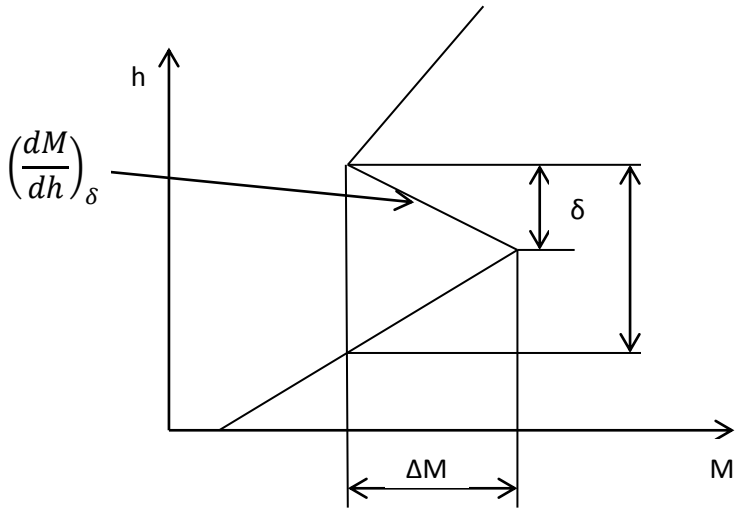

Figure 3.24: Radiometric characteristics of a ducting layer [15].

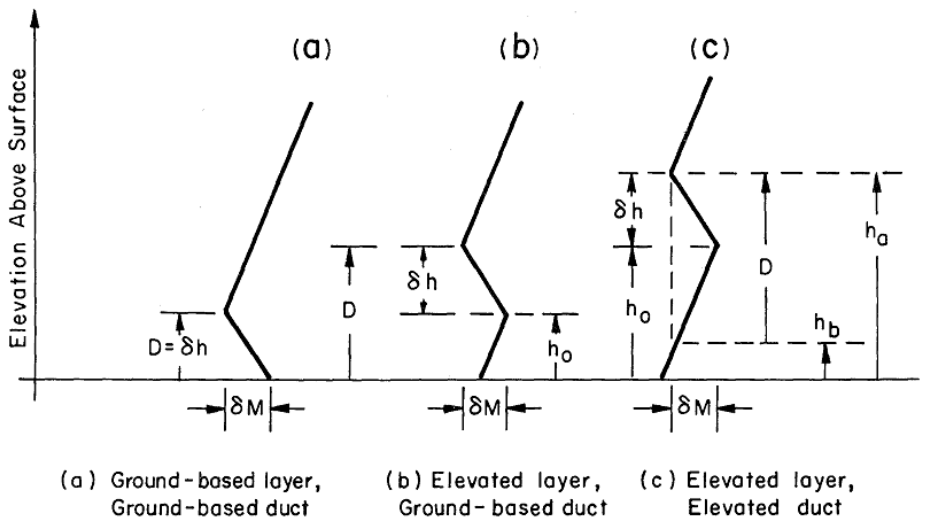

Figure 3.25: Ground-based, elevated surface and elevated ducts [70].

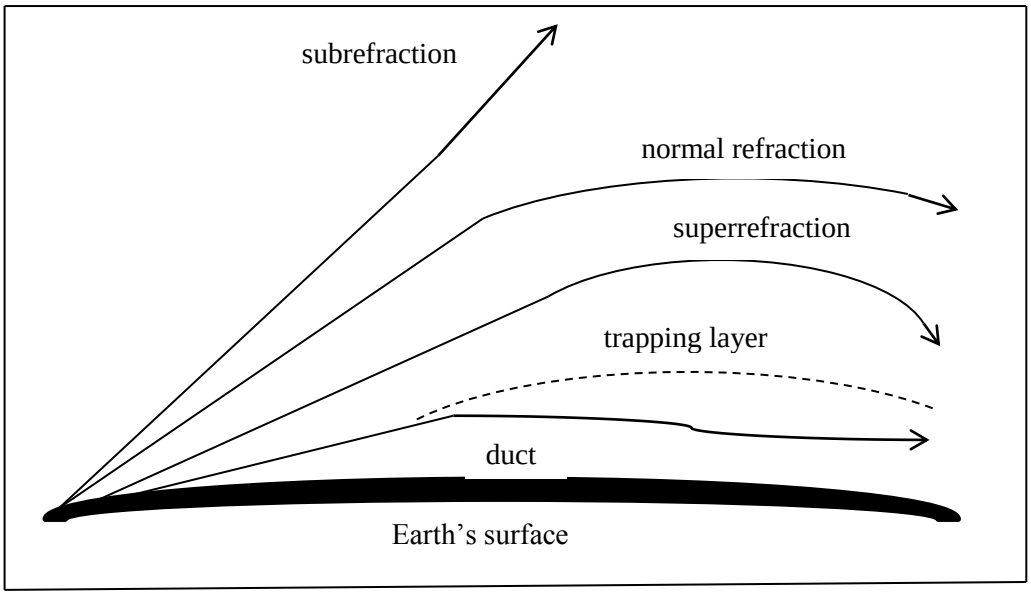

Figure 3.26: Refractive conditions in the troposphere [72].

(iv) Use of both Low Resolution (LRES) that report after every 10sec (50m) and High Resolution (HRES) radiosondes that report after every 2sec (10m) of ascent. The radiosondes attached to balloons filled with helium gas and then launched from ground stations. Radiosondes comprise of sensors that are able to record humidity, pressure and temperature of the atmosphere together with an oscillator that encodes the output from the sensors into an audio tone and a radio frequency transmitter that send the information back to the ground station. The received audio tones are then converted to pre-calibrated standard units and logged as balloon ascends , essentially providing vertical profile of the readings. Considering the large number of

meteorological stations worldwide, radiosondes are able to provide a very good global coverage, and are the most widely used instrument for upper air refractivity measurements.

b) Refractometer method: This method is usually known as the direct method as it measures the refractivity directly. The process involves the measurement of resonant frequency using a cavity open to the atmosphere, which changes as the refractive index of the air passing through the cavity changes. The refractometer is usually mounted to an aircraft or permanently on a tower and then maintained to give the most accurate readings. Although more complex, it is the most accurate of the three. This method is expensive and is rarely used.
c) Sodar: This is an acoustic sounding system, which is very useful for studying temperature inversions that are mainly responsible for the ducting phenomenon.

3.2.2 The Effective Earth Radius Factor (k-factor)

The earth over which the electromagnetic waves travel over is not flat but spherical. Also, the electromagnetic waves travelling over the earth do not travel in straight lines but are actually bent (refracted) either away from or towards its surface. Therefore, geometrical analysis to characterize the degree of bending of the waves over the earth's surface would be very complex in reality. Normally, it's assumed that the waves travel in straight lines over the earth which leads to a transformation of the actual radius of the earth to an imaginary one, often referred to as the effective earth radius. The relationship between the effective earth radius and the true earth radius is normally defined by what is known as the effective earth radius factor , normally abbreviated as the k-factor, which essentially defines the extent to which the waves bent as they traverse the atmosphere. Thus the k-factor can be obtained from [62]:

$$k = \frac{r_e}{r} \tag{3.91}$$

where k is the k-factor, r_e is the effective earth radius and r is the actual (true) earth radius.

The k-factor has been adopted by the ITU-R [4], as the single most appropriate parameter that defines of the refraction of radio waves as they travel through the atmosphere. The appropriate k-factor is normally used by transmission design engineers to achieve adequate path clearance in radio link design. Two distinct but very critical values of the k-factor are the effective value ($k_{99.9\%}, k_e$) and the median value ($k_{50\%}$) [4]. It is these two important values of the k-factor that are used by engineers during link planning to determine the appropriate antenna heights necessary for adequate path clearance.

Normally, the median value of the k-factor varies between 1 and 2, with lower values mainly being found in cold or dry climate and at high altitudes. Higher median k-factor values are commonly found in coastal areas which are known to be humid and hot. On the other hand, super high values of the median k-factor ranging between 2 to infinity and low values from 1 to 0.5 are an indication of anomalous propagation [50]. In general, the value of the k-factor is geographical and height dependent. In standard atmosphere, more so in temperate climates, the median value of the k-factor is 1.33 and that of the effective value is 0.67 and in places where data is not available, these are the

values used for design the world over. However, it often prudent for the design engineer to draw path profiles for different values of the k-factor so as to see which one provides adequate path clearance and eliminates any chances of diffraction fading occurring. The value that provides the desired path clearance is the one that determines the height of the antenna masts (towers) [3, 4]. Examples of some path profiles for different k-factor values over a spherical earth are shown in Figure 3.27. The k-factor is dependent on the state of the atmosphere and is a function of the vertical gradient of the refractivity. Thus, the k-factor varies depending on the seasonal and daily cycle variations and the meteorological conditions at the particular time. The 4/3 value of the median k-factor in standard atmospheres is normally very close to the value in most climates, more so in the temperate zones. Around this median value for standard atmospheres, the deviations from it is quite wide in tropical regions due to rising temperatures as well as increasing humidity, while for temperate and cold climatic zones, there is less variation [27].

Experimental investigations have shown that, for example, the probability that k-factor<0.6 in temperate climatic zones is less than 1%. For the same k-factor range in tropical climates, the probability is between 5% to 10%. This therefore means that there is higher chance of abnormal propagation occurring resulting from extreme values of the k-factor in tropical regions. Under minimum k-factor conditions, there is a reduction in the clearance over the ground and therefore the chances of getting an obstruction are at maximum. Normally, the interest is not the minimum value of the local k-factor but its effect throughout the entire path length. Thus an equivalent value of the k-factor is usually defined, whose minimum value for given climatic conditions will be dependent on the length of the path. On long radio paths, the equivalent k-factor is likely not to be far from the standard atmosphere value since atmospheric conditions that are extreme are not likely to be present at the same time over the entire path length while for short radio paths, there is more likelihood of the same atmospheric conditions existing for the entire path length, thus producing lower values of the equivalent k-factor [4, 27].

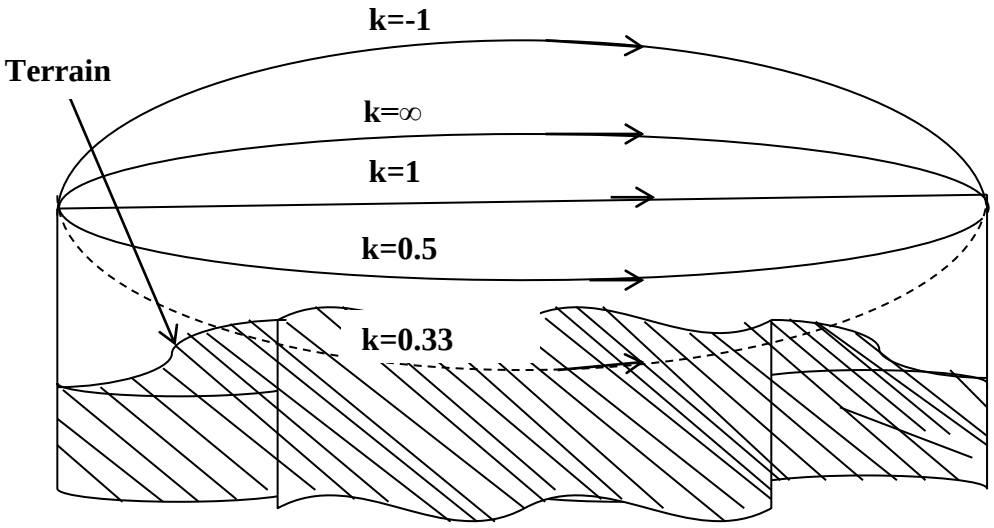

Figure 3.27: Path profiles for different values of the k-factor over a spherical earth [3].

The variation of the minimum (equivalent or effective) k-factor, $k_{99.9\%}, k_e$ with the path length (hop) is shown in Figure 3.28.

The k-factor is normally computed from the refractive index or refractivity gradient measurements. Using the refractive index gradient, the statistics of the k-factor are then calculated from the following expression [73]:

$$k = \left(1 + r\frac{dn}{dh}\right)^{-1} \tag{3.92}$$

where $\frac{dn}{dh}$ is the refractive index gradient. Other parameters are as defined in (3.91). Also, from (3.74), $N = (n-1)10^6$, so that:

$$\frac{dn}{dh} = \frac{dN}{dh}(10^{-6}) \tag{3.93}$$

If the value of $\frac{dn}{dh}$ in (3.93) is substituted into (2.30) and then we simplify the expression, we obtain the following equation for the k-factor [23, 60]:

$$k = \left[1 + {}^{dN}\!/_{dh}\,{}_{157}\right]^{-1} \tag{3.94}$$

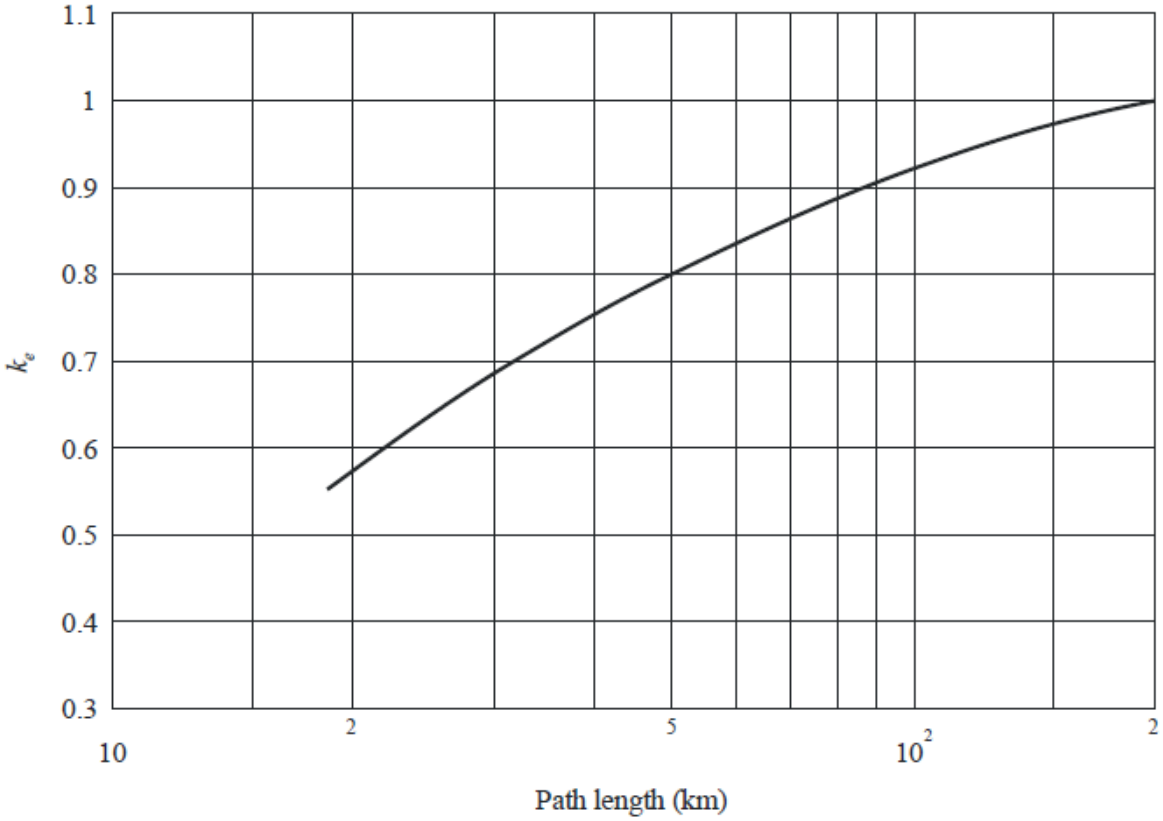

Figure 3.28: Minimum k-factor values as a function of the path length [4].

The following steps are used in the determination of the appropriate radio link antenna heights for temperate and tropical climates using median and effective values of the k-factor [4, 74]:

(i) Determine the antenna heights using the median value of the point k-factor at a path clearance of 100 % of the first Fresnel zone, F_1 over the highest obstacle. The median k-factor value of 4/3 is normally used in cases where local data is not available.

(ii) Determine the antenna heights using the effective value of the k-factor at a path clearance of 60% of the first Fresnel zone, for path lengths that are greater than about 30km in tropical climates, or path clearance of 30% of the first Fresnel zone in temperate climates if there is a path obstruction extended along a given segment of the radio path.

(iii) Choose the larger of the antennas in steps (i) and (ii) above for the radio link design.

3.2.3 Previous Studies the Effective Earth Radius Factor in Southern Africa

3.2.3.1 Palmer and Baker model

Based on the possibility that the cumulative distribution of the k-factor could be represented by the product of two independent cumulative distributions, one corresponding to the 'dry' term and the other corresponding to the 'wet' term, Palmer and Baker proposed the following model [23, 24]:

$$\psi_{eff}(k) = \psi_{dry} \times \psi_{wet} \tag{3.95}$$

where:

$$\psi_{dry} = exp\left[-\frac{(k'-1)^2}{2\sigma_{dry}^2}\right] \tag{3.96}$$

$$\psi_{wet} = exp\left[-\frac{(k'-k_{ref})^2}{2\sigma_{wet}^2}\right] \tag{3.97}$$

By substituting for the values of ψ_{dry} and ψ_{wet} as given by Equations (3.96) and (3.97) respectively in Equation (3.95), the following model was obtained:

$$\psi_{eff}(k) = exp\left[-(\frac{(k'-1)^2}{2\sigma_{dry}^2} + \frac{(k'-k_{ref})^2}{2\sigma_{wet}^2})\right] \tag{3.98}$$

where σ^2 is the variance and the subscripts 'dry' and 'wet' identify the climatic conditions giving rise to the relevant terms. k_{ref} is the reference value for the refractive index and was determined from the data used for the modeling through regression analysis. It was specifically assumed here that the meteorological conditions giving rise to the two terms are statically independent and that therefore Equation (3.95) would be valid. This model was found to be more applicable to inland summer rainfall areas. Using the results from this model, they were able to develop contours of the k-factor exceeded 0.001 of the time. In order to include the height and geographic latitude dependence of the refractivity gradient, the authors then extended the model; and proposed that the refractivity gradient variation could be described as [64]:

$$\frac{dN}{dh}/50\pi = a \times \left\{\left(\frac{h}{h_t}\right)^{\frac{2}{3}} - 1\right\} \tag{3.99}$$

where a is an invariant value of the normalized refractivity gradient at the sea level. The "pseudo" height of the tropopause is given by [64]:

$$h_t = \left\{\left(\frac{3}{2}\right) - \left(\frac{X}{90}\right)^{\frac{2}{3}}\right\} * 12km \tag{3.100}$$

where X is the geographic latitude of the measurement location.

This model is referred to as the double elliptic model.

3.2.3.2 Odedina and Afullo Model

Odedina and Afullo proposed a probability density function (pdf) of the k-factor after analysis of three years and ten months radiosonde data for Maun, Botswana and Durban, South Africa respectively. The minimum integral of square error between the measured pdf, $g(k)$and the analytical estimation of the pdf, $f(k)$ forms the basis of this model. Using the proposed pdf, they developed models covering the height ranges covered 0-200m and 0-500m above ground level for Maun, Botswana and Durban, South Africa. They proposed the following pdf format for the k-factor [18, 28]:

$$f(k) = Ae^{-\alpha(k-\mu_k)^2} \tag{3.101}$$

where A is the value of $f(k)$ is the mean value μ_k, and the parameter α determines the girth of $f(k)$. To determine A, μ_k, and α, the following two conditions have to be satisfied [18, 28]:

$$\int_{-\infty}^{\infty} f(k)dk = \int_{-\infty}^{\infty} A\, e^{-\alpha(k-\mu_k)^2} dk = 1 \tag{3.102}$$

$$E(k) = \int_{-\infty}^{\infty} kA\, e^{-\alpha(k-\mu_k)^2} dk = \mu_k \tag{3.103}$$

To ascertain $f(k)$ as the 'best' approximation for g(k), there was need to optimize cost function related to the error $\varepsilon(k)$. The integral of the square (ISE) was the cost function chosen.

$$\varepsilon(k)=[f(k) - g(k)] \tag{3.104}$$

$$\text{ISE}=\int_{-\infty}^{\infty}[f(k) - g(k)]^2 dk \tag{3.105}$$

The reader is referred to [18, 28] for further details on the model. In [20, 56], Afullo, Motsoela and Molotsi also reported on refractivity studies for Botswana. Using three-year data measurements (1996-1998), they were able to determine a mean value of the k-factor to be 1.1 while that of the effective k-factor value, k_e was found to be 0.7. When ducting data was included, they found k_e to be 0.61 while that of the mean value was 1.03.

3.3 Chapter Summary

Terrestrial electromagnetic waves travelling through the atmosphere under clear-air conditions are mainly affected by free space loss, multipath fading and diffraction fading. Free space loss is a function of the path length and the frequency of the operation. On the other hand, multipath and diffraction fading are dependent on the refractive gradients of the air. These refractive gradients are in turn dependent on the temperature, humidity and pressure of the air. Thus these three parameters are very important in the accurate prediction of how signals will be affected as they traverse the atmosphere. The parameters can either be modeled as refractivity gradients or in terms of the effective earth radius factor from a diffraction fading point of view or in terms of the geoclimatic factor for multipath applications. Different models that are used to describe free space loss, diffraction and multipath fading have been presented here. The effective earth radius factor is the design parameter used in terrestrial radio link design to determine accurate antenna heights that are required for adequate path clearance. Thus, with the accurate determination of the local effective earth radius factor for all regions, diffraction fading will not be much of a problem in terrestrial LOS links, and this sets the platform for the next chapter.

Chapter 4

Effective Earth Radius Factor (k-factor) Modelling and Characterization

4.1 Introduction

The effective earth radius factor (k-factor) is an important parameter in the planning and design of both terrestrial microwave and UHF/VHF line-of-sight links. It is for this reason that the structure and variations in the effective earth radius factor in the first 200m of the atmosphere is critical to radio link planners and optimization engineers alike. The atmospheric composition changes from time to time, place to place and even with height and hence the need for accurate determination and prediction of the k-factor. The four thirds (4/3) value given for the median k-factor in average temperate climate should only be used for gross planning but where data is available, the actual values of the same should be determined. This will ensure well designed links with minimum outage experienced due to k-factor related problems i.e. diffraction (k-type) fading and thus avoiding expensive reverse engineering and optimization procedures. In this chapter, three years radiosonde measurements data sourced from the South African Weather Service (SAWS) is processed and only k-factor statistics for the first 200m above ground level considered for further analysis. Both non-parametric and parametric methods are used to model solutions for the distribution characteristics of the k-factor across seven locations in South Africa. From the models obtained, both median ($k_{50\%}$) and k-factor values exceeded 99.9% of the time (k_e) are determined. Comparisons between the measured, curve-fitting and kernel values of the k-factor also done.

Radiosonde data measurements have a poor spatial and time resolution, thus are not able to capture diurnal variations in the refractivity gradient effectively. To counter this drawback, surface measurements can be done several times in a day from ground stations. But, surface measurements fail to capture data that can be used to study the vertical profile of the refractivity. This demerit associated with surface measurements can be overcome by the use of sensors mounted at different heights above ground level on a tower. Alternatively, a refractometer mounted on an aircraft could also be used to measure the refractivity directly. However, these three alternative methods are more expensive compared to radiosondes. Therefore, radiosondes are still the more preferred method applied in the study of atmospheric refractivity, backed up by the use of some measures of fit to check their performance and their wide coverage globally.

4.2 Data Collection, Processing and Analysis

Raw radiosonde data measurements for seven locations in South Africa were obtained from the South African Weather Service (SAWS) for three years, covering the period between January 2007 and December 2009. The seven locations were Bloemfontein ($29^o06'$S, $26^o18'$E), Cape Town ($33^o59'$S, $18^o36'$E), Durban ($29^o58'$S, $30^o57'$E), Polokwane ($23^o54'$S, $29^o28'$E), Pretoria ($25^o55'$S, $28^o13'$E), Upington ($28^o24'$S, $21^o16'$E) and Bethlehem ($28^o15'$S, $28^o20'$E). The original source files containing the data were notepad files. The data was then extracted from the notepad files and copied to Microsoft Excel files, each file containing data for the twelve months in a particular year for every location for the three separate years considered. This would ensure that k-factor data could easily be extracted for the three-year period or on seasonal basis for further

analysis, modelling and mapping procedures. A sample extract of the raw data is shown below in Table 4.1. From this table, we see that the radiosonde instrument used for the measurements has a resolution of 10 seconds and would ideally report after every 50 m of ascent. However, the micro-structural and inhomogeneous atmosphere it ascends through will cause some slight variations in the ideal reporting height ranges above ground level. The trend observed is nonetheless satisfactory and produces enough samples for the study, which is focused mainly on the first 200 m above ground level. The choice of the 200 m cut-off is informed by the fact that this is where much of terrestrial communications takes place. Some of the unnecessary data columns, for example, wind direction; wind speed and dew point, in Table 4.1 have been deleted due to space constraints. The radiosonde launches were done between 11.00 PM and 12. 00 AM and again between 11.00AM and 12.00 PM.

Among all the measurements recorded by the radiosonde, only four are vital for the present study, that is, the pressure, temperature, humidity and geopotential height (GPM). From the humidity and temperature measurements, the water vapour pressure was computed for each set of measurements using Equation (3.78). The saturation water vapour for each set of measurements was obtained using Equation (3.79).

The dry part of the refractivity, N_{dry} , the wet part of the refractivity, N_{wet}, and the total refractivity, N_{total}, for each set of measurements were then computed using Equations (3.76), (3.77) and (3.75) respectively. The k-factor values were then computed from Equation (3.94). Some of the rogue data values, mainly resulting from some incomplete data sets, were filtered out during the initial data sorting stages.

Table 4.1: Sample raw radiosonde data for Bloemfontein

	DateT	DeltaT (s)	Pressure (hPa)	Temperature (℃)	Humidity (%)	GPM (m)
BLOEMFONTEIN WO	1/1/2007 11:16:00PM	0	871.2	15.4	74	1353
BLOEMFONTEIN WO	1/1/2007 11:16:00PM	10	865.8	15.8	70	1405
BLOEMFONTEIN WO	1/1/2007 11:16:00PM	20	860.8	15.5	71	1455
BLOEMFONTEIN WO	1/1/2007 11:16:00PM	30	855.9	15	73	1502
BLOEMFONTEIN WO	1/1/2007 11:16:00PM	40	851.1	14.6	74	1550
BLOEMFONTEIN WO	1/1/2007 11:16:00PM	50	845.8	14.1	76	1604
BLOEMFONTEIN WO	1/1/2007 11:16:00PM	60	839.8	13.4	79	1664
BLOEMFONTEIN WO	1/1/2007 11:16:00PM	70	834.5	13	80	1717
BLOEMFONTEIN WO	1/1/2007 11:16:00PM	80	829	13	77	1773
BLOEMFONTEIN WO	1/1/2007 11:16:00PM	90	823.3	14	68	1830
BLOEMFONTEIN WO	1/1/2007 11:16:00PM	100	817.9	15	65	1886

A sample of the refractivity and k-factor calculations is shown below in Table 4.2 for the raw data measurements in Table 4.1. Then, the k-factor values for each location for the first 200m above ground level (a.g.l) were extracted to different work sheets for modelling and characterization. From this requirement, for example, only the first five k-factor values from Table 4.2 would be used. The measured k-factor probability density functions were then developed. The k-factor values obtained were then subjected to both parametric and non-parametric data modelling so as to draw a comparison between the measured pdfs and the models. The curve-fitting method was chosen as the preferred parametric method while the kernel density estimation (kde) was selected as the non-parametric technique.

4.3 Modelling and Characterization

Data modelling methods mainly fall in two categories: non-parametric and parametric. Non-parametric methods involve direct fitting of the model straight from the data set and does not impose any parameters on the data structure. They tend to follow the measured data as much as possible and produce much less errors as compared to the parametric techniques. On the other hand, parametric data modelling techniques are defined by certain coefficients which are the constituent elements of a model or an equation that best describes the structure of some data set. These coefficients include the mean, variance, slope, y-intercept, standard deviation, exponent, median or the logarithmic base depending on the particular model used to fit the best curve. As such, these methods tend to be rigid by imposing such restrictions on the data structure [75]. The parametric model does not follow the measured data pdf as much as the non-parametric counterpart, thereby producing greater errors. They are however easier to interpret and are described in terms of their coefficients (parameters). One non-parametric method (kernel density estimation) and one parametric method (curve fitting –specifically the Gaussian fit) have been applied to model the k-factor in South Africa for the seven locations considered and are explained further below.

Table 4.2: Sample calculations of the refractivity and the k-factor for Bloemfontein

N_{dry}	N_{wet}	N_{total}	dN	dh	$dN/_{dh}$	k-factor
234.4144	58.08012	292.4945	-3.64498	0.052	-70.0957	1.806585
232.6388	56.21079	288.8496	-1.26853	0.05	-25.3705	1.192742
231.5358	56.04524	287.581	-0.96719	0.047	-20.5786	1.150846
230.6175	55.99635	286.6138	-1.49841	0.048	-31.2169	1.24818
229.6431	55.47232	285.1154	-1.1545	0.054	-21.3796	1.157643
228.6105	55.35042	283.9609	-1.17226	0.06	-19.5376	1.14213
227.5436	55.24511	282.7887	-1.70992	0.053	-32.2626	1.258644
226.4238	54.65499	281.0788	-3.54187	0.056	-63.2477	1.674625
224.9315	52.60543	277.5369	-5.69211	0.057	-99.8616	2.747713
222.6066	49.23824	271.8448	-1.60641	0.056	-28.6859	1.22356
220.3786	49.85976	270.2384	-270.238	-1.886	143.2865	0.522834

4.3.1 Curve Fitting Method

The main aim of curve fitting is to provide a theoretical model or equation that can be used to describe a set of data. The models are characterized by some coefficients which are derived from the data set by analysing the measured data characteristics, mainly by using a scatter plot and applying some residual minimization criteria to derive an optimized solution. Thus, curve fitting seeks to find the best line of fit through some experimental data. There is no single curve fitting method that can be declared superior or more suitable without first being tested on a particular problem. Hence, the choice of the particular model to use depends on the observed data structure or historical knowledge about the measured data.

The curve fitting model chosen for the k-factor modelling is the Gaussian model. This decision was informed by the shape of the scatter plot of the measured data for the seven locations and previous studies on the k-factor in Maun, Botswana and Durban, South Africa by Odedina and Afullo [18, 28, 76]. In all the seven locations where the k-factor statistics were available, the k-factor distribution was observed to be bell-shaped, centred almost symmetrically around a mean value, μ_k. The proposed probability density function for modelling the k-factor for Maun, Botswana and Durban, South Africa by Afullo and Odedina is adopted for the curve fitting modelling in this study. The model has been explained in Subsection 3.2.3.2. Both annual and seasonal models of the k-factor are determined in this study. The seasonal values were determined for the months (seasons) of February, May, August and November.The initial coefficients of the model, A, $\propto$ and μ_k, were obtained from the measured k-factor scatter plot and then the integral of square error was used to find the optimum model by minimizing the error between the data points and the model. The minimum error obtained by varying the parameters A and μ_k gives the final and best model of the k-factor.

4.3.2 Kernel Density Estimation

Kernel density estimation is a data modelling technique that belongs to a category of data methods that are modelled directly from the data samples. This is to say that, no initial assumptions are made concerning the shape or form of the data structure but the model is used to point to the actual data distribution attributes. The kernel density estimate has not always been the traditional preferred non-parametric method, but histograms have. However, histograms suffer from serious drawbacks, including their reliance on the bin width, and their characterization by very abrupt and sharp transitions from bin to bin. If large bin sizes are chosen for histogram data fitting, only a few of the data regions will be sufficiently represented and fine structural elements of the data structure may be missed out. On the contrary, if very small bins are used, some of the bins may turn out to contain no data samples or very few data samples, which is difficult to interpret. Kernel density estimates were introduced to counter the shortcomings associated with histograms. Thus, just like the histograms, they impose no restrictions on the final outcome of the data structure. Kernel density estimates are characterized by a very critical parameter that determines how best the data is modelled. This parameter is known as the smoothing parameter, h. Some other literature refer to it as the window width or the bandwidth [76, 77, 78].

The kernel density estimate of a variable is obtained by centering a kernel function, symmetric about zero, on each data point and then summing these functions around the points for which the kernel

estimate is defined resulting in smooth estimate of the variable. Although the smoothing effect of kernel estimates on the data variable may not be as smooth as that of parametric distributions, the optimum estimate usually follows the initial measured probability density estimate as much as possible and produces very good error performance. The kernel density estimate of a variable k is given by [77-79]:

$$f(k) = \frac{1}{nh}\sum_{i=1}^{n} K\left(\frac{k - X_i}{h}\right) \tag{4.1}$$

where n is the number of data points, h is the smoothing parameter, X_i is the ith data point and K is the kernel function.

The choice of the kernel function does not so much influence the final outcome, but the optimum value of the smoothing parameter does. The optimum value of the smoothing parameter is defined in terms of the error calculated between the measured pdf and the fitted pdf. The optimum value of the smoothing parameter is obtained when the error computed is at minimum. The smoothing parameter varies from one data set to another depending on the kernel type and the number of data samples. As the number of the data points tends to infinity, the value of the smoothing parameter tends to zero, and vice versa. Two main error criteria have been adopted in the past for optimizing kernel estimates. These are; the integral of square error (ISE) and the mean integral of square error ($MISE$). These errors are given by, respectively [77-81]:

$$ISE = \int_{-\infty}^{\infty} [f(k) - f^*(k)]^2 \, dk \tag{4.2}$$

$$MISE = E[\int_{-\infty}^{\infty} [f(k) - f^*(k)]^2 \, dk] \tag{4.3}$$

where $f(k)$ is the kernel estimate value $f^*(k)$ is the measured value and $E[.]$is the mathematical expectation. The ISE is the error criteria chosen for this study. There are several techniques that have been put forward in an effort to solve the issue of the choice of the optimum value of the kernel estimate. Most of these are plug-in methods that have proposed different formulae for the value of h, depending on the kernel function type [18, 80, 81]. If the choice of the smoothing parameter is too small, the resulting estimate in usually very spiky and hard to interpret, which is usually referred to as under-smoothing. On the other hand, a choice of the smoothing parameter that is too large will result in over-smoothed estimates that tend to miss out on fine details of the data structure.The following equations hold true for all kernel functions [80, 81]:

$$\int_{-\infty}^{+\infty} K(k)dk = 1 \tag{4.4}$$

$$\int_{-\infty}^{+\infty} kK(k)dk = 0 \tag{4.5}$$

$$\int_{-\infty}^{+\infty} k^2 K(k) dk > 0 \tag{4.6}$$

The kernel function is a true pdf and it follows that the kernel density estimate is a true pdf as well. There are several kernel functions used to model data. These are: Rectangular (box) kernel, Triangular kernel, Gaussian kernel, Epanechnikov kernel, Biweight kernel, among others. Among these, the Epanechnikov, Triangular, Gaussian and Rectangular kernels have been chosen to model the k-factor for South Africa. These kernel functions, their efficiencies and their plug-in formula for computing the optimum value of the smoothing parameter are shown in Table 4.3. We however note that these plug-in formulae normally produce over-smoothed estimates that may be misleading in many aspects. Thus, an iterative procedure is used to determine the optimum value of the smoothing parameter, and such, the value of the smoothing parameter computed using these formulas is just a guide to get one started with the modeling process.

Using the *ksdensity* function in MATLAB, a program for modeling the k-factor for South Africa was written, which included all the four kernels shown in Table 4.3. The steps below were then used to calculate the optimum kernel density estimate:-

1. As a first estimate, calculate the value of the smoothing parameter using the plug-in formula for the different kernels as shown in Table 4.3.
2. Estimate the error (in our case the ISE) of the resulting estimate.
3. Choose a value of the smoothing parameter that is smaller than the one obtained in step, else choose a larger value.
4. Calculate the error of the estimate obtained using the value of h in step 3.
5. If the error in step 4 is smaller than the one in step 2, choose an even smaller (greater) value of h and compute the error once more.
6. Repeat the above procedure until the error starts increasing and then the minimum error will be obtained as the last value before it starts increasing, which points to the optimum value of h.

4.3.3 Three-year Curve Fitting and Kernel Results and Discussion

Table 4.4 shows the three-year annual Gaussian curve fitting models of the k-factor developed for the seven locations in South Africa. Table 4.5 shows the values of the ISE and the parameters A and u_k obtained. Figures 4.1-4.7 show the plots of the measured pdf, initial estimate and final estimate of the k-factor. The initial estimate parameter values are obtained from the measured pdf plot and then the final values of the same are determined by minimizing the ISE between the measured pdf and the final estimate. The minimum ISE is obtained by first varying the parameter A until the minimum ISE is achieved and then again varying parameter μ_k until another error minimum is achieved. These sets of values are the ones that determine the final curve fitting model (final estimate) of the k-factor. From Figures 4.1-4.7 and Table 4.5, the median value of the k-factor is 1.24 for Bloemfontein, while it is 1.29 for Cape Town. The corresponding values are 1.27 for Durban, 1.23 for Polokwane, 1.19

for Pretoria, 1.17 for Upington and 1.20 for Bethlehem. From Table 4.5, Bethlehem produces the largest error while Durban produces the least. Table 4.6 is a tabulation of the kernel median k-factor and ISE values for three different values of the bandwidth. Many other values of the bandwidth were tested and the ones shown in this table are just a sample.

Table 4.3: Kernel functions used for modeling [80, 81]

Kernel	Kernel function, $K(k)$	Efficiency (%)	Optimal window width
Epanechnikov	$K(k) = \begin{cases} \frac{3}{4\sqrt{5}}\left(1-\frac{1}{5}k^2\right), -\sqrt{5} \le k \le \sqrt{5} \\ 0, elsewhere \end{cases}$	100	$\frac{2.34\sigma}{n^5}$
Triangular	$K(k) = \begin{cases} \frac{15}{16}(1-k), -1 \le k \le 1 \\ 0, elsewhere \end{cases}$	98.6	$\frac{2.58\sigma}{n^5}$
Gaussian	$K(k) = \frac{1}{\sqrt{2\pi}} e^{-\left(\frac{k^2}{2}\right)}, -\infty < k < \infty$	95.1	$\frac{1.06\sigma}{n^5}$
Rectangular	$K(k) = \begin{cases} \frac{1}{2}, -1 \le k \le 1 \\ 0, elsewhere \end{cases}$	93	$\frac{1.84\sigma}{n^5}$

Table 4.4: Three-year curve-fitting distribution models

Location	Gaussian distribution Model
Bloemfontein	$1.2e^{-4.53(k-1.24)^2}$
Cape Town	$1.2e^{-4.53(k-1.29)^2}$
Durban	$1.37e^{-5.90(k-1.27)^2}$
Polokwane	$1.64e^{-8.45(k-1.23)^2}$
Pretoria	$1.8e^{-10.18(k-1.19)^2}$
Upington	$1.41e^{-6.25(k-1.17)^2}$
Bethlehem	$2.4e^{-18.10(k-1.20)^2}$

Table 4.5: Three-year curve-fitting parameters and ISE values

Location	Initial estimates from measurements			Final estimates from curve fitting		
	u_k	A	ISE	u_k	A	ISE
Bloemfontein	1.22	1.82	0.23	1.24	1.2	0.19
Cape Town	1.29	1.60	0.13	1.29	1.2	0.11
Durban	1.27	1.33	0.102	1.27	1.37	0.101
Polokwane	1.26	1.52	0.11	1.23	1.64	0.09
Pretoria	1.20	2.04	0.14	1.19	1.8	0.13
Upington	1.18	1.36	0.14	1.17	1.41	0.13
Bethlehem	1.16	1.96	0.46	1.20	2.4	0.38

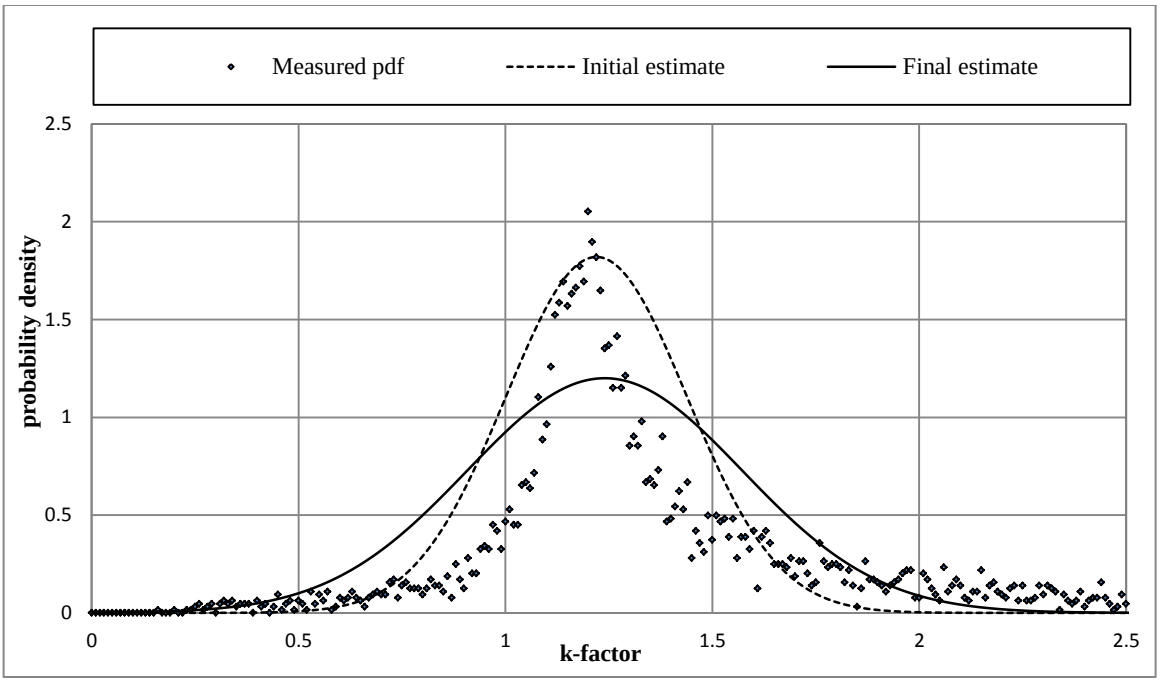

Figure 4.1: Bloemfontein Gaussian curve fitting estimates, 200m a.g.l

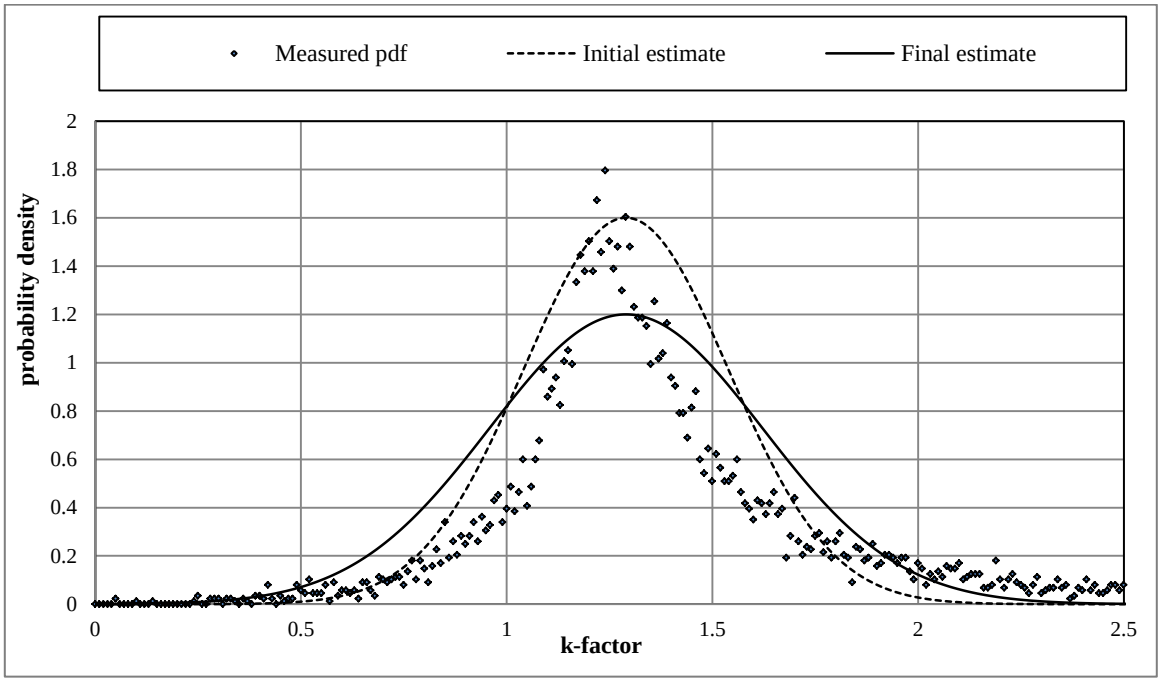

Figure 4.2: Cape Town Gaussian curve fitting estimates, 200m a.g.l

However, for all the kernels used, the value of the optimum bandwidth is among the ones tabulated and it can be identified as the one that produces the minimum error. Due to space constraints, only the best kernel model for each location is plotted here. These models are shown in Figures 4.8-4.14.

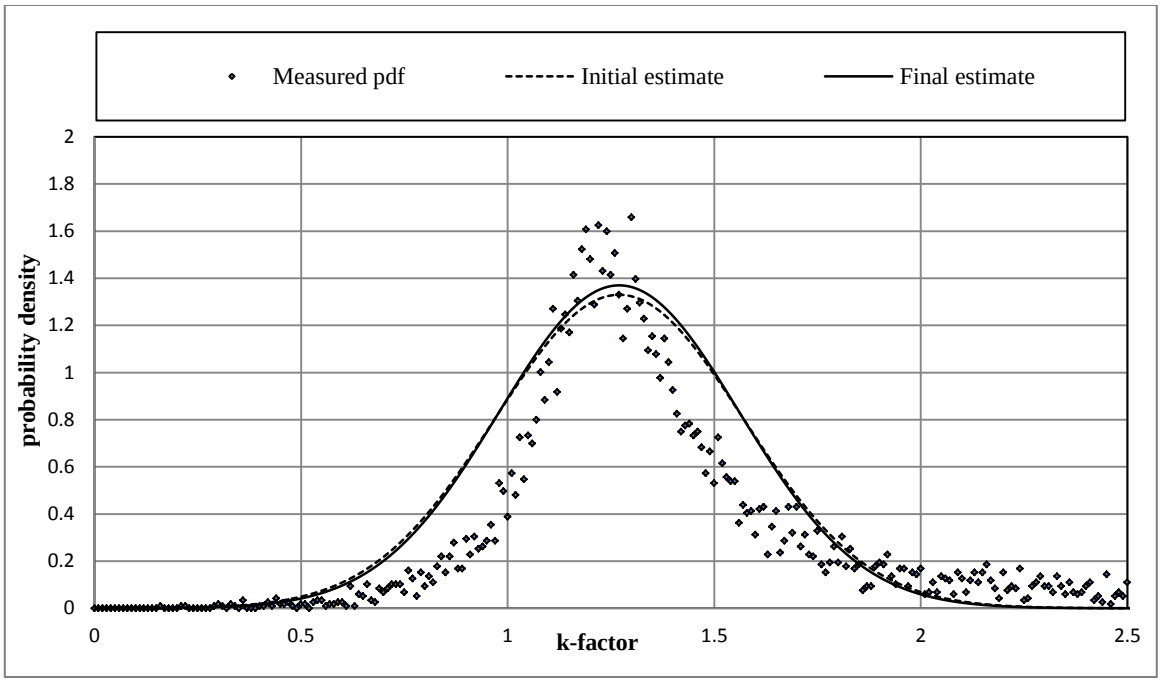

Figure 4.3: Durban Gaussian curve fitting estimates, 200m a.g.l

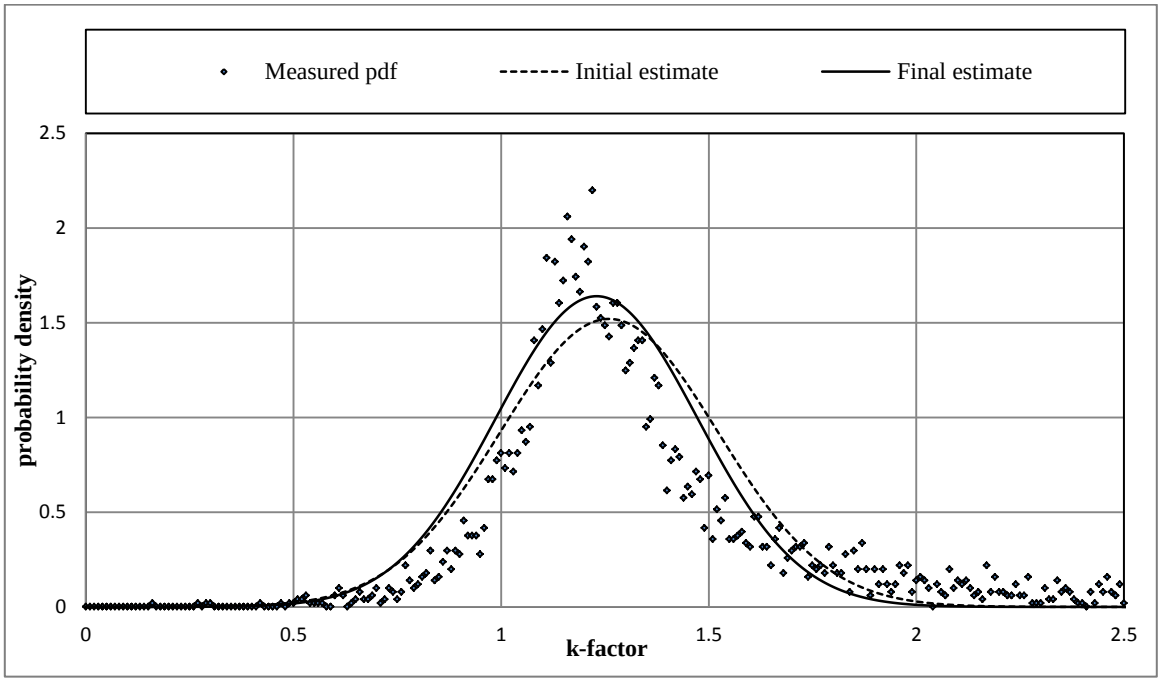

Figure 4.4: Polokwane Gaussian curve fitting estimates, 200m a.g.l

From Table 4.6 and Figures 4.8-4.14, the best kernel model for Bloemfontein is Gaussian with an optimum bandwidth of 0.009 and an ISE of 0.0329. For Cape Town the best kernel model is Epanechnikov with an optimum bandwidth of 0.006 and ISE of 0.0146.

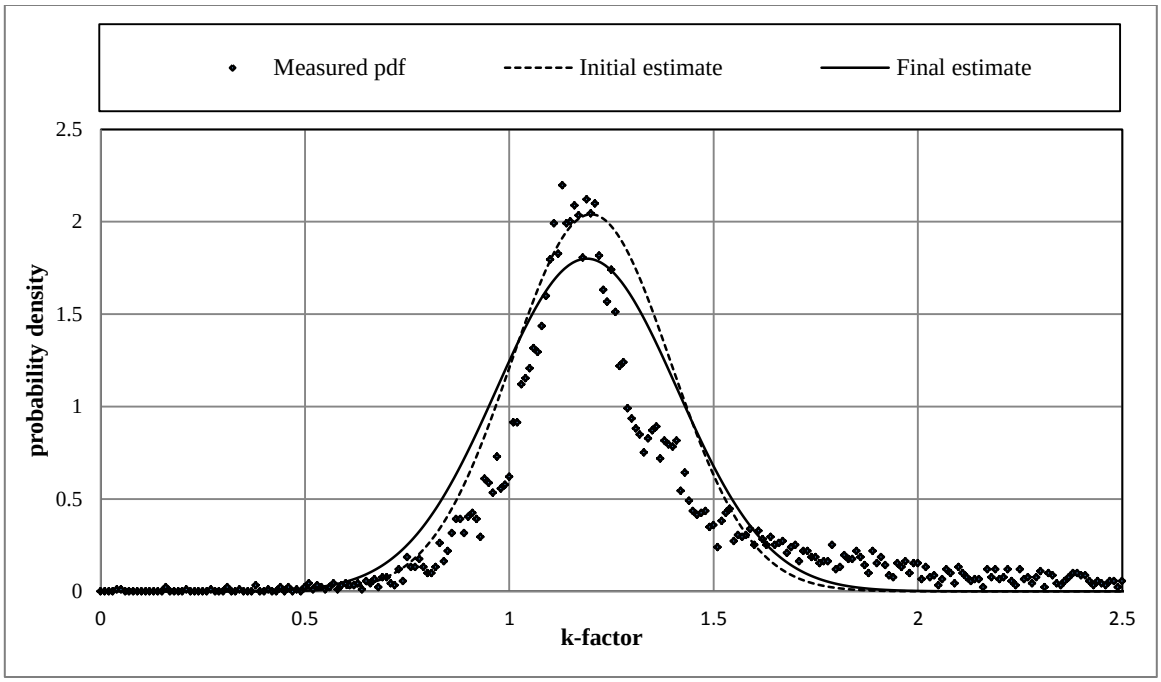

Figure 4.5: Pretoria Gaussian curve fitting estimates, 200m a.g.l

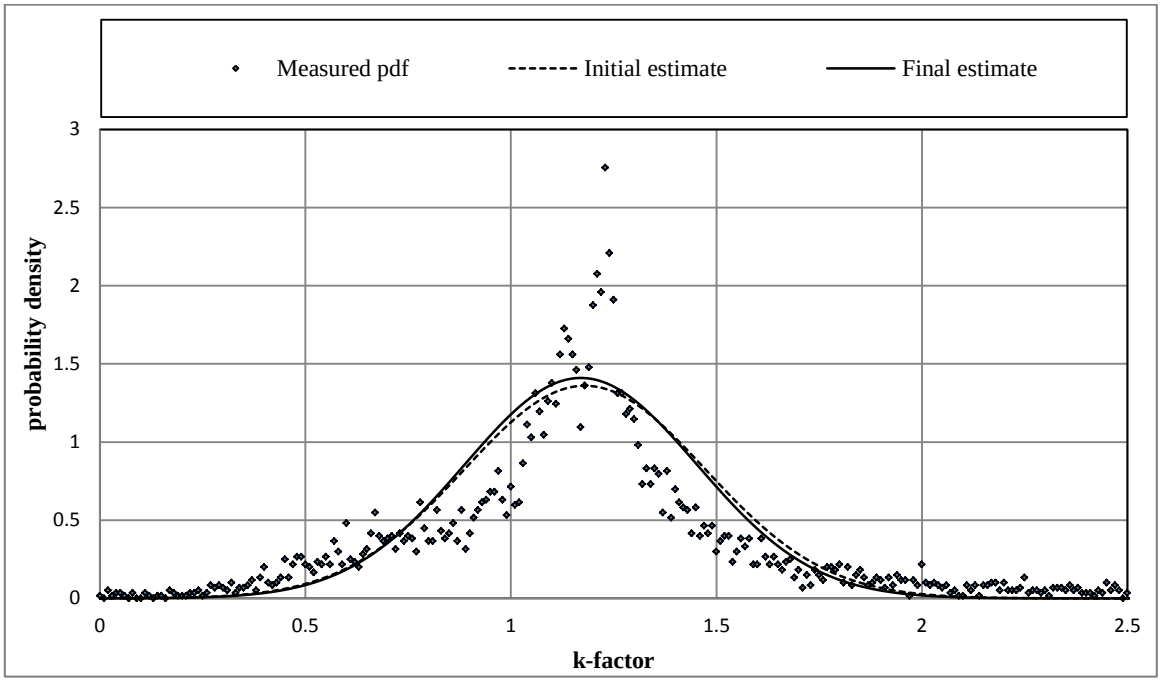

Figure 4.6: Upington Gaussian curve fitting estimates, 200m a.g.l

The best kernel model for Durban is Rectangular with a bandwidth of 0.006 and ISE of 0.0149 while, for Polokwane the best kernel model is also Rectangular with an optimum bandwidth of 0.006 and an ISE of 0.0193.The best kernel model for Pretoria is Rectangular with an optimum

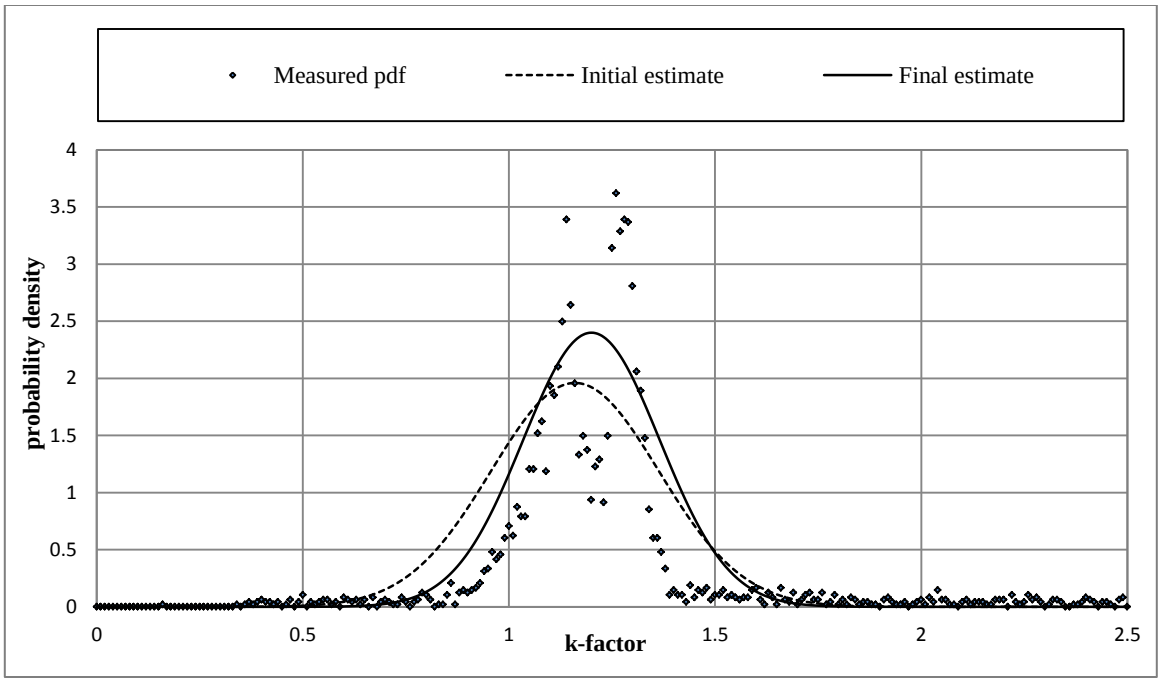

Figure 4.7: Bethlehem Gaussian curve fitting estimates, 200m a.g.l.

Table 4.6: Three-year kernel bandwidth, median *k*-factor and ISE values

Locations	Bandwidth, h	Kernel							
		Gaussian		Triangular		Epanechnikov		Rectangular	
		Media	ISE	Media	ISE	Median	ISE	Media	ISE
Bloemfonten	0.007	1.21	0.0332	1.21	0.033	1.21	0.0331	1.22	0.0334
	0.008	1.21	0.0330	1.21	0.033	1.21	0.0332	1.22	0.0343
	0.009	1.21	0.0329	1.21	0.033	1.21	0.0333	1.22	0.0349
Cape Town	0.006	1.27	0.0149	1.26	0.014	1.26	0.0146	1.25	0.0147
	0.007	1.27	0.0147	1.26	0.014	1.26	0.0148	1.25	0.0158
	0.008	1.27	0.0148	1.26	0.015	1.26	0.0153	1.25	0.0160
Durban	0.006	1.26	0.0153	1.25	0.015	1.26	0.0152	1.25	0.0149
	0.007	1.26	0.0151	1.25	0.015	1.26	0.0153	1.25	0.0159
	0.008	1.26	0.0152	1.25	0.015	1.26	0.0155	1.25	0.0163
Polokwane	0.006	1.26	0.0211	1.25	0.020	1.25	0.0197	1.25	0.0193
	0.007	1.26	0.0203	1.25	0.020	1.25	0.0198	1.25	0.0195
	0.008	1.26	0.0200	1.25	0.020	1.25	0.0199	1.25	0.0208
Pretoria	0.006	1.20	0.0107	1.20	0.010	1.21	0.0104	1.21	0.0099
	0.007	1.20	0.0105	1.20	0.010	1.21	0.0105	1.21	0.0111
	0.008	1.20	0.0104	1.20	0.010	1.21	0.0107	1.21	0.0112
Upington	0.005	1.20	0.0131	1.21	0.012	1.20	0.0121	1.20	0.0113
	0.006	1.20	0.0126	1.21	0.013	1.20	0.0127	1.20	0.0128
	0.007	1.20	0.0127	1.21	0.013	1.20	0.0132	1.20	0.0149
Bethlehem	0.006	1.17	0.0567	1.18	0.056	1.18	0.0555	1.17	0.0546
	0.007	1.17	0.0556	1.18	0.056	1.18	0.0556	1.17	0.0576
	0.008	1.17	0.0552	1.18	0.055	1.18	0.0563	1.17	0.0569

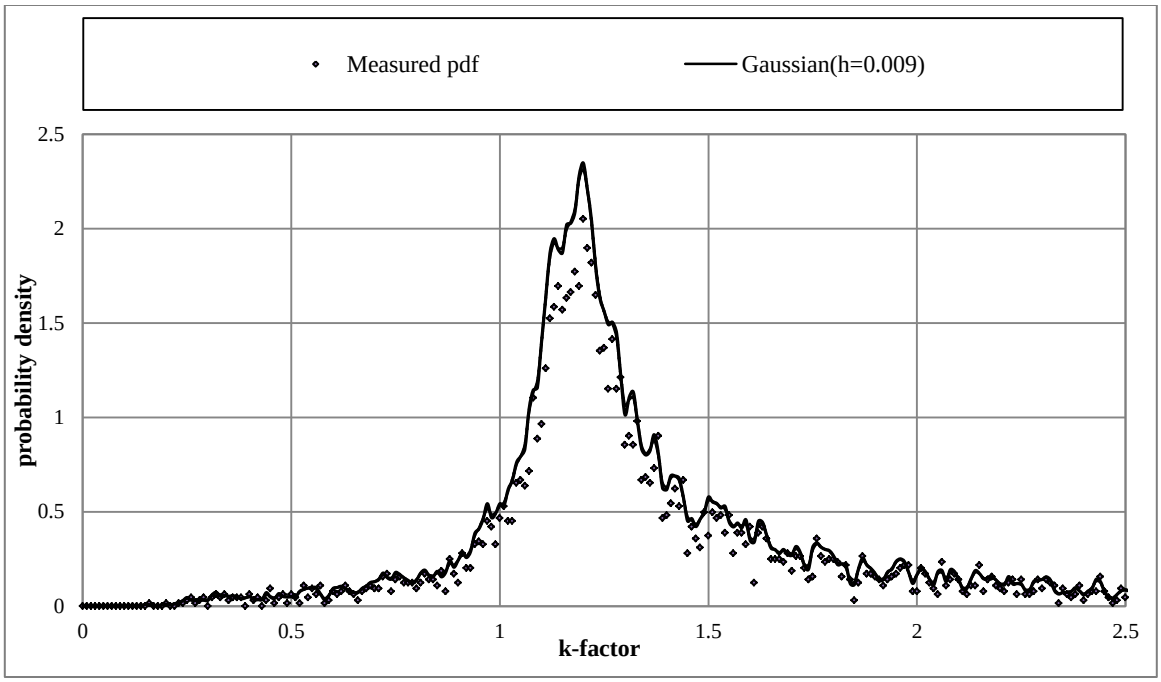

Figure 4.8: Bloemfontein Gaussian kernel density estimate, 200m a.g.l

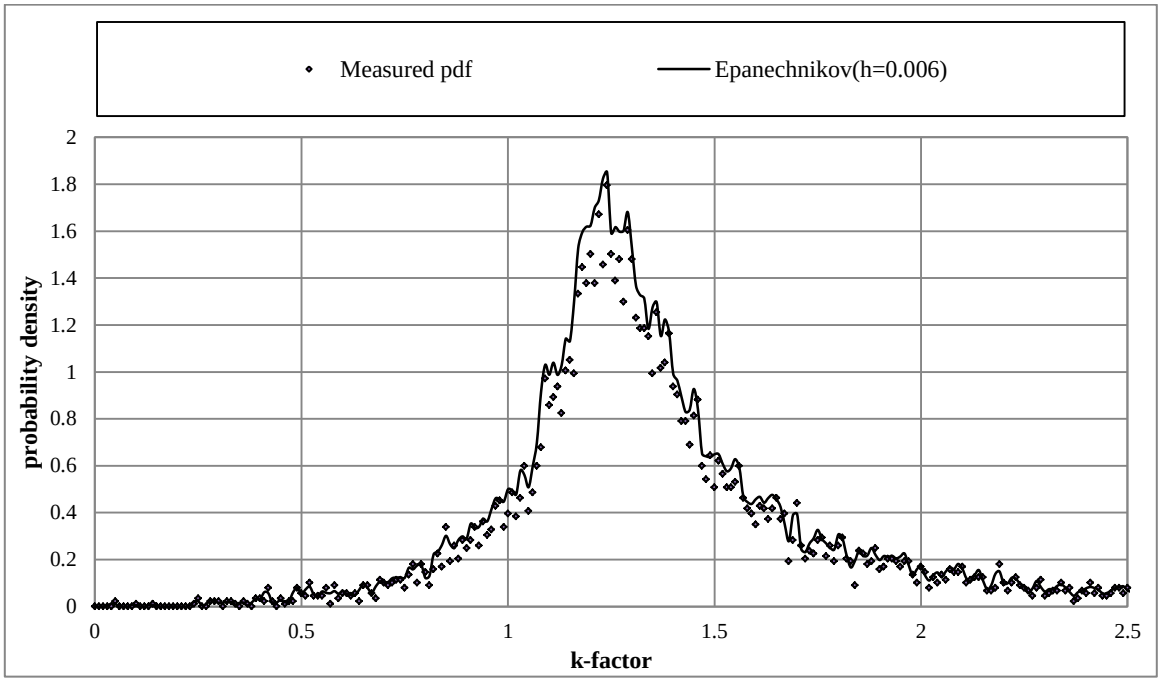

Figure 4.9: Cape Town Epanechnikov kernel density estimate, 200m a.g.l

bandwidth of 0.006 and an ISE of 0.010. For Upington, the best kernel model is Rectangular with an optimum bandwith of 0.005 and an ISE of 0.0113. Finally, the best kernel model for Bethlehem is Rectangular with an optimum bandwidth of 0.006 and an ISE of 0.0546.

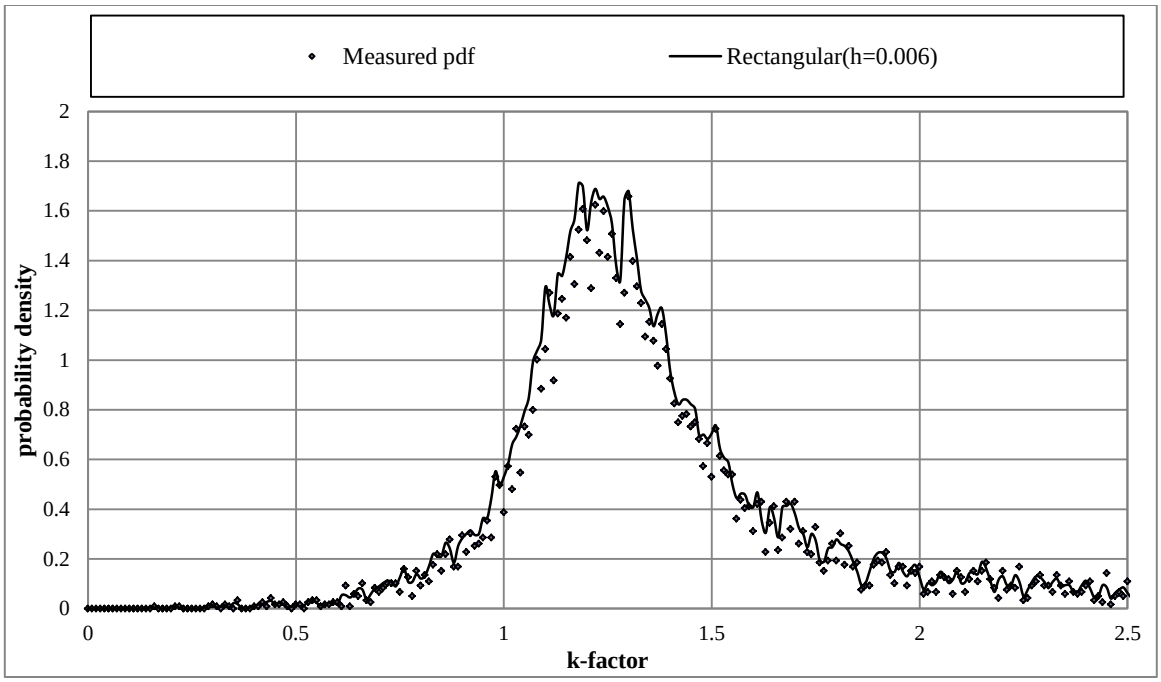

Figure 4.10: Durban Rectangular kernel density estimate, 200m a.g.l

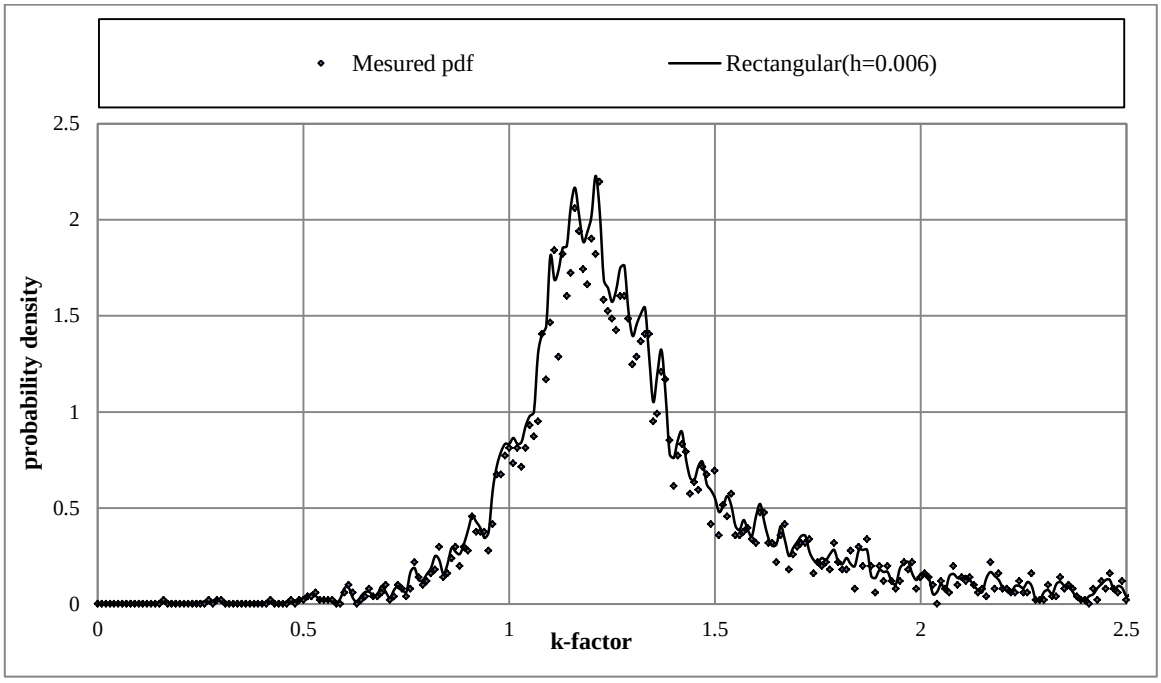

Figure 4.11: Polokwane Rectangular kernel density estimate, 200m a.g.l

Thus, we see that the Rectangular kernel is the best kernel model for five of the seven locations while Epanechnikov and the Gaussian Kernel are optimal for one location each. Also, Bethlehem

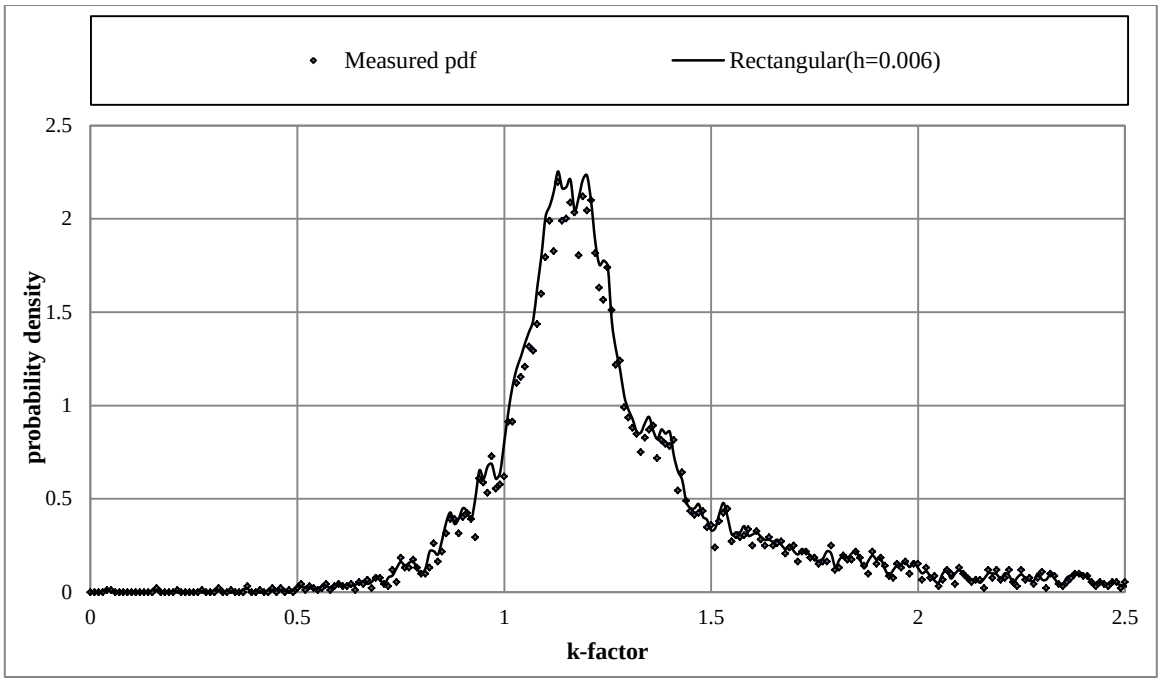

Figure 4.12: Pretoria –Rectangular kernel density estimate, 200m a.g.l

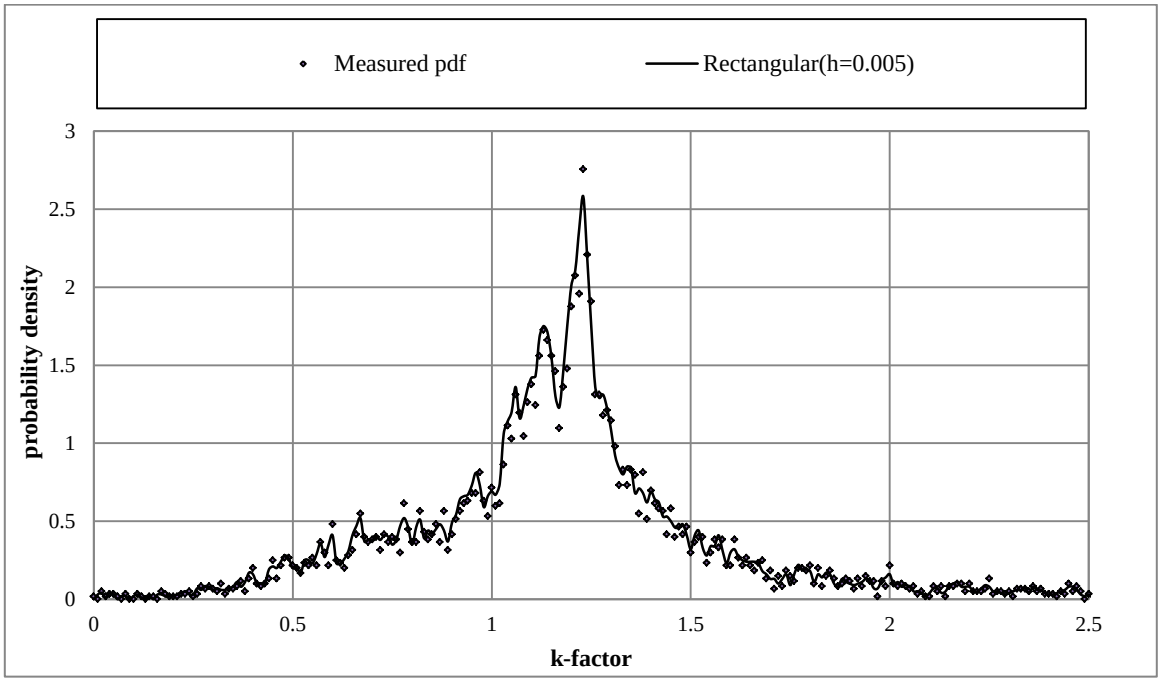

Figure 4.13: Upington Rectangular kernel density estimate, 200m a.g.l

produces the worst error performance while Pretoria is the best. From Figures 4.8-4.14 and Table 4.6, the kernel median k-factor obtained is 1.21 for Bloemfontein, 1.26 for Cape Town, 1.25 for Durban, 1.25 for Polokwane, 1.21 for Pretoria, 1.20 for Upington and 1.17 for Bethlehem.

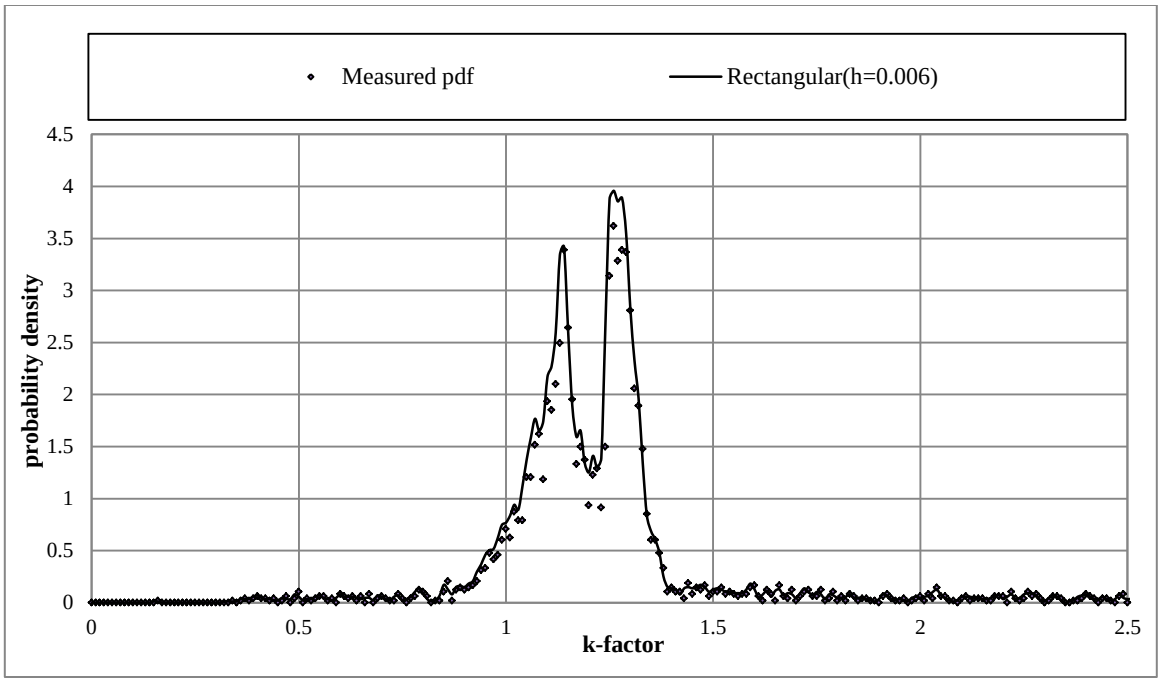

Figure 4.14: Bethlehem Rectangular kernel density estimate, 200m a.g.l

The three-year annual measured, curve fitting and kernel median k-factor value are compared in Table 4.7. From this table, we see that the values obtained are quite close to each other for each location. Also, a similar comparison is drawn in Table 4.8 for the effective values of the k-factor.

Table 4.7: Median ($k_{50\%}$) values compared, 200m a.g.l

Location	Measured	Curve-fitting	Kernel
Bloemfontein	1.22	1.24	1.21
Cape Town	1.29	1.29	1.26
Durban	1.27	1.27	1.25
Polokwane	1.26	1.23	1.25
Pretoria	1.20	1.19	1.21
Upington	1.18	1.17	1.20
Bethlehem	1.16	1.20	1.17

Table 4.8: k_{eff} ($k_{99.9\%}$) values compared, 200m a.g.l

Location	Measured	Curve-fitting	Kernel
Bloemfontein	0.51	0.53	0.52
Cape Town	0.49	0.51	0.50
Durban	0.53	0.55	0.55
Polokwane	0.63	0.64	0.64
Pretoria	0.66	0.68	0.67
Upington	0.49	0.50	0.53
Bethlehem	0.73	0.75	0.77

Again, from this table, the values obtained per location are seen to quite close for the different models and those from measurements as well.

Thus, for the Curve fitting method, we see that the highest value of the median k-factor is obtained in Cape Town, which has a Mediterranean kind of climate while the lowest value is obtained in Upington which is semi-arid. The low value of the median k-factor for semi-arid Upington is consistent with the 1.1 value obtained for Maun Botswana, which is arid, by Odedina and Afullo [18, 20], while the high value of the median k-factor for Cape Town is in line with results obtained by Palmer and Baker [64] using ground observations, albeit their value being higher possibly due to difference at which the k-factor was determined. Overall, see that the k-factor varies from place to place depending on the altitude and climate. For the kernel results, the highest value of the median k-factor are obtained in Cape Town as well but the lowest is obtained in Bethlehem. The highest value of the effective k-factor for the curve fitting method is obtained in Bethlehem while the smallest is obtained in Upington. The corresponding values for the kernel method are obtained in Bethlehem and Cape Town respectively.

4.3.4 Three-year Seasonal Curve Fitting Results and Discussion

Table 4.9 shows the values of the parameters and the ISE obtained from both measurements and curve fitting modeling. Table 4.10 shows the curve-fitting models obtained. The final estimate is the best estimate since the error achieved is at the very minimum. Figures 4.15-4.42 are the plots of the curve fitting models obtained. From Table 4.10 and Figures 4.15-4.42, the curve fitting seasonal median k-factor values for Bloemfontein are found to be 1.24 for February, 1.22 for May, 1.21 for August and 1.25 for November. For Cape Town, the values are 1.27 for February, 1.29 for May, 1.29 for August and 1.27 for November. For Durban, the values are 1.26 for February, 1.26 for May, 1.25 for August and 1.26 for November. For Polokwane, the values are 1.24 for February, 1.24 for May, 1.21 for August and 1.21 for November. For Pretoria, the values are 1.20 for February, 1.18 for May, 1.17 for August and 1.20 for November. For Upington, the values are 1.13 for February, 1.21 for May, 1.19 for August and 1.15 for November. For Bethlehem, the values are 1.20 for February, 1.21 for May, 1.19 for August and 1.21 for November.

Also, from Table 4.9, for Bloemfontein, the largest error is found to be 0.334 for the month of August while the least error is found to be 0.184 for the month of February. For Cape Town, the largest error is 0.156 for the month of August while the least error is found to be 0.104 for the month of February. For Durban, the largest error is 0.137 for the month of August while the least error is found to be 0.091 for the month of February. For Polokwane, the largest error is 0.178 for the month of November while the least error is found to be 0.124 for the month of February. For Pretoria, the largest error is 0.209 for the month of August while the least error is found to be 0.109 for the month of February. For Upington, the largest error is 0.257 for the month of November while the least error is found to be 0.146 for the month of February. For Bethlehem, the largest error is 1.27 for the month of May while the least error is found to be 0.333 for the month of February.

Also, from Figures 4.15-4.42, the effective k-factor value for Bloemfontein is 0.52 for February, 0.55 for May, 0.52 for August and 0.48 for November. For Cape Town, it is 0.44 for February, 0.51 for May, 0.51 for August and 0.46 for November. For Durban, it is 0.58 for February, 0.59 for May, 0.57 for August and 0.65 for November. For Polokwane, it is 0.68 for February, 0.55 for May, 0.71

Table 4.9: Seasonal curve-fitting values of A, u_k and ISE

Location	Initial estimates from measurements				Final estimates from curve-fitting		
	Month	u_k	A	ISE	u_k	A	ISE
Bloemfontein	Feb	1.24	1.52	0.188	1.24	1.37	0.184
	May	1.21	2.49	0.338	1.22	1.6	0.244
	Aug	1.21	2.7	0.425	1.21	1.79	0.334
	Nov	1.22	1.87	0.275	1.25	1.30	0.220
Cape Town	Feb	1.26	1.17	0.105	1.27	1.16	0.104
	May	1.29	2.11	0.209	1.29	1.45	0.133
	Aug	1.3	1.63	0.157	1.29	1.7	0.156
	Nov	1.27	1.45	0.1153	1.27	1.48	0.115
Durban	Feb	1.28	1.24	0.099	1.26	1.37	0.091
	May	1.26	1.45	0.133	1.26	1.37	0.131
	Aug	1.26	1.51	0.141	1.25	1.64	0.137
	Nov	1.26	1.54	0.102	1.26	1.66	0.098
Polokwane	Feb	1.27	2.32	0.228	1.24	1.66	0.124
	May	1.27	1.26	0.20	1.24	1.55	0.174
	Aug	1.23	1.96	0.185	1.21	2.08	0.174
	Nov	1.23	2	0.191	1.21	1.79	0.178
Pretoria	Feb	1.22	1.29	0.122	1.20	1.5	0.109
	May	1.19	2.39	0.165	1.18	2.2	0.157
	Aug	1.19	3.01	0.258	1.17	2.45	0.209
	Nov	1.20	1.75	0.123	1.20	1.79	0.122
Upington	Feb	1.14	1.63	0.152	1.13	1.46	0.146
	May	1.20	1.82	0.184	1.21	1.58	0.175
	Aug	1.19	1.6	0.224	1.19	1.59	0.223
	Nov	1.16	1.08	0.279	1.15	1.38	0.257
Bethlehem	Feb	1.16	2.09	0.370	1.20	2.09	0.333
	May	1.21	1.23	2.06	1.21	3.53	1.27
	Aug	1.17	1.46	0.947	1.19	2.92	0.569
	Nov	1.14	4.15	1.51	1.21	2.03	0.623

for August and 0.63 for November. For Pretoria, it is 0.58 for February, 0.60 for May, 0.66 for August and 0.64 for November. For Upington, it is 0.41 for February, 0.41 for May, 0.49 for August and 0.41 for November. For Bethlehem, it is 0.75 for February, 0.86 for May, 0.54 for August and 0.64 for November.

From these results, we see that the highest value of the median k-factor for Bloemfontein is in November while the lowest is in August. For Cape Town, the highest corresponding value is obtained in May and August, while the lowest value is observed in February and November. For Durban, the value for February, May and November is the same and slightly larger than that recorded in August. For Polokwane, we observe that the highest corresponding value is observed in February and May, while the lowest value is recorded in August and November. For Pretoria, the largest median k-factor is recorded in February and November, while the lowest value is in August. The corresponding values for Upington are obtained in the months of May and November

Table 4.10: Seasonal Gaussian curve-fitting *k*-factor distribution models

Location	Month	Gaussian distribution model
Bloemfontein	Feb	$f(k) = 1.37e^{-5.9(k-1.24)^2}$
	May	$f(k) = 1.6e^{-8.04(k-1.22)^2}$
	Aug	$f(k) = 1.79e^{-10.07(k-1.21)^2}$
	Nov	$f(k) = 1.30e^{-5.31(k-1.25)^2}$
Cape Town	Feb	$f(k) = 1.16e^{-4.23(k-1.27)^2}$
	May	$f(k) = 1.45e^{-6.61(k-1.29)^2}$
	Aug	$f(k) = 1.7e^{-9.08(k-1.29)^2}$
	Nov	$f(k) = 1.48e^{-6.88(k-1.27)^2}$
Durban	Feb	$f(k) = 1.37e^{-5.9(k-1.26)^2}$
	May	$f(k) = 1.37e^{-5.9(k-1.26)^2}$
	Aug	$f(k) = 1.64e^{-8.45(k-1.25)^2}$
	Nov	$f(k) = 1.66e^{-8.66(k-1.26)^2}$
Polokwane	Feb	$f(k) = 1.66e^{-8.66(k-1.24)^2}$
	May	$f(k) = 1.55e^{-7.55(k-1.24)^2}$
	Aug	$f(k) = 2.08e^{-13.59(k-1.21)^2}$
	Nov	$f(k) = 1.79e^{-10.07(k-1.21)^2}$
Pretoria	Feb	$f(k) = 1.5e^{-7.07(k-1.20)^2}$
	May	$f(k) = 2.2e^{-15.21(k-1.18)^2}$
	Aug	$f(k) = 2.45e^{-18.86(k-1.17)^2}$
	Nov	$f(k) = 1.79e^{-10.07(k-1.20)^2}$
Upington	Feb	$f(k) = 1.46e^{-6.7(k-1.13)^2}$
	May	$f(k) = 1.58e^{-7.84(k-1.21)^2}$
	Aug	$f(k) = 1.59e^{-7.94(k-1.19)^2}$
	Nov	$f(k) = 1.38e^{-5.98(k-1.15)^2}$
Bethlehem	Feb	$f(k) = 2.09e^{-13.72(k-1.20)^2}$
	May	$f(k) = 3.53e^{-39.15(k-1.21)^2}$
	Aug	$f(k) = 2.92e^{-26.79(k-1.19)^2}$
	Nov	$f(k) = 2.03e^{-12.95(k-1.21)^2}$

respectively. The highest median k-factor for Bethlehem is observed in May and November, while the lowest is observed in August. The months of February, May, August and November correspond to the seasons of summer, autumn, winter and spring respectively in South Africa.

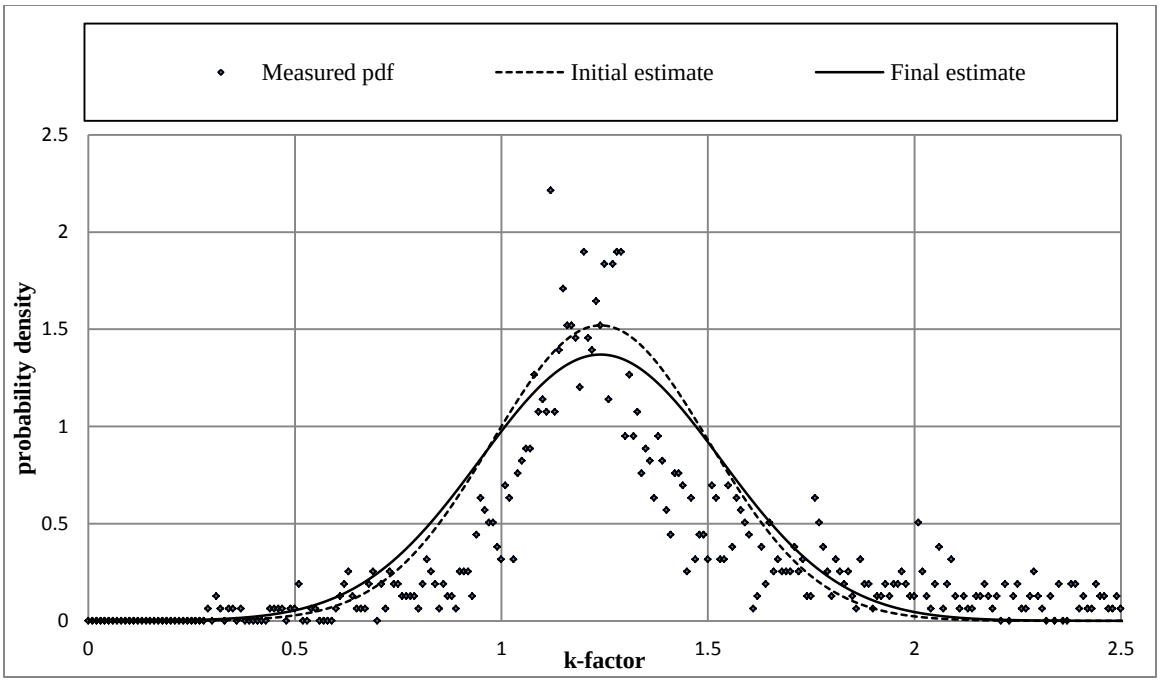

Figure 4.15: Gaussian curve fitting estimates, Bloemfontein, February, 200 m a.g.l

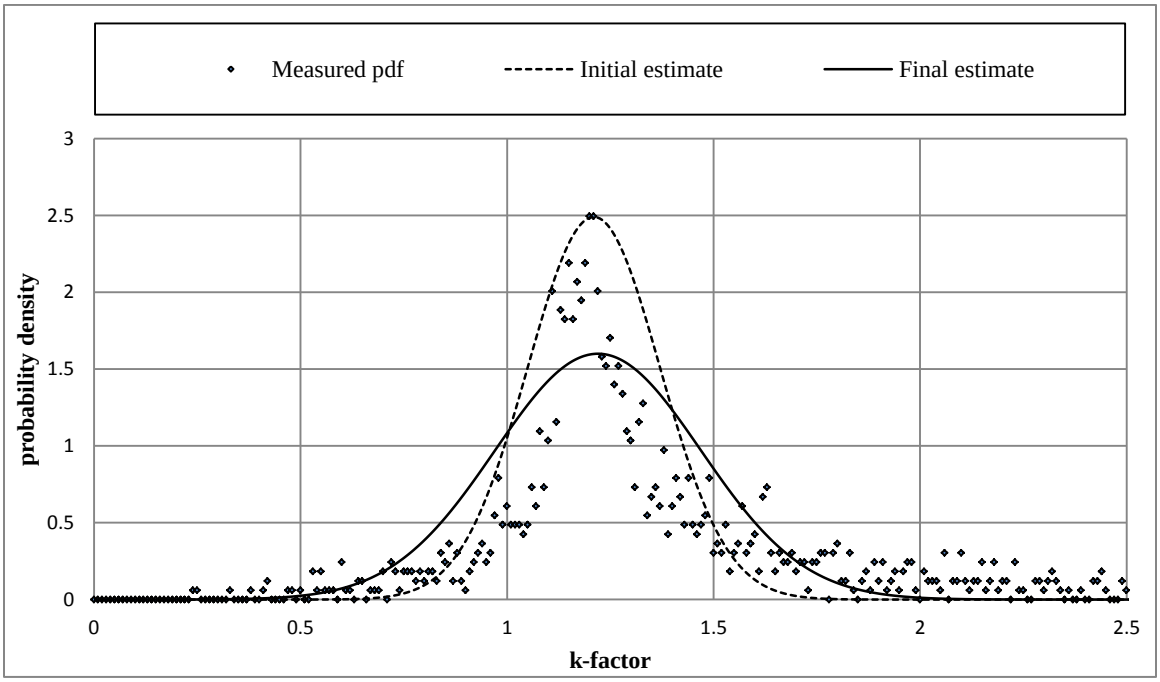

Figure 4.16: Gaussian curve fitting estimates, Bloemfontein, May, 200 m a.g.l

Also, from these results, the lowest value of the effective k-factor for Bloemfontein is recorded in November, while the largest is recorded in May. The corresponding values of the same for Cape Town are recorded in February and, May and August respectively. The lowest corresponding value

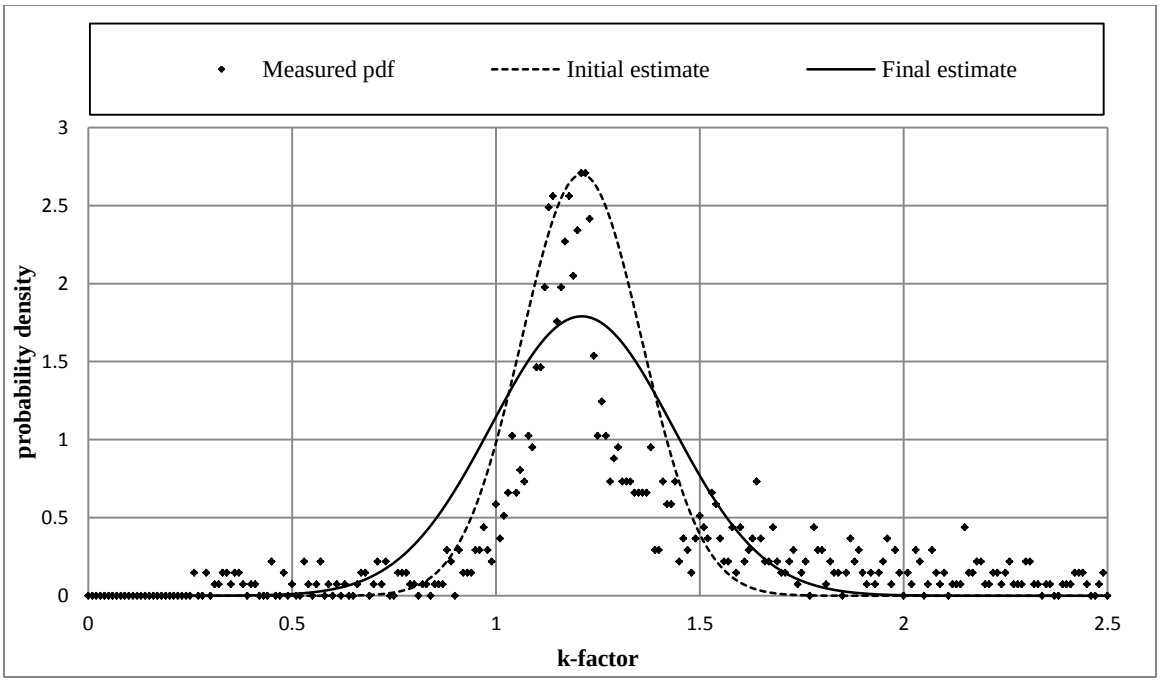

Figure 4.17: Gaussian curve fitting estimates, Bloemfontein, August, 200 m a.g.l

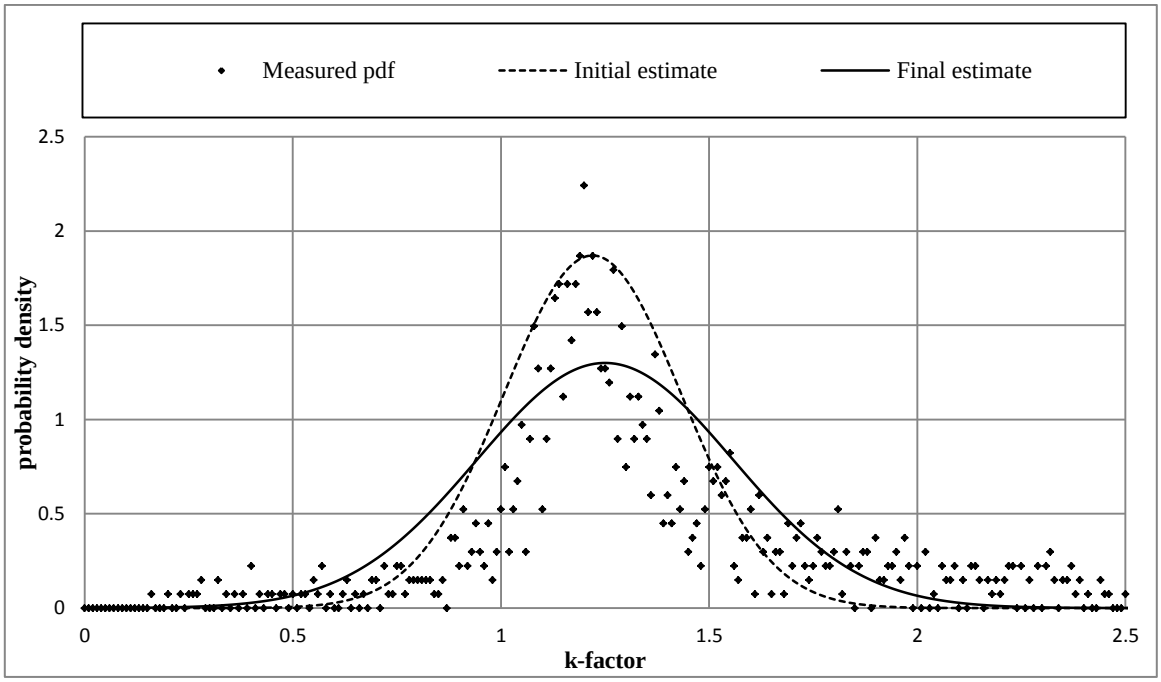

Figure 4.18: Gaussian curve fitting estimates, Bloemfontein, November, 200 m a.g.l

for Durban is recorded in August while the highest is in November. The highest corresponding value for Polokwane is found in August, while the lowest is found in May.For Pretoria, the smallest value is found in Ferbuary, while the largest value is found in August. For Upington, the lowest effective

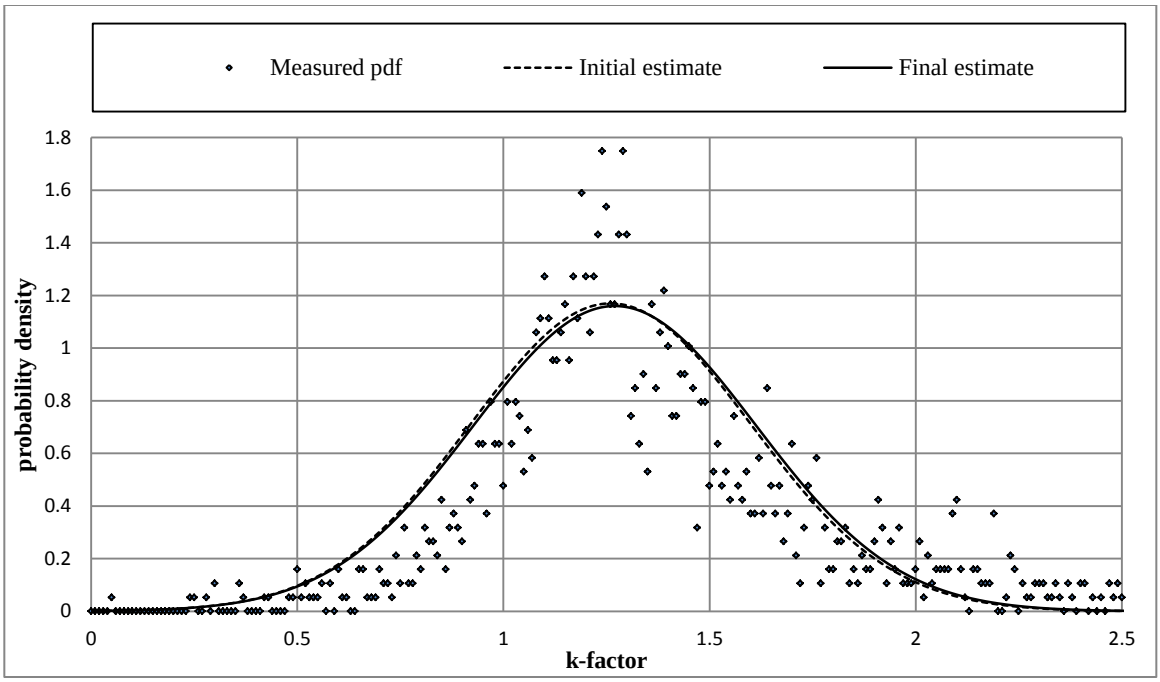

Figure 4.19: Gaussian curve fitting estimate, Cape Town, February, 200 m a.g.l

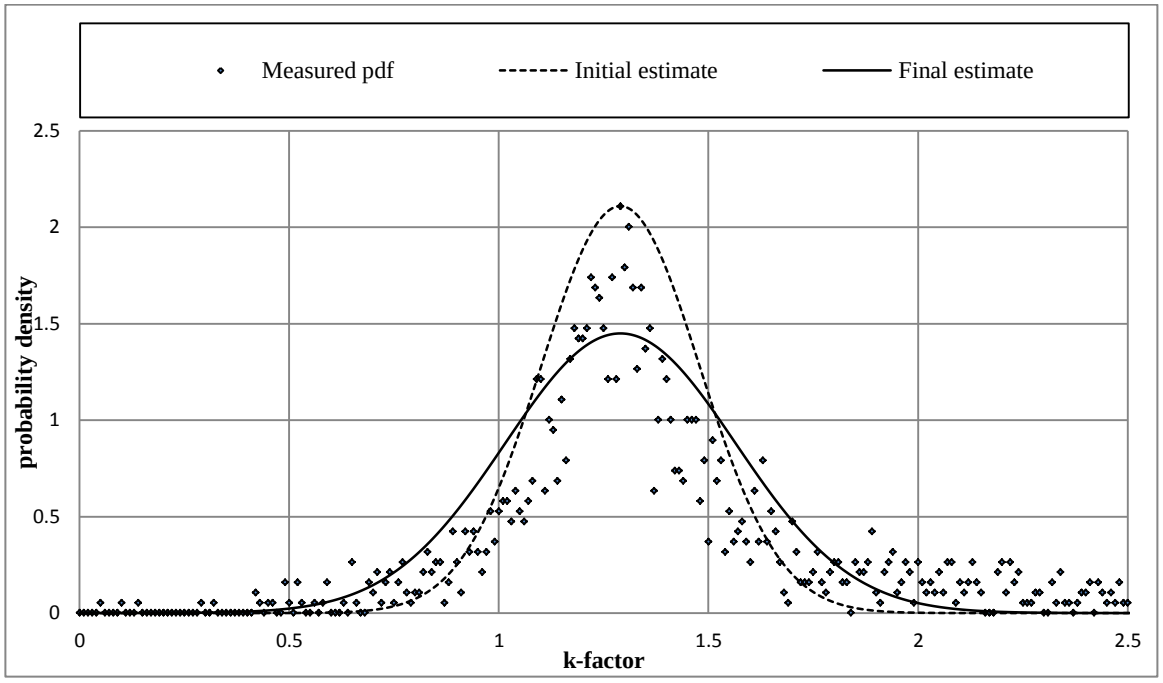

Figure 4.20: Gaussian curve fitting estimates, Cape Town, May, 200 m a.g.l

k-factor is recorded in February, May and November, while the largest is recorded in August. The corresponding values for Bethlehem are recorded in August and May respectively.

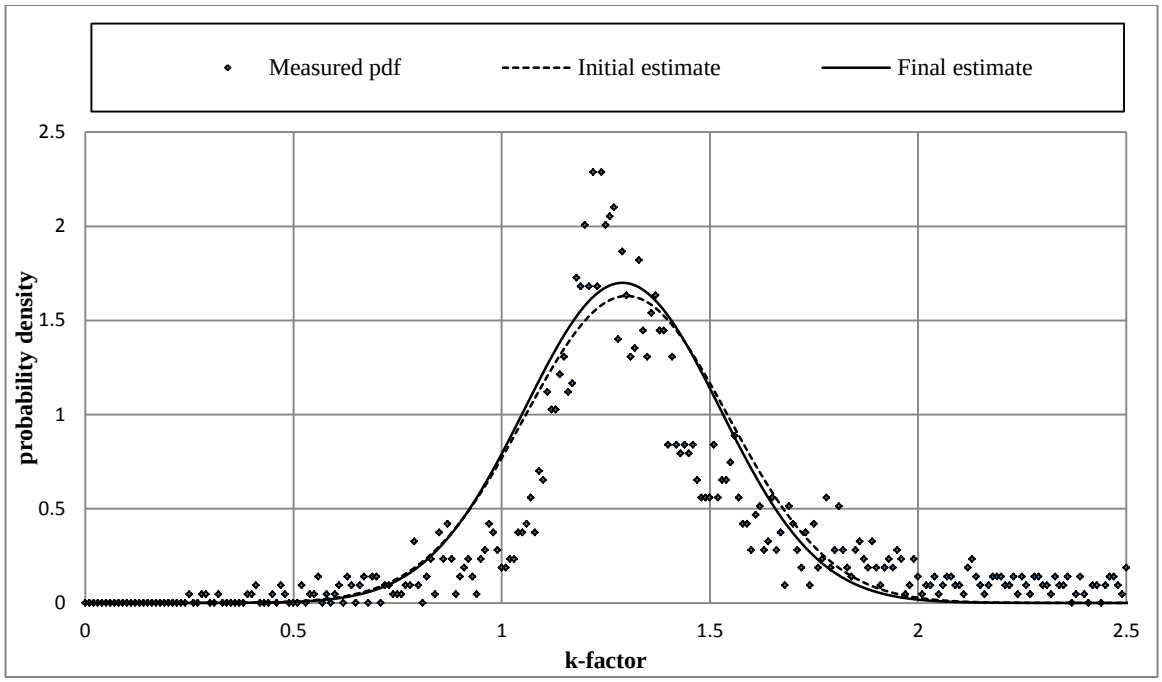

Figure 4.21: Gaussian curve fitting estimates, Cape Town, August, 200 m a.g.l

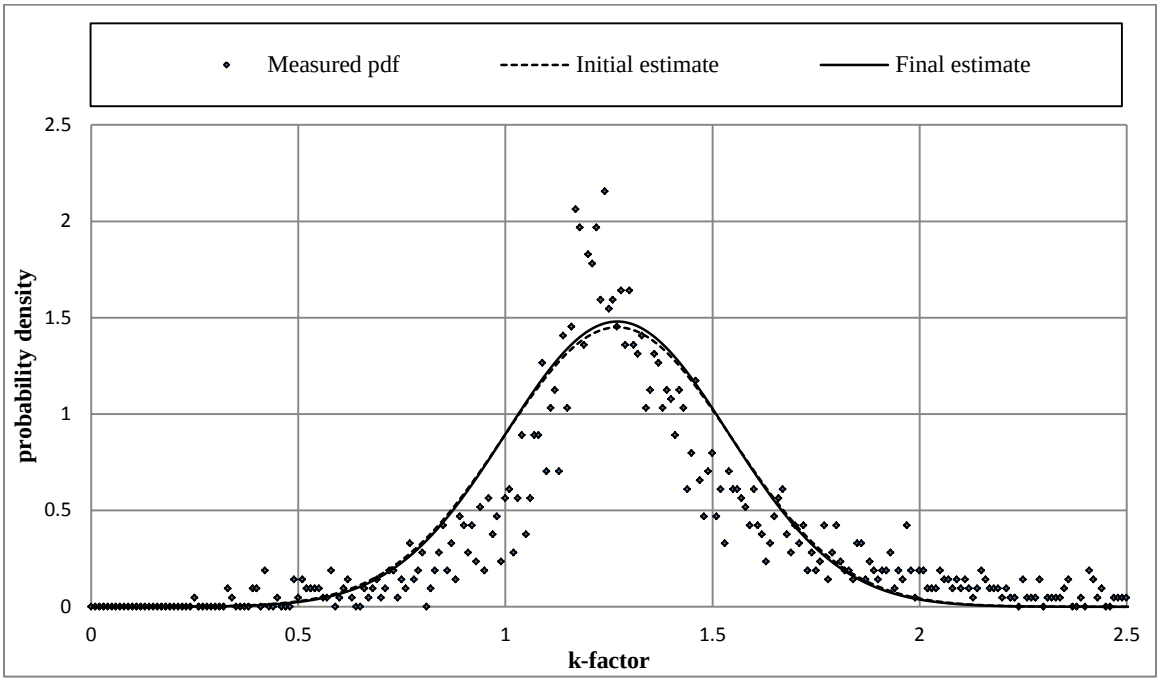

Figure 4.22: Gaussian curve fitting estimates, Cape Town, November, 200 m a.g.l

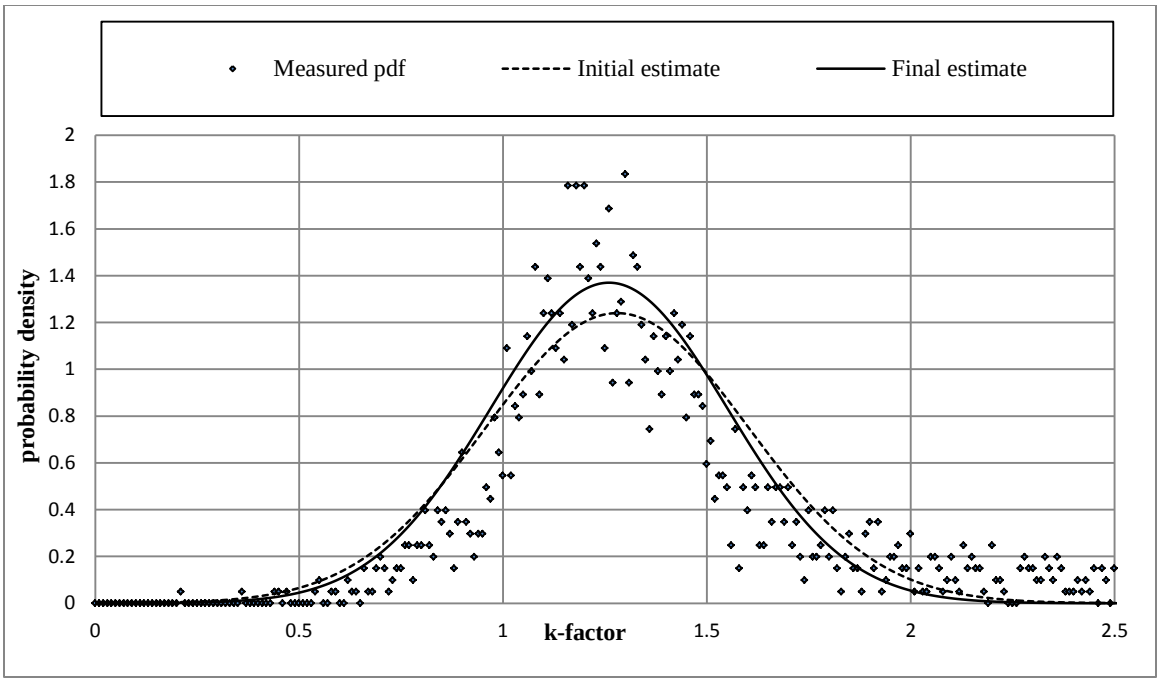

Figure 4.23: Gaussian curve fitting estimates, Durban, February, 200 m a.g.l

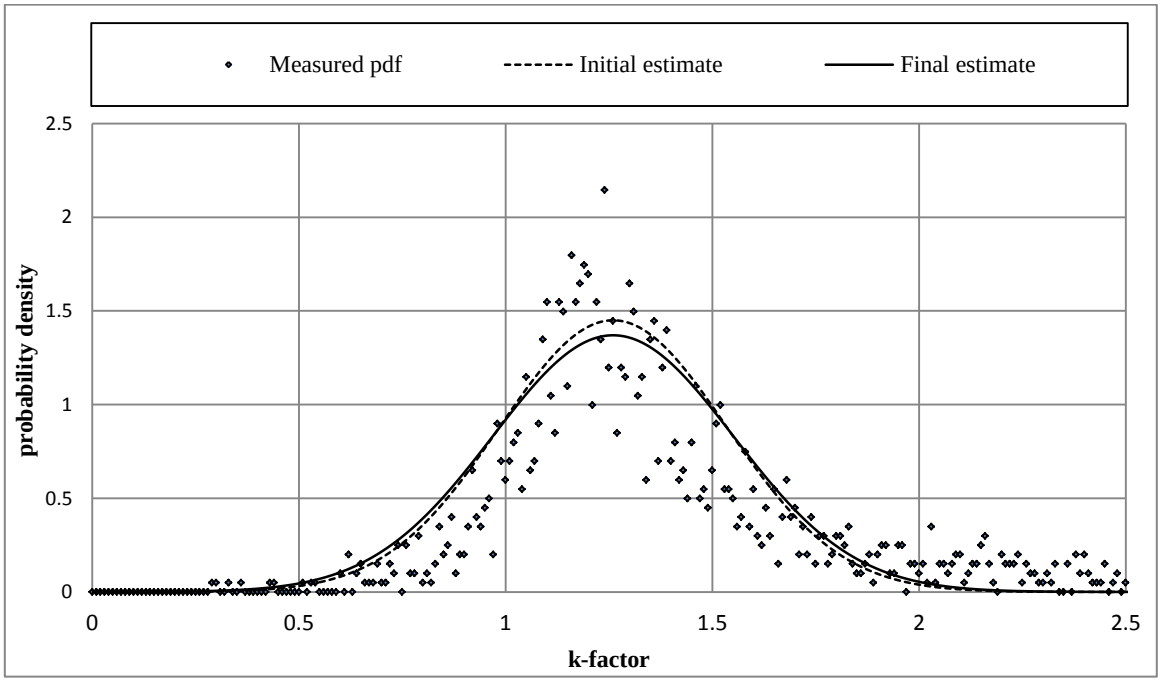

Figure 4.24: Gaussian curve fitting estimates, Durban, May, 200 m a.g.l

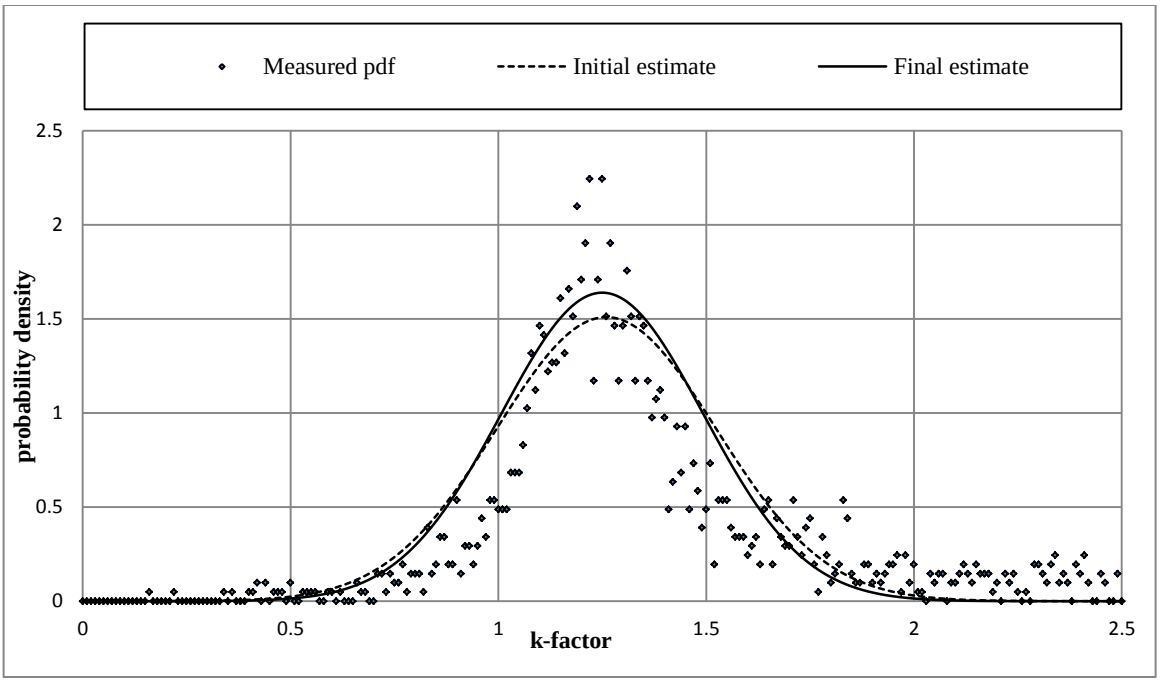

Figure 4.25: Gaussian curve fitting estimates, Durban, August, 200 m a.g.l

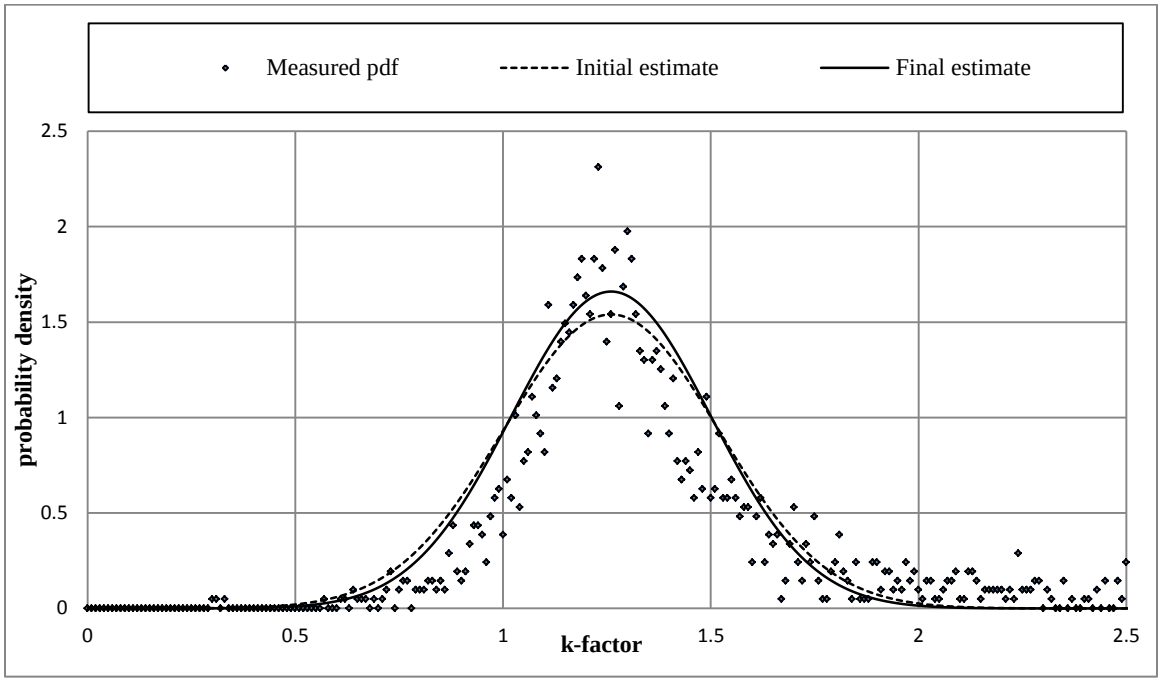

Figure 4.26: Gaussian curve fitting estimates, Durban, November, 200 m a.g.l

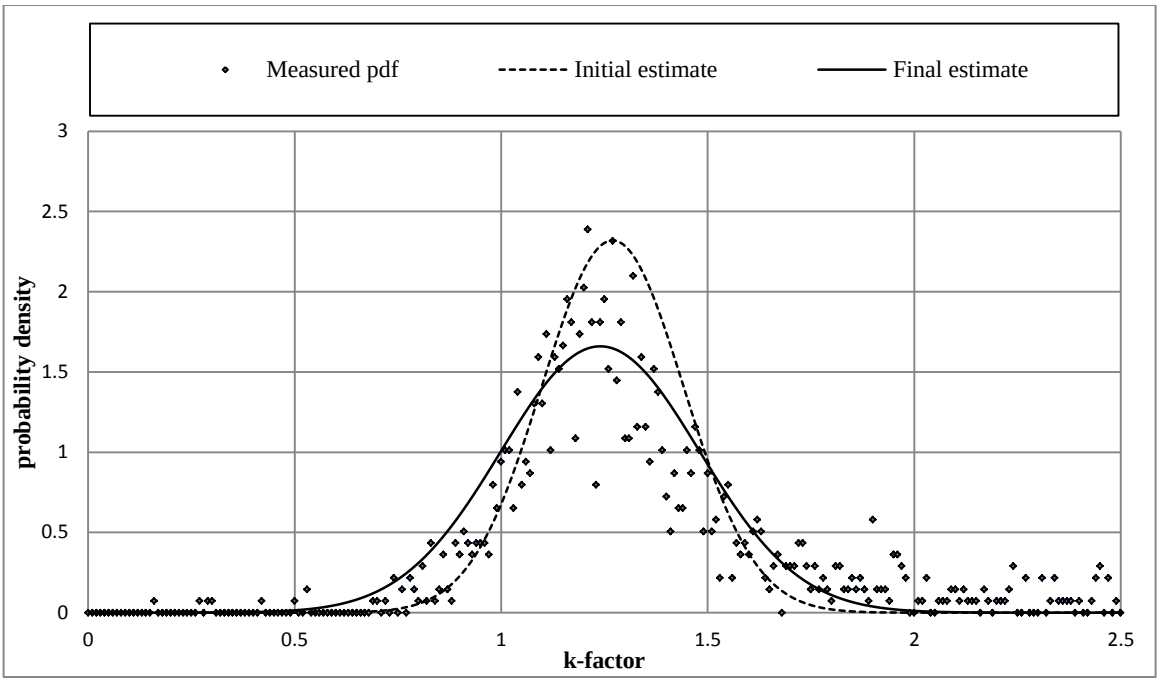

Figure 4.27: Gaussian curve fitting estimates, Polokwane, February, 200 m a.g.l

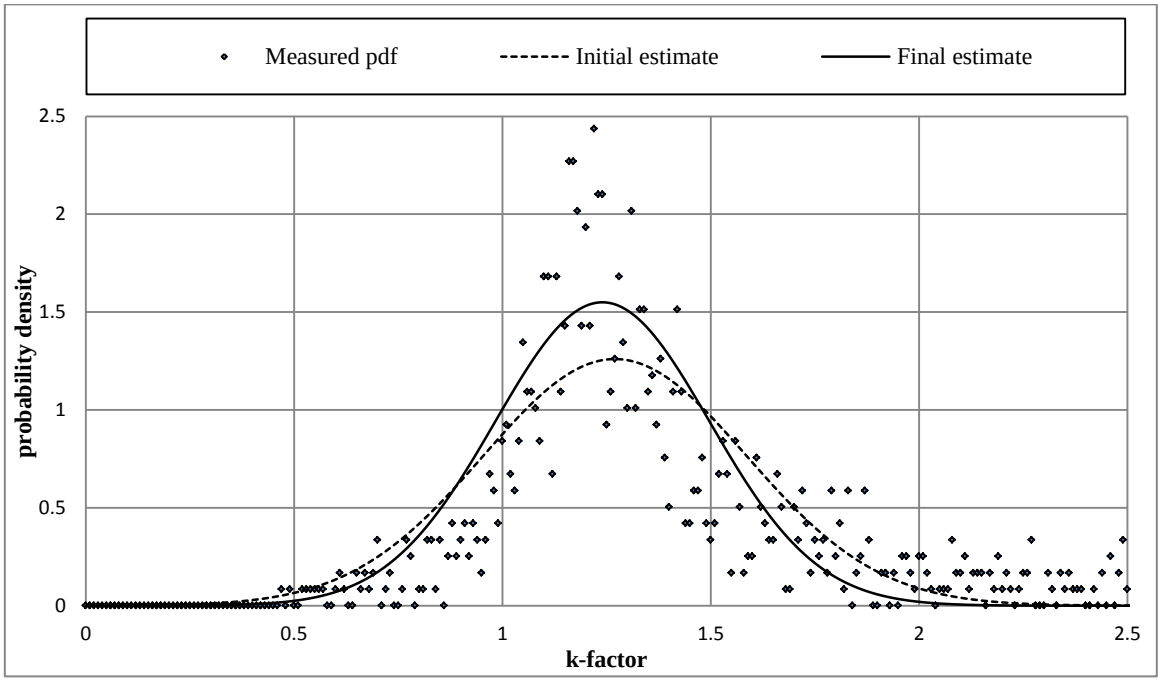

Figure 4.28: Gaussian curve fitting estimates, Polokwane, May, 200 m a.g.l

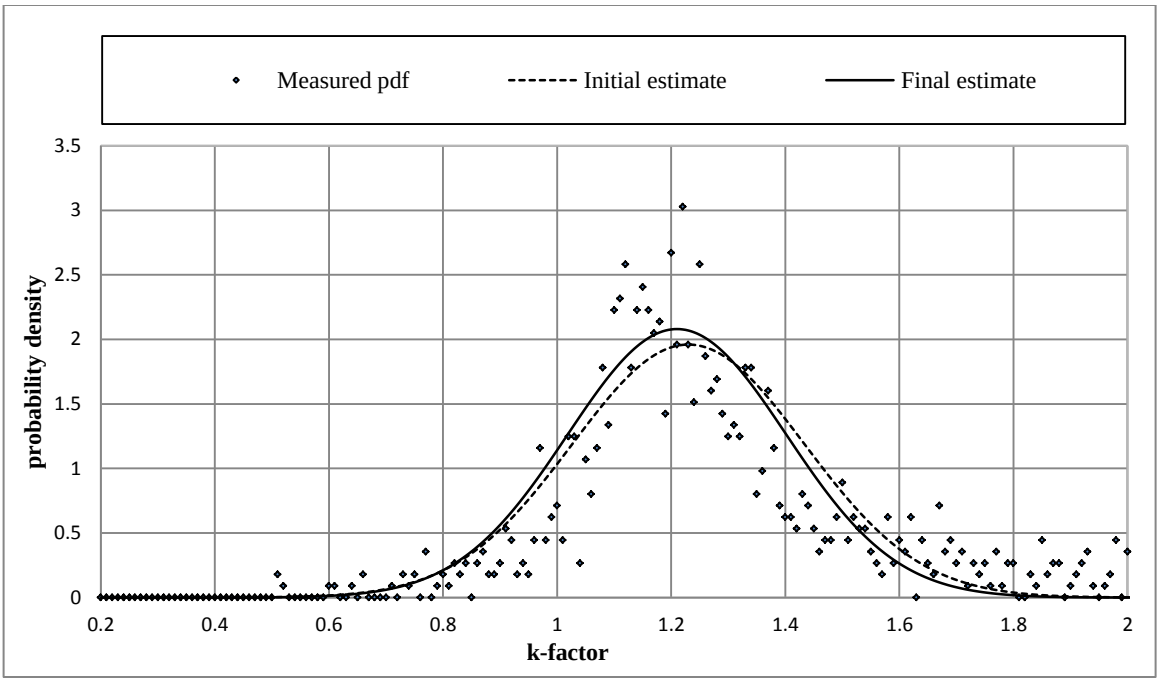

Figure 4.29: Gaussian curve fitting estimates, Polokwane, August, 200 m a.g.l

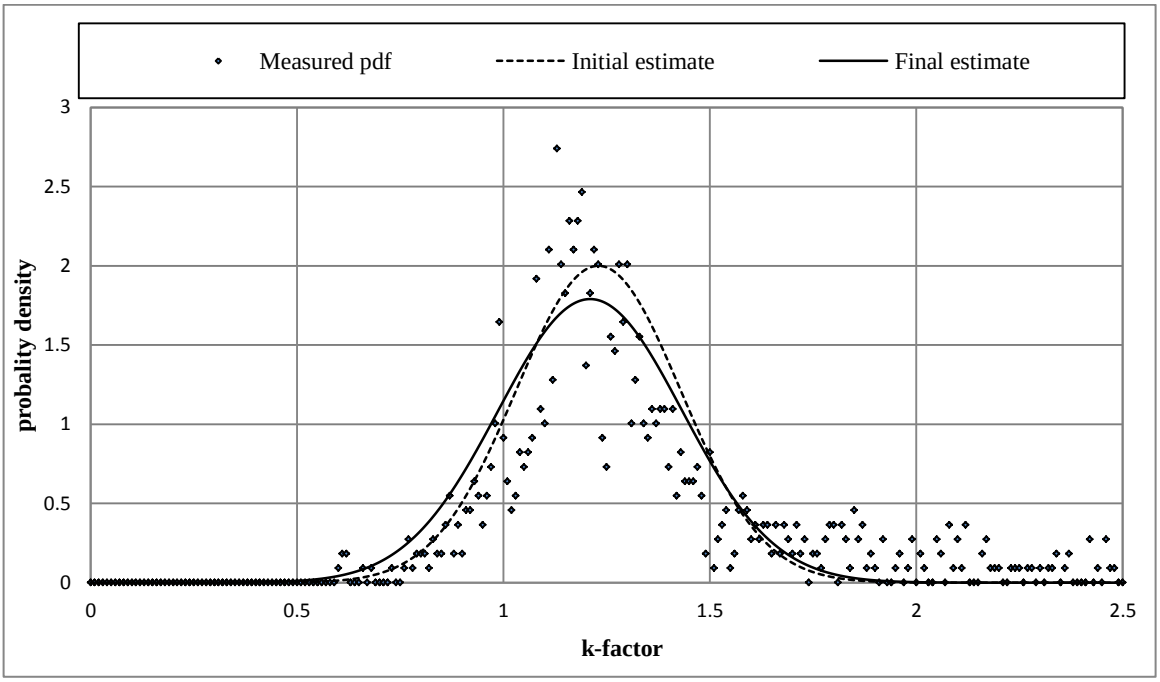

Figure 4.30 :Gaussian curve fitting estimates, Polokwane, November, 200 m a.g.l

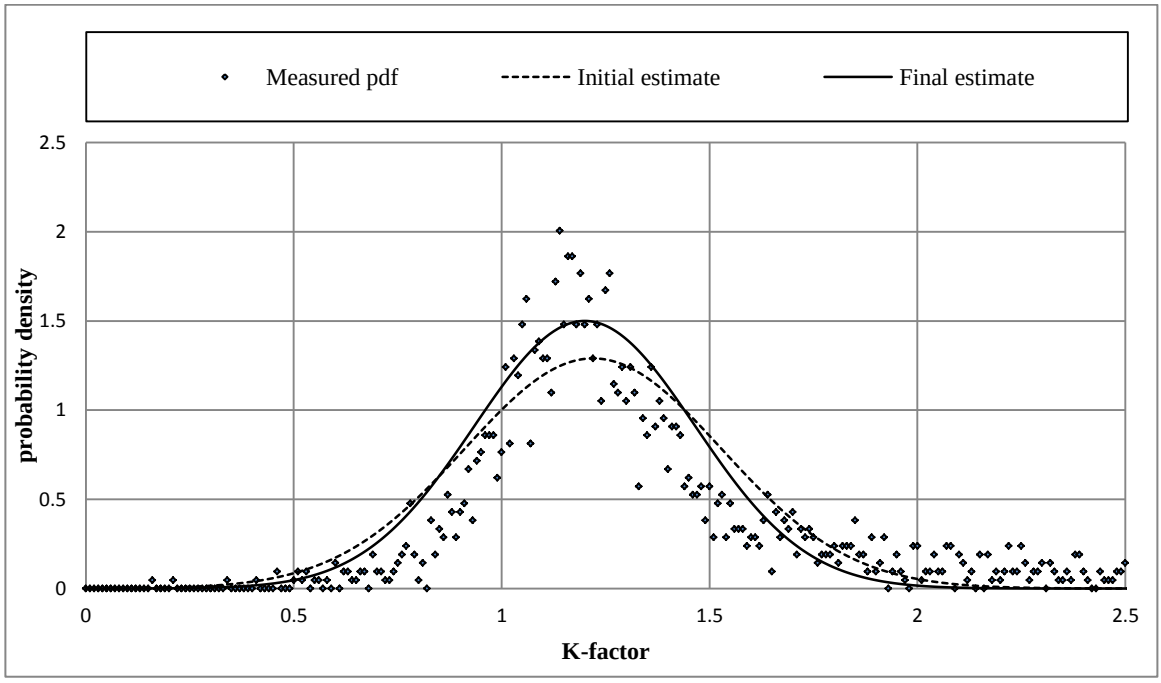

Figure 4.31: Gaussian curve fitting estimates, Pretoria, February, 200 m a.g.l

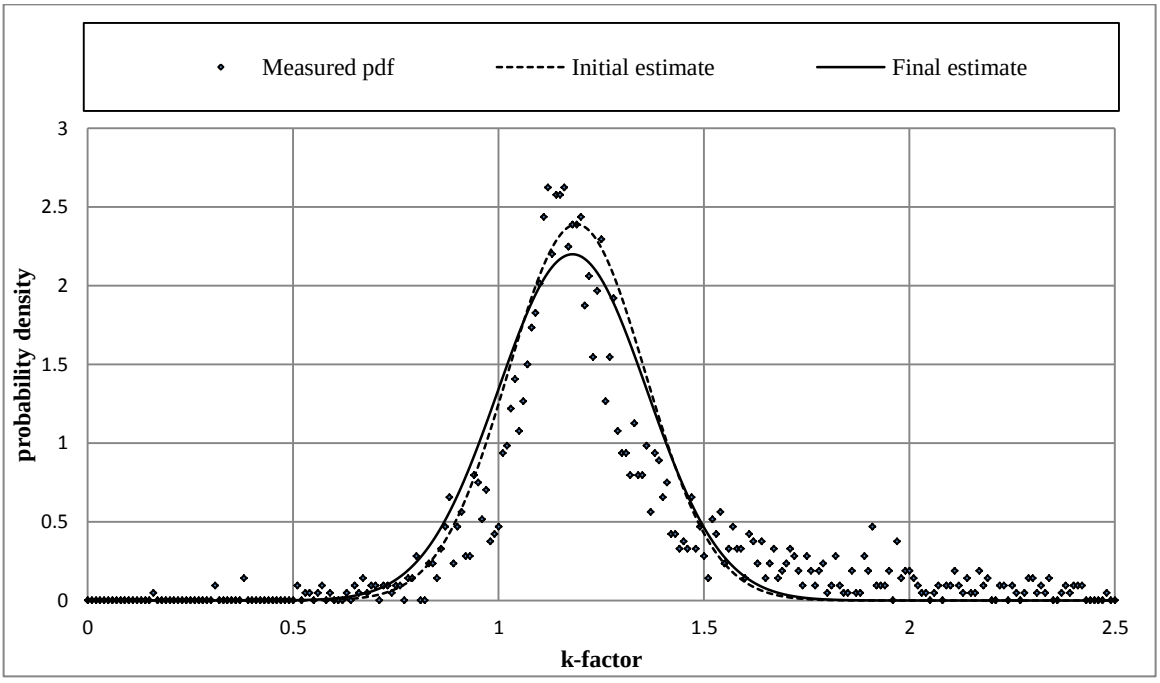

Figure 4.32: Gaussian curve fitting estimates, Pretoria, May, 200 m a.g.l

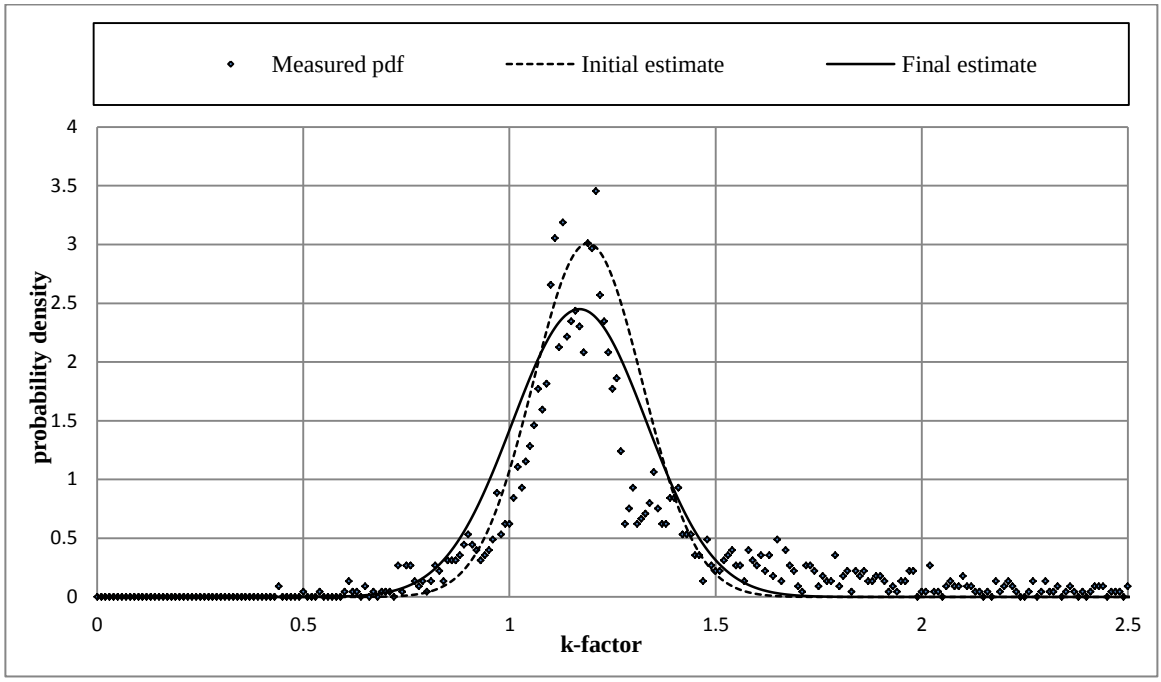

Figure 4.33: Gaussian curve fitting estimates, Pretoria, August, 200 m a.g.l

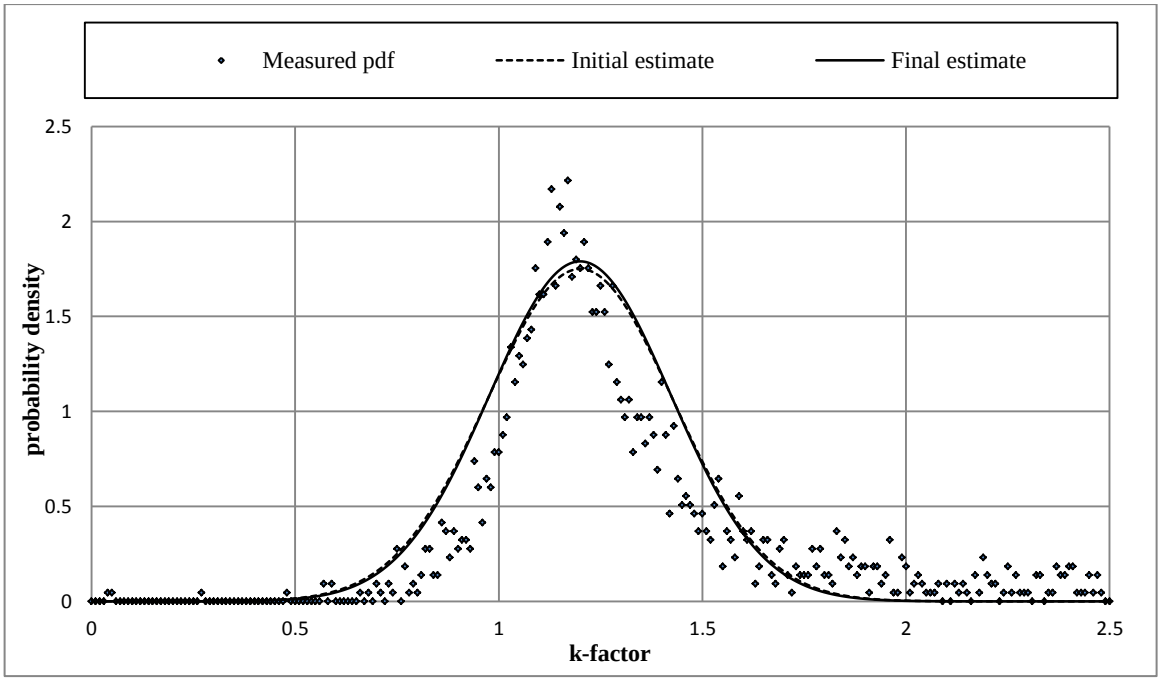

Figure 4.34: Gaussian curve fitting estimates, Pretoria, November, 200 m a.g.l

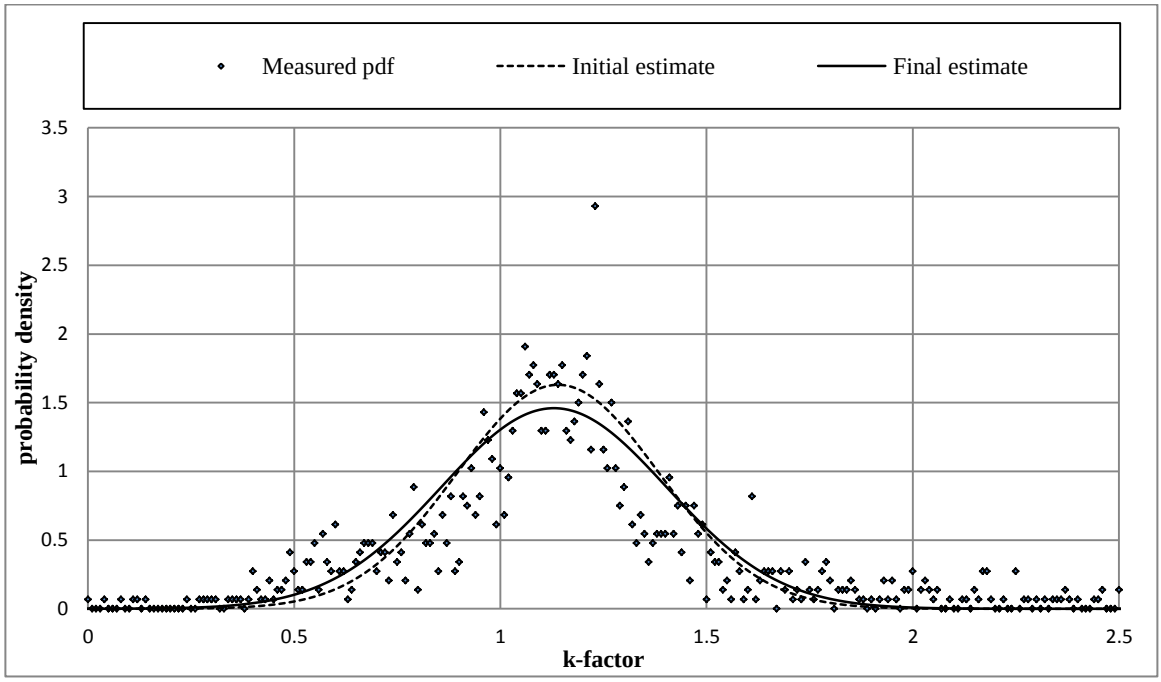

Figure 4.35: Gaussian curve fitting estimates, Upington, February, 200 m a.g.l

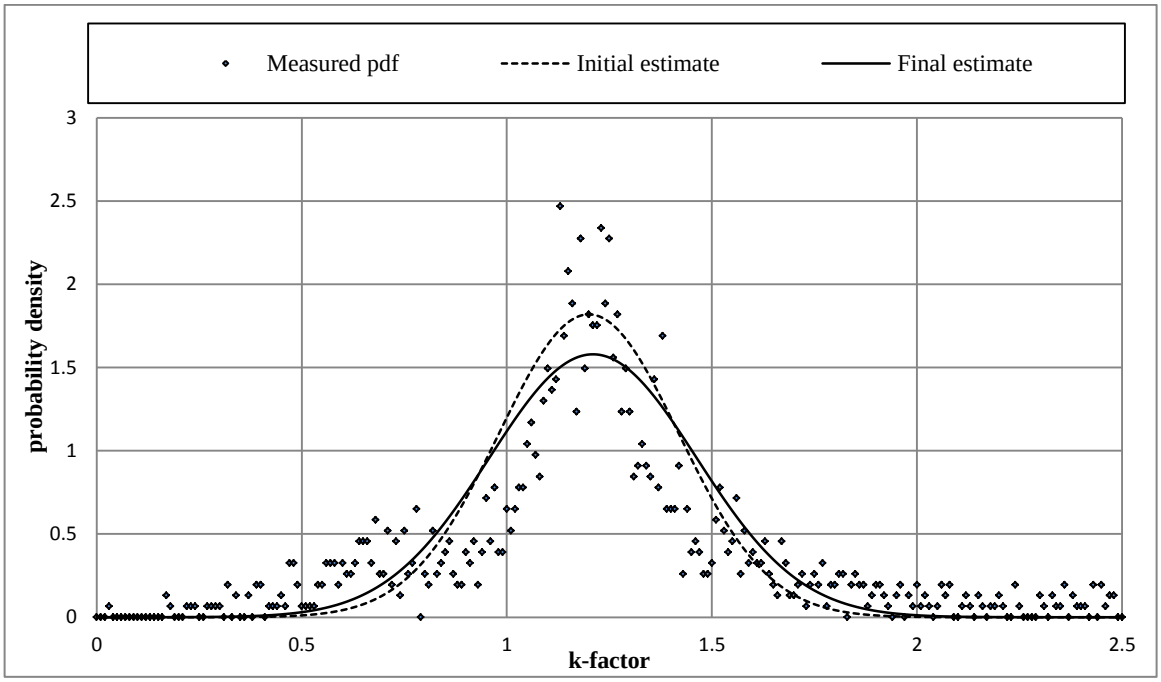

Figure 4.36: Gaussian curve fitting estimates, Upington, May, 200 m a.g.l

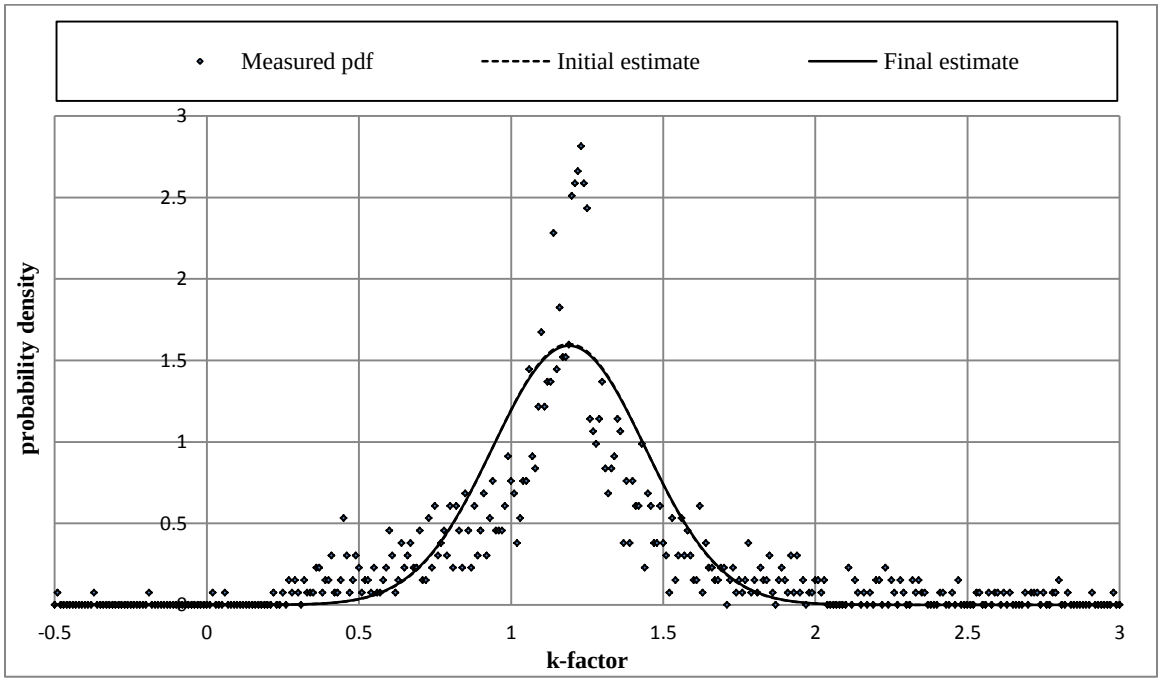

Figure 4.37: Gaussian curve fitting estimates, Upington, August, 200 m a.g.l

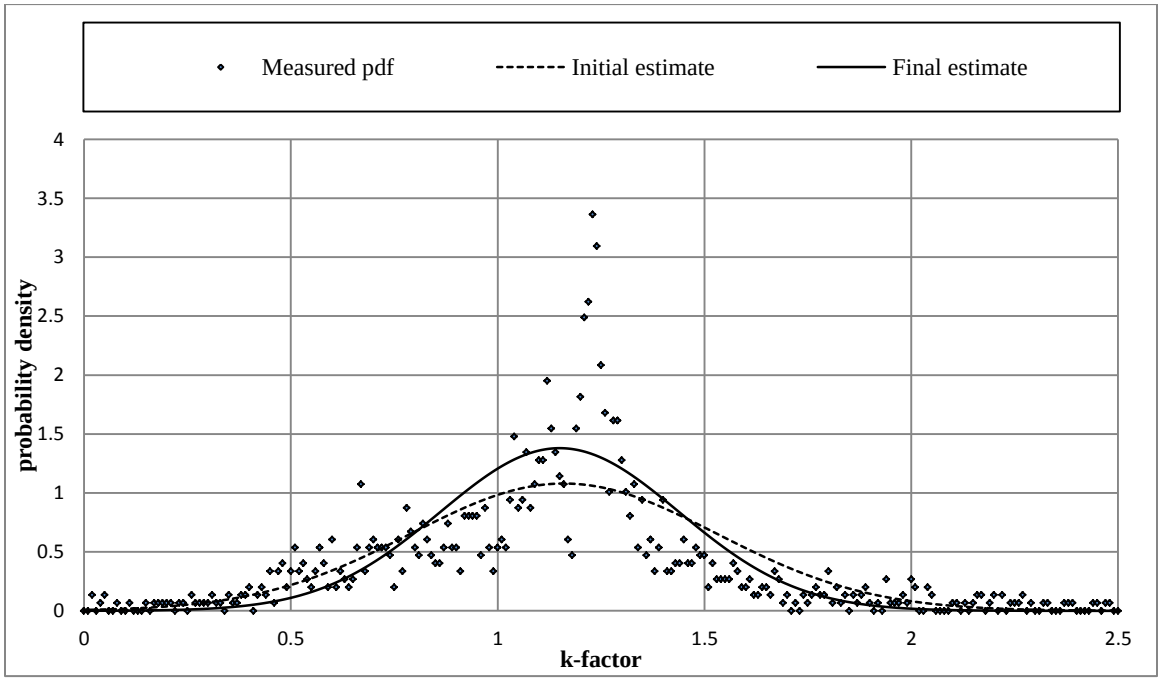

Figure 4.38: Gaussian curve fitting estimates, Upington, November, 200 m a.g.l

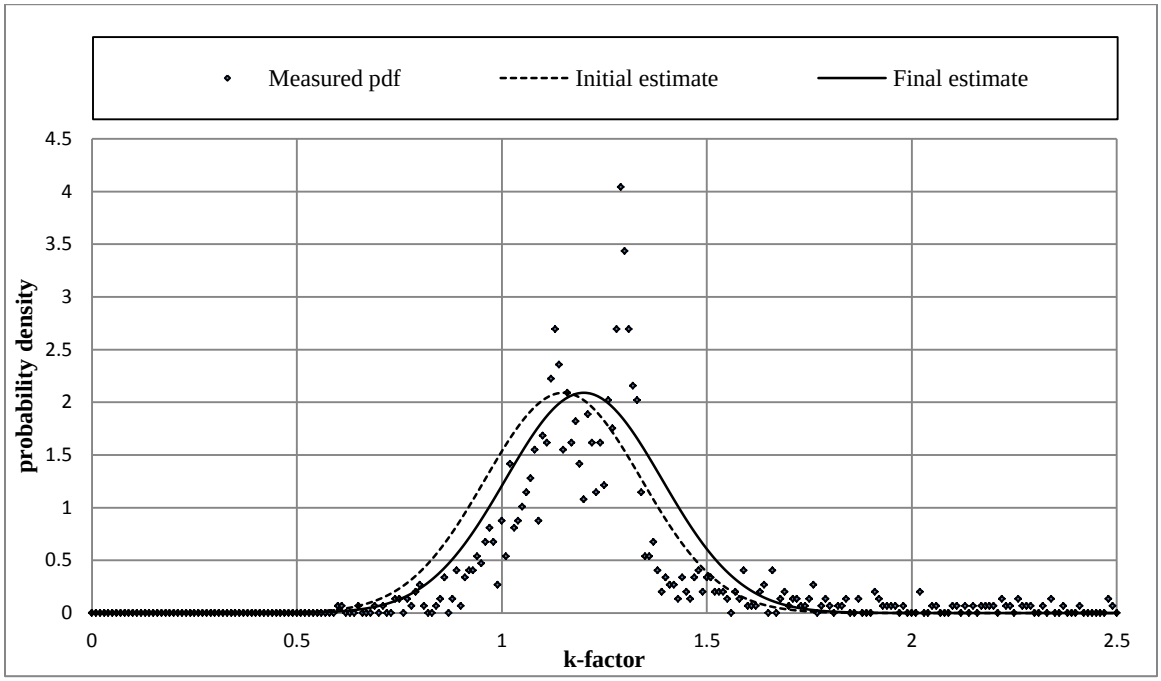

Figure 4.39: Gaussian curve fitting estimates, Bethlehem, February, 200 m a.g.l

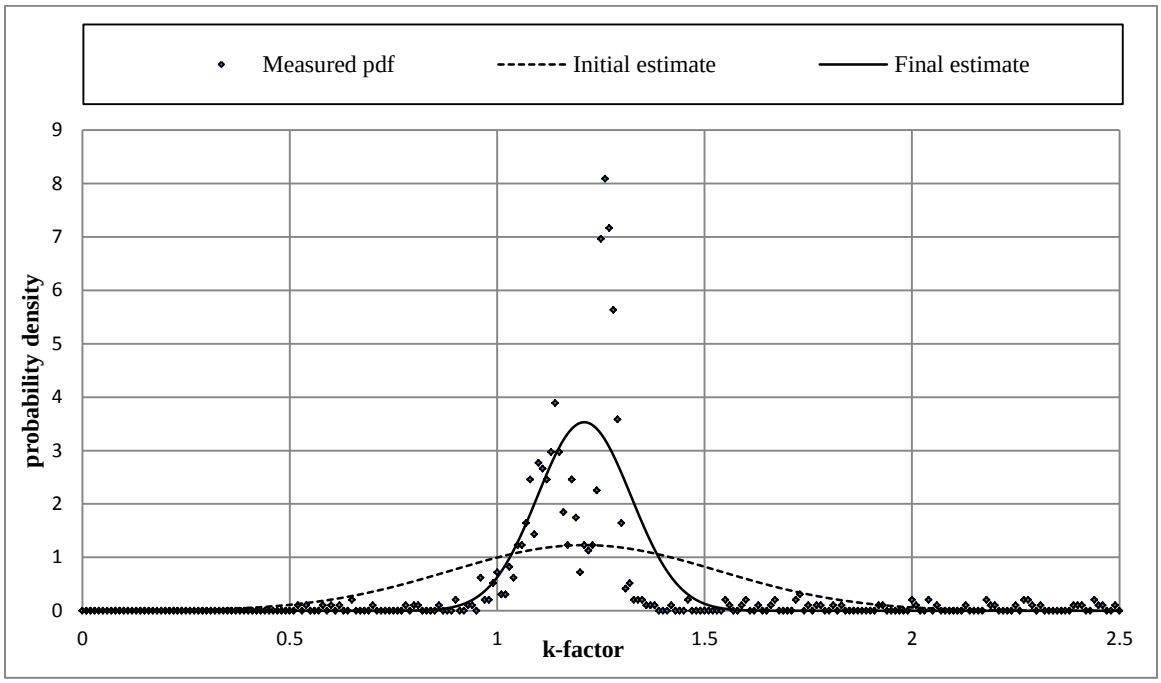

Figure 4.40: Gaussian curve fitting estimates, Bethlehem, May, 200 m a.g.l

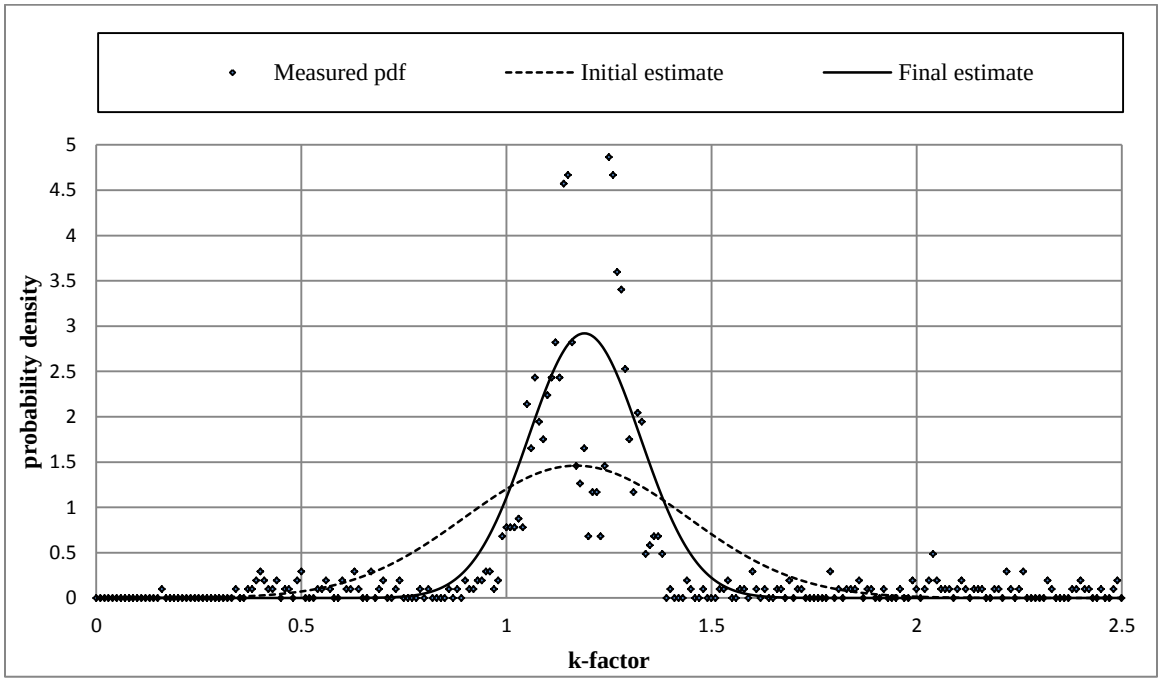

Figure 4.41: Gaussian curve fitting estimates, Bethlehem, August, 200 m a.g.l

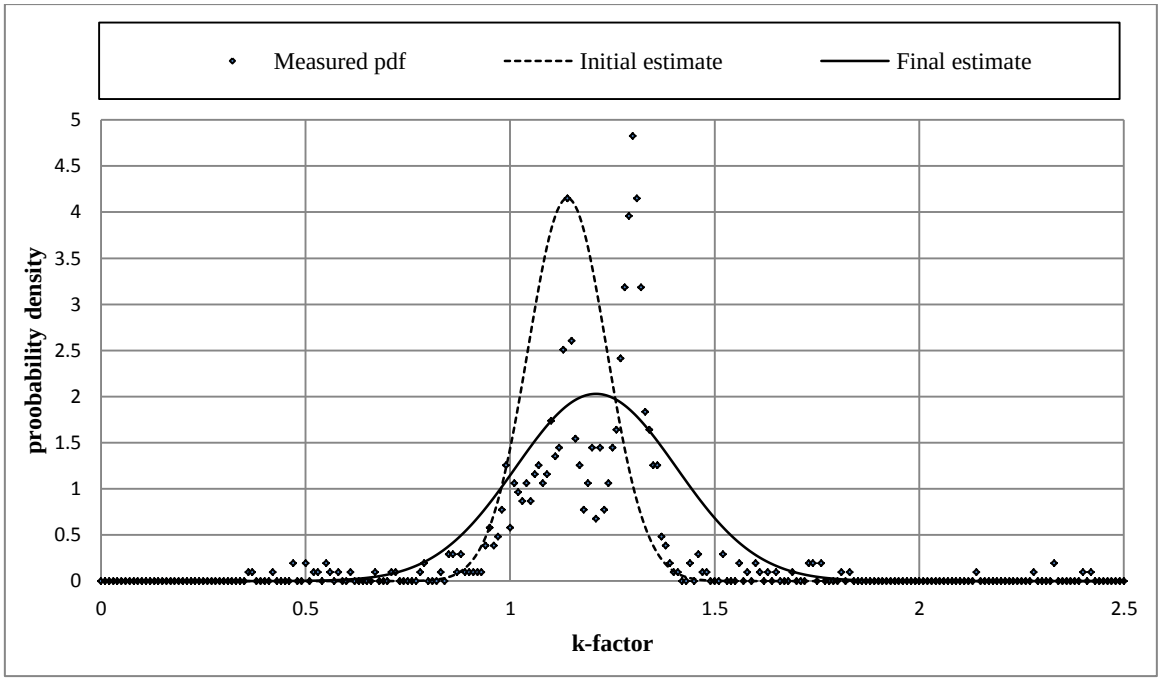

Figure 4.42: Gaussian curve fitting estimates, Bethlehem, November, 200 m a.g.l

4.3.5 Three-year Seasonal Kernel Results and Discussion

Table 4.11 is a tabulation of some of the some different values of the bandwidth considered for every season for each location together with their corresponding median k-factor values and the ISE associated with them. Out of the three values of the bandwidth tabulated for each location, one is the optimum value and is identified as the one where minimum error is achieved. However, due to space consideration, only the best kernel model, that is, the one that produces the least error among the four kernel models is used, and its optimum value of the bandwidth is the only one presented in Figures 4.43-4.70. Just as was the case with the three-year annual kernel models, the ISE error criterion is used to optimize the all kernel model solutions. From Table 4.11 and Figures 4.43-4.70, the best kernel models for Bloemfontein are Rectangular for all the four seasons and the optimum bandwidth, *h*, is 0.006 for all the four seasons. For Cape Town, the best kernel model for February and May is Rectangular with an optimum bandwidth of 0.006 while the Epanechnikov kernel with an optimum bandwidth of 0.006 is the best for August and November. For Durban, the best model for February and August is Rectangular with an optimum bandwidth of 0.006 while for May, the Triangular kernel model with an optimum bandwidth of 0.006 the best and for November, the Epanechnikov kernel model with an optimum bandwidth of 0.006 is the best. The Epanechnikov kernel model with an optimum bandwidth of 0.006 is the best for Polokwane in February while for May, the Epanechnikov with an optimum bandwidth of 0.007 is the best, and for November, the Epanechnikov kernel with bandwidth of 0.005 is the best, while the Rectangular model with an optimum bandwidth of 0.006 is the best for August. The Rectangular model with an optimum bandwidth of 0.006 is the best for all the four seasons in Pretoria. For Upington, the Rectangular model with an optimum bandwidth of 0.006 is the best for February and May while, the Gaussian (with an optimum bandwidth of 0.007) and Epanechnikov (with an optimum bandwidth of 0.006) models are the best for August and the Epanechnikov model with an optimum bandwidth of 0.005 is best for November. The Rectangular model with an optimum bandwidth of 0.006 is the best for all the four seasons in Bethlehem.

From these models the median and effective k-factor values are then obtained. For Bloemfontein the median k-factor value is 1.22 for February, 1.20 for May, 1.21 for August and 1.20 for November. For Cape Town, it is 1.23 for February, 1.29 for May, 1.29 for August and 1.26 for November. For Durban, it is 1.29 for February, 1.26 for May, 1.26 for August and 1.24 for November. For Polokwane, it is 1.25 for February, 1.26 for May, 1.23 for August and 1.22 for November. For Pretoria, it is 1.21 for February, 1.19 for May, 1.20 for August and 1.21 for November. For Upington, it is 1.15 for February, 1.21 for May, 1.18 for August and 1.17 for November. For Bethlehem, it is 1.17 for February, 1.21 for May, 1.16 for August and 1.15 for November.

For Bloemfontein, the effective value of the k-factor from the kernel models is found to be 0.5 for February, 0.52 for May, 0.5 for August and 0.46 for November. For Cape Town, it is 0.44 for February, 0.48 for May, 0.49 for August and 0.44 for November. For Durban, it is 0.56 for February, 0.58 for May, 0.54 for August and 0.65 for November. For Polokwane, it is 0.66 for February, 0.59 for May, 0.67 for August and 0.60 for November. For Pretoria, it is 0.61 for February, 0.57 for May, 0.63 for August and 0.63 for November. For Upington, it is 0.44 for February, 0.39 for May, 0.46 for August and 0.38 for November. For Bethlehem, it is 0.74 for February, 0.79 for May, 0.55 for August and 0.67 for November.

Table 4.11 (a): Seasonal kernel median k-factor, μ_k, ISE and h values

Location	Month	h	Kernel							
			Gaussian		Triangular		Epanechnikov		Rectangular	
			μ_k	ISE	μ_k	ISE	μ_k	ISE	μ_k	ISE
Bloemfontein	Feb	0.006	1.23	0.0353	1.24	0.0343	1.24	0.0324	1.22	0.0321
		0.007	1.23	0.0343	1.24	0.0345	1.24	0.0327	1.22	0.0330
		0.02	1.24	0.0453	1.25	0.0457	1.25	0.0478	1.24	0.0535
	May	0.006	1.20	0.0350	1.21	0.0336	1.20	0.0317	1 20	0.0302
		0.007	1.20	0.0332	1.21	0.0331	1.20	0.0316	1.20	0.0326
		0.008	1.20	0.0328	1.21	0.0336	1.20	0.0331	1.20	0.0349
	Aug	0.006	1.22	0.0324	1.21	0.0313	1.22	0.0301	1.21	0.0300
		0.007	1.22	0.0313	1.21	0.0316	1.22	0.0320	1.21	0.0339
		0.02	1.20	0.0471	1.21	0.0482	1.19	0.0510	1.19	0.0572
	Nov	0.005	1.21	0.0427	1.22	0.0408	1.21	0.0391	1.20	0.0435
		0.006	1.21	0.0405	1.22	0.0402	1.21	0.0396	1.20	0.0385
		0.02	1.19	0.0581	1.19	0.0590	1.19	0.0623	1.19	0.0683
Cape Town	Feb	0.006	1.24	0.0263	1.24	0.0253	1.25	0.0240	1.23	0.0220
		0.007	1.24	0.0251	1.24	0.0249	1.25	0.0241	1.23	0.0250
		0.008	1.24	0.0250	1.24	0.0255	1.25	0.0251	1.23	0.0277
	May	0.006	1.30	0.0340	1.30	0.0326	1.29	0.0316	1.29	0.0304
		0.007	1.30	0.0326	1.30	0.0321	1.29	0.0311	1.29	0.0313
		0.008	1.30	0.0323	1.30	0.0326	1.29	0.0320	1.29	0.0320
	Aug	0.005	1.28	0.0267	1.28	0.0260	1.29	0.0247	1.28	0.0254
		0.006	1.28	0.0247	1.28	0.0243	1.29	0.0236	1.28	0.0255
		0.007	1.28	0.0244	1.28	0.0253	1.29	0.0248	1.28	0.0271
	Nov	0.006	1.25	0.0281	1.26	0.0280	1.26	0.0272	1.27	0.0277
		0.007	1.25	0.0277	1.26	0.0285	1.26	0.0285	1.27	0.0316
		0.02	1.24	0.0353	1.24	0.0355	1.25	0.0370	1.26	0.0398
Durban	Feb	0.005	1.29	0.0300	1.28	0.0292	1.28	0.0284	1.29	0.0304
		0.006	1.29	0.0290	1.28	0.0293	1.28	0.0287	1.29	0.0282
		0.02	1.28	0.0361	1.26	0.0363	1.27	0.0374	1.26	0.0395
	May	0.003	1.24	0.0514	1.24	0.0496	1.24	0.0486	1.25	0.0481
		0.006	1.25	0.0340	1.26	0.0337	1.27	0.0338	1.25	0.0353
		0.04	1.23	0.0591	1.23	0.0582	1.23	0.0595	1.21	0.0602
	Aug	0.006	1.25	0.0277	1.26	0.0273	1.25	0.0263	1.26	0.0233
		0.007	1.25	0.0268	1.26	0.0268	1.25	0.0268	1.26	0.0283
		0.02	1.23	0.0349	1.23	0.0353	1.23	0.0368	1.24	0.0401
	Nov	0.006	1.24	0.0225	1.24	0.0222	1.24	0.0215	1.25	0.0219
		0.007	1.24	0.0223	1.24	0.0224	1.24	0.0218	1.25	0.0241
		0.02	1.25	0.0333	1.25	0.0337	1.26	0.0357	1.26	0.0392
Polokwane	Feb	0.006	1.26	0.0470	1.26	0.0451	1.25	0.0444	1.27	0.0468
		0.007	1.26	0.0462	1.26	0.0460	1.25	0.0452	1.27	0.0460
		0.02	1.25	0.0655	1.25	0.0670	1.25	0.0707	1.25	0.0780
	May	0.006	1.27	0.0635	1.26	0.0601	1.26	0.0565	1.25	0.0487
		0.007	1.27	0.0595	1.26	0.0576	1.26	0.0548	1.25	0.0552
		0.008	1.27	0.0584	1.26	0.0584	1.26	0.0555	1.25	0.0566
	Aug	0.006	1.22	0.0552	1.21	0.0548	1.23	0.0538	1.22	0.0532
		0.007	1.22	0.0553	1.21	0.0566	1.23	0.0564	1.22	0.0548

Table 4.11 (b): Seasonal kernel median k-factor, μ_k, ISE and h values

Location	Month	h	Kernel							
			Gaussian		Triangular		Epanechnikov		Rectangular	
			μ_k	ISE	μ_k	ISE	μ_k	ISE	μ_k	ISE
Polokwane	Aug	0.008	1.22	0.0565	1.21	0.0587	1.23	0.0599	1.22	0.0634
	Nov	0.005	1.23	0.0531	1.22	0.0521	1.22	0.0517	1.22	0.0552
		0.006	1.23	0.0533	1.22	0.0541	1.22	0.0548	1.22	0.0547
		0.007	1.23	0.0548	1.22	0.0567	1.22	0.0591	1.22	0.0662
Pretoria	Feb	0.006	1.21	0.0265	1.22	0.0256	1.23	0.0245	1.21	0.0228
		0.007	1.21	0.0253	1.22	0.0252	1.23	0.0244	1.21	0.0268
		0.008	1.21	0.0252	1.22	0.0256	1.23	0.0251	1.21	0.0264
	May	0.006	1.18	0.0275	1.19	0.0266	1.20	0.0255	1.19	0.0235
		0.007	1.18	0.0265	1.19	0.0265	1.20	0.0260	1.19	0.0289
		0.008	1.18	0.0264	1.19	0.0271	1.20	0.0273	1.19	0.0298
	Aug	0.006	1.20	0.0300	1.20	0.0291	1.21	0.0279	1.20	0.0261
		0.007	1.20	0.0291	1.20	0.0290	1.21	0.0281	1.20	0.0294
		0.008	1.20	0.0290	1.20	0.0295	1.21	0.0289	1.20	0.0293
	Nov	0.006	1.21	0.0220	1.22	0.0215	1.22	0.0207	1.21	0.0190
		0.007	1.21	0.0210	1.22	0.0211	1.22	0.0210	1.21	0.0222
		0.008	1.21	0.0209	1.22	0.0213	1.22	0.0215	1.21	0.0251
Upington	Feb	0.005	1.14	0.0476	1.14	0.0458	1.15	0.0447	1.15	0.0467
		0.006	1.14	0.0458	1.14	0.0456	1.15	0.0448	1.15	0.0433
		0.01	1.13	0.0510	1.14	0.0522	1.15	0.0543	1.15	0.0592
	May	0.006	1.20	0.0454	1.21	0.0445	1.20	0.0418	1.21	0.0382
		0.007	1.20	0.0433	1.21	0.0435	1.20	0.0422	1.21	0.0452
		0.008	1.20	0.0428	1.21	0.0437	1.20	0.0432	1.21	0.0460
	Aug	0.006	1.20	0.0398	1.19	0.0399	1.18	0.0393	1.18	0.0406
		0.007	1.20	0.0393	1.19	0.0400	1.18	0.0406	1.18	0.0449
		0.008	1.20	0.0398	1.19	0.0408	1.18	0.0419	1.18	0.0481
	Nov	0.005	1.18	0.0380	1.17	0.0372	1.17	0.0357	1.16	0.0393
		0.006	1.18	0.0363	1.17	0.0367	1.17	0.0359	1.16	0.0371
		0.007	1.18	0.0361	1.17	0.0368	1.17	0.0370	1.16	0.0405
Bethlehem	Feb	0.006	1.16	0.0454	1.17	0.0442	1.18	0.0428	1.17	0.0404
		0.007	1.16	0.0450	1.17	0.0451	1.18	0.0438	1.17	0.0459
		0.04	1.19	0.1341	1.18	0.1413	1.17	0.1514	1.18	0.1675
	May	0.002	1.19	0.2313	1.19	0.2220	1.19	0.2296	1.18	0.2318
		0.006	1.20	0.1382	1.21	0.1356	1.20	0.1345	1.21	0.1332
		0.05	1.22	0.9576	1.23	1.012	1.23	1.120	1.22	1.2658
	Aug	0.003	1.16	0.1193	1.16	0.1156	1.16	0.1176	1.15	0.1308
		0.006	1.17	0.0968	1.18	0.0960	1.18	0.0950	1.16	0.0944
		0.05	1.18	0.4128	1.19	0.4303	1.19	0.4682	1.20	0.5204
	Nov	0.005	1.15	0.0648	1.14	0.0608	1.14	0.0599	1.15	0.0638
		0.006	1.15	0.0618	1.14	0.0614	1.14	0.0601	1.15	0.0582
		0.007	1.15	0.0613	1.14	0.0622	1.14	0.0633	1.15	0.0670

From the above results of the median k-factor, we see that the highest value for Bloemfontein is attained in February, while the lowest value is achived in May and November. The corresponding

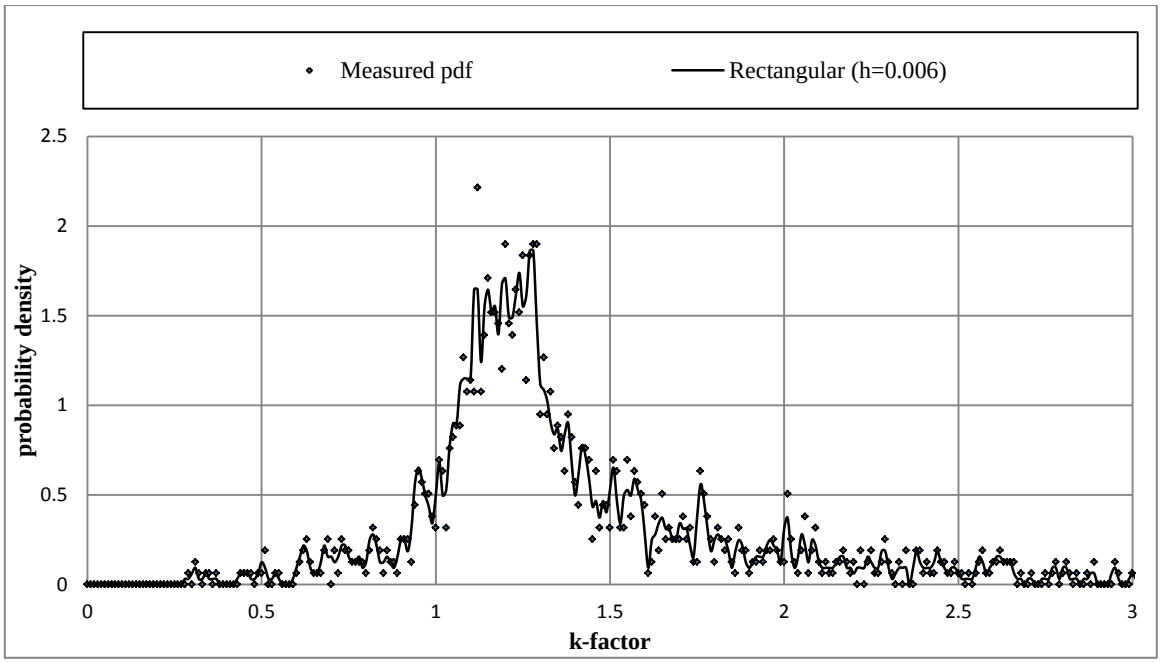

Figure 4.43 Rectangular kernel density estimate, Bloemfontein, February, 200 m a.g.l

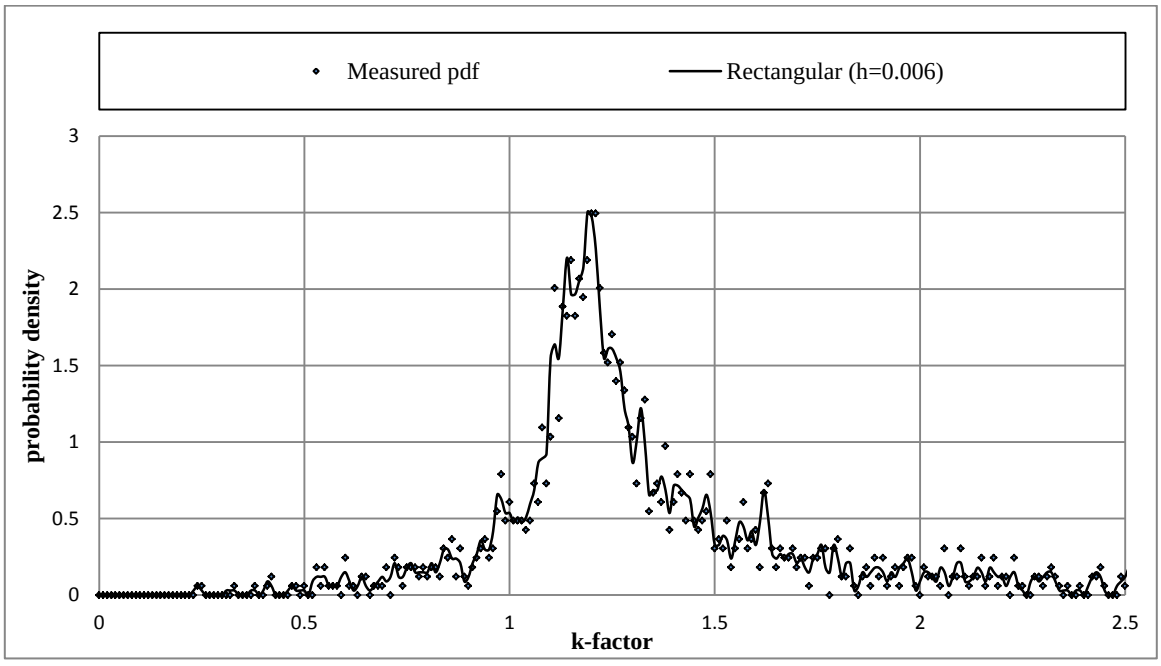

Figure 4.44: Rectangular kernel density estimate, Bloemfontein, May, 200 m a.g.l

values are obtained in May and August, and February respectively for Cape Town. The corresponding values are attained in February and November for Durban respectively. Also the corresponding values are attained in May and November for Polokwane respectively. For Pretoria,

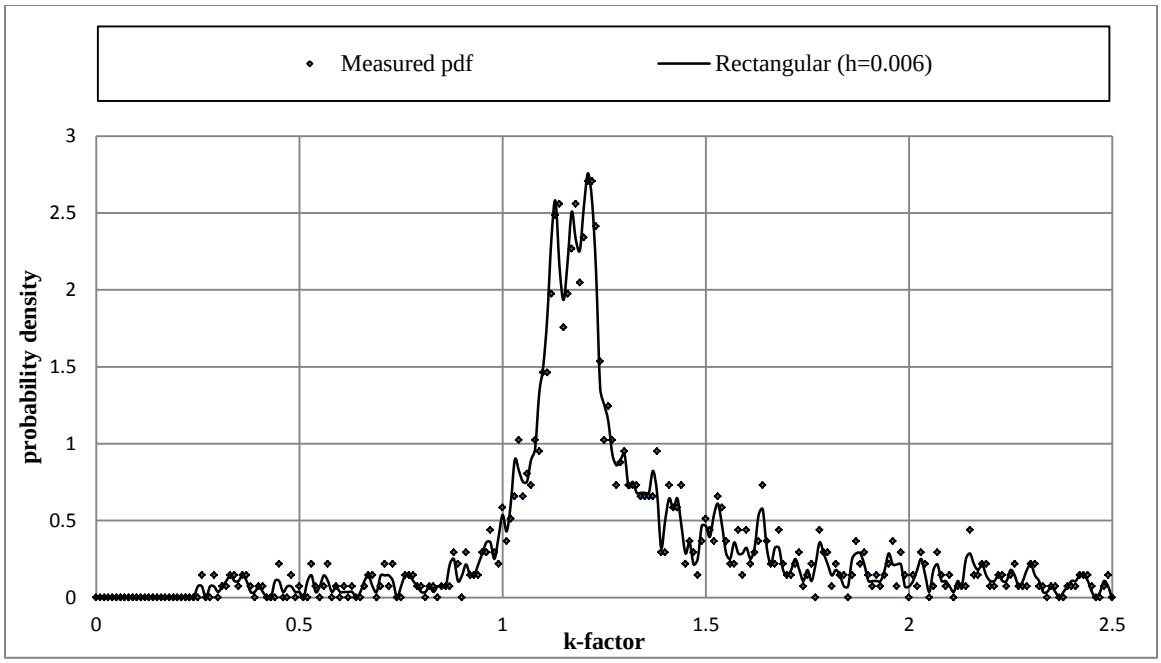

Figure 4.45: Rectangular kernel density estimate, Bloemfontein, August, 200 m a.g.l

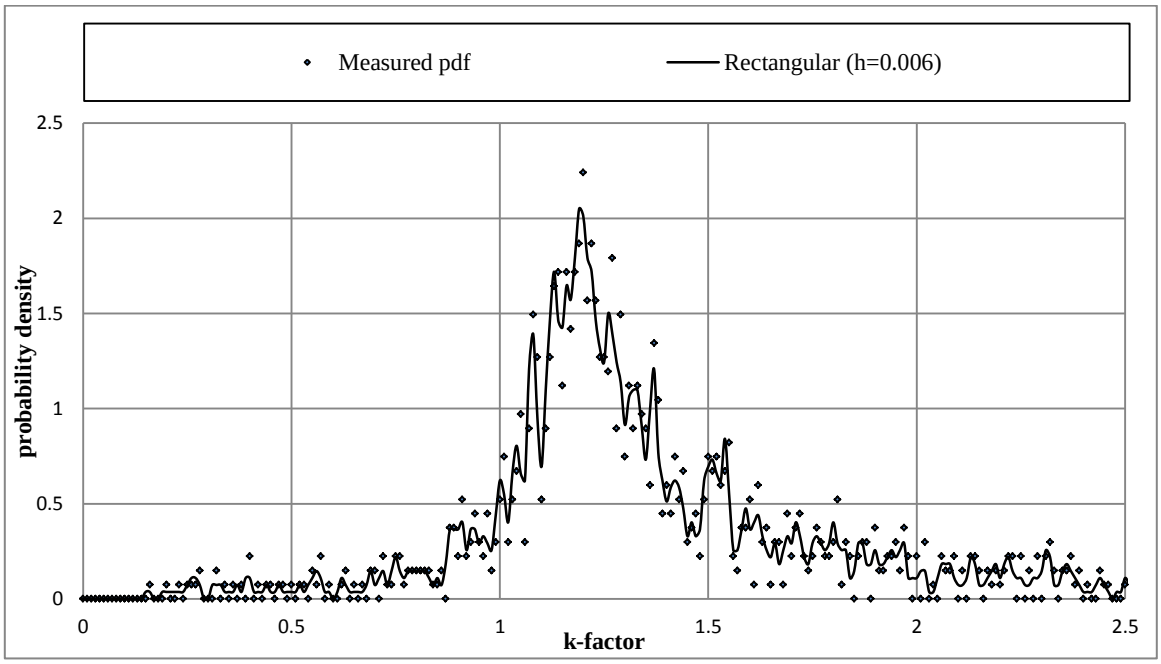

Figure 4.46: Rectangular kernel density estimate, Bloemfontein, November, 200 m a.g.l

the corresponding values are attained in February and November, and May respectively. The correponding values for Upington are attained in May and February respectively. For Bethlehem, the corresponding values are obtained in May and November respectively. From the effective k-factor results above, we also observe that the highest value for Bloemfontein is obtained in May,

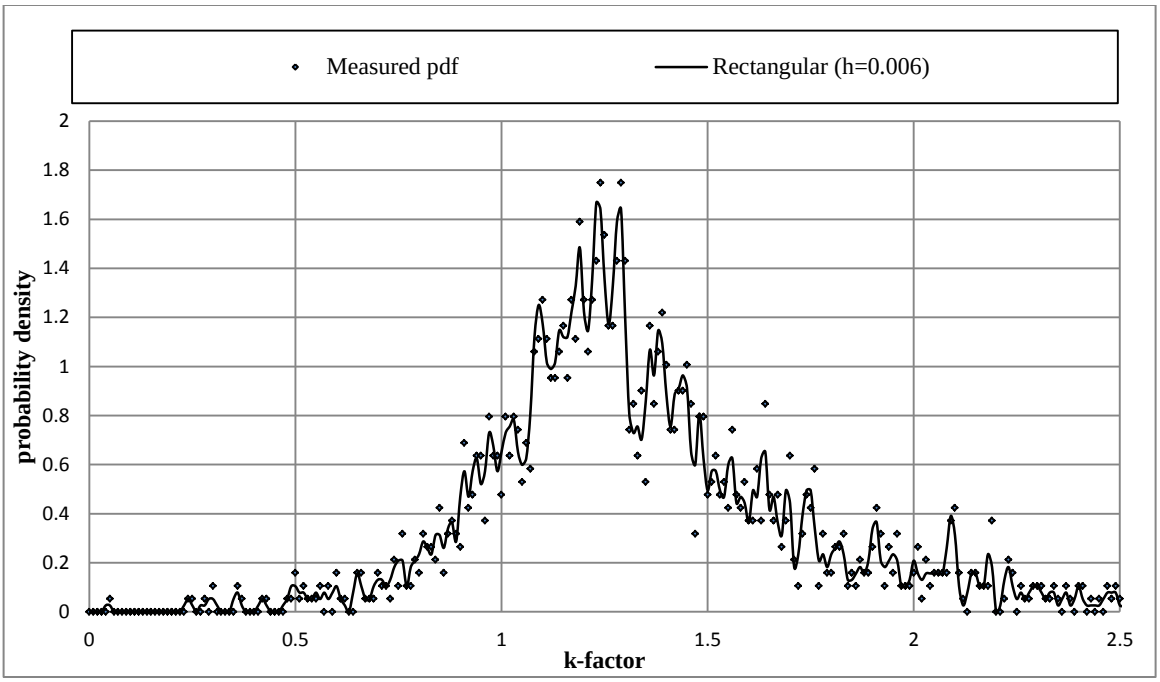

Figure 4.47: Rectangular kernel density estimate, Cape Town, February, 200 m a.g.l

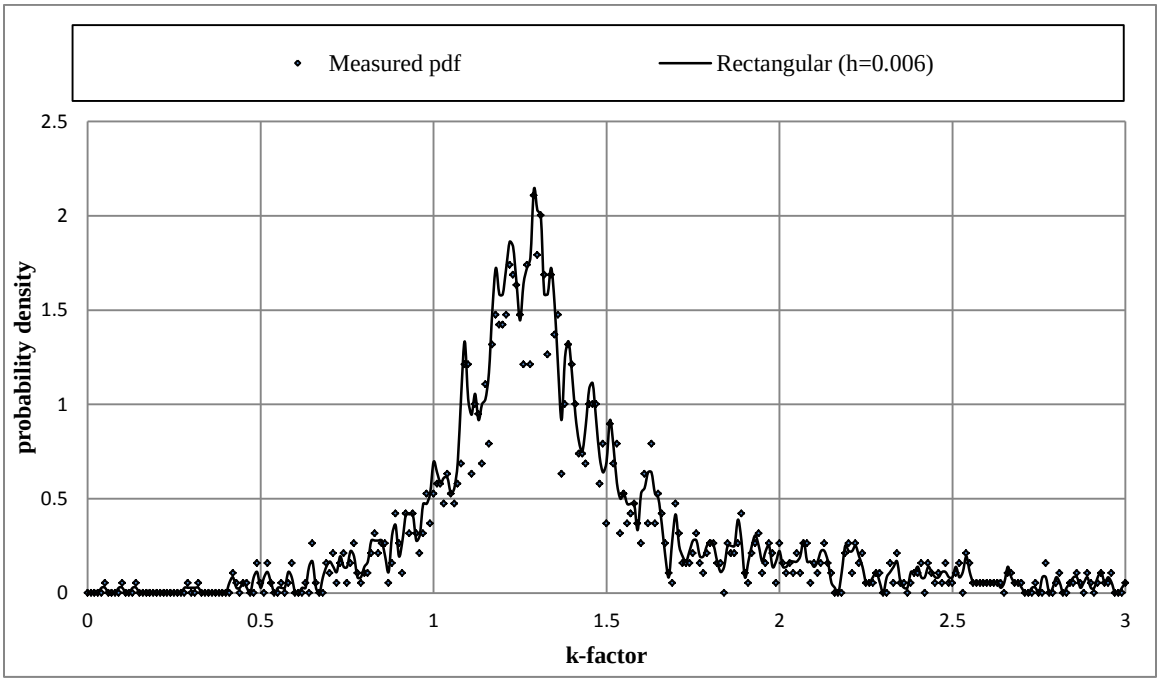

Figure 4.48: Rectangular kernel density estimate, Cape Town, May, 200 m a.g.l

while the lowest is in November. The corresponding values for Cape Town are achieved in August and, February and November respectively. The corresponding values for Durban are obtained in the months of November and August respectively. The corresponding values for Polokwane are observed in August and May respectively. The corresponding values for Pretoria are observed in

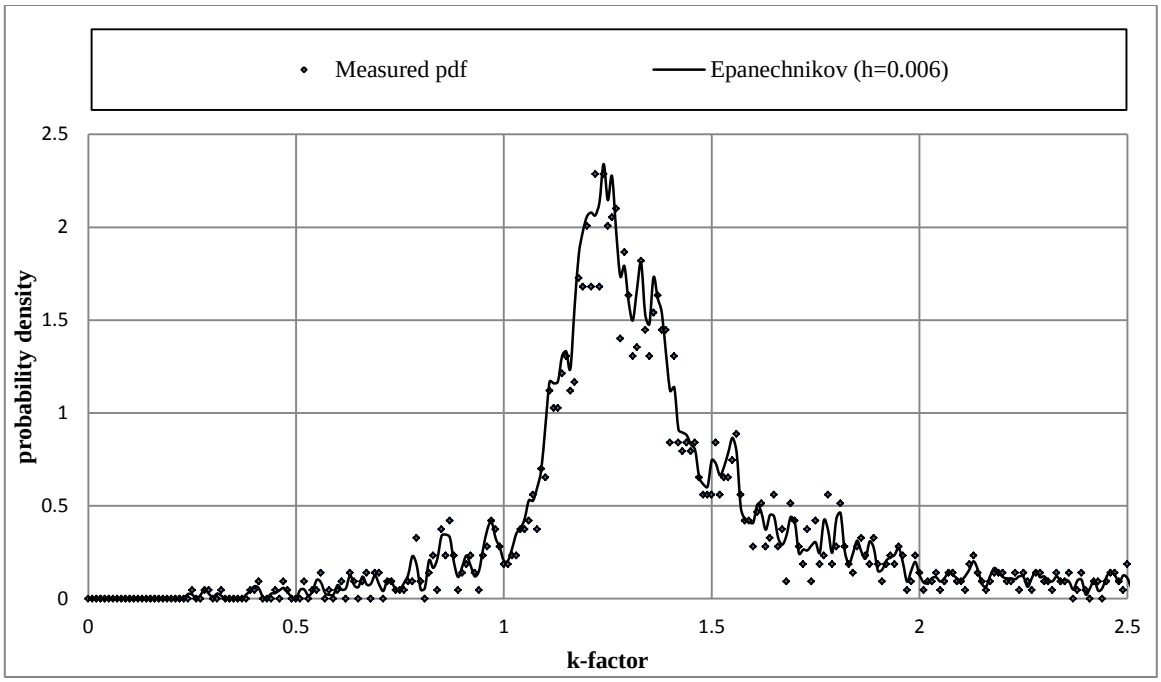

Figure 4.49: Epanechnikov kernel density estimate, Cape Town, August, 200 m a.g.l

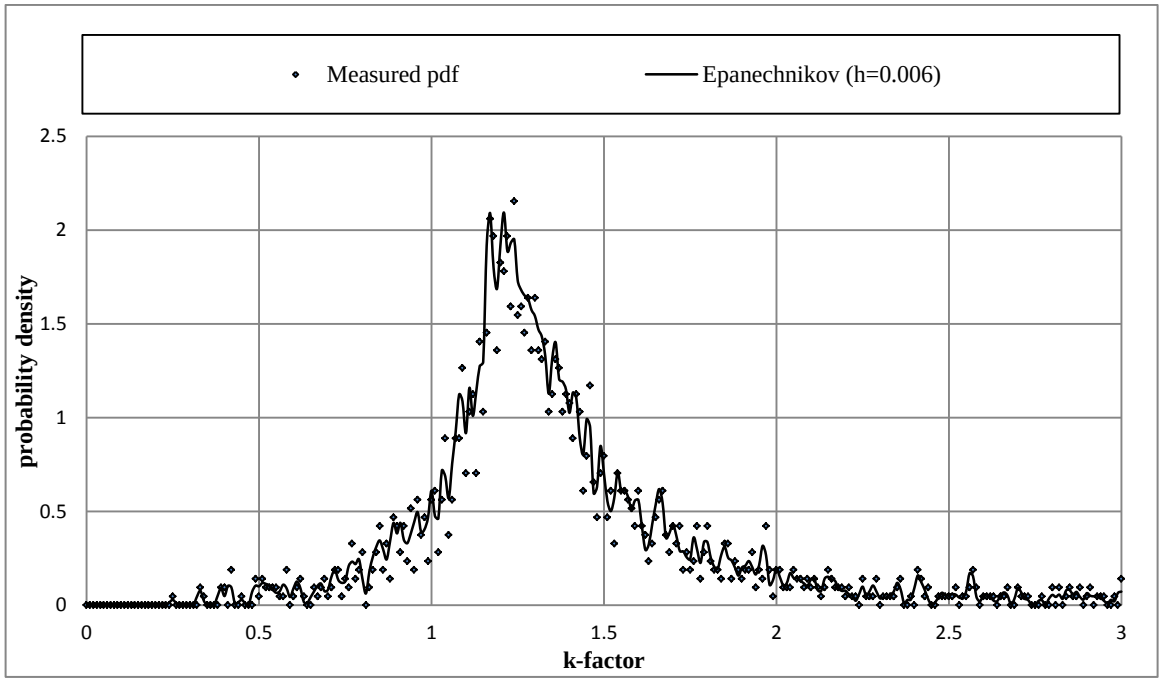

Figure 4.50: Epanechnikov kernel density estimate, Cape Town, November, 200 m a.g.l

the months of August and November, and May respectively. The corresponding values for Upington are obtained in August and November respectively. Lastly, the corresponding values for Bethlehem are obtained in the months of May and August respectively. Thus, there is no common seasonal trend

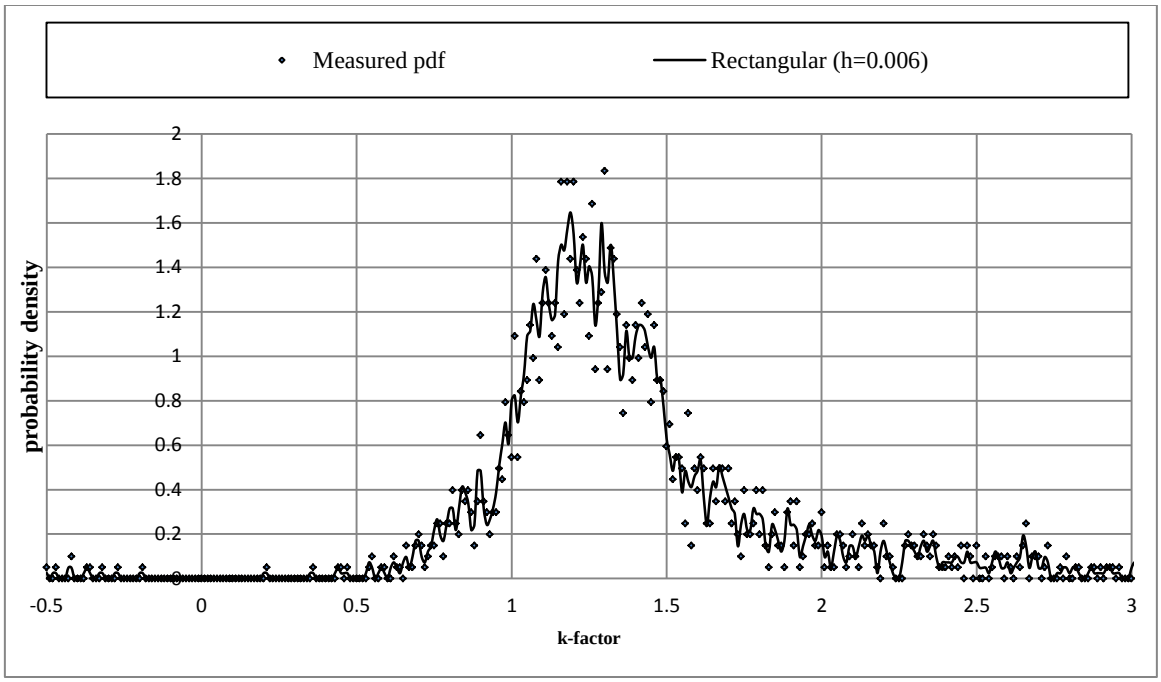

Figure 4.51: Rectangular kernel density estimate, Durban, February, 200 m a.g.l

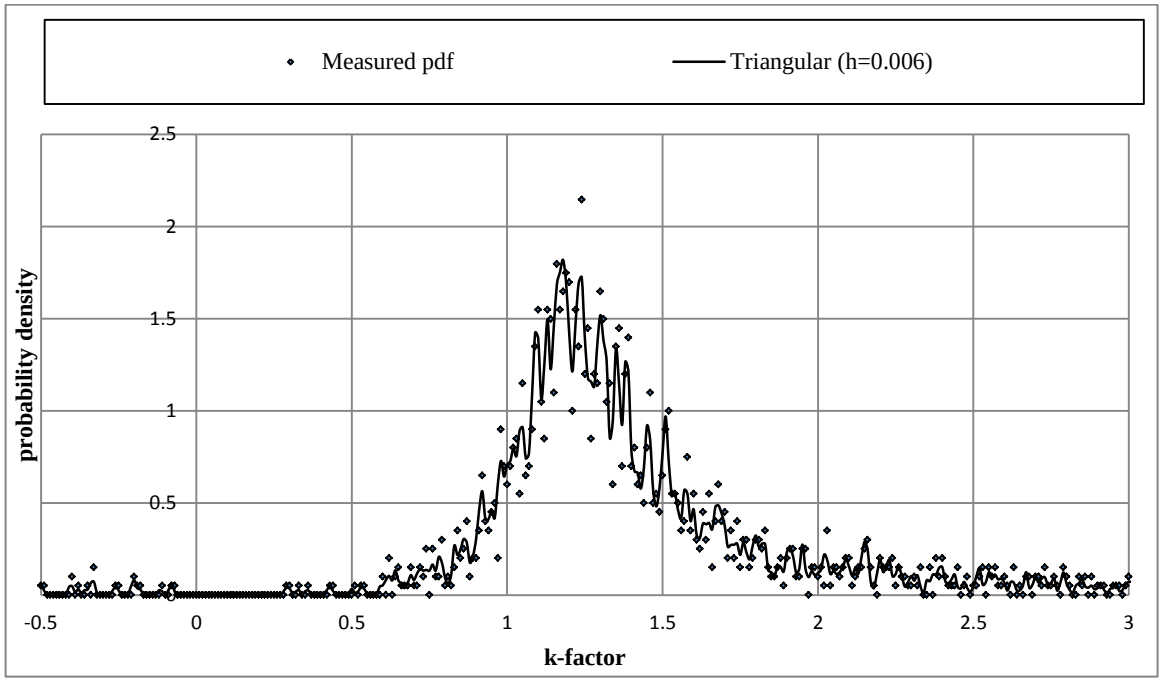

Figure 4.52: Triangular kernel density estimate, Durban, May, 200 m a.g.l

of the k-factor variation across the seven locations in South Africa, although higher values are still obtained in coastal Cape Town and lower values in inland Upington and Bethlehem.

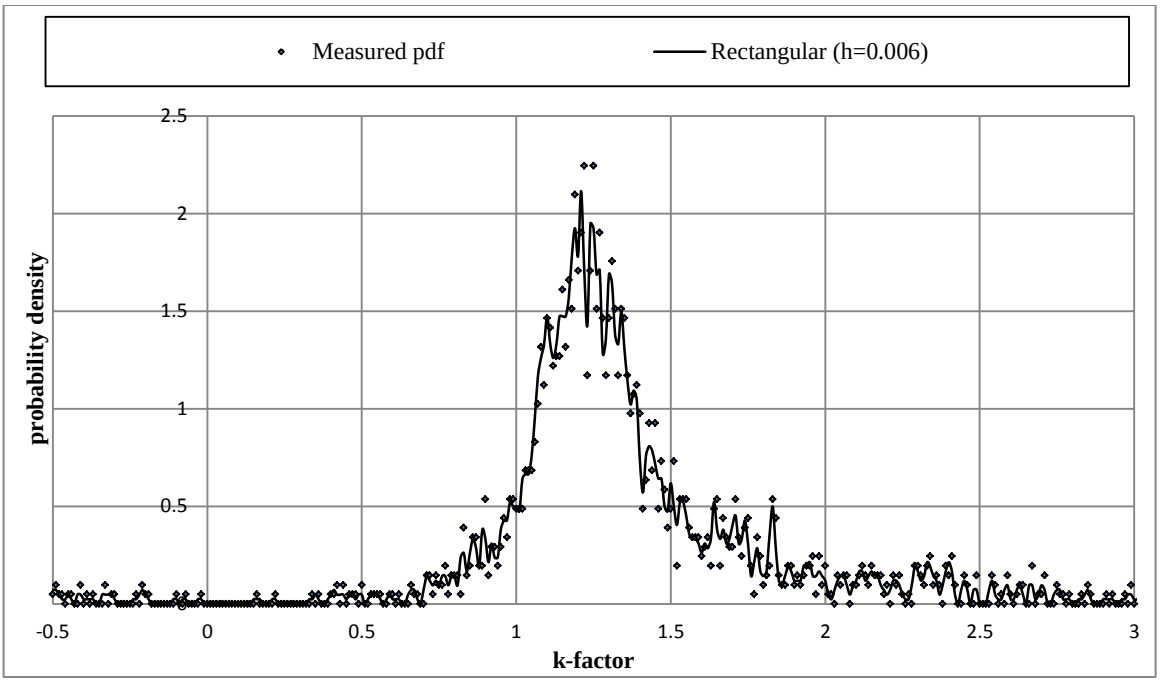

Figure 4.53: Rectangular kernel density estimate, Durban, August, 200 m a.g.l

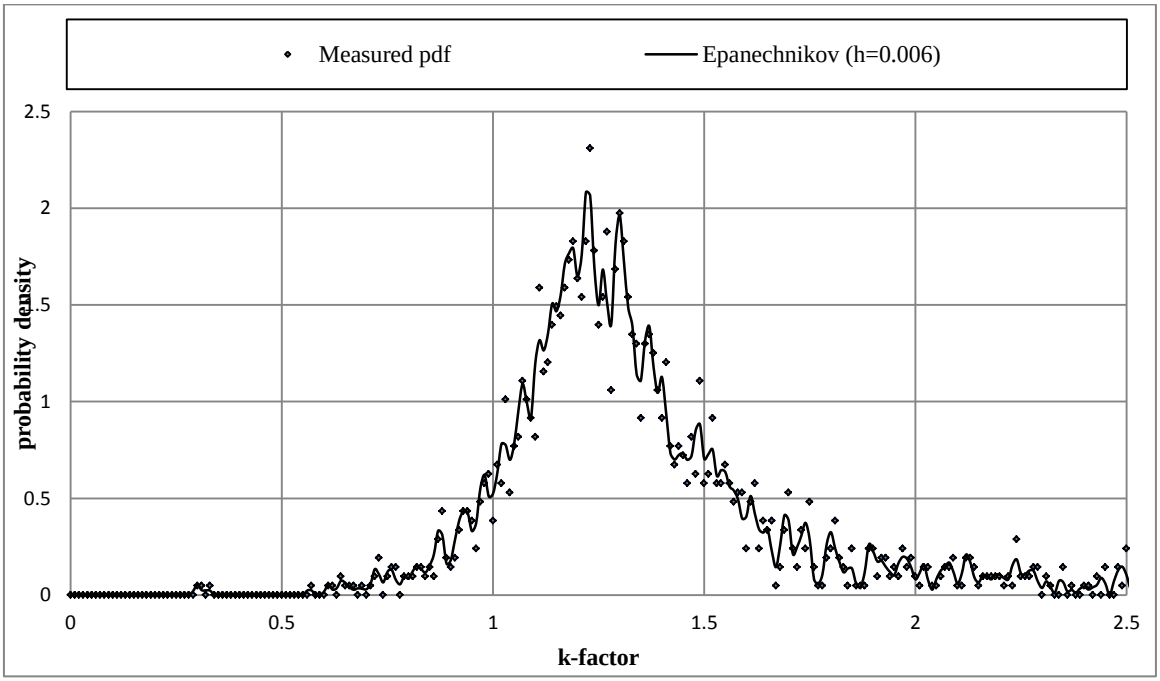

Figure 4.54: Epanechnikov kernel density estimate, Durban, November, 200 m a.g.l

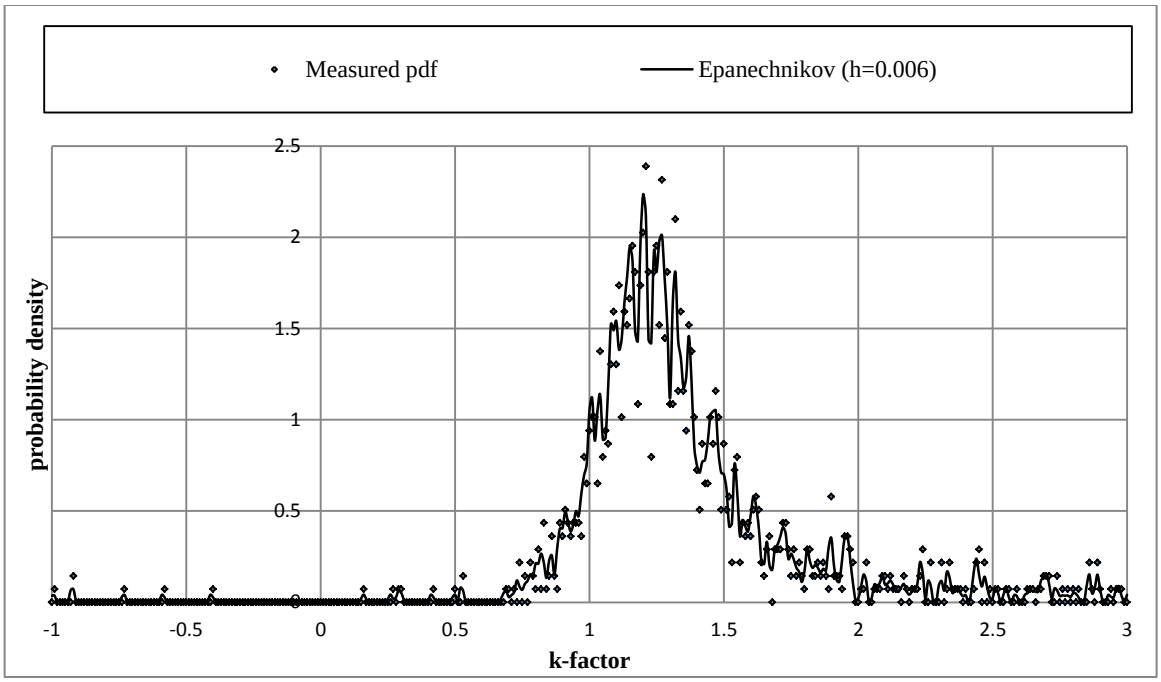

Figure 4.55: Epanechnikov kernel density estimate, Polokwane, February, 200 m a.g.l

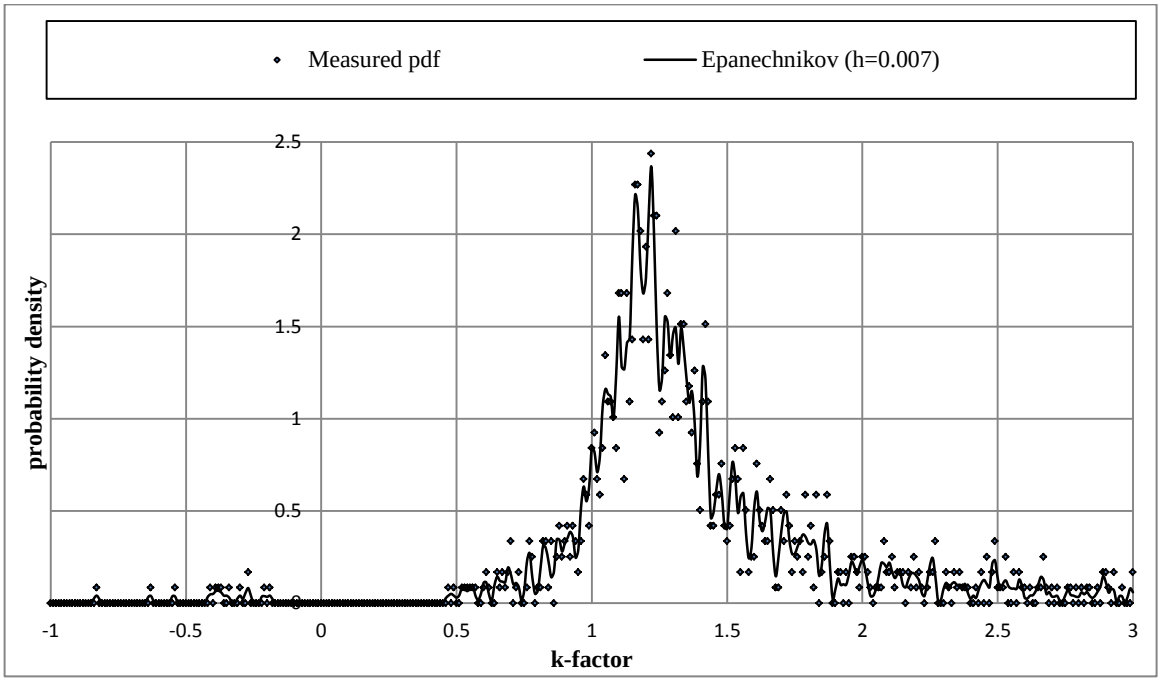

Figure 4.56: Epanechnikov kernel density estimate, Polokwane, May, 200 m a.g.l

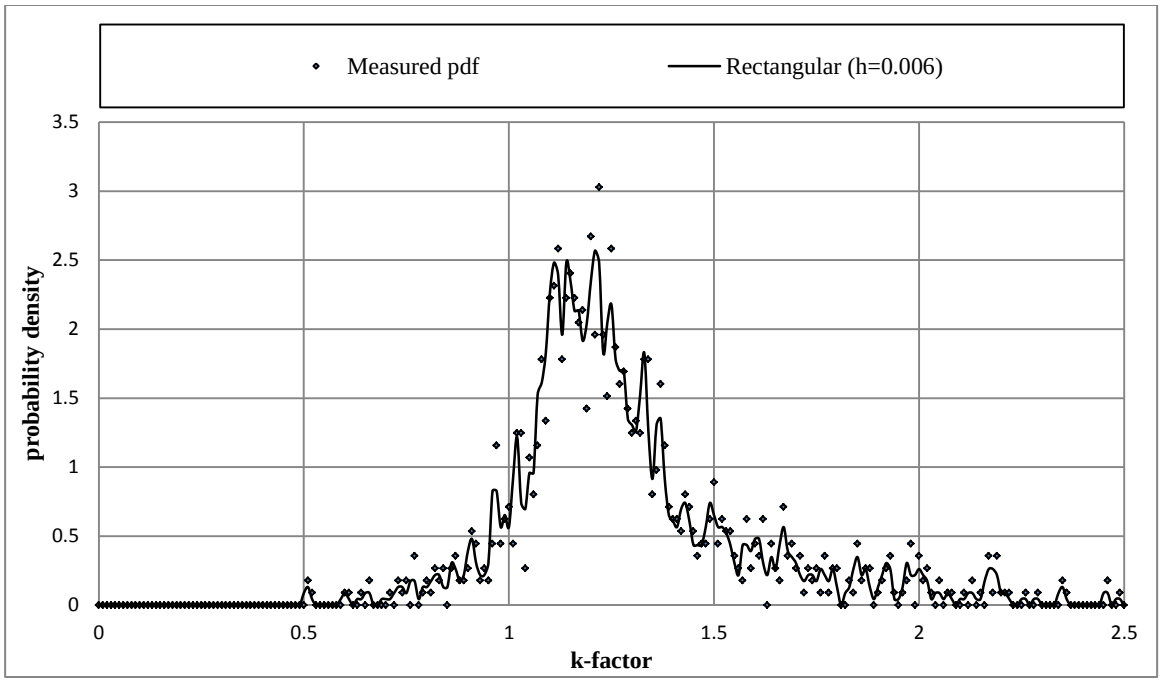

Figure 4.57: Rectangular kernel density estimate, Polokwane, August, 200 m a.g.l

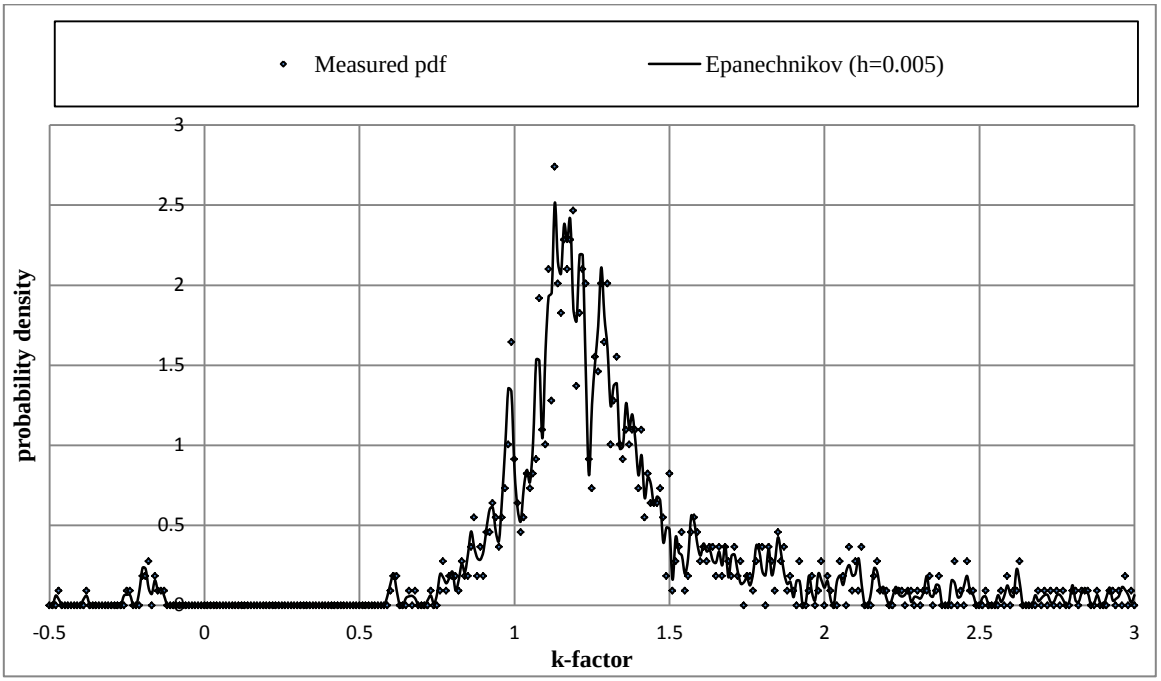

Figure 4.58: Epanechnikov kernel density estimate, Polokwane, November, 200 m a.g.l

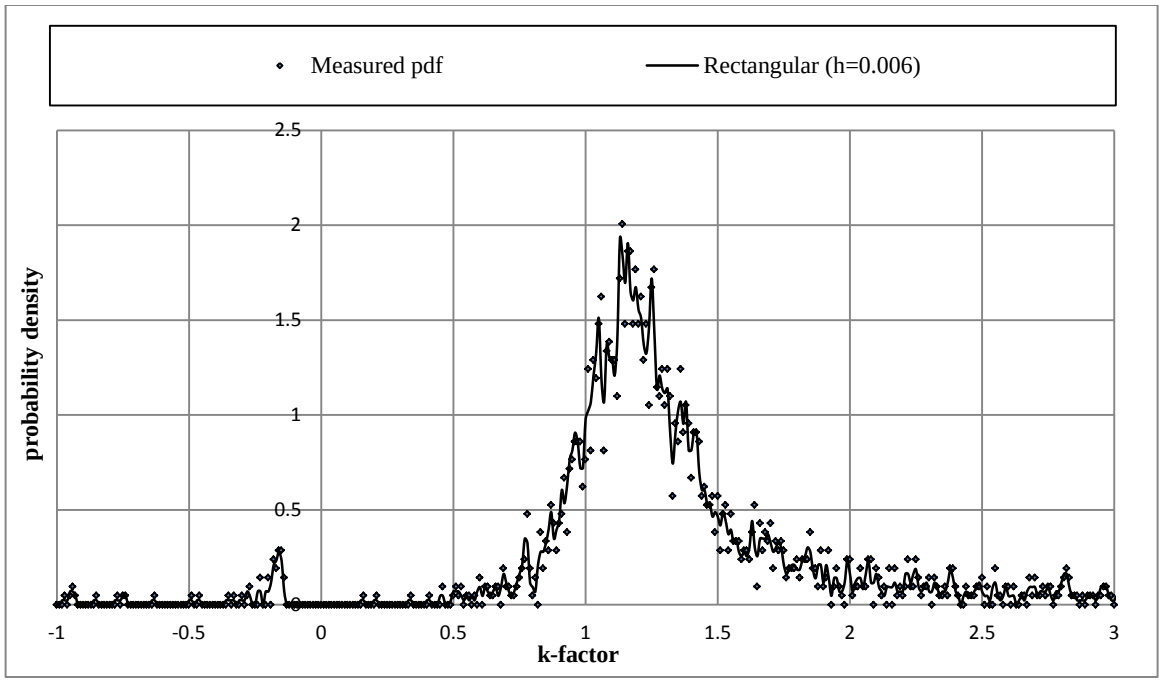

Figure 4.59: Rectangular kernel density estimate, Pretoria, February, 200 m a.g.l

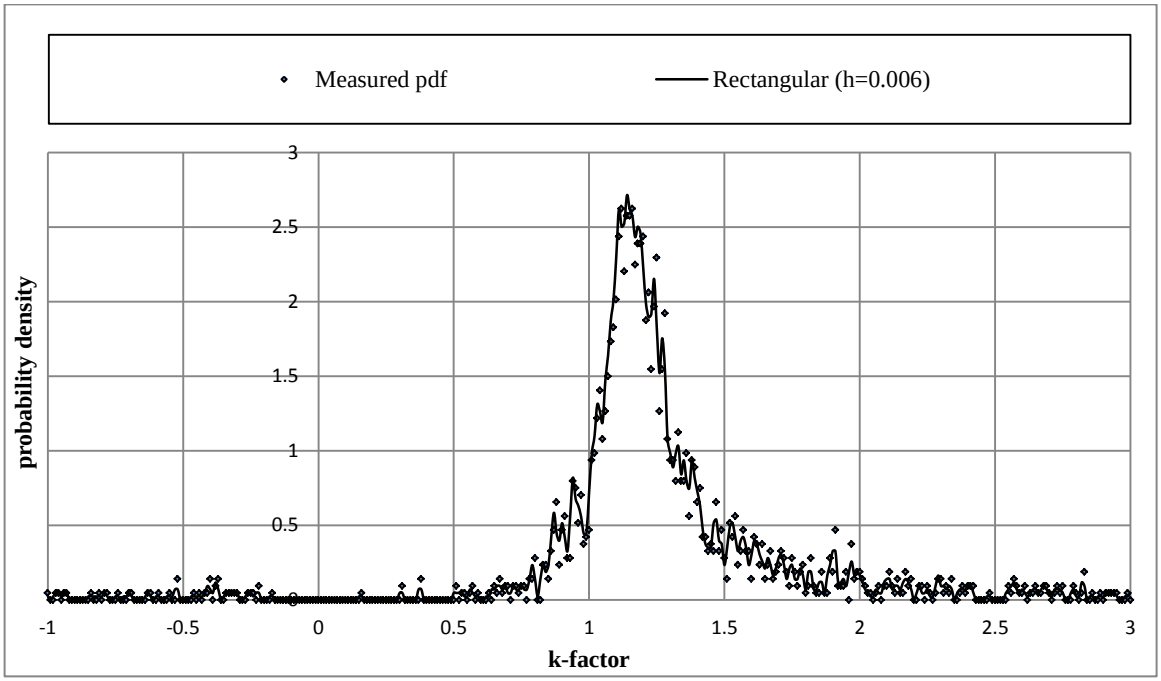

Figure 4.60: Rectangular kernel density estimate, Pretoria, May, 200 m a.g.l

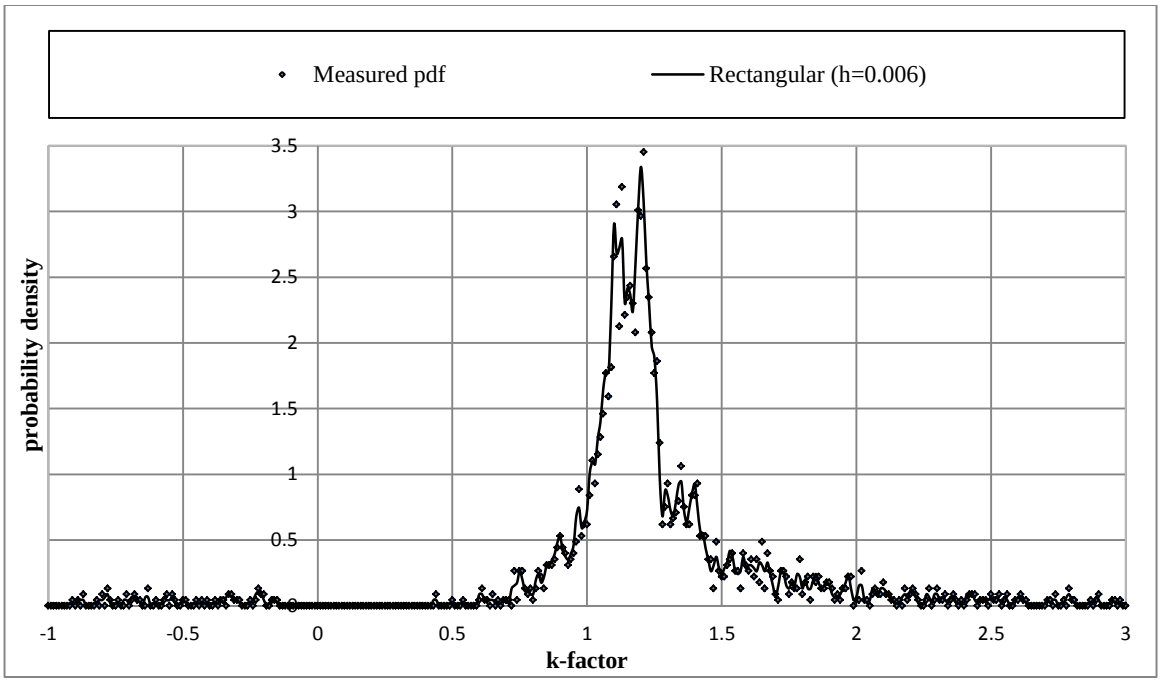

Figure 4.61: Rectangular kernel density estimate, Pretoria, August, 200 m a.g.l

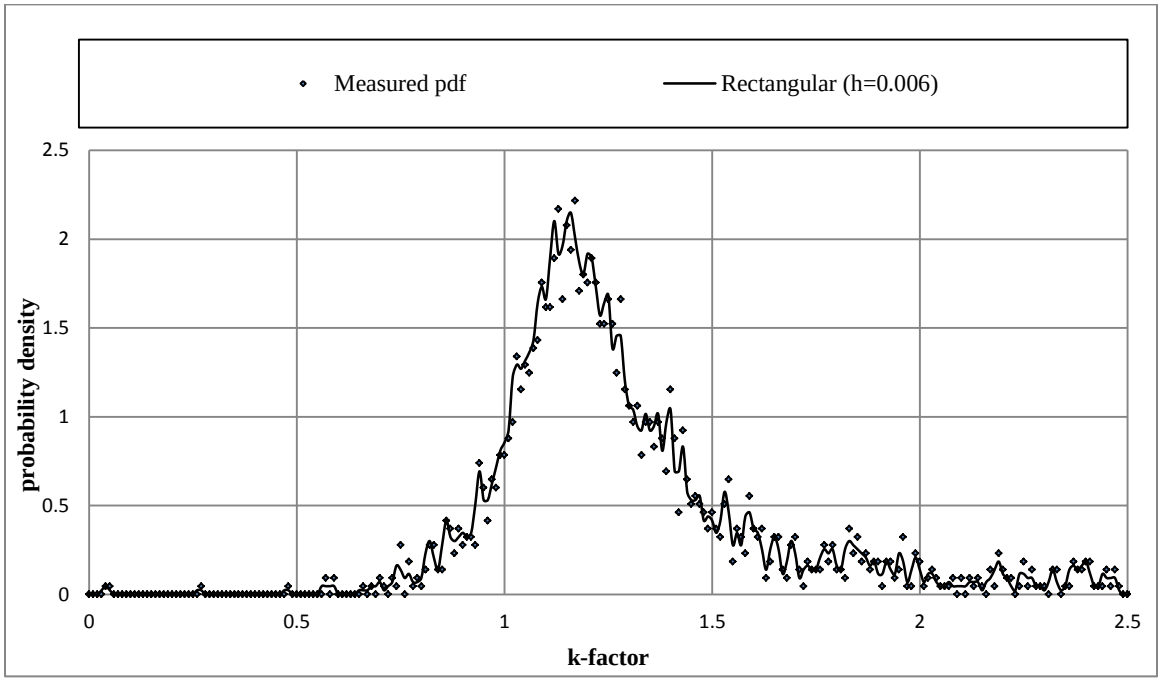

Figure 4.62: Rectangular kernel density estimate, Pretoria, November, 200 m a.g.l

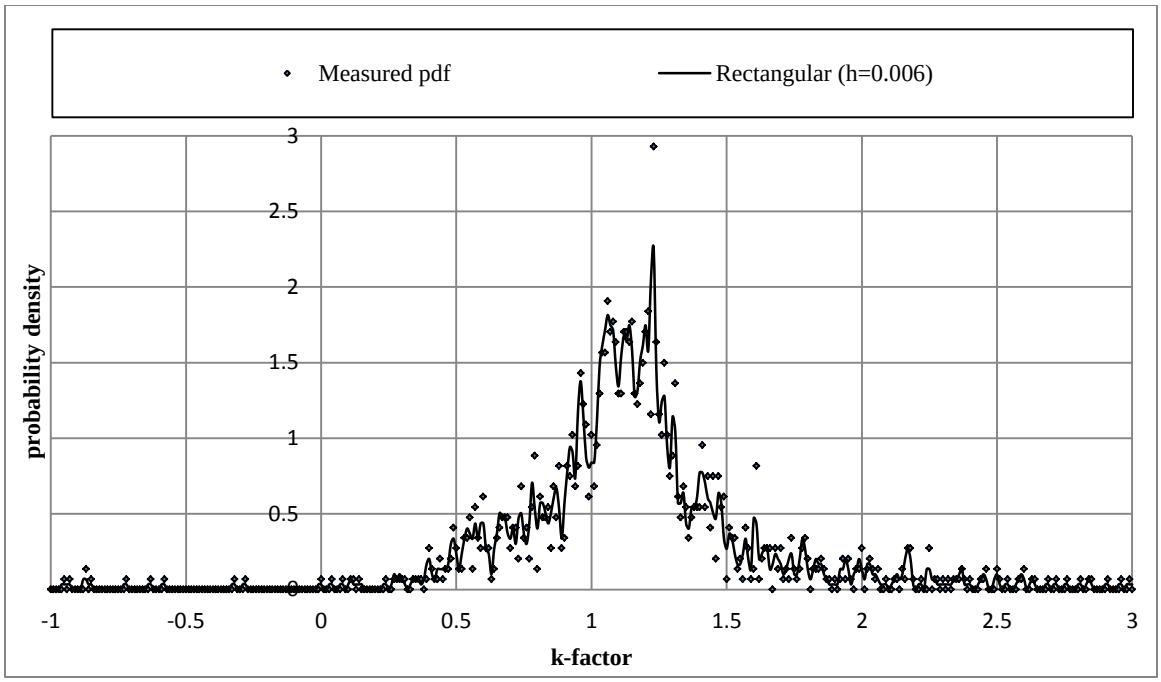

Figure 4.63: Rectangular kernel density estimate, Upington, February, 200 m a.g.l

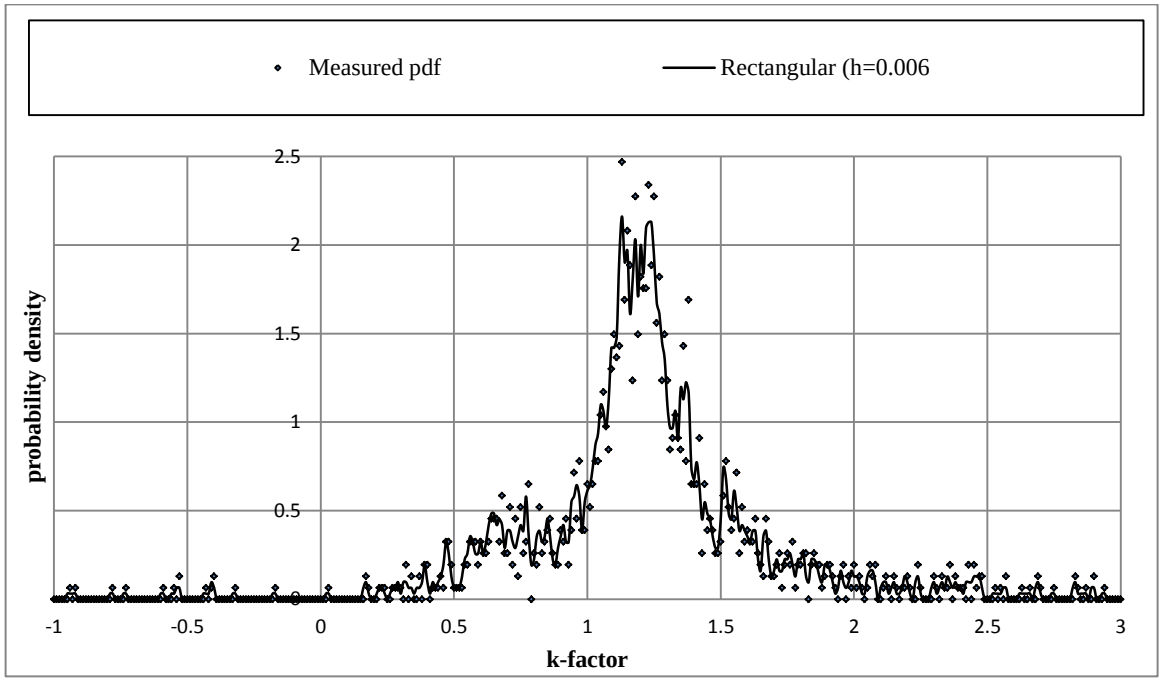

Figure 4.64: Rectangular kernel density estimate, Upington, May, 200 m a.g.l

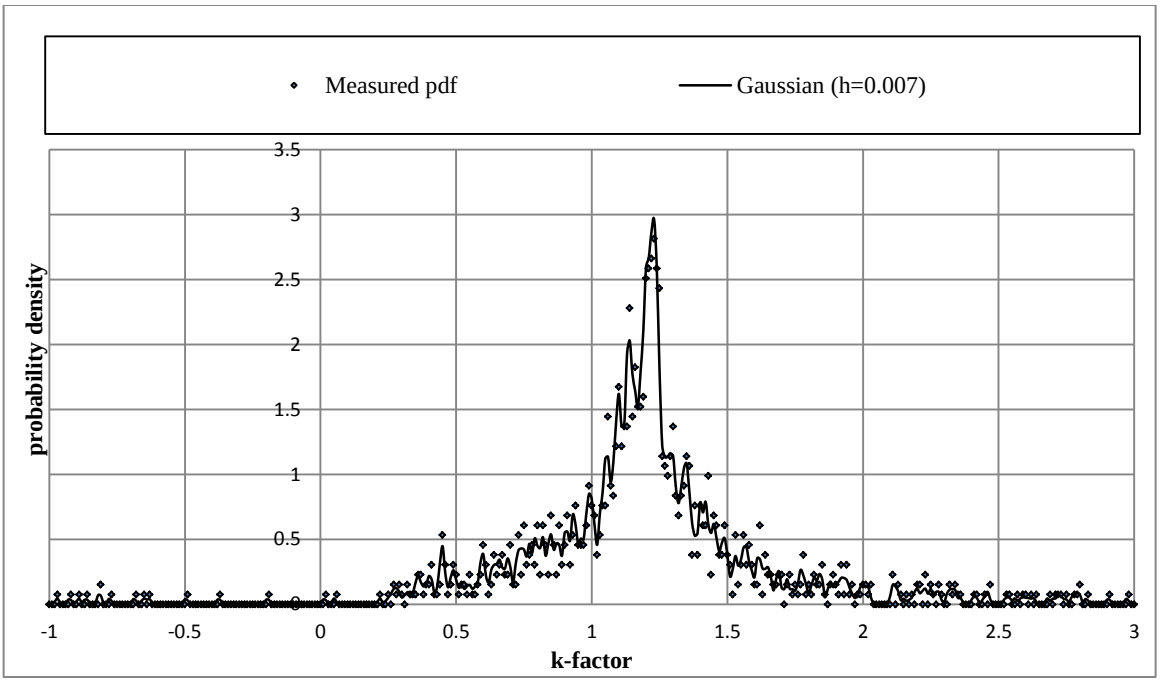

Figure 4.65: Gaussian kernel density estimate, Upington, August, 200 m a.g.l

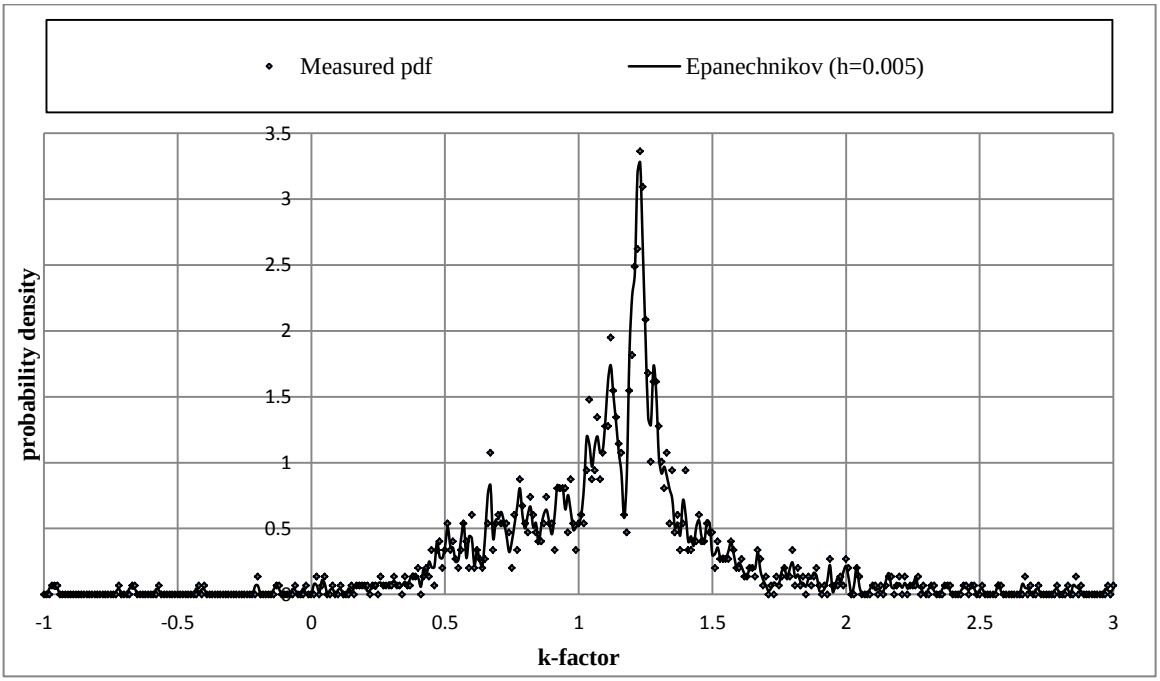

Figure 4.66: Epanechnikov kernel density estimate, Upington, November, 200 m a.g.l

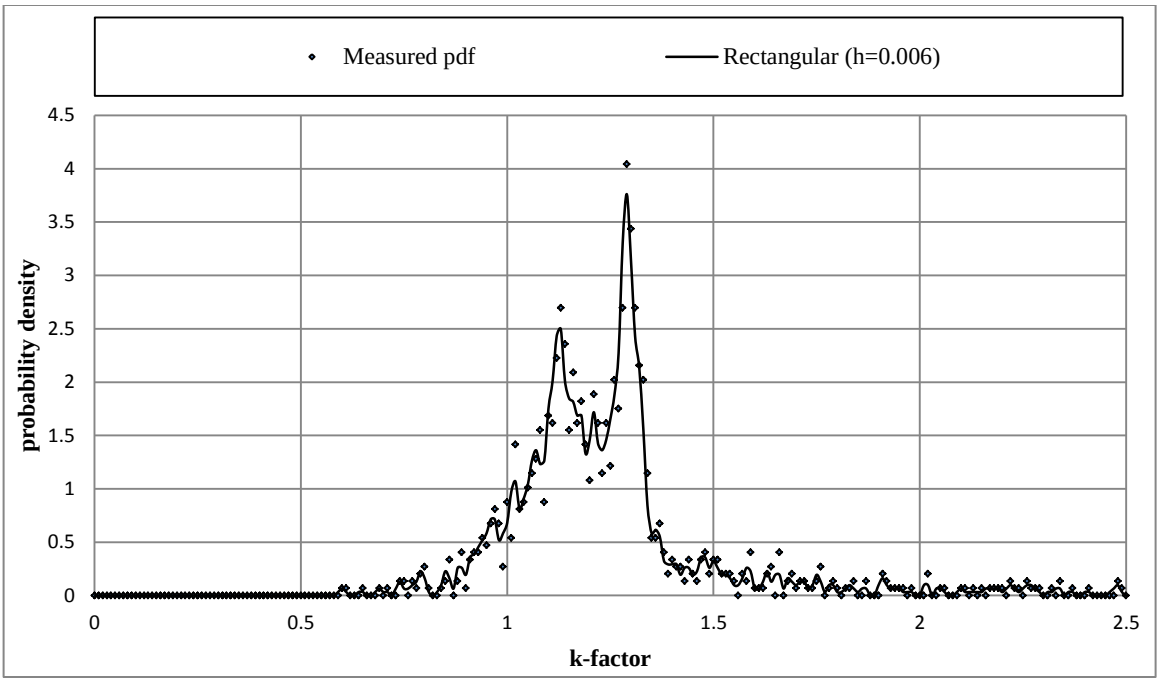

Figure 4.67: Rectangular kernel density estimate, Bethlehem, February, 200 m a.g.l

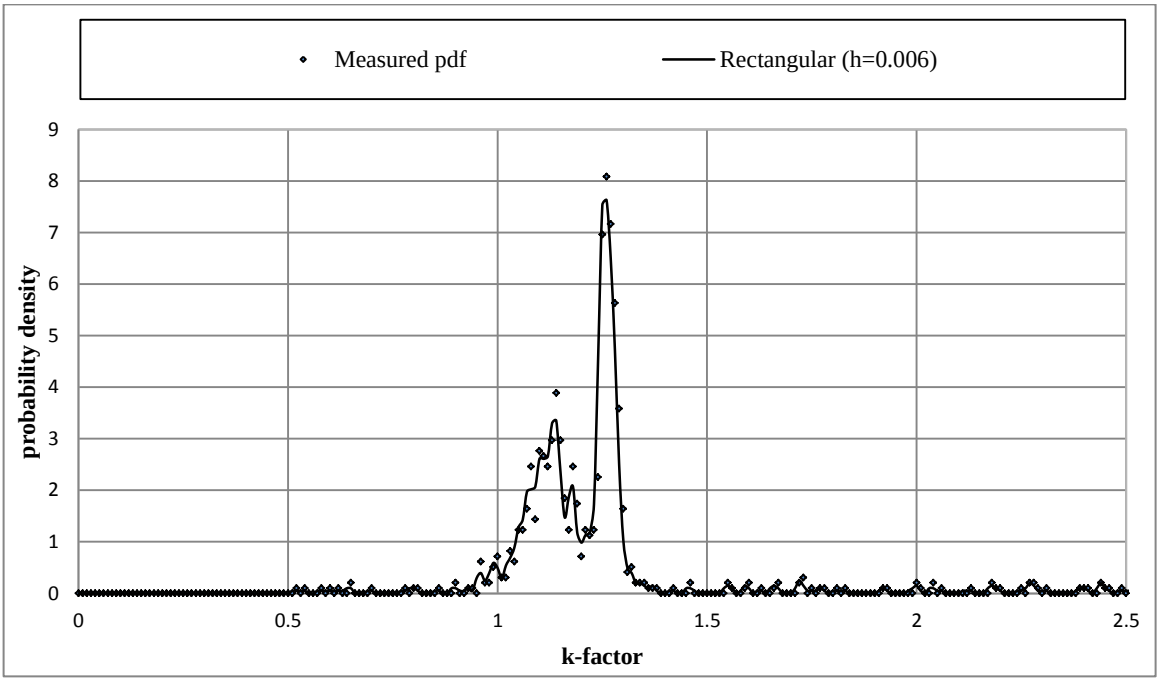

Figure 4.68: Rectangular kernel density estimate, Bethlehem, May, 200 m a.g.l

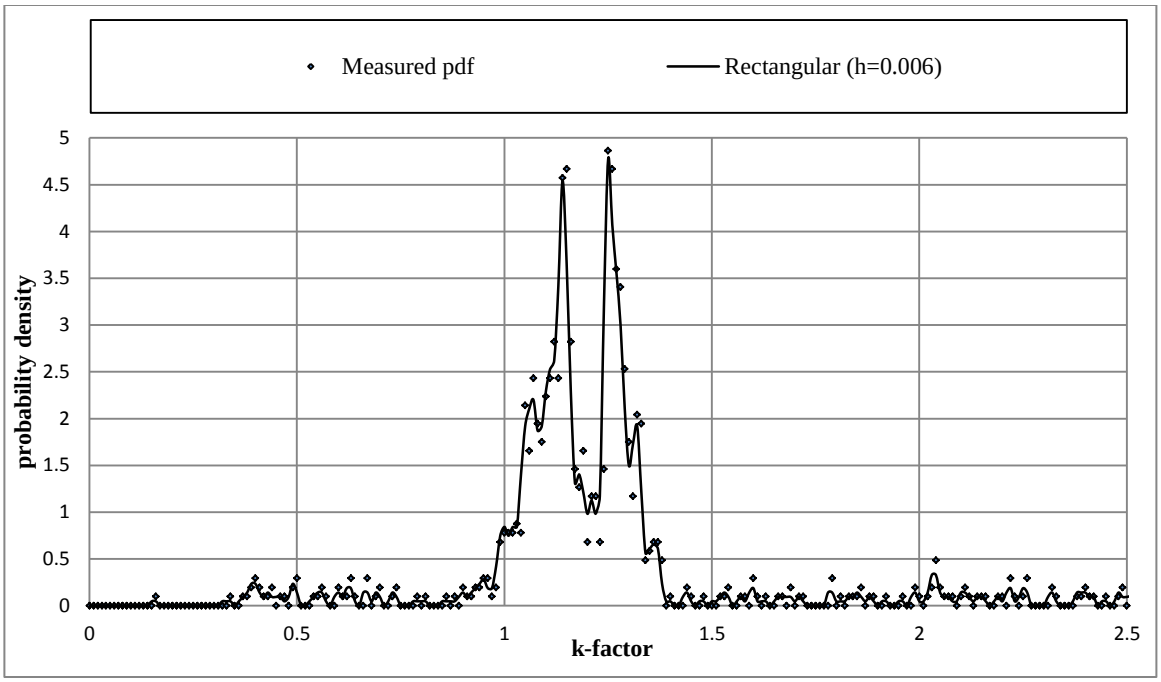

Figure 4.69: Rectangular kernel density estimate, Bethlehem, August, 200 m a.g.l

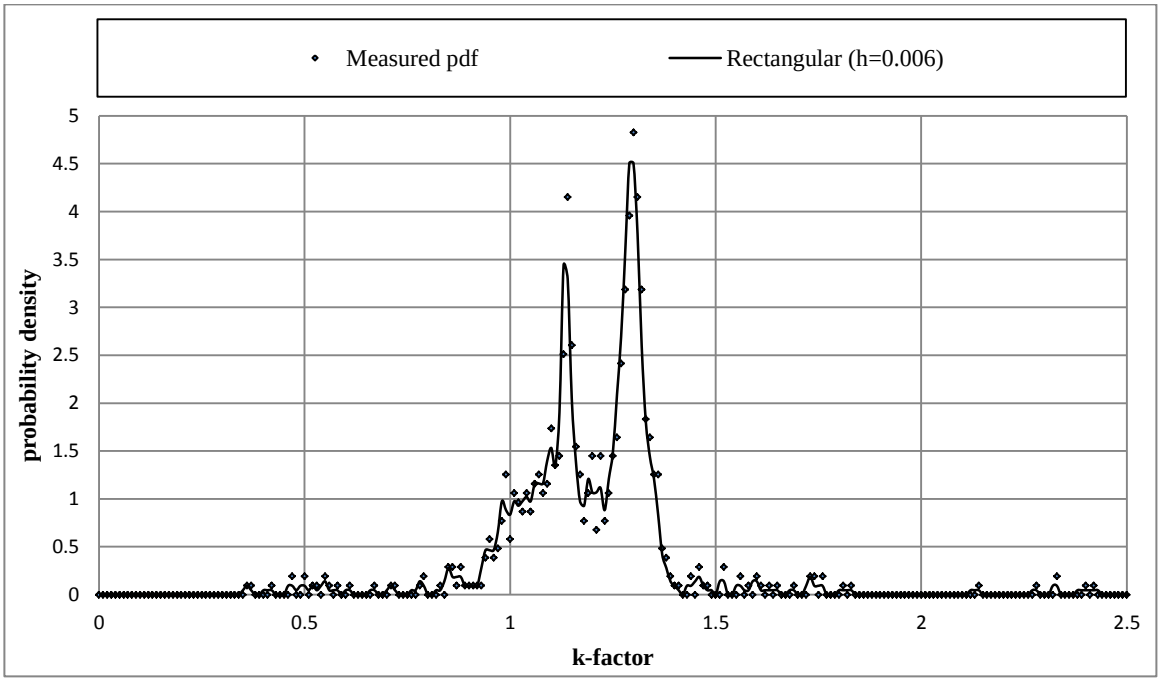

Figure 4.70: Rectangular kernel density estimate, Bethlehem, November, 200 m a.g.l

Tables 4.12 and 4.13 show the comparison of seasonal measured, curve fitting and kernel median and effective k-factor values respectively.

4.3.6 Validation of Results

Odedina and Afullo [20] obtained a median k-factor value of 1.21 for Durban using one year data (2003/04) for the height range of 0-500 m above ground level. They also obtained also obtained the following seasonal values; 1.21 for February, 1.15 for May, 1.27 for August and 1.20 for November. Thus, we see that the values obtained from their study are slightly lower than those obtained in this study. This is due to the fact that the height range considered is higher than the one used for the study (0-200 m above ground level). This is explained by the fact the k-factor decreases with height and so the higher the height range considered, the lower the median value of the k-factor obtained.

Table 4.12: Comparison of seasonal median k-factor values

Location	season	measured	curve fitting	kernel
Bloemfonten	Feb	1.24	1.24	1.22
	May	1.21	1.22	1.20
	Aug	1.21	1.21	1.21
	Nov	1.22	1.25	1.20
Cape Town	Feb	1.26	1.27	1.23
	May	1.29	1.29	1.29
	Aug	1.3	1.29	1.29
	Nov	1.27	1.27	1.26
Durban	Feb	1.28	1.26	1.29
	May	1.26	1.26	1.26
	Aug	1.26	1.25	1.26
	Nov	1.26	1.26	1.24
Polokwane	Feb	1.27	1.24	1.25
	May	1.27	1.24	1.26
	Aug	1.23	1.21	1.23
	Nov	1.23	1.21	1.22
Pretoria	Feb	1.22	1.20	1.21
	May	1.19	1.18	1.19
	Aug	1.19	1.17	1.20
	Nov	1.20	1.20	1.21
Upington	Feb	1.14	1.13	1.15
	May	1.20	1.21	1.21
	Aug	1.19	1.19	1.18
	Nov	1.16	1.15	1.17
Bethlehem	Feb	1.16	1.20	1.17
	May	1.21	1.21	1.21
	Aug	1.17	1.19	1.16
	Nov	1.14	1.21	1.15

Table 4.13: Comparison of seasonal effective k-factor values

Location	season	measured	curve fitting	kernel
Bloemfonten	Feb	0.49	0.52	0.5
	May	0.53	0.55	0.52
	Aug	0.54	0.52	0.5
	Nov	0.50	0.48	0.46
Cape Town	Feb	0.41	0.44	0.44
	May	0.48	0.51	0.48
	Aug	0.52	0.51	0.49
	Nov	0.46	0.46	0.44
Durban	Feb	0.54	0.58	0.56
	May	0.58	0.59	0.58
	Aug	0.55	0.57	0.54
	Nov	0.63	0.65	0.65
Polokwane	Feb	0.64	0.68	0.66
	May	0.57	0.55	0.59
	Aug	0.66	0.71	0.67
	Nov	0.64	0.63	0.6
Pretoria	Feb	0.59	0.58	0.61
	May	0.58	0.60	0.57
	Aug	0.61	0.66	0.63
	Nov	0.62	0.64	0.63
Upington	Feb	0.43	0.41	0.44
	May	0.38	0.41	0.39
	Aug	0.44	0.49	0.46
	Nov	0.37	0.41	0.38
Bethlehem	Feb	0.72	0.75	0.74
	May	0.78	0.86	0.79
	Aug	0.58	0.54	0.55
	Nov	0.64	0.64	0.67

Another factor that could explain the slight difference in values is the fact that data for one year may not be sufficient in providing a comprehensive trend for a radioclimatic variable, for example the k-factor variation on a seasonal or annual basis.

Also, Palmer and Baker [64] obtained the following values of the median k-factor using ground based observations; 1.46 for Durban, 1.44 for Cape Town, 1.36 for Upington, 1.32 for Pretoria. The values obtained in their study are much higher than those obtained in this study since they are evaluated near the ground and as stated in paragraph above, the k-factor is higher near the ground and diminishes as the height from ground level increases. However, one common thing stands out between their results and the ones obtained in this study; the highest k-factor is obtained in Durban and Cape Town. This is so because the k-factor is higher in lower humid coastal areas and its decreases as we move away from the sea. However, this statement should not be misinterpreted to

mean that the variation of the k-factor is that simplistic as it varies with geographical location and climatic conditions. A similar explanation for the slight variations between the effective k-factor values obtained in this study and those for the researchers mentioned above would also suffice.

4.4 Chapter Summary

The distribution attributes of the k-factor for seven locations in South Africa has been treated in this chapter. More specifically, both annual and seasonal three-year models of the k-factor have been formulated for the seven locations. The kernel method results have shown that the kernel models perform better in terms of the error as compared to the curve fitting method. This can be attributed to the fact that the kernel models are directly formulated from the data and that the optimum choice of the smoothing parameter ensures that the model follows the measured pdf as much as possible, while at the same time producing a smoothed model. On the other hand, the curve fitting method produced much smoother models as compared to the kernel models and is also easier to interpret in terms of its parameters. Overall, we note from the both the kernel and curve fitting models that the distribution of the k-factor for six of the seven locations studied is bell-shaped, centred almost symmetrically around the median value. The k-factor distribution for Bethlehem, is however clearly doubly-peaked and this calls for further investigation through more data measurements and modelling. Both the median and effective k-factor are seen to vary from season to season, and from place to place. This is so because the atmosphere is inhomogeneous, with its properties varying with height above sea level and topographical setting. Also, higher k-factor values are obtained in the low altitude, high humidity coastal areas, while lower k-factor values are obtained in the higher altitude, northern drier parts of South Africa, like Upington. From the kernel models, we note that there is no preferred kernel method over another, but the choice of the kernel model to use for a particular set of data points is purely driven by some error-based mechanism. In this study, the rectangular kernel is seen to produce the least ISE errors for most of the locations, on both annual and seasonal basis, and is proposed as the best non-parametric method for the modelling the k-factor in South Africa.

Chapter 5

Interpolation and Mapping of the k-factor

5.1 Introduction

Interpolation refers to the process of predicting data values at locations where samples are not available using data from surrounding locations within a particular geographical range (area) [81, 82]. There are two broad categories of interpolation techniques namely: global and local methods. Global methods consider all known samples to estimate the value at a given location. Local methods consider only a fixed number of samples within a certain search radius to the point being estimated. Global methods are known to produce smooth estimates but are very sensitive to outliers. On the other hand, local methods produce less smooth surfaces but are less sensitive to outliers. Global methods include trend surfaces, Fourier series and many others while local methods include Radial Basis Functions, Kriging and Inverse Distance Weighting (IDW) [81, 83], among others. The most commonly used interpolation techniques are spatial and they include: Radial Basis Functions (RBFs), Kriging and Inverse Distance Weighting (IDW). Spatial interpolation techniques are based on the proposition that things which are closer to each other are more alike than those further apart.

Due to the tedious nature of processing clear-air meteorological data, and the cost involved in launching radiosondes, the three spatial interpolation techniques listed above have been employed here in extending both the median and effective k-factor statistics obtained in Chapter 4 to cover the whole of South Africa. A comparison of the interpolation methods is drawn by using the Mean Absolute Error (MAE) and Root Mean Square Error (RMSE) criteria and then the interpolated and gridded values are presented in contour maps. The RMSE is sensitive to outliers while the MAE is not; hence both errors complement each other. Both error criteria provide an excellent averaged summary of the variation between measured and predicted values.

5.2 Inverse Distance Weighting (IDW)

IDW is a deterministic interpolation technique. In this method, data values that are closer to each other are assumed to be more similar than those farther apart. IDW uses a weighting scheme to evaluate the impact individual data points have on the predicted value with data points that are closer to the prediction point being assigned more weight, hence having more impact on the predicted value than those farther from the predicted value [12, 81]. The weighting policy in IDW is based only on the Euclidian distance between the known data points and the prediction point. The predicted estimate is then a linear combination of the weighted measured values. The weight assignment in IDW is controlled by a power parameter, p that determines how much influence data points have on the predicted value as the Euclidian distance varies. The higher the power parameter, the more the influence closer points have on the predicted value and vice versa. Typically, the power parameter is assigned value of 2 or 3 but the choice can also be made based on error measurement resulting in optimal IDW [10, 81]. Mathematically, the IDW predictor is given by [10, 11, 81]:

$$k(x,y) = \sum_{i=1}^{N} w_i k(x_i, y_i) \tag{5.1}$$

where $k(x,y)$ is the IDW predictor, N is the number of known data points, $k(x_i,y_i)$ is the known data value at the point (x_i,y_i) and w_i is the weight assigned to $k(x_i,y_i)$. The weight w_i, is given by [14, 81]:

$$w_i = \frac{d_i^{-p}}{\sum_{i=1}^{N} d_i^{-p}} \tag{5.2}$$

where p is the power parameter, d is the Euclidian distance between the prediction point and the known data point and is given by [11] :

$$d = \sqrt{(x - x_i)^2 + (y - y_i)^2} \tag{5.3}$$

where all parameters are as described in (5.1) and (5.2).The weighting in IDW is such that the sum of all the weights sum to unity [10] :

$$\sum_{i=1}^{N} w_i = 1 \tag{5.4}$$

Since IDW uses a simple weighting scheme that is only based on the Euclidian distance between the known data point and the prediction point alone, the level of computational subjectivity is low hence computation speeds are faster compared to other sophisticated methods like kriging.

5.3 Kriging

Kriging is a stochastic interpolator but similar to IDW in that it also employs weighting to predict unknown values. Just as in IDW, the predicted value is a linear combination of the known weighted samples [81, 82]. Points closer to the prediction point are also assigned more weight compared to those farther apart. However, the weighting used in kriging is more complex and involves spatial correlation between the predicted point and known data points [14]. This spatial correlation and interdependence in kriging is modeled using the semivariogram. The semivariogram is a plot of the semivariances against the separation distances (lag distances) of the known data points. The mathematical relationship that best describes the semivariogram is then used to build covariance matrices necessary for the determination of the kriging weights. The semivariance is a measure of the dissimilarity of a measured variable and is given by the average squared difference between the data values and is given by [14, 81, 84]:

$$\gamma(h) = \frac{1}{2N(h)} \sum_{(i,j|h_{ij}=h)} \left(k_i - k_j\right)^2 \tag{5.5}$$

where $N(h)$ is the number of data values separated by a distance h.There are several empirical sevariogram models that can be used to model the semivariance. They include; spherical semivariogram, exponential semivariogram, cubic semivariogram, Bessel semivariogram, j-Bessel semivariogram and Gaussian semivariogram, among others [81, 83].

The semivariogram is characterized by three main coefficients namely; the range, the sill and the nugget. The range is defined as the maximum lag distance between two points for which the semivariance between them can be determined. This is to say that, if the lag distance between two data values is greater than the range, then the points are not spatially correlated or interdependent. The sill is the value of the semivariance between two data values at the lag distance equal to the range. Ideally, when the lag distance is zero, the semivariance is supposed to be zero also. This is not always the case and at times a non-zero value of the semivariance is obtained when the lag distance is zero, and this value of the semivariance is what is referred to as the nugget effect, or simply the nugget. The nugget is usually an indicator of the interpolation error and can also be attributed to spatial sources of variation at distances smaller than the sampling interval. There are different kriging techniques, namely: ordinary kriging, simple kriging, cokriging, kriging with trend and universal kriging [82].Of these, ordinary kriging is the one used in the current study and is the only one discussed further.

5.3.1 Ordinary Kriging

In ordinary kriging, the mean is assumed constant and unknown in the local neighbourhood of the prediction point. The kriging weights sum to unity and are computed from [81, 84, 85]:

$$w_{ok} = Z_{ok}^{-1} M_{ok} \tag{5.6}$$

where λ_{ok} is the kriging weights vector matrix, Z_{ok}^{-1} is the covariance matrix for the known data points and M_{ok} is the covariance vector matrix between the prediction data point and known data points. The kriging predictor is then given by [81, 85, 86]**:**

$$k_{ok}^{*}(x, y) = \sum_{i=1}^{N} w_{oki} k_{oki}(x_i, y_i) \tag{5.7}$$

where $k_{oki}(x_i, y_i)$ is the data value at point (x_i, y_i), λ_{oki} is the weight associated with it and N is as defined in (5.1). Normally, the weights are determined by minimizing the variance of the interpolation error, otherwise referred to as the estimation error variance, σ_E^2. This is usually achieved by the introduction of a function L which contains the Lagrange parameter, λ given by [82]:

$$L = \sigma_E^2 + 2\lambda\left[1 - \sum_{i=1}^{N} w_{oki}\right] \tag{5.8}$$

The minimization of the estimation error variance is then done by taking the derivative of the above function and then equating it to zero, that is, [74, 82]:

$$\frac{1}{2}\frac{\partial L}{\partial \lambda} = 1 - \sum_{i=1}^{N} w_{oki} = 0 \tag{5.9}$$

Then, the ordinary kriging weights are computed from the following matrix equation [74, 86]:

$$\begin{bmatrix} Z(1,1) & Z(1,2)\cdots Z(1,n) & 1 \\ Z(2,1) & Z(2,2)\cdots Z(2,n) & 1 \\ \vdots & \vdots & \vdots \\ Z(n,1) & Z(n,2)\cdots Z(n,n) & 1 \\ 1 & 1 \quad \ldots \quad 1 & 0 \end{bmatrix} \begin{bmatrix} w_{ok1} \\ w_{ok2} \\ \vdots \\ w_{okn} \\ \lambda \end{bmatrix} = \begin{bmatrix} M(0,1) \\ M(0,2) \\ \vdots \\ M(0,n) \\ 1 \end{bmatrix} \tag{5.10}$$

where Z(i,j) is the covariance between measured locations i and j, $M(0,j)$ is the covariance between the prediction location 0 and measured location j, and w_{oki} is the simple kriging weight for measured location i. The four different kriging semivariogram models shown in Table 5.1 are used in the interpolation of the k-factor for South Africa in this study. In Table 5.1, c is the nugget, S is the sill and h is the value of the lag distance divided by the range.

5.4 Radial Basis Functions (RBFs)

RBFs are real-valued, continuous univariate functions that are radialized by composition with the Euclidian distance as the norm, R^d [87]. Radial basis functions can be thought of as fitting rubber-sheeted surface through measured data values using a mathematical function [88]. Radial basis functions (RBFs) are an efficient way of making predictions when one encounters scattered data problems [89]. Scattered data may not be of much use since one will be interested in knowing or estimating the values where data is not available, for continuity purposes. Interpolation and 1-D derivative approximations are well performed using RBFs especially where the data does not form a regular grid [90]. In [90], Carr, Fright and Beatson emphasize that RBFs do not impose any restrictions on the geometry of the measured data and therefore are very well suited for scattered data. RBFs are also known to produce sufficiently accurate interpolated values from relatively few data points and are able to retain small features of the data geometry as well as spatial distribution [11]. Also, in [91], Franke reports that multiquadrics and thin plate splines produced the best outcome for the interpolation of scattered data. RBFs can interpolate values that fall outside the range of the measured data values. They are also known to be very sensitive to outliers. The most basic form of the RBF interpolant is given by [92]:

$$s(x) = \sum_{k=1}^{n} \lambda_k \phi(\|x - x_k\|) \tag{5.11}$$

where $\|x - x_k\|$ denotes the Euclidian distance, r, and $\phi(r)$ is some RBF, n is the number of RBFs and λ_k is the real-valued weighting coefficient associated with each RBF.

Table 5.1: Semivariogram models used [81, 85]

Model	Model Equation
Cubic	$\gamma(h) = \begin{cases} c + S \cdot (7h^2 - 8.75h^3 + 3.75h^5 - 0.75h^7) & h \le 1 \\ c + S & h \ge 1 \end{cases}$
Gaussian	$\gamma(h) = c + S \cdot \left(1 - exp(h^2)\right)$
Exponential	$\gamma(h) = c + S \cdot \left(1 - exp(-3h)\right)$
Spherical	$\gamma(h) = \begin{cases} c + S \cdot \left(\frac{3}{2}h - \frac{1}{2}h^3\right) & h \le 1 \\ c + S & h \ge 1 \end{cases}$

Thus, RBF methods employ a linear combination of translates for one function $\phi(r)$ of a single variable. In some cases, it is pertinent to add a polynomial of first degree, $P(x)$, that describes the constant as well as the linear portions of RBF interpolant in Equation (5.11), and in turn maintains positive-definiteness and stability of the solution; resulting in the following new expression for the RBF interpolant [93]:

$$S(x) = \sum_{k=1}^{n} \lambda_k \phi(\|x - x_k\|) + P(x) \tag{5.12}$$

Radial basis functions fall in two main categories: the piece-wise smooth and the infinitely smooth. Piece-wise smooth RBFs include powers (linear, cubic and quantic among others) and thin plate splines (TPS). The power RBFs are given by [94]:

$$\phi\,(r) = r^{2n-1}\,, n = 1,2,3,\ldots\ldots \tag{5.13}$$

The TPS is defined by [87, 92]:

$$\phi(r) = r^2 lnr \tag{5.14}$$

Infinitely smooth RBFs include inverse multiquadrics (IQ), multiquadric (MQ) and the Gaussian (GA) and are defined by the following expressions respectively [92, 95]:

$$\phi(r) = \frac{1}{\sqrt{1+(\varepsilon r)^2}} \tag{5.15}$$

$$\phi(r) = \sqrt{1 + (\varepsilon r)^2} \tag{5.16}$$

$$\phi(r) = e^{-(\varepsilon r)^2} \tag{5.17}$$

where ε is the shape parameter.

The TPS and the MQ are the ones used for the interpolation of the k-factor for South Africa and are discussed briefly next. TPSs are inspired by the concept of bending an infinitely thin metal plate. They belong to a class of RBFs commonly referred to as polyharmonic or simply surface splines. Polyharmonic RBFs do not contain a shape parameter. Thin plate splines mathematically realize the idea that, when a metal plate is fixed at certain heights vertical to the plane, it tends towards a form of minimal energy, which is the form of minimal curvature [96]. They are more attractive method since they provide C' continuity and minimize the energy function below [90]:

$$E(s) = \int_{R^2}' \frac{\partial^2 s}{\partial x^2} + 2\left(\frac{\partial^2 s}{\partial x \partial y}\right)^2 + \left(\frac{\partial^2 s}{\partial y^2}\right)^2 dx\, dy \tag{5.18}$$

over all interpolants for which the energy functional is well defined. Thus in this particular sense, the TPS is the smoothest RBF interpolant.

The function f, which minimizes the following factor, below, (5.19), is an example of an exact RBF technique and is specifically referred to as the exact spline method [97, 98]:

$$A(f) + \sum_{i=1}^{n} w_i^2\,[f(x_i) - y(x_i)]^2 \tag{5.19}$$

where $y(x_i) = z(x_i) + \varepsilon(x_i)$ is the source of random error, z is the measured value at point x_i and ε is the random error associated with it. The term $A(f)$ represents the smoothness of the function f and the second term represents the proximity to the measured values. The smoothing function $A(f)$ determines the level of smoothness with respect to the accuracy of the interpolation. When the function is taken to zero, one performs interpolation but without any smoothing. Alternatively, pushing the value of the function to infinity results in least square fit of the data. Thus, it is important that one maintains a good smoothing trade-off for optimal interpolation. One of the best ways to achieve this is by performing generalized cross validation [84], and this is the approach adopted for this study. Cross validation statistics are the ones used for the error computations. Cross validation involves the removal of one data point at a time and then interpolating its value. This is done in turns for all data points and then the overall error statistics are calculated.

The MQ, on the other hand, is popular for many applications and has some good approximation and interpolation properties. It represents a class of RBFs that are global in nature, containing a shape parameter and are infinitely differentiable [95, 98]. The MQ can also be optimized by performing cross validation and this is the technique used here.

The RMSE and MAE are used to compare the performance of the different interpolation methods used. These errors are given by [14, 85, 98]:

$$RMSE = \sqrt{\left(\frac{1}{N}\sum_{i=1}^{N}(k^* - k)^2\right)} \tag{5.20}$$

$$MAE = \frac{1}{N}\sum_{i=1}^{N}|k^* - k| \tag{5.21}$$

where k^* is the measured value and k is the cross value.

5.5 Methodology

The measured k-factor values obtained in Tables 4.7, 4.8, 4.12 and 4.13 are interpolated to cover the rest of South Africa using both MATLAB and PAST open source statistical package. PAST is an open source statistical package distributed under GNU/GPL licence. The following steps are used:

1. The seasonal and annual median and effective k-factor values are entered into a grid together with the location's coordinates; the longitude and the latitude.
2. For the case of kriging interpolation, the semivariogram model is then chosen. For RBF, the particular choice of the RBF is done. Else the method chosen is the IDW.
3. The values are then interpolated to cover the rest of the country between the coordinates; latitude (15^o S, 35^o S) and longitude (22^o E, 35.2^o E) using PAST.
4. Cross validation of the interpolation statistics is then performed and then the associated RMSE and MAE errors computed.

5. This process is repeated for the four semivariogram models in Table 5.1, the TPS and MQ RBFs, and for IDW where the minimum error criteria are used as the optimal value power parameter.
6. The interpolated values for the method that produces the least error (best interpolation method) are then copied and saved in either Microsoft Excel or notepad files.
7. The latitude, longitude and the k-factor matrices are then exported to MATLAB.
8. An appropriate MATLAB code is then written for the mapping of the k-factor and used to develop the contour maps of the seasonal and annual k-factor for South Africa.

5.6 Interpolation Results and Discussion

The interpolation errors are tabulated in Tables 5.2-5.5. Table 5.2 shows the seasonal median k-factor interpolation errors. From this table, we see that for the months of February, August and November, the Gaussian semivariogram model produces the worst error performance while IDW produces the least error. For the month of May, IDW produces the least RMSE error while the cubic semivariogram model produces the least MAE error. Table 5.3 shows the annual median k-factor interpolation errors. From this table, we see that IDW method produces the least RMSE and MAE errors while the Gaussian semivariogram model produces the largest interpolation errors. Table 5.4 shows the annual effective k-factor interpolation errors. From this table, IDW produces the least errors while Gaussian semivariogram model produces the largest RMSE error and TPS produces the largest MAE error. Table 5.5 shows the seasonal effective k-factor interpolation errors. From this table, we see that IDW performs best in terms of the two error criteria used for the months of February, May and November. For the month of August, the best RMSE performance is produced by IDW while the best MAE is produced by the Gaussian semivariogram model. Also, from the same table, the Gaussian semivariogram model posts the largest errors for the months of February and May while for August the largest errors are produced by the MQ. For November, the TPS produces the largest RMSE errors while the MQ produces the largest MAE.

Thus, overall, we note that the IDW method posts the best error performance in terms of either the RMSE or the MAE or both. The error performance variations can be attributed to differences in k-factor values for both seasonal and annual cases as well as median and effective values as well. Also the errors variations are subject to the different parameters in each individual interpolation function as well as the spatial distribution of the data. It is worthy to note there is always no preferred interpolation method over another and that is why the two different measures of fit are used to determine the best method in different application scenarios. In our case, the IDW comes out as the best method (in terms of error) and is the one chosen for the mapping of the k-factor. The strong IDW error performance could be attributed to the fact that all its interpolated values fall within the range of the measured values. All the other methods used can interpolate values outside the range of the measured data. The dismal performance exhibited by the RBFs could be attributed to the fact that they do well with gently varying data and this is not the case with the values measured. Figures 5.1-5.5 show the contour maps for the annual and seasonal median k-factor. Figures 5.6-5.10 show the contour maps for the annual and seasonal effective k-factor.

Table 5.2: Seasonal median k-factor interpolation errors

	Errors	Kriging semivariogram models				Radial Basis Functions		Inverse Distance weighting
		Spherical	Exponential	Gaussian	Cubic	TPS	MQ	
Feb	RMSE	0.064	0.065	0.205	0.096	0.099	0.090	0.046
	MAE	0.059	0.060	0.174	0.081	0.091	0.081	0.037
May	RMSE	0.038	0.042	0.080	0.038	0.054	0.065	0.034
	MAE	0.030	0.033	0.055	0.029	0.038	0.049	0.031
Aug	RMSE	0.037	0.040	0.091	0.049	0.056	0.061	0.033
	MAE	0.039	0.036	0.074	0.043	0.050	0.051	0.029
Nov	RMSE	0.056	0.055	0.204	0.088	0.088	0.076	0.040
	MAE	0.051	0.052	0.177	0.074	0.078	0.70	0.032

Table 5.3: Annual median k-factor interpolation errors

Errors	Kriging semivariogram models				Radial basis functions		Inverse distance weighting
	Cubic	Exponential	Spherical	Gaussian	TPS	MQ	
RMSE	0.071	0.053	0.052	0.134	0.076	0.078	0.042
MAE	0.061	0.049	0.047	0.110	0.069	0.068	0.033

Table 5.4: Annual effective k-factor interpolation errors

Errors	Kriging semivariogram models				Radial basis functions		Inverse distance weighting
	Cubic	Exponential	Spherical	Gaussian	TPS	MQ	
MAE	0.126	0.086	0.088	0.023	0.126	0.112	0.057
RMSE	0.146	0.101	0.105	0.285	0.159	0.134	0.066

Table 5.5: Seasonal effective k-factor interpolation errors

	Errors	Kriging semivariogram models				Radial Basis Functions		Inverse Distance weighting
		Spherical	Exponential	Gaussian	Cubic	TPS	MQ	
Feb	RMSE	0.106	0.102	0.402	0.169	0.176	0.138	0.067
	MAE	0.086	0.085	0.355	0.157	0.147	0.114	0.046
May	RMSE	0.134	0.129	0.447	0.20	0.218	0.179	0.080
	MAE	0.110	0.105	0.392	0.181	0.173	0.142	0.062
Aug	RMSE	0.058	0.063	0.056	0.052	0.105	0.107	0.044
	MAE	0.042	0.046	0.030	0.038	0.068	0.075	0.036
Nov	RMSE	0.060	0.065	0.094	0.058	0.106	0.106	0.048
	MAE	0.050	0.055	0.075	0.047	0.076	0.081	0.045

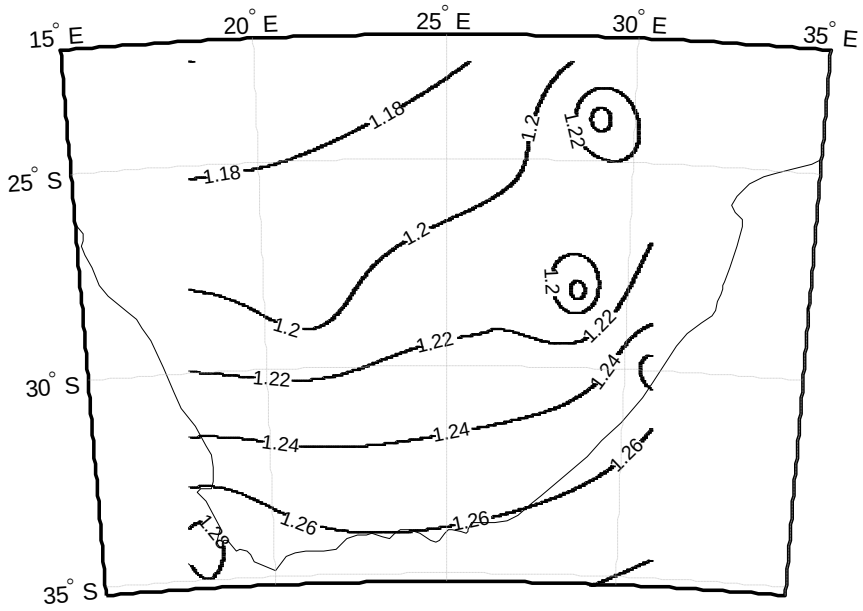

Figure 5.1: Three-year annual median k-factor contours for South Africa

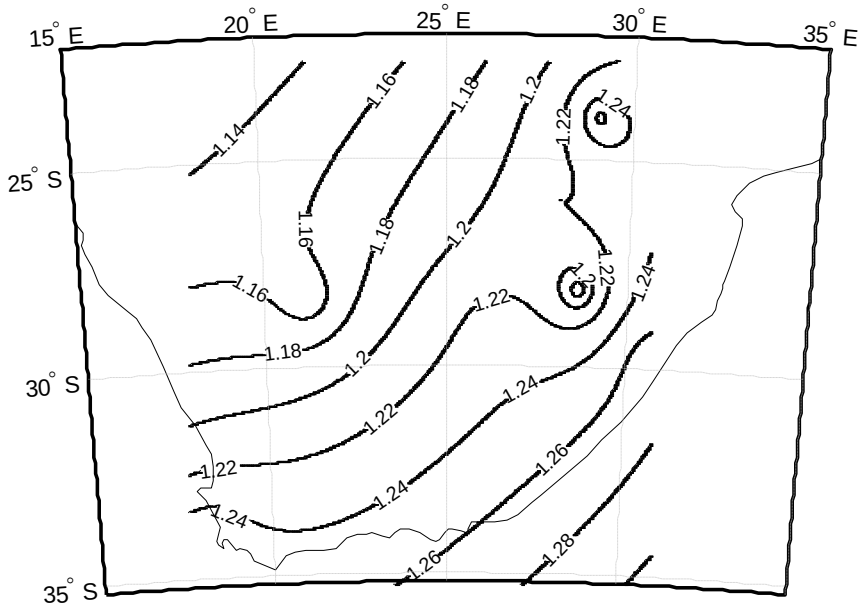

Figure 5.2: Three-year seasonal median k-factor contours for South Africa for the month of February

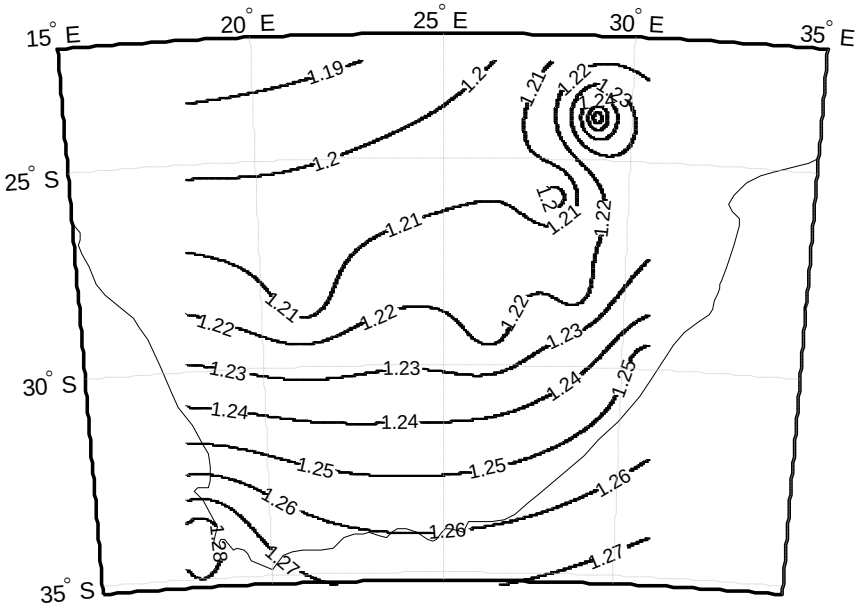

Figure 5.3: Three-year seasonal median k-factor contours for South Africa for the month of May

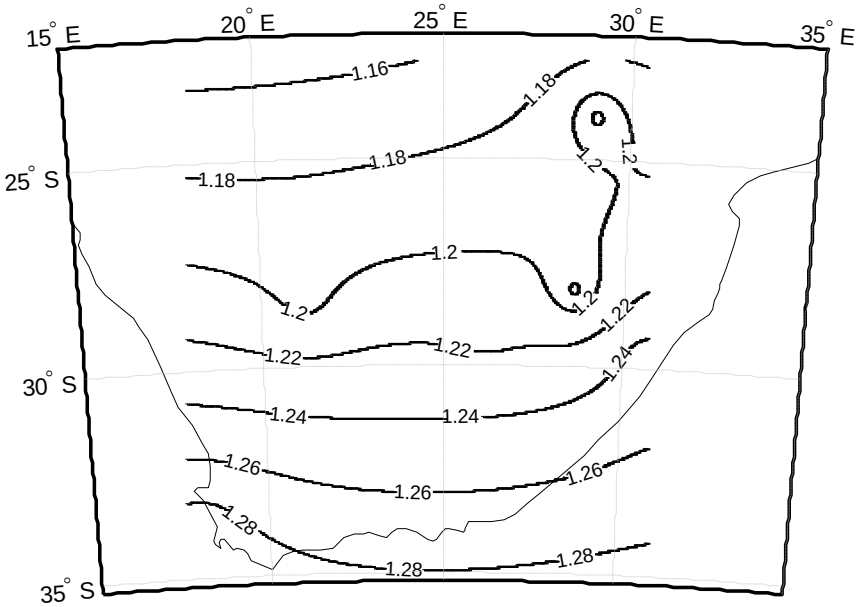

Figure 5.4: Three-year seasonal median k-factor contours for South Africa for the month of August

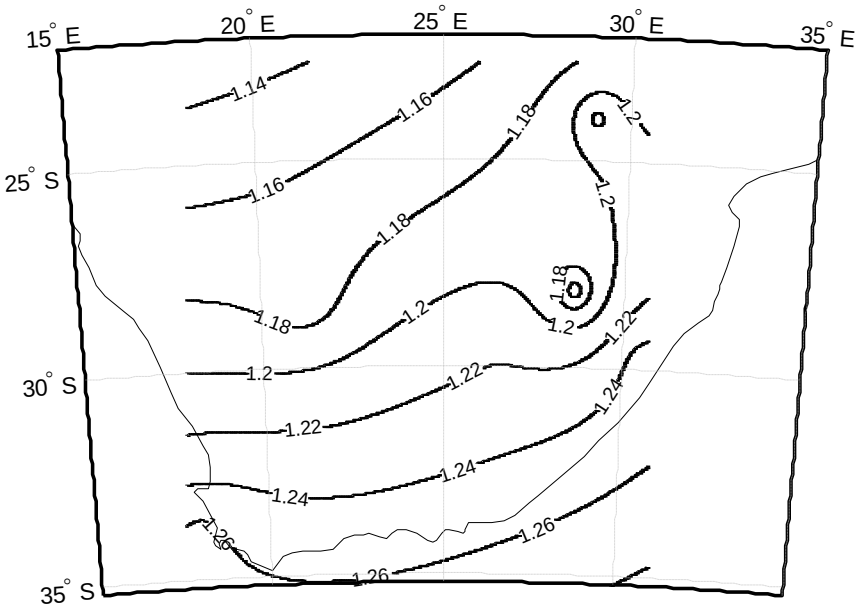

Figure 5.5: Three-year seasonal median k-factor contours for South Africa for the month of November

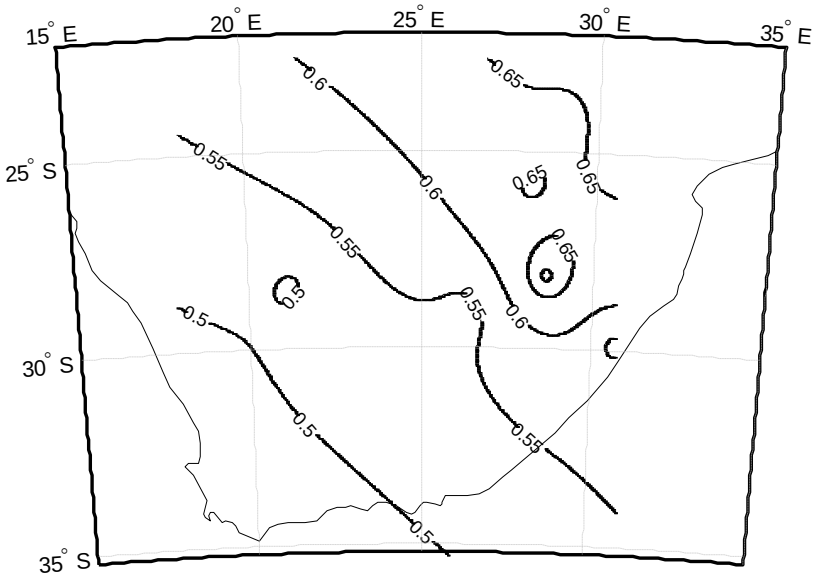

Figure 5.6: Three-year annual effective k-factor contours for South Africa

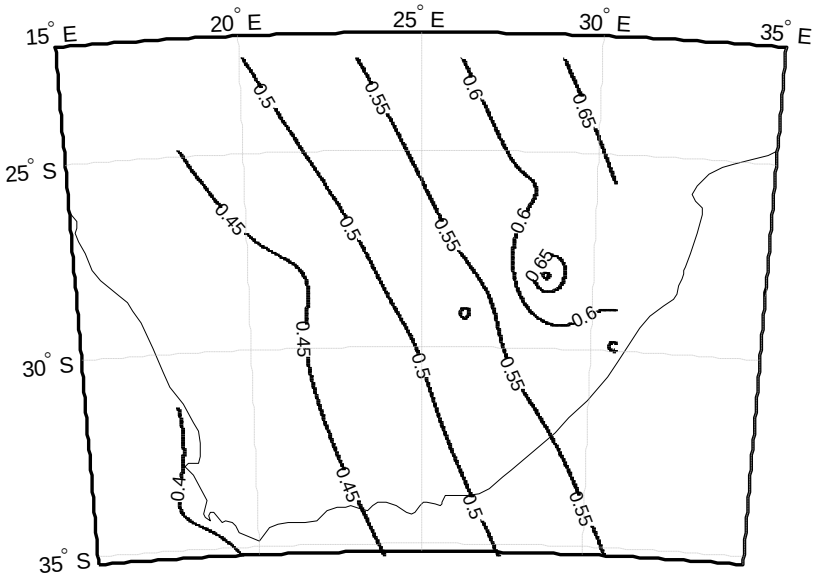

Figure 5.7: Three-year seasonal effective k-factor contours for South Africa for the month of February

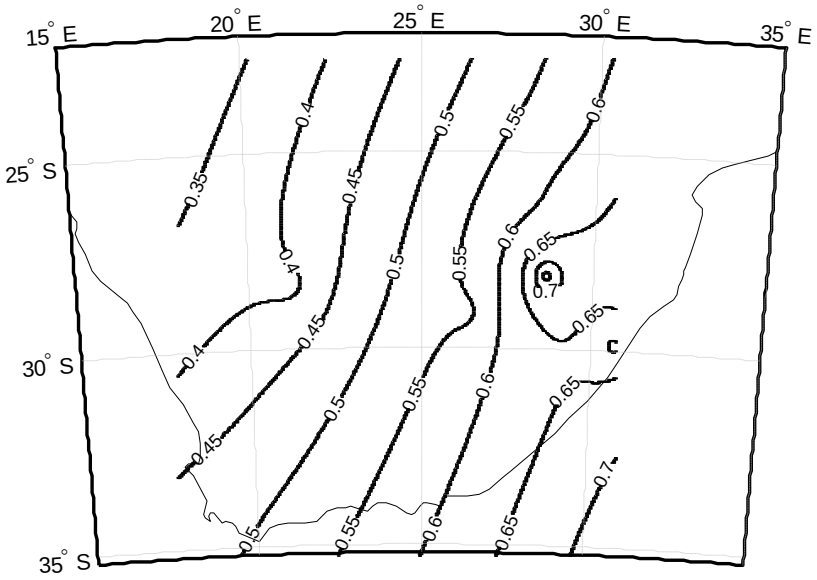

Figure 5.8: Three-year seasonal effective k-factor contours for South Africa for the month of May

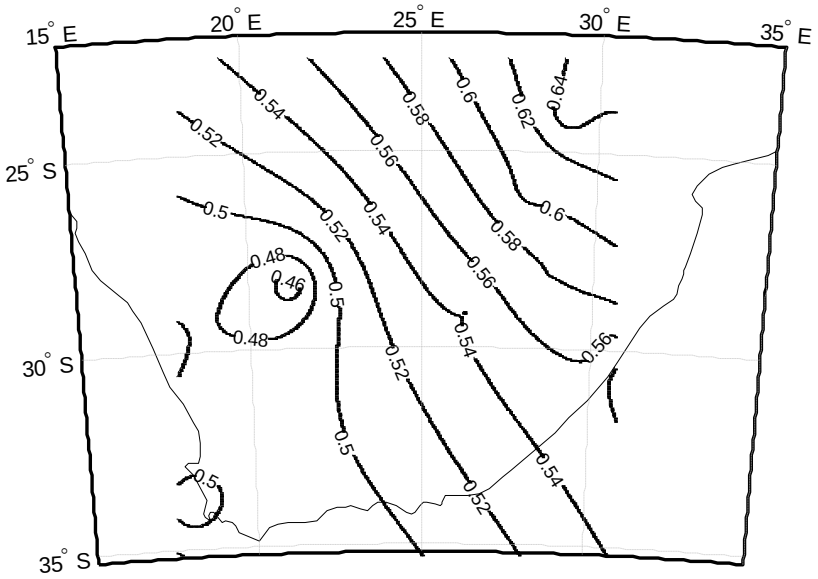

Figure 5.9: Three-year seasonal effective k-factor contours for South Africa for the month of August

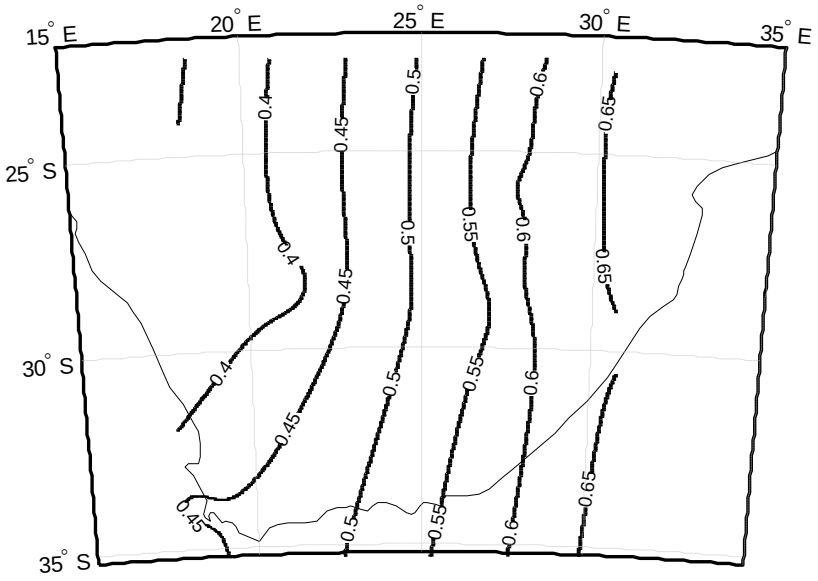

Figure 5.10: Three-year seasonal effective k-factor contours for South Africa for the month of November

5.7 Chapter Summary

In this chapter, three spatial interpolation methods with seven different interpolation options have been considered in an effort to extend discrete k-factor values measured at seven locations in South Africa to cover the rest of the country. In order to determine which method best fits the k-factor values measured, two error criteria have been used to identify the most appropriate method. The performance of any spatial interpolation method is driven by the geometrical distribution of the data, the variation between the maximum and minimum values as well as the interpolation function used and the parameters that control the interpolation. The IDW method has been used to generate the contour maps of the k-factor for South Africa owing to its strong error performance as compared to all the other six options considered. Overall, the median k-factor contours show a decreasing trend of the k-factor as we move from the coastal regions towards the semi-arid regions in the northern and north-western parts of South Africa. Also, the effective k-factor contours show a decreasing trend of the k-factor as we move from east to west. The decreasing trend of the k-factor is consistent with the values obtained by Afullo and Odedina for Maun, Botswana [20]. This would mean that, moving further north towards Botswana, the k-factor values would diminish and a value close to the one obtained in their earlier reports would be obtained. All the interpolated values lie between the respective maximum and the values of the k-factor observed and, thus, the theory of the "edge effect" associated with IDW interpolation has been proven.

Chapter 6

Conclusion

6.1 Concluding Remarks

The performance of terrestrial microwave links is affected by both clear-air and precipitation conditions. In precipitation conditions, rain attenuation is the biggest source of signal distortion while in clear-air conditions it is mainly multipath and diffraction effects. Multipath and diffraction fading effects are mainly dependent on the refractive conditions of the atmosphere. Extreme refractivity gradients are responsible for these clear-air effects. For example, under extremely positive values of the refractivity gradients, which translate to low values of the k-factor, the signal is bent so severely downwards that the earth bulge obstructs the radio path. Again, under extreme negative values of the refractivity gradient, which in turn translates to negative values of the k-factor, the signal is bent rapidly upwards. Under these conditions, there is the possibility that the radio wave is trapped between two layers and can be guided over very long distances resulting in anomalous propagation (ducting). Ducting conditions are responsible for long range transmission which then means that the radio signal energy overshoots the receiver. The refractive properties of the atmosphere are determined by the temperature, pressure and humidity variations. These three atmospheric parameters vary geographically, seasonally and with height above the ground level. Thus the modeling of these parameters is strictly region based. This calls for local determination of the trends in their variations. These three parameters can be measured using radiosondes, meteorological sensors or tethered balloon systems, from which the radio refractivity is then determined. Else, the radio refractivity can be measured directly using a refractometer. The k-factor is one of the ways in which one is able to define the refractive conditions of the atmosphere. Thus, the knowledge of its variations is critical in the determination of how electromagnetic waves are bent as they traverse the atmosphere. The k-factor is used in the determination of the appropriate antenna heights in terrestrial LOS links, as per the procedures outlined in ITU-R Recommendation P.530-14.

Radiosonde data obtained for seven locations in South Africa has been used for the processing of k-factor statistics. These k-factor statistics have been studied on an annual and seasonal basis. From these k-factor statistics, at a cut-off height of 200 m above ground level for each location, both curve fitting and kernel models have been determined. The ISE error criterion has been used to optimize the models obtained in both cases. The kernel models are seen to produce better error performance as compared to curve fitting models. This is attributed to the optimized choice of the smoothing parameter which then means that the model follows the measured probability density plot as much as possible, while still providing smoothing. Curve fitting models are rigid, with fixed parameters defining them, and this explains their poor error performance compared to kernel models which are modeled directly from the data. However, they are usually smoother and easier to interpret as compared to kernel models. For the four kernel models used, the Rectangular kernel posts the best error performance and is therefore the preferred method for the non-parametric modeling of the k-factor for South Africa. From both the curve fitting and kernel models and the measured data scatter plot, we conclude that the distribution of the k-factor is bell-shaped, centered almost symmetrically around the median value. From these models and measurements, both effective and median values of the k-factor have been determined. Comparisons of the obtained values have also been drawn.

From these results, we conclude that the annual median k-factor varies from location to location, with the highest value being found in the coastal Cape Town (1.29) and the lowest value in inland Bethlehem (1.17) and Upington (1.17). The annual effective k-factor varies from 0.50 (Upington) to 0.77 (Bethlehem). The seasonal k-factor is seen to vary in a random manner from location to location. For Bloemfontein, the seasonal median k-factor varies from 1.20 (May) to 1.25(November). For Cape Town, the same varies from 1.23 (February) to 1.29 (May and August). For Durban, the same varies from 1.24 (November) to 1.29 (February). For Polokwane, the same varies from 1.21 (August and November) to 1.26 (May). For Pretoria, the same varies from 1.17 (August) to 1.21 (February and November). For Upington, the same varies from 1.13 (February) to 1.21 (May). Lastly, for Bethlehem, the same varies from 1.15 (November) to 1.21 (May). The seasonal effective k-factor also varies randomly from location to location. For Bloemfontein, the seasonal effective k-factor varies from 0.46 (November) to 0.55 (May). For Cape Town, the same varies from 0.44 (February and November) to 51 (May and August). For Durban, the same varies from 0.54 (August) to 0.65 (November). For Polokwane, the same varies from 0.55 (May) to 0.71 (August). For Pretoria, the same varies from 0.57 (May) to 0.66 (August). For Upington, the same varies from 0.38 (November) to 0.49 (August). Lastly, for Bethlehem, the same varies from 0.54 (August) to 0.86 (May). The median k-factor for standard temperate climate is 1.33 while the effective value is 0.67. Thus, we conclude that at height of 200 m above ground level, the median k-factor values obtained are lower than those of the standard temperate climate, which is not a common climate type in South Africa, especially in the regions studied. The same is true for the effective k-factor for most of the locations both annually and seasonally. Annually, higher values are only found in Pretoria and Bethlehem. Seasonally, higher values are obtained in Polokwane (February and August) and Bethlehem (February, May and November).

The annual and seasonal values obtained in this study are slightly higher than those obtained by Odedina and Afullo [20] for Durban. This can be attributed to the fact that the height range considered was different (0-500m above ground level). This is so because the k-factor diminishes with height as the height above ground level increases. The fact that the amount of data used may not have been sufficient (eight months data) could also explain the slight difference in the values. Again, the values are much lower than those obtained by Palmer and Baker [64] for Cape Town, Durban, Upington and Pretoria. This could be attributed to the difference in the height above ground level that was considered, since their values were evaluated using ground observations.

The values obtained in the seven locations present scattered data. These scattered k-factor data has been extended to cover the rest of South Africa by use of spatial interpolation methods. Three spatial interpolation techniques namely, inverse distance weighting, kriging and radial basis functions have been applied. In the kriging method, four semivariogram models have been used. For the radial basis functions, both the multiquadrics and the thin plate splines have been used. The root mean square error and the mean absolute error have been used to determine the best method for the interpolation and mapping of the k-factor for South Africa. From the error analysis, the IDW method is seen to be the best. This can be attributed to the fact that IDW does not interpolate values outside the range of the measure values. Also, the geometrical arrangement as well as the way the values vary for one point to the other could be other driving factors behind the impressive error performance. However, this does not mean that the IDW is the best method always. The suitability of different interpolation techniques for any particular application is based on some measure of fit, and therefore the choice

varies on case by case basis. Therefore the IDW is optimal here only in terms of the measures of fit used. The contour maps show a decreasing trend of the median k-factor as we move towards the semi-arid northern parts of South Africa, which points to even lower values of the k-factor as we go into arid Botswana; if the contour maps are extended, where a value 1.1 for the median k-factor was obtained by Afullo and Odedina for Maun [20].

6.2 Recommendations for Future Work

More data measurements covering more locations in South Africa should be done. A refractometer should be used to measure the refractivity statistics since it's more accurate. Also, direct link measurements should be done to determine how the k-factor values obtained in this study impact diffraction fading in the regions where the values have been determined. Other interpolation methods should be explored to ascertain the accuracy of the predictions made in this study. A universal model based on geographic or climatic variation should also be sought after.

References

[1] M.R. Mahmud and Z.S Khan, "Analysis and planning microwave link to establish efficient wireless communications," MSc. Thesis, Blekinge Institute of Technology, September 2009.

[2] J.S. Seybold, *Introduction to RF propagation,* WILEY-INTERSCIENCE: John Wiley & Sons Inc., New York, 2005.

[3] R. L. Freeman, *Radio system design for telecommunications,* Third Edition, WILEY-INTERSCIENCE: John Wiley & Sons Inc., New York, 2007.

[4] ITU-R, "Propagation data and prediction methods required for the design of terrestrial Line-of-Sight Systems," ITU-R Recommendation P.530-14.

[5] A.R. Webster and T.S Meritt, "Multipath angles-of-arrival on a terrestrial microwave link," *IEEE Transactions on Communications,* vol. 38, No. 1, pp. 25-30 January 1990.

[6] A.T. Adediji and M.O Ajewole, "Vertical profile of the radio refractivity gradient in Akure, South-West Nigeria", *Progress in Electromagnetics Research C,* vol. 4, pp. 157-168, 2008.

[7] ITU-R, "The Radio Refractive Index: Its formula and refractivity data", ITU-R Recommendation P.453-10.

[8] R.L. Olsen, "Radioclimatological modeling of propagation effects in clear-air and precipitation conditions: Recent advances and future directions," *Proceedings of the Third Regional Workshop on Radiocommunications in Africa,* Gaborone, Botswana, pp. 81-83, October 1999.

[9] C.S. Yang, S.P Kao, F.B Lee and P.S Hung, "Twelve different interpolation methods: A case study of Surfer 8.0," *Proceedings of the XXth ISPRS*, paper No. 231, 2004.

[10] J. Li and A.D. Heap, "A review of spatial interpolation methods for environmental scientists," *Geoscience*, Record 2008/23, Australia, 2008.

[11] M. Azpurua and K. Ramos, "A comparison of spatial interpolation methods for estimation of average electromagnetic field magnitude," *Progress in Electromagnetics Research M*, vol. 14, pp. 135-145, 2010.

[12] P.K. Odedina and T.J. Afullo "Use of spatial interpolation technique for the determination of the geoclimatic factor and fade calculation for South Africa," *Proceedings of IEEE Africon Conference*, Namibia, pp. 1-6, September 26-28, 2007.

[13] C.A. Schloeder, N.E. Zimmerman and M.J. Jacobs, "Comparison of methods for interpolating soil properties using limited data," *Soil Science Society of America Journal,* vol. 65, pp. 470-479, 2001.

[14] J. Bello-Pineda and J.L. Hernandez-Stefanoni, "Comparing the performance of two interpolation methods for creating a digital bathymetric model of the Yucatan submerged

platform," Pan-American *Journal of Applied Aquatic Sciences*, vol. 2, No. 3, pp. 247-254, 2007.

[15] G.O. Ajayi, Physics of Tropospheric radio propagation, ICTP Internal Report No. IC/89/23, Miramare, Trieste, February 1989.

[16] T.G. Hayton, S.L Lystad, A.K. Marsh and K.H Craig, "Characterization of clear-air parameters derived from high resolution radiosondes," *Proceedings of the URSI Commission F Open Symposium on Climatic Parameters in Radiowave propagation Prediction*, Ottawa, Canada, pp. 1-8, April 1998.

[17] J.W. Nel, S.J. Erasmus and S. Mare, "The establishment of a radio refractivity database for Southern Africa," COMSIG 88, Pretoria, *IEEE* catalogue Number TH0219-6/88/0000-0144, pp. 144-147.

[18] P.K. Odedina, "Effective earth radius factor (k-factor) distribution for Southern Africa", *Masters Dissertation in Electrical Engineering in Telecommunications and Information Technology*, 2005.

[19] E.S. Falodun and L.B. Kolawale, "Studies of super-refractivity and ducting of radio waves in Nigeria," *Nigerian Journal of Pure and Applied Physics*, vol. 1, pp. 5-10, 2000.

[20] T.J. Afullo and P.K Odedina, "On the k-factor distribution and diffraction fading for Southern Africa," *SAIEE Africa Research Journal*, vol. 97(2), pp. 172-181, 2006.

[21] A.T. Adediji and M.O. Ajewole, "Vertical profile of the radio refractivity gradient in Akure, South-West Nigeria," *Progress in Electromagnetics Research C*, vol. 4, pp. 157-168, 2008.

[22] J. Ong and S. Ong, "Refractivity gradient statistics for Singapore over 7 years," *Proceedings of ISAP2000*, Fukuoka, Japan, pp. 1-4, 2000.

[23] A.J Palmer and D.C Baker, "A Novel Semi-Empirical Model of the effective earth radius factor," *IEEE Transactions on Broadcasting*, vol.52, No.4, pp. 557-565, December 2006.

[24] A.J Palmer and D.C Baker, "A proposed empirical Model of the effective earth radius factor for telecommunications use in South Africa," *IEEE Africon Proceedings*, pp. 511-516, 2002.

[25] T. Manning, *Microwave Radio Transmission Design Guide*. Second Edition, Artech House, Boston, London, 2009.

[26] T.W Manning, "Design of terrestrial microwave radio links," *IEEE Africon Proceedings*, pp. 564-569, 1996.

[27] L. Moreno, *Point-to-point radio link engineering: A self-learning e-book based course*. Radio Engineering Services, 2001-2010, Torino, Italy.

[28] P.K. Odedina, "Effective earth radius factor (the k-factor) distribution for Southern Africa," MSc. Thesis, University of KwaZulu-Natal, 2005.

[29] K. Naicker and S.H. Mneney, "Propagation measurements and multipath channel modeling for line-of-sight links at 19.5 GHz," *SAIEE African Research Journal*, vol. 97(2), pp.162-171, 2006.

[30] R.L Freeman, *Telecommunication system engineering*, Fourth Edition, John Wiley and Sons Inc., Hoboken, New Jersey, 2004.

[31] M.F Young, Planning a microwave link, YDI Wireless, 8000 Lee Highway, Falls Church, VA 22042, 703-205-0600, 2008.

[32] SAF, An introduction to microwave radio link design, SAF Tehnika A/S 2002.

[33] U. Kesavan, A.R Tharek, M.R Islam, "Comparison of microwave path lengths between temperate and tropical region based on effects of rain," *Progress in Electromagnetics Research Symposium Proceedings*, Moscow, Russia, pp. 504-507, August 19-23, 2012.

[34] P. Angueira and J. Romo, *Microwave Line of sight link Engineering*, John Wiley & Sons, August 2012.

[35] ITU-R, World Radiocommunication Conference: Resolutions and Recommendations, Geneva, Switzerland, 2012.

[36] http://www.itu.int/ITU-R/index.asp?category=conferences&rlink=rrb&lang=en. Web page last accessed on 21st May 2013.

[37] ITU-R, "Radio-frequency arrangements for fixed service systems," ITU-R Recommendation F.746-10, 2012.

[38] ITU-R, "Radio-frequency channel arrangements for fixed wireless systems operating in the 10.7-11.7 GHz band," ITU-R Recommendation F.387-12, 2012.

[39] D. M. Pozar, *Microwave Engineering*, Third Edition, University of Massachusetts at Amherst, John Wiley and Sons Inc., 2005.

[40] R.N Pupala, Introduction to Wireless Electromagnetic Channels and Large Scale Fading, Department of Electrical Engineering, Rutgers University, Piscataway, NJ 08854, 2005.

[41] P. Barsocchi, Channel Models for Terrestrial Wireless Communications: A Survey, National Research Council-ISTI Institute, 2006.

[42] B. Sklar, *Digital Communications: Fundamental and Applications*, Second Edition, Prentice-Hall, Englewood Cliffs, NJ, 2001.

[43] T.S. Rappaport, *Wireless Communications*, Prentice-Hall, Second Edition, Upper Saddle River, New Jersey, 2002.

[44] P.K. Odedina and T.J. Afullo, "Estimation of secondary radioclimatic variables and its application to terrestrial LOS link design in South Africa," *Southern Africa Telecommunication Networks and Applications Conference Proceedings*, 2008.

[45] B. H. Walke, *Mobile Radio Networks: Networking and Protocols*, Second Edition, John Wiley and Sons Ltd, 1999.

[46] R.E Collin, *Foundations for Microwave Engineering*, Second Edition, John Wiley and Sons, Inc., 2001.

[47] M. Younis and L. Zwirello, Advanced Radio Communication: Radio Wave Propagation Fundamentals, 2012.

[48] A.F Molisch, *Wireless Communications*, Second Edition, John Wiley and Sons Ltd, 2011.

[49] C. Haslett, *Essentials of Radio Wave Propagation: The Cambridge Wireless Essentials Series*, Cambridge University Press, New York, 2008.

[50] Naval Shore Electronics, Line-Of-Sight microwave and tropospheric scatter communication systems, NAVELEX 0101,112, U.S Department of the Navy, Washington D.C, 1972.

[51] J.D. Parsons, *The Mobile Radio Propagation Channel*, Second Edition, John Wiley and Sons Ltd, 2000.

[52] ITU-R, "Propagation by diffraction," ITU-R Recommendation P.526-12, 2012.

[53] R. Deepa, R. Baskaran, P. Unnikrishnan and A. Kumar, "A study of spatial diversity schemes in multiple antenna systems," *Journal of Theoretical and Applied Information Technology*, vol. 5 No. 5, pp. 619-624, 2009.

[54] B.L. Agba, O. Ben-Sik-Ali, R. Morin and G. Bergeron, "Recent evolution of ITU method for prediction of multipath in terrestrial microwave links," *Progress in Electromagnetics Research Symposium Proceedings*, Marrakesh, Morocco, pp. 1375-1380, , March 20-23, 2011.

[55] P.K. Odedina and T.J.O Afullo, "Multipath propagation modeling and measurement in clear-air environment for LOS link design application," *Southern Africa Telecommunication Networks and Applications Conference Proceedings*, 2009.

[56] T.J Afullo,T. Motsoela and D.F Molotsi, "Refractivity gradient and k-factor in Botswana," *Proceedings of the Third Regional Workshop on Radio Africa*, Gaborone, Botswana, October 25-29 1999, pp. 107-110.

[57] S.M. Babin, "A case study of subrefractive conditions at Wallops Island, Virginia," *Journal of Applied Meteorology*, vol. 34, pp. 1028-1038, 1995.

[58] Cost 255 Final Report, "Radiowave propagation modelling for Satcom services at Ku-Band and above", European Space Agency, SP-125*2*, March 2002.

[59] B.R. Bean and G.D. Thayer, "Models of the atmospheric radio refractive index," *Proceedings of the IRE*, pp. 740-755, May 1959.

[60] N.K. Chaudhary, D.K. Trivedi and R. Gupta, "The impact of k-factor on the wireless link in Indian semi-desert terrain," *International Journal Advanced Networking and Applications*, vol. 2, Issue 04, pp. 776-779, 2011.

[61] M. Grabner and V. Kvicera, "Refractive index measurements in the lowest troposphere in the Czech republic," *Journal of Atmospheric and Solar-Terrestrial Physics*, vol. 68, pp.1334-1339, 2006.

[62] D. Serdega and G. Ivanovs, "Refraction seasonal variation and that influence on to GHz range microwaves availability," *Electronics and Electrical Engineering*, vol. 6, No. 78, pp. 39-42, 2007.

[63] D. Rezacova, O. Fiser and L.R. Saez, "Statistics of radio refractivity derived from Prague radiosounding data," *Radioengineering*, vol. 12, No. 4, December 2003.

[64] A.J. Palmer and D.C Baker, "Predicting the long-term average of the effective earth radius factor for South Africa using ground based observations," *SAIEE Africa Research Journal*, vol. 97, No. 2, pp. 182-185, June 2006.

[65] B.G Ayantunji, P.N Okeke, J.O Urama and Y. Najib, "A semi-empirical model for extrapolation of surface refractivity over Nigeria," *African Review of Physics*, vol. 6, No. 14, pp. 121-128, 2011.

[66] K. Al-Ansari, A.A. Al-Mal and R. Kamel, "Statistical analysis of refractivity in the UAE," *International Symposium on Rainfall Rate and Radio Wave Propagation*, pp. 232-247, 2007.

[67] S.C. Majumdar, "Tropospheric radio refractivity over India," *The Radio and Electronic Engineer*, vol. 38, No.2, pp. 99-108, 1969.

[68] H.N Kheirallah and M.R.M Rizk, "Refractivity statistics for two countries in the Middle East," *Engineering Journal of Qatar University*, vol.2, pp. 333-349, 1989.

[69] S.D Gunashekar, D.R Siddle and E.M Warrington "The Effect of tropospheric weather conditions on VHF and UHF radio paths over the sea," *Resonance*, pp. 51-62, January 2006.

[70] H.T Dougherty and E.J Dutton, The role of elevated ducting for radio service and interference fields, NTIA Report No. 81-69, 1981.

[71] P. Valtr, P. Pechac, V. Kvicera and M. Grabner, "Estimation of the refractivity structure of the lower troposphere from measurements on a terrestrial multiple-receiver radio link," *IEEE Transactions on Antennas and Propagation*, vol.59, No. 5 , pp. 1707-1715, May 2011.

[72] J.F. Ferrari, "Refractive conditions of Amazon environment and its effects on ground and airborne radar and ESM systems," Thesis, Naval Postgraduate School, September 2003.

[73] A. Abu-Almal and K. Al-Ansari, "Calculation of effective earth radius and point refractivity gradient for UAE," *International Journal of Antennas and Propagation*, vol. 2010, Article ID 245070, pp. 1-4, May 2010.

[74] Fulgence D., "Effective earth radius distribution for Central Africa: Rwanda and north-western Tanzania," MSc. Thesis, National University of Rwanda, August 2012.

[75] T. Hoskin, Parametric and non-parametric: demystifying the terms, Mayo Clinic CTSA BERD Resource.

[76] T.J Afullo and P.K Odedina, "Effective earth radius factor characterization for line of sight paths in Botswana," *IEEE Africon Proceedings*, pp. 227-232, 2004.

[77] A.M. Nyete and T.J.O Afullo, "Non-parametric and parametric modelling and characterization of the effective earth radius factor for South Africa," *Progress in Electromagnetics Research Symposium Proceedings*, Taipei, Taiwan, pp. 653-659, March 25-28, 2013.

[78] S. J. Sheather, "Density estimation," *Statistical Science*, vol.19, No. 4, pp. 588-597, 2004.

[79] W. Zucchini, Applied smoothing techniques, part 1: kernel density estimation, October 2003.

[80] D. F. Froehlich and M. Rahman, "A note on the choice of the smoothing parameter in the kernel density estimate,'' *BRAC University Journal*, vol. VI, No.1, pp. 59-68, 2009.

[81] A.M. Nyete and T.J.O Afullo, "Seasonal distribution modelling and mapping of the effective earth radius factor for microwave link design in South Africa," *Progress in Electromagnetics Research B,* vol. 51, 1-32, 2013.

[82] G. Bohling, Kriging, Kansas Geological Survey, C&PE 940 Report, 19th October 2005.

[83] K. Johnston, J.M. Hoef, K. Krivoruchko and N. Lucas, Using ArcGIS Geostatistical Analyst, GIS by ESRI, USA, 2001.

[84] Boer E.P.J, K.M de Beurs and A.W Hartkamp, "Kriging and thin plate splines for mapping climatic variables," *JAG*. vol. 3, No. 2, pp. 146-154, 2001.

[85] A.M Nyete and T.J.O Afullo, "Interpolation and mapping of the median k-factor for terrestrial link applications in South Africa," *IEEE AFRICON2013 Proceedings*, 9-12 September 2013, Mauritius, pp. 208-211.

[86] N. E. LeMay, Jr., "Variogram modeling and estimation," MSc. Thesis in Applied Mathematics, University of Colorado, 1995.

[87] S.A Sarra, "Integrated multiquadric radial basis function approximation methods," *Computers and Mathematics with Applications* 0 (2006), 1-0 Elsevier Science Ltd.

[88] S. Anderson, "An evaluation of spatial interpolation methods on air temperature in Phoenix, AZ," *Tempe, AZ 85287-0104*, Department of Geography, Arizona State University.

[89] J.B Cherrie, R.K Beatson and G.N Newsam, "Fast evaluation of radial basis function: Methods for generalized multiquadrics in R^n," *AMS* subject classifications 65D07, 41A15, 41A58, pp. 1-24.

[90] J.C Carr, W.R Fright and R.K Beatson "Surface interpolation with radial basis function for radial imaging," *IEEE Transactions on Medical Imaging*, vol. 16, No.1, pp.96-107, February 1997.

[91] R. Franke, "Scattered data interpolation: Tests of some method," *Mathematics of Computation*, vol. 38, No. 157, pp. 181-200, 1982.

[92] B. Fornberg and N. Flyer, Accuracy of radial basis function interpolation and derivative approximations on 1-D infinite grids, University of Colorado and National Center for Atmospheric Research.

[93] Morse *et. al*., Interpolating implicit surfaces from scattered surface data using compactly supported radial basis functions, Department of Computer Science, Brigham Young University.

[94] S.R Karur and P.A Ramachandran, "Augmented thin plate spline approxomation in DRM," *Boundary Element Communications*, vol. 6 pp.55-58, 1995.

[95] Sarra *et al*., Multiquadric radial basis function approximation methods for the numerical solution of partial differential equations, Marshall University, June 2009.

[96] Lux *et al*., "Effects of early activator treatment in patients with class II malocclusion evaluated by thin-plate spline analysis," *Angle Orthodontist*, vol. 71, No.2, pp. 120-126, 2001.

[97] C.G Karydas *et al*., "Evaluating spatial interpolation techniques for mapping agricultural topsoil proprties in Crete," *EARSeL eProceedings 8*, 1/2009, pp. 26-39.

[98] A.M Nyete and T.J.O Afullo, "On the application of radial basis functions for the interpolation of the seasonal effective earth radius factor for South Africa," *Southern Africa Telecommunication Networks and Applications Conference*, 1-4 September 2013, Spier, Stellenbosch, Western Cape, South Africa, pp. 365-368.

Annexes

Annex 1: RF channel arrangement for FWS operating in bands below 7 GHz [37]

Band (GHz)	Frequency range (GHz)	Recommendations ITU-R F Series	Channel separation (MHz)
0.4	0.4061-0.430 0.4130-0.450	1567, Annex 1 1567, Annex 1	0.05; 0.1; 0.15; 0.2; 0.25; 0.6; 0.25; 0.3; 0.5; 0.6; 0.75; 1; 1.75; 3.5
1.4	1.35-1.53	1242	0.25; 0.5; 1; 2; 3.5
2	1.427-2.69 1.7-2.1; 1.9-2.3 1.9-2.3 1.9-2.3 1.9-2.3 2.3-2.5 2.29-2.67	701 382 1098 1098, Annexes 1,2 1098, Annex 3 746, Annex 1 1243	0.5 (pattern) 29 3.5; 2.5 (patterns) 14 10 1; 2; 4; 14; 28 0.25; 0.5; 1; 1.75; 2; 3.5; 7; 14; 2.5 (pattern)
3.6	3.4-3.8 3.4-3.8	1488, Annex 1 1488, Annex 2	$25^{(1)}$ $0.25^{(2)}$
4	3.8-4.2 3.7-4.2 3.6-4.2 3.6-4.2	382 382, Annex 1 635 635, Annex 1	29 28 10 (pattern) 90; 80; 60; 40;30
U4	4.4-5.0 4.4-5.0 4.4-5.0 4.54-4.9	1099 1099, Annex 1 1099, Annex 3 1099, Annex 2	10 (pattern) 40; 60; 80 28 40; 20
L6	5.925-6.425 5.85-6.425 5.925-6.425 5.925-6.425 5.925-6.425	383 383, Annex 1 383, Annex 1 383, Annex 2 383, Annex 3	29.65 90; 60; 40 28 40; 20; 10; 5
U6	6.425-7.11 6.425-7.11 6.425-7.11	384 384, Annexe 1 384, Annex 2	40; 30; 20; 10; 5 80 30; 14; 7; 3.5
7	7.25-7.55 7.425-7.725$(7.125-7.425)^{(3)}$ $(7.250-7.550)^{(3)}$ $(7.550-7.850)^{(3)}$ 7.125-7.425 7.425-7.725 7.435-7.75 7.11-7.75 7.425-7.90	385, Annex 5 385 385, Annex 1 385, Annex 1 385, Annex 2 385, Annex 3 385, Annex 4	3.5 7; 14; 28 1.75; 3.5; 7; 14; 28 1.75; 3.5; 7; 14; 28 5; 10; 20 28 28

(1) Frequency block bandwidth
(2) Basic frequency slot for aggregating wider frequency block bandwidth
(3) Alternative bands in parentheses

Annex 2: RF channel arrangement for FWS operating in bands above 7 GHz [37]

Band (GHz)	Frequency range (GHz)	Recommendations ITU-R F Series	Channel separation (MHz)
8	7.725-8.275 8.725-8.5 7.9-8.4 7.725-8.275 8.025-8.5 7.725-8.275 8.2-8.5	386, Annex 1 386, Annex 2 386, Annex 3 386, Annex 4 386, Annex 5 386, Annex 6 386, Annex 7	30; 20; 10; 5; 2.5; 1.25 14; 7 28; 14; 7 40; 20; 10; 5 28; 14; 7 29.65 11.662
10	10.0-10.68 10.0-10.68 10.15-10.65 10.15-10.65 10.15-10.65 10.5-10.68 10.55-10.68	747 747, Annex 4 747, Annex 3 1568, Annex 1 1568, Annex 2 747, Annex 1 747, Annex 2	1.25 and 3.5 patterns 3.5; 7; 14; 28 (patterns) 3.5; 7; 14; 28 (patterns) $28^{(1)}$ $30^{(1)}$ 7; 3.5 5; 2.5; 1.25 (patterns)
11	10.7-11.7 10.7-11.7 10.7-11.7 10.7-11.7 10.7-11.7	387 387, Annex 2 387, Annex 1 387, Annex 3 387, Annex 4	40 60 80 5; 10; 20 7; 14; 28
12	11.7-12.5 12.2-12.7	746, Annex 2 § 3 746, Annex 2, § 2	19.18 20 (pattern)
13	12.75-13.25 12.7-13.25	497 746, Annex 2, § 1	28; 14; 7; 3.5 25; 12.5
14	14.25-14.5 14.25-14.5	746, Annex 3 746, Annex 4	28; 14; 7; 3.5 7; 14; 28
15	14.4-15.35 14.5-15.35 14.5-15.35	636 636, Annex 1 636, Annex 2 636, Annex 3	56; 28; 14; 7; 3.5 2.5 (pattern) 2.5 5; 10; 20; 20; 30; 40; 50
18	17.7-19.7 17.7-19.7 17.7-19.7 17.7-19.7 17.7-19.7 17.7-19.7 17.7-19.7 18.58-19.16	595 595, Annex 1 595, Annex 2 595, Annex 3 595, Annex 4 595, Annex 5 595, Annex 6 595, Annex 7 595, Annex 7	220; 110; 55; 27.5 60 (block) 50; 40; 30; 20; 10; 5; 2.5 7; 3.5 27.5; 13.75; 7.5 7; 3.75; 1.75 55; 110 55; 27.5; 13.75 60

Annex 2 (*continued*)

Band (GHz)	Frequency range (GHz)	Recommendations ITU-R F Series	Channel separation (MHz)
23	21.2-23.6 21.2-23.6 22.0-23.6 21.2-23.6 21.2-23.6	637 637, Annex 1 637, Annex 2 637, Annex 3 637, Annex 4	3.5; 2.5 (patterns) 112 to 3.5 112 to 3.5 2.5; 5; 7.5; 10; 15; 20; 40; 50 112 to 3.5
27	24.25-25.25 24.25-25.25 25.25-27.5 25.27-26.98 24.5-26.5 27.5-29.5 27.5-29.5	748 748, Annex 3 748 748, Annex 3 748, Annex 1 748 748, Annex 2	3.5; 2.5 (patterns) $40^{(1)}$ 3.5; 2.5 (patterns) $60^{(1)}$ 112 to 3.5 3.5; 2.5 (patterns) 112 to 3.5
31	31.0-31.3 31.0-31.3	746, Annex 5 746, Annex 6	25; 50 28; 14; 7; 3.5
32	31.8-33.4 31.8-33.4	1520, Annex 1 1520, Annex 2	3.5; 7; 14; 28; 56; 112 $56^{(1)}$
38	36.0-40.5 36.0-37.0 37.0-39.5 38.6-39.48 38.6-40.0 39.5-40.5	749 749, Annex 2 749, Annex 1 749, Annex 2 749, Annex 2 749, Annex 3	3.5; 2.5 (patterns) 112 to 3.5 112; 56; 28; 14; 7; 3.5 $60^{(1)}$ $50^{(1)}$ 112 to 3.5
42	40.5-43.5 40.5-43.5 40.5-43.5	F.2005, Annex 1 F.2005, Annex 2 F.2005, Annex 3	112; 56; 28; 14; 7 Variable size blocks Mixed 112 to 7 and blocks
52	51.4-52.6	1496, Annex 1	56; 28; 14; 7; 3.5
57	55.78-57.0 57-59.0	1497, Annex 1 1497, Annex 2	56; 28; 14; 7; 3.5 100; 50
70/80	71-76 / 81-86 71-76 / 81-86 71-76 / 81-86 71-76 / 81-86	F.2006 F.2006, Annex 1 F.2006, Annex 2 F.2006, Annex 2	125 MHz (pattern) $n \times 250$ MHz blocks (n=1, …, 20) $n \times 250$ MHz channels (n=1, …, 18) $n \times 250$ MHz channels (n=1, …, 7)
94	92.0-94 / 94.1-95	F.2004	50, 100, $N \times 100$

(1)Frequency block bandwidth